Fundamental Physics of Ferroelectrics and Related Materials 2012

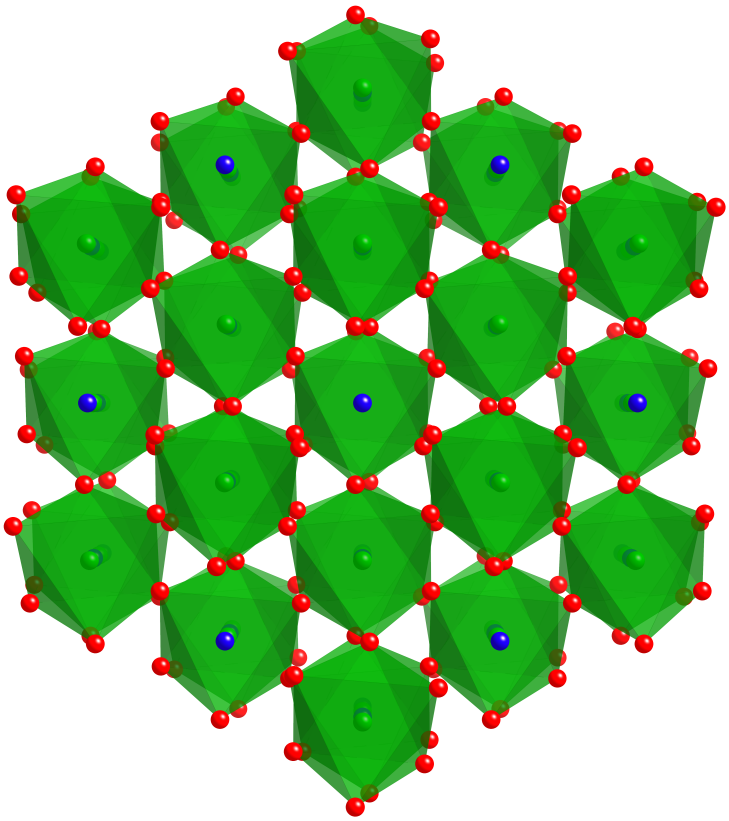

Argonne National Laboratory
Argonne, IL USA
January 29 - February 1, 2012

Organizers

Serge M. Nakhmanson, Argonne National Laboratory
Dillon D. Fong, Argonne National Laboratory
David J. Singh, Oak Ridge National Laboratory

Sponsors

Materials Theory Institute, Argonne National Laboratory
Physical Sciences & Engineering, Argonne National Laboratory
Advanced Photon Source, Argonne National Laboratory
Argonne, IL USA
www.anl.gov

CrysTec GmbH
Berlin, Germany
www.crystec.de

Workshop Web site

www.msd.anl.gov/science/fpf

Table of Contents

PROGRAM

Sunday, January 29, 2012 (ANL Guest House)

5:00-7:00pm: Registration and Welcome Reception

Monday, January 30, 2012 (TCS Conference Center, Bldg. 240)

7:30-8:00am: Registration
8:00-8:05am: Welcome/Announcements (P. B. Littlewood)
8:05-8:10am: In memoriam: R. Blinc (delivered by J. F. Scott)

Session 1: Novel materials: multiferroics (Session Chair: D. J. Singh)

8:15-8:45am: J. F. Scott (invited) - A New Room-Temperature Multiferroic (Ferromagnetic Ferroelectric): Lead iron-tantalate-zirconium-titanate $Pb(Fe,Ta,Zr,Ti)O_3$
8:45-9:05am: B. Dabrowski - Prediction and Realization of Breakthrough Multi-Ferroic Perovskites
9:05-9:35am: S. Kamba (invited) - Infrared studies of strained magnetoelectric thin films of EuO, $SrMnO_3$ and $Ca_3Mn_2O_7$
9:35-10:05am: A. A. Belik (invited) - High-pressure synthesis of new ferroelectric and multiferroic perovskite materials

10:05-10:30am: COFFEE

Session 2: Novel materials: ferroelectrics (Session Chair: D. Vanderbilt)

10:30-11:00am: R. E. Cohen (invited) - Ferroelectricity under applied pressure and applied electric fields
11:00-11:20am: Y. Uesu - Ferroelectric $(PbSnTi)O_3$ thin films synthesized by nucleation-mixture depositions and their structural and dielectric properties
11:20-11:40am: W. Parker - Epitaxial Strain Tunes Polarization and Electronic Band Gap in perovskite $SnTiO_3$

11:40am-1:00pm: LUNCH (ANL Guest House)

Session 3: Surface/interface compensation (Session Chair: J. A. Eastman)

1:00-1:30pm: M. J. Highland (invited) - Polarization of Ultrathin $PbTiO_3$ with Controlled Surface Compensation
1:30-1:50pm: K. Garrity - Ferroelectric Surface Chemistry: a first-principles study of the $PbTiO_3$ surface
1:50-2:10pm: Y. Watanabe - Properties of intrinsic ferroelectric surface in extreme clean limit: Giant 2D conduction on atomically clean surface of stoichiometric $BaTiO_3$ in UHV
2:10-2:30pm: Y.-M. Kim - Interface Mediated Stabilization of Ferroelectric and Non-Polar Phases of $BiFeO_3$

2:30-3:00pm: COFFEE

Session 4: Topological defects and domains (Session Chair: P. G. Evans)

3:00-3:30pm: L. Bellaiche (invited) - Binding of Electric Vortices with Electric Antivortices in Ferroelectrics and Multiferroics
3:30-4:00pm: S. Kalinin (invited) - Static and dynamics conductance of topological defects in ferroelectrics
4:00-4:20pm: C. Dubourdieu - Study of ferroelectricity in tetragonal $BaTiO_3$ epitaxial films grown on $SrTiO_3$-buffered Si(001) - Can this system exhibit negative capacitance?

4:20-4:40pm: MINI-BREAK

4:40-5:00pm: D. Su - Origin of 90° Domain Wall Pinning in $Pb(Zr_{0.2}Ti_{0.8})O_3$ Heteroepitaxial Thin Films
5:00-5:20pm: Q. Zhang - Domain Wall Dynamics of Ferroelectric Ultrathin Films
5:20-5:40pm: W. Wu - Conduction of topologically-protected charged ferroelectric domain walls
5:40-6:00pm: M. V. Holt – Elastic Relaxation and Local Strain in $BiFeO_3$ Nanostructures

7:00pm DINNER (Maggiano's Little Italy, Oak Brook, IL)

Tuesday, January 31, 2012 (TCS Conference Center, Bldg. 240)

Session 5: **Superlattices (Session Chair: S. M. Nakhmanson)**

8:00-8:30am: P. G. Evans (invited) - Nanosecond Dynamics in Ferroelectric/Dielectric Superlattices

8:30-8:50am: M. Dawber - New $PbTiO_3$ based superlattices with exceptional properties

8:50-9:20am: J. Junquera (invited) - Highly-confined spin-polarized two-dimensional electron gas in $SrTiO_3/SrRuO_3$ superlattices

9:20-9:50am: COFFEE

Session 6: **Phase Transitions (Session Chair: L. Bellaiche)**

9:50-10:10am: A. R. Damodaran - Phase Evolution and Stabilization in Highly-Strained Epitaxial $BiFeO_3$ Films: Implications for Enhanced Electromechanical Response

10:10-10:30am: S. Prosandeev - Novel Properties in $BiFeO_3$ Films

10:30-10:50am: A. Roytburd - Stability and Field Induced Response of Heterophase Nanostructures in Constrained Ferroelectrics and Ferroelastics

10:50-11:10am: Z.-G. Ye - Tricritical Points and Related Properties of $Pb(Zr_{1-x}Ti_x)O_3$ Single Crystals

11:10-11:30am: A. Bussmann-Holder - Tuning the structural instability of $SrTiO_3$ by Eu doping: the phase diagram of $Sr_{1-x}Eu_xTiO_3$

11:30am-1:00pm: LUNCH (ANL Guest House)

Session 7: **Relaxors (Session Chair: R. E. Cohen)**

1:00-1:30pm: A. M. Rappe (invited) - Molecular Dynamics Study of Dielectric Response in a Relaxor Ferroelectric

1:30-1:50pm: C. Stock - Magnetic and ferroelectric relaxor properties in $PbFe_{1/2}Nb_{1/2}O_3$

1:50-2:10pm: S. Vakhrushev - Diffuse scattering in perovskites

2:10-2:40pm: P. M. Gehring (invited) - Anisotropic Acoustic Lattice Dynamics in $PbMg_{1/3}Nb_{2/3}O_3$

2:40-3:00pm: COFFEE

Session 8: **Flexoelectricity (Session Chair: J. Junquera)**

3:00-3:20pm: D. Vanderbilt - First-principles theory of flexoelectricity

3:20-3:40pm: A. Tagantsev - Flexoelectric effect in finite samples

3:40-4:00pm: I. Naumov - Flexoelectric effect in 2D sp^2-bonded crystals

4:00-6:00pm: **POSTERS (TCS Conference Center, Bldg. 240)**

Wednesday, February 1, 2012 (TCS Conference Center, Bldg. 240)

Session 9: **Modeling (Session Chair: K. M. Rabe)**

8:00-8:30am: R. Resta (invited) - Dynamical matrix in magnetoelectrics

8:30-8:50am: N. Benedek - Coexistence of ferroelectricity and octahedral rotations in ABX_3 perovskites

8:50-9:10am: H. Moriwake – Structural analysis of ferroelectric phase of $CdTiO_3$ from first-principles calcuations

9:10-9:30am: J. Hong - Spin-phonon coupling effects in transition-metal perovskites: a DFT+U and hybrid-functional study

9:30-9:50am: E. Walter - First-principles calc of Sc NMR parameters in $Pb(Sc_{2/3}W_{1/3})O_3$

9:50-10:10am: J. Wojdel - All-atom ab-initio models for perovskite ferroelectrics and lattice mode interactions in $PbTiO_3$

10:10-10:40am: COFFEE

Session 10: **Techniques (Session Chair: M. J. Highland)**

10:40-11:00am: N Barrett - Full field electron spectromicroscopy of ferroelectric materials

11:00-11:20am: J. W. Freeland - Structural Control of Magnetic Anisotropy in a Multiferroic $EuTiO_3$ Thin Film

11:20-11:40am: Y. Li - Ultrafast optical manipulation of the ferroelectric order in multiferroic bismuth ferrite

11:40-12:00pm: A. Lindenberg - Ultrafast terahertz and x-ray probes of ferroelectric structural and electronic dynamics

12:00pm: LUNCH (ANL Guest House) and adjourn

Poster Session, Tuesday, Jan 31, 4-6pm (TCS Conference Center, Bldg. 240)

	Author(s)	Title	Subject
PS01	M.C. Ehmke, J.E. Blendell, K.J. Bowman	The Influence of Phase Coexistence and Ferroelastic Domain Texture on the Performance in $Ba(Zr_{0.2}Ti_{0.8})O_{3-x}(Ba_{0.7}Ca_{0.3})TiO_3$ Piezoceramics	Domains
PS02	J. Karthik, A. R. Damodaran, L. W. Martin	Effect of 90° domain walls on the dielectric and pyroelectric susceptibilities of epitaxial ferroelectric thin films	Domains
PS03	T. Nishimatsu, K. Aoyagi, T. Kiguchi, T.J. Konno, Y. Kawazoe, A. Kumar, U.V. Waghmare	Heating-up and cooling-down molecular-dynamics simulations of 90-degree domain structures in $PbTiO_3$	Domains
PS04	C.M. Schlepütz, Y. Yang, C. Adamo, D.G. Schlom, R. Clarke	Stripe domain evolution in ultrathin $BiFeO_3$ films grown on $TbScO_3$ (110)	Domains
PS05	T. Sluka, A.K. Tagantsev, D. Damjanovic, M. Gureev, N. Setter	Enhanced Electromechanical Response of Ferroelectrics Due to Charged Domain Walls	Domains
PS06	Z. Zhao, J. Blendell, K. Bowman, R. Edwin Garcia	Modeling Domain Dynamics in Single- and Polycrystalline Ferroelectrics	Domains
PS07	R. Adhikari, H. Fu	Electronic structure of LaO doped $SrTiO_3$	Modeling
PS08	S. Amisi, E. Bousquet, K. Katcho, P. Ghosez	First-principles study of structural and vibrational properties of $SrZrO_3$	Modeling
PS09	Y. Cao, S. Bhattacharya, C.A. Randall, L.Q. Chen	Phase-field modeling of resistance degradation and I-V characteristics in perovskite-based ferroelectric oxides	Modeling
PS10	R. Grigalaitis, S. Lapinskas, J. Banys, E.E. Tornau	Dynamics of Relaxation Times in the Three-Dimensional Ising Model	Modeling
PS11	R. Herchig, K. Schultz, K. McCash, I. Ponomareva	Terahertz Frequency Dynamics of Ferrolectric Nanowires	Modeling
PS12	S. Liu, T. Hiroyuki, I. Grinberg, A.M. Rappe	Development of Classical Potential for $PbTiO_3$	Modeling
PS13	N. Ng, K. Bhattacharya	Multiphysics model of semiconducting ferroelectrics and its application to memory devices	Modeling
PS14	A. Prikockytė, C. Dubourdieu, P. Ghosez	Role of electrical and mechanical boundary conditions on the ferroelectric properties of $YMnO_3$ epitaxial thin films	Modeling
PS15	A. Raeliarijaona, H. Fu	Response of zone-center phonon structure to epitaxial strain in $BaTiO_3$	Modeling
PS16	D. Rahmedov, L. Bellaiche, D. Wang, J. Iniguez	Magnetic cycloid of $BiFeO_3$ from atomistic simulations	Modeling
PS17	M. Rose, R.E. Cohen	The Electrocaloric Effect and the Relationship Between Homogenous Polarization Switching and Phase Transitions in Ferroelectrics	Modeling
PS18	S. Subramanian, T. Ozaki, K. Yamauchi, T. Oguchi, N. Baskaran	A first principle structure dynamics study of doping lone pair A cations to $HoMnO_3$	Modeling
PS19	L.F. Wan, T. Nishimatsu, S.P. Beckman	The piezoelectric tensor components of the known phases of $KNbO_3$ calculated by first-principle methods	Modeling
PS20	N. Barrett, J. L. Wang, A. Pancotti, P. Jégou, G. Niu, B. Gautier, Y.Y. Mi, L. Tortech, S. Yin, B. Vilquin	Ferroelectricity in Quasi-Amorphous BaTiO3 Ultra-thin Film	Novel Materials
PS21	J.W. Bennett, K.F. Garrity, K.M. Rabe, D. Vanderbilt	Switchable polarization in stuffed wurtzite compounds, a new class of ferroelectrics	Novel Materials

PS22	V.R. Cooper, S. Takagi, D.J. Singh	First principles prediction of morphotropic phase boundaries in Bi-based ferroelectrics	Novel Materials
PS23	S. Ducharme	Applications of ferroelectric polymer and oligomer thin films	Novel Materials
PS24	C. Fancher, J.E. Blendell, K.J. Bowman	Poling Induced Fatigue in <100> Textured Lead-Free Piezoelectric $Na_{0.5}Bi_{0.5}TiO_3$ (NBT)	Novel Materials
PS25	A.T. Mulder, N.A. Benedek, C.J. Fennie	Crossover between hybrid improper ferroelectricity and proper ferroelectricity in layered perovskites	Novel Materials
PS26	W. Ren, Y. Yang, W. Chen, L. You, Z. Chen, Y. Qi, X. Zou, J. Wang, T. Sritharan, P. Yang, L. Chen, L. Bellaiche	Sm-doped $BiFeO_3$ films under compressive strain	Novel Materials
PS27	S.K. Saha, P. Ghosez	Structural, electronic, and vibrational properties of chloride-based perovskites : A first-principles study	Novel Materials
PS28	Z. Gui, S. Prosandeev, L. Bellaiche	Properties of epitaxial (110) $BaTiO_3$ films from first principles	Phase Transitions
PS29	D. K. Jackson, R. Pattnaik, J. Toulouse	Temperature evolution of the linear birefringence in striated single crystals of $KTa_{1-x}Nb_xO_3$ (KTN)	Phase Transitions
PS30	F. Kadlec, C. Kadlec, P. Kuzel, J. Petzelt	Ferroelectric phase transition in GeTe studied by time-domain THz spectroscopy	Phase Transitions
PS31	A. Kvasov, A. Tagantsev	Can we trust the temperature - misfit strain thin film phase diagrams?	Phase Transitions
PS32	K. McCash, A. Srikanth, I. Ponomareva	Polarization Reversal in Ultrathin Ferroelectric Nanowires under High Electric Fields	Phase Transitions
PS33	Y. Xie, A.A. Bokov, X. Long, Z.-G. Ye	Studies of Domain Structure and Phase Transitions in $PbZr_{1-x}Ti_xO_3$ Single Crystals	Phase Transitions
PS34	M. Ahart, S. Kojima, Z.-G. Ye, R.J. Hemley	Structural transition in $Pb(In_{1/2}Nb_{1/2})O_3$ under pressure	Relaxors
PS35	A. Al-Barakaty, L. Bellaiche	The effects of Oxygen vacancies on properties of PMN-25%PT: a first-principles-based study	Relaxors
PS36	P. Ondrejkovic, M. Kempa, J. Hlinka, J. Kulda, H. Luo, Q. Zhang	Waterfall anomaly in $(Na_{0.5}Bi_{0.5})_{0.96}Ba_{0.04}TiO_3$ single crystal	Relaxors
PS37	H. Takenaka, I. Grinberg, A.M. Rappe	Molecular Dynamics Study of Local Structure and Dynamics in a Relaxor Ferroelectric	Relaxors
PS38	S.J. Callori, J. Gabel, D. Su, J. Sinsheimer, M.V. Fernandez-Serra, M. Dawber	Compositional inversion symmetry breaking in $PbTiO_3/SrRuO_3$ superlattices	Superlattices
PS39	R.S. Katiyar, N. Ortega, A. Kumar	Ferroelectric and Dielectric Properties of $BaTiO_3/Ba_{(1-x)}Sr_xTiO_3$ Superlattices	Superlattices
PS40	J. Sinsheimer, S.J. Callori, Y. Benkara, B. Bein, J. Daley, D. Su, M. Dawber	Engineered polarization rotation in $PbTiO_3/CaTiO_3$ superlattices	Superlattices
PS41	Y. Yang, W. Ren, M. Stengel, X.H. Yan, L. Bellaiche	Phase transitions in epitaxial $PbTiO_3/BiFeO_3$ superlattice from first principles	Superlattices
PS42	V. Železný, C. Kadlec, A. Soukiassian, X.X. Xi, D.G. Schlom	Folded acoustic phonons in infrared spectroscopy of $BaTiO_3/SrTiO_3$ superlattices	Superlattices
PS43	J. Banys, S. Rudys, M. Ivanov, R. Grigalaitis, N.P. Vyshatko, A.D. Shilin, A.N. Salak	Meyer-Neldel rule for electrical conductivity observation in xNBT–(1-x)LMT ceramics	Techniques
PS44	E. Buixaderas, I. Gregora, J. Hlinka, J. Dec	Raman and IR phonons in $Sr_xBa_{1-x}Nb_2O_6$ single crystals	Techniques

PS45	I.S. Golovina, B.D. Shanina, I.N. Geifman	EPR study of $KTaO_3$:Mn nanopowder	Techniques
PS46	N. Inoue, R.A. Maier, A. Honda, H. Takagi, C.A. Randall	Evaluation of defect dipole dissociation energy in rare earth and magnesium co-doped $BaTiO_3$ by TSDC (Thermally Stimulated Depolarization Current) measurement	Techniques
PS47	Y.-M. Kim, M.D. Biegalski, J. He, H.M. Christen, S.T. Pantelides, S.J. Pennycook, A.Y. Borisevich	Direct Atomic-Scale Measurement of Oxygen Stoichiometry in Cobaltite Thin Films	Techniques
PS48	J.H. Lee, S.-H. Chang, I.C. Tung, S.M. Nakhmanson, J. Eastman, D. Fong, H. Hong, J.W. Freeland	Development of molecular-beam epitaxy for in-situ synchrotron x-ray study of layered complex oxides	Techniques
PS49	B. Ma, M. Narayanan, S. Liu, S. Chao, S. Tong, U. Balachandran	Ferroelectric PLZT Films Grown on Metal Foils by Chemical Solution Deposition	Techniques
PS50	I. C. Tung, J. Liu, B. Gray, J. Chakhalian, J.M. Rondinelli, E.A. Karapetrova, J.H. Lee, M.J. Bedzyk, J.W. Freeland	Influence of Symmetry on the Octahedral Rotations of Epitaxial $RNiO_3$ Thin Films	Techniques
PS51	Y. Yang, C.M. Schlepütz, C. Adamo, D.G. Schlom, R. Clarke	Structural Investigation of Ultrathin $BiFeO_3$ Films on $SrTiO_3$ (001) Substrates	Techniques

Withdrawn:

	E. Iolin	Neutron Scattering by the Transverse Optic Wave in Relaxors. Effect of Interaction between TOW Vortex and Polarized Nano Regions	Relaxors

Professor Robert Blinc – In Memoriam

On September 26, 2011, Professor Robert Blinc passed away. Robert Blinc was born on October 31, 1933, in Ljubljana, Slovenia. He graduated in 1958 and completed PhD in 1959 in physics at the University of Ljubljana. His doctoral research on proton tunneling in ferroelectrics with short hydrogen bonds was supervised by Professor Dušan Hadži. After a postdoctoral year spent in the group of Professor John Waugh at M.I.T., Cambridge, Mass., Robert Blinc was appointed as a professor of physics at the University of Ljubljana at a time when there was scarce research in the field of condensed matter physics in Slovenia. With his far-sighted mind, Robert Blinc initiated the NMR laboratory at the Jožef Stefan Institute in Ljubljana. He immediately realized the enormous potential of NMR methods in the research of structure, dynamics, and phase transitions in solids. In the subsequent years he made significant contributions in applying magnetic resonance to the research of ice, ferroelectric materials, liquid crystals, incommensurate dielectrics, pseudospin glasses, relaxor ferroelectrics, fullerenes, and fullerene nanomagnets. His work led to the detailed understanding of the

microscopic nature and properties of those materials. To mention only a few of his achievements: Robert Blinc and coworkers elucidated the isotopic effect in ferroelectric crystals, developed the tunneling model of hydrogen bonded ferroelectrics (known as the Blinc–de Gennes model), predicted the phason Goldstone mode in helicoidal ferroelectric liquid crystals and the first theory of unwound ferroelectric liquid crystals, discovered the relaxation mechanism via nematic order fluctuations in liquid crystals (the Pincus–Blinc model), detected solitons and phasons in incommensurate systems using NMR, determined the Edwards-Anderson order parameter in proton and deuteron glasses, developed the random bond–random field Ising model of proton and deuteron glasses (the Pirc–Tadić–Blinc model), developed the spherical random bond–random field model of relaxors, revealed the nature of ferromagnetism in organic ferromagnet TDAE-C_{60} and discovered the origin of giant electromechanical effect in PMN-PZT relaxors via the existence of critical end point. He also pioneered the application of NMR to the nondestructive oil-content measurements in plant seeds, the hardening-rate determination of cements and concrete by NMR relaxometry and the TNT explosive detection by nitrogen NQR, where he is the holder of three patents . In the early stage of the double resonance technique, he succeeded in obtaining the first nitrogen NMR spectra in nucleic acids and peptides.

The bibliography of Robert Blinc is very rich, containing more than 700 original research papers in international scientific journals. Among these, he has published three papers in *Nature* (1958, 1966, 2006), two in *Science* (both in 1996) and 47 in *Physical Review Letters*. His publications were cited more than 14.000–times in SCI. One of the most important achievements of Professor Robert Blinc, which attracted considerable attention in the broad scientific community, is the book *Soft Modes in Ferroelectrics and Antiferroelectrics* (North Holland, 1974), written together with Boštjan Žekš. The book was translated into Russian (1975) and Chinese (1982) and belongs to the 600 most-cited scientific books in the world. Another of his books, written together with Igor Muševič and Boštjan Žekš, *The Physics of Ferroelectric and Antiferroelectric Liquid Crystals*, was published in 2000 by World Scientific. His last book *Advanced Ferroelectricity* (Oxford Science Publications) appeared in August 2011, shortly before he passed away.

Being a professor of physics at the University of Ljubljana, Robert Blinc was the supervisor of 67 diploma works and 35 PhD theses in the field of condensed matter physics and NMR spectroscopy. He was the founder and the head of the Condensed Matter Physics Department at the Jožef Stefan Institute for 47 years and a member (and vice-president in the years 1980–1999) of the Academy of Science and Arts of Slovenia. Robert Blinc maintained a wide range of contacts with scientists worldwide. To mention only a few of them, he was a visiting professor at the University of Washington in Seattle; ETH Zurich, Switzerland; Federal University of Minas Gerais in Belo Horizonte, Brazil; University of Vienna in Austria; University of Utah in Salt Lake City; Kent State University in Ohio, Argonne National Laboratory, and several others. In the years 1990–1996 he was the president of the Groupement AMPERE, and the president of the European Steering Committee on Ferroelectricity (1986–1999). He was a member of seven foreign Academies of Sciences and has received numerous national and international scientific prizes.

As the head of the Condensed Matter Physics Department at the Jožef Stefan Institute, Robert Blinc promoted, in addition to NMR, other experimental techniques: ESR, dielectric measurements, optical spectroscopy and atomic force microscopy. He took active part in solving theoretical problems related to the systems under study. He can therefore be recognized as the founder and tireless promoter of the condensed matter physics research in Slovenia. We, his former students and coworkers, owe him a debt of gratitude for his enthusiasm and dedication to the phenomena of solid-state physics and magnetic resonance spectroscopy. He will remain in our memories.

Prof. dr. Janez Dolinšek
J. Stefan Institute, University of Ljubljana, Jamova 39, SI-1000 Ljubljana, Slovenia
AMPERE Vice-president

Abstracts for Oral Presentations

(Listed in order of presentation)

Session 1
Novel materials: multiferroics

A New Room-Temperature Multiferroic (Ferromagnetic Ferroelectric): Lead iron-tantalate-zirconium-titanate $Pb(Fe,Ta,Zr,Ti)O_3$

J. F. Scott,[1,2] A. Kumar,[2] Nora P. Ortega,[2] and R. S. Katiyar[2]

1) Dept. Physics, Cavendish Laboratory, Cambridge University, Cambridge, U.K.
2) Dept. Physics, Speclab, Univ. Puerto Rico, San Juan, Puerto Rico, USA

Until now only one room-temperature multiferroic ($BiFeO_3$) has been known since 1959. Here we report ball milling single-phase bulk ceramic specimens of PFT [$PbFe_{1/2}Ta_{1/2}O_3$] mixed with PZT [$PbZr_{0.53}Ti_{0.47}O_3$]. The results for 40% PFT exhibit long-range order and four phases: cubic *Pm3m* for T > 1123K; tetragonal *4mm* for 520K < T < 1123K; orthorhombic *mm2* for 250K < T < 520K; and rhombohedral for T < 250K, analogous to those in $BaTiO_3$. The *4mm* and *mm2* phases are ferroelectric with low loss hysteresis curves, large polarization (ca. 30 $\mu C/cm^2$) and high dielectric constants (ca. 30). The *4mm-mm2* transition appears to be second-order. Magnetic hysteresis at 300K is also well-defined, and a weak (2%) shift in magnetization at *E*=35 kv/cm is measured.

There are several known room-temperatures magnetoelectrics, but not room-temperature multiferroics. Although Cr_2O_3 is a room-temperature magnetoelectric (Astrov; Dzyaloshinskii 1959), it is not a ferromagnetic ferroelectric; and the recently reported $EuTiO_3$ under stress is strongly ferromagnetic and ferroelectric at cryogenic temperatures (Schlom *et al.,* Nature 2011), bismuth ferrite remains the only room-temperature ferroelectric ferromagnet. Discovered by Smolensky and Agranovskaya in 1959, its preparation as high-quality thin films by Ramesh *et al.* in 2003 has sparked great interest in applications of multiferroics to devices. Here we report the growth and characterization of a second family of room-temperature ferroelectric ferromagnets, prepared as bulk ceramics via ball milling. The materials are single-phase combinations of $PbFe_{1/2}Ta_{1/2}O_3$ and "PZT" $PbZr_{0.53}Ti_{0.47}O_3$. These are very low loss materials (ca. 2-3% loss tangent), an advantage over bismuth ferrite.

In the figures below we illustrate the polarization hysteresis at room temperature for 30% and 40% PFT and 70-60% PZT. (Figs. 1-4 in the talk have been eliminated from this extended abstract to save space.)

The figure labeled 5 shows good low-loss ferroelectric hysteresis in both 30/70% and 40/60% PFT/PZT single phase bulk ceramics. The figure labeled 6 shows ferroelectric hysteresis as a function of temperature in both the *4mm* and *mm2* ferroelectric phases. And the figure labeled 7 shows magnetic hysteresis at 295K in both samples.

In earlier work we examined related materials, emphasizing $PbFe_{2/3}W_{1/3}0_3$ mixed with PZT and prepared as pulsed laser deposited (PLD) thin films [1]; however, these were found to be relaxor materials with no long-range order at any temperature. And the sample characteristics were difficult to reproduce. The present study of ball-milled PFT/PZT ceramics finds no relaxor behavior (e.g., no frequency dependent dielectric losses). We believe that this important difference can be understood in terms of the 1981 work by Setter and Cross on $PbSc_{1/2}Ta_{1/2}O_3$ "PST". They found that Sc and Ta ordered perfectly in carefully annealed specimens but not at all in other specimens. $PbSc_{1/2}Ta_{1/2}O_3$ is very similar to $PbFe_{1/2}Ta_{1/2}O_3$, with Sc^{+3} or Fe^{+3} ions sharing B-sites with Ta^{+5}. In the present case there are four kinds of B-site ions: Fe^{+3}, Ta^{+5}, Zr^{+4}, and Ti^{+4}, and their clustering is apparently sensitive to processing (see the magnetic resonance study by Blinc *et al.* on pure PFT). One evidence for Fe clustering is that T_{Neel} is higher than would be estimated from the percentage of Fe^{+3} ions at the B-site (15-20% in our specimens).

Finally we note that this system may be amenable to *ab initio* modeling. Athough the ratio of Fe, Ta, Zr, Ti in the present experiment would require very large unit cells, an initial effort might consider only 1/6 Fe, 1/6 Ta, 1/3 Zr, and 1/3 Ti [that is, 33% PFT, and 67% $PbZr_{0.5}Ti_{0.5}O_3$] and perfectly ordered B-site ions. This is probably within the limits of present *ab initio* techniques.

Reference:

[1] Kumar A, Sharma G L, Katiyar R S, Pirc R, Blinc R, and Scott J F, *Magnetic control of large room temperature polarization*, JOURNAL OF PHYSICS CONDENSED MATTER **21**, 382204 (2009).

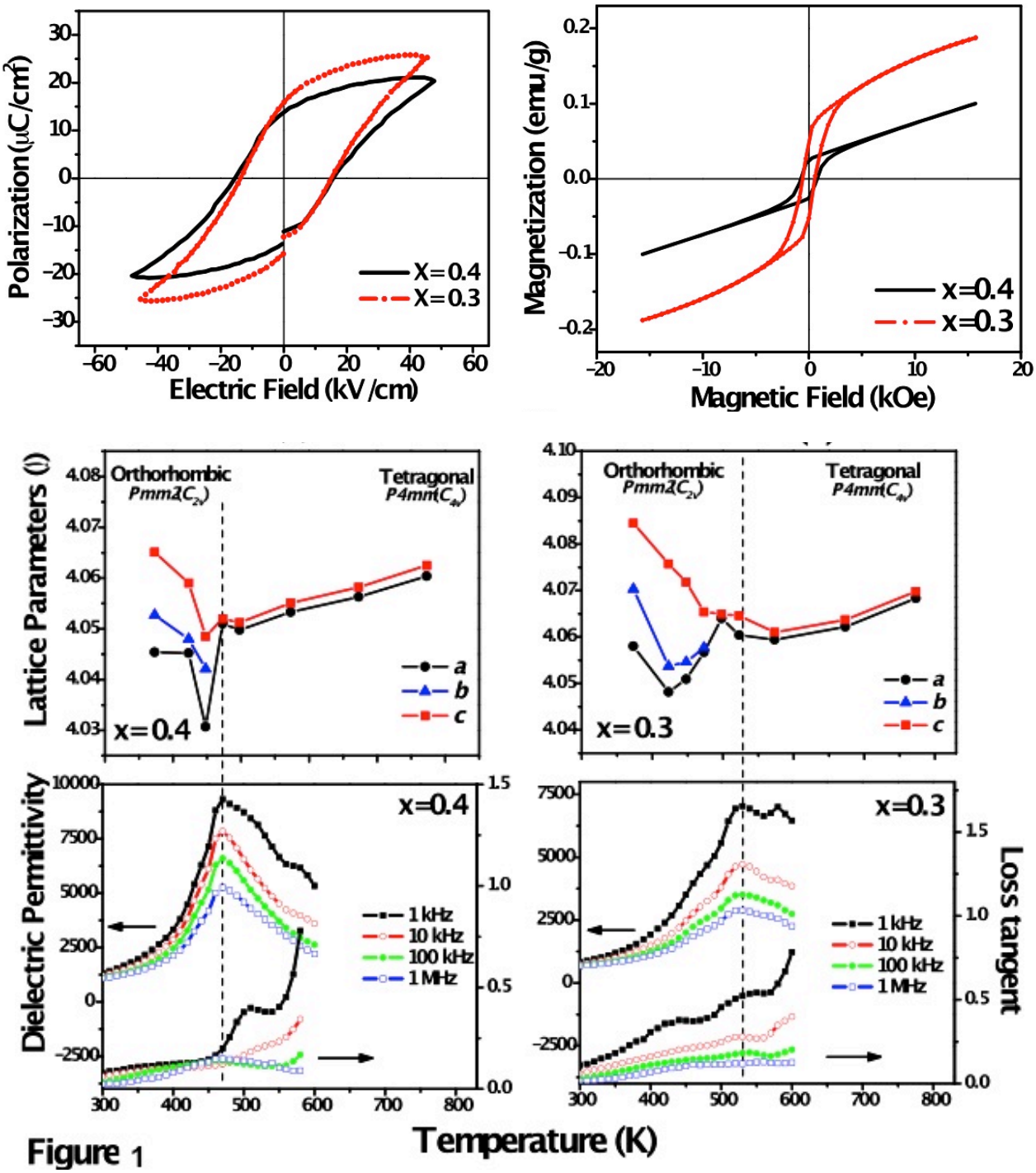
Polarization (μC/cm²)
Electric Field (kV/cm)
X=0.4
X=0.3
Magnetization (emu/g)
Magnetic Field (kOe)
x=0.4
x=0.3
Lattice Parameters (Å)
Orthorhombic
Pmm2(C2v)
Tetragonal
P4mm(C4v)
a
b
c
x=0.4
x=0.3
Dielectric Permittivity
Loss tangent
1 kHz
10 kHz
100 kHz
1 MHz
Temperature (K)

Figure 1

Prediction and Realization of Breakthrough Multi-Ferroic Perovskites

Bogdan Dabrowski,
Northern Illinois University, DeKalb, IL, USA

Abstract

Search for multi-ferroic materials, where magnetism and ferroelectricity are strongly coupled, is of fundamental technological and theoretical importance. Room temperature magnetic ferroelectricity, showing unique sensitivity to applied magnetic fields could lead to several new revolutionary magneto-electronic devises. Typically, both phenomena tend to be mutually exclusive because ferroelectricity is usually present for d^0 (for example M=Ti^{4+}, V^{5+}, Nb^{5+}) and magnetism for non-d^0 (for example, M=Cr^{4+}, Mn^{3+}, Mn^{4+}, Fe^{3+}, Co^{3+}) transition metals. Coupling between post-transition metal's (for example, Pb^{2+}, Bi^{3+}) ferroelectricity of s- and p-electrons and transition metal's d-electrons magnetism is known (for example, $Bi^{3+}Fe^{3+}O_3$), but it is weak and not of practical usage.

As a result of over 20 years of research on transition metal perovskites AMO_3 we have developed empirical "tolerance factor synthesis-properties design rules" for predicting and obtaining perovskite compounds exhibiting unique properties [1,2]. These "design rules" rely on simple geometrical factors; for example, tolerance factor $t = [A\text{-}O]/\sqrt{2}[M\text{-}O]$ to correlate stability of the perovskite structure and it's properties to the M–O–M bond angle, the M formal valence, and the [A-O] and [M-O] equilibrium interatomic distances. By using temperature dependent neutron diffraction studies in conjunction with thermogravimetric analysis we have observed that t = t(x,T,d) is a strong function of chemical composition, temperature, and oxygen non-stoichiometry (see Fig. 1 for measured and modeled compositional and temperature dependence of t(x,T) for $Sr_{1-x}Ca_xMnO_3$ system (a) and $CaTiO_3$ (b)). When t = 1 perovskites exhibit cubic crystal structure because lengths of [A-O] and [M-O] bonds are perfectly matched. Vast majority of known perovskites have t < 1 at room temperature. Their bonds lengths mismatch is accommodated by rotations of the MO_6 octahedral units, which decrease the M–O–M bond angles form 180^o and lower the crystal symmetry. When t > 1 the mismatch is accommodated by elongation of [M-O] bonds beyond their equilibrium lengths but cubic crystal structure it usually retained (see Fig. 2 (a) for room temperature extrapolated t(x) for Alkaline Earths substituted Lanthanum titanates). In a few cases when the tension is too large (for example, $Ba^{2+}Ti^{4+}O_3$), the classical ferroelectric effects occur above room temperature at $T_F \sim 400$ K, once the M (d^0) ions move out of the center of the MO_6 octahedral units resulting in large electric dipole for each unit cell.

We have projected that similar effects should be observed for non-d^0 insulating and antiferromagnetic ($T_N \sim 240$ K) perovskites of Mn^{4+} (d^3), resulting thus, in a strong ferroelectric-magnetic coupling of the same d-electrons of Mn [3]. Figure 2(b) shows extrapolated room temperature t(x) for Alkaline Earths substituted Lanthanum manganites. Clearly, t(x,T) are much larger than 1 at room temperature and should achieve even higher values on heating for both La-Sr-Ba substituted titanates and manganites. However, to date we were not able to observe ferroelectric distortion in manganites because the [Mn-O] bonds have not been put under

sufficient tension; for example, we were able to synthesize the $Sr_{1-x}Ba_xMnO_3$ samples only with $x \leq 0.4$ [4]. Recently, Tokura group [5] managed to achieve x = 0.45 and 0.50 compositions and observed spectacularly strong multi-ferroic behavior with $T_F \sim 400$ K and $T_N \sim 220$ K. I will describe our recent attempts to obtain these and similar magnetic manganites with elongated Mn-O bonds. Structural, magnetic and ferroelectric properties will be discussed.

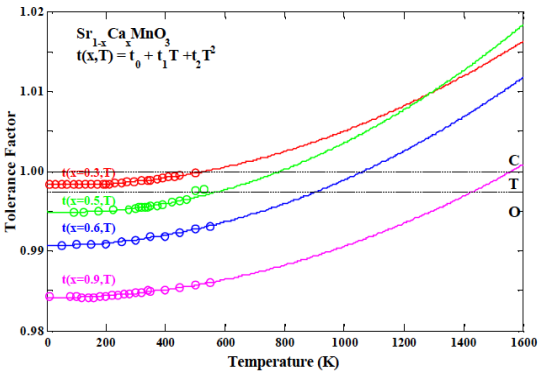

Fig. 1 (a)

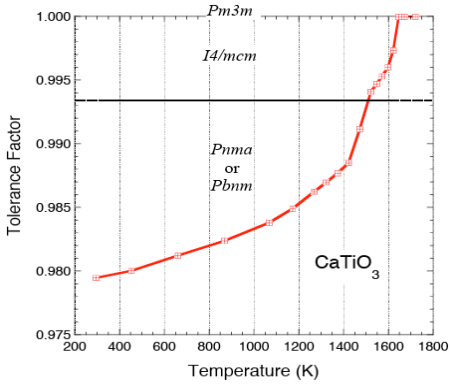

Fig. 1 (b)

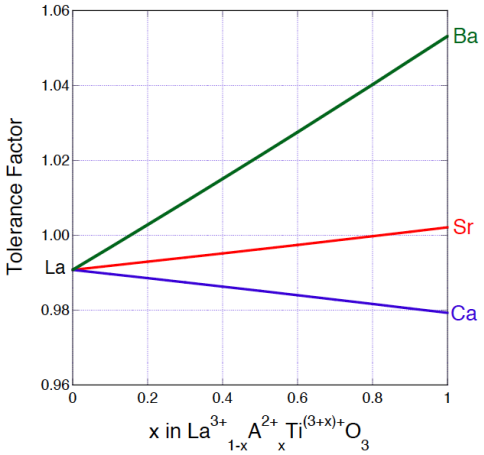

Fig. 2 (a)

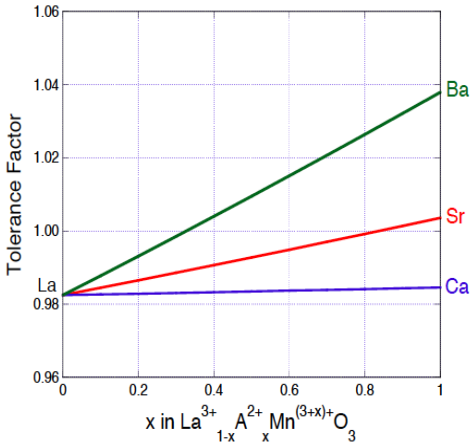

Fig. 2 (b)

References

[1] Tolerance Factor Rules for $Sr_{1-x-y}Ca_xBa_yMnO_3$ Perovskites. B. Dabrowski, O. Chmaissem, J. Mais, S. Kolesnik, J.D. Jorgensen, and S. Short, J. Solid State Chem. 170, 154-164 (2003);

[2] Design Rules for Manganites with Novel Magnetic and Electronic Properties. B. Dabrowski, O. Chmaissem, J. Mais, and S. Kolesnik, Acta Physica Polonica A 105, 45-56 (2004)

[3] New Pathways to Strongly Correlated and Multi-Functional Transition Metal Perovskites: Phase Stability and Properties by Design. Bogdan Dabrowski, Proposal submitted to NSF, 2006

[4] Relationship between structural parameters and Néel temperature in Sr1-xCaxMnO3 ($0 \leq x \leq 1$) and Sr1-yBayMnO3 ($y \leq 0.2$), O. Chmaissem, B. Dabrowski, S. Kolesnik, J. Mais, D.E. Brown, R. Kruk, P. Prior, B. Pyles, J.D. Jorgensen, Phys. Rev. B 64, 134412 (2001); J. Mais, et. al., unpublished

[5] Displacement-Type Ferroelectricity with Off-Center Magnetic Ions in Perovskite Sr1-xBaxMnO3. H. Sakai, J. Fujioka, T. Fukuda, D. Okuyama, D. Hashizume, Kagawa, H. Nakao, Y. Murakami, T. Arima, A. Q. R. Baron, Y. Taguchi, and Y. Tokura, Phys. Rev. Lett. 107, 137601 (2011)

Infrared studies of strained magnetoelectric thin films of EuO, $SrMnO_3$ and $Ca_3Mn_2O_7$

S. Kamba, V. Goian, M. Kempa, V. Bovtun, D. Nuzhnyy, P. Vaněk

Institute of Physics, Academy of Sciences of the Czech Republic, Na Slovance 2, 18221 Prague 8, Czech Republic

C. Adamo, C.M. Brooks, A. Melville, D.G. Schlom
Department of Materials Science and Engineering, Cornell University, Ithaca, New York, 14853-1501, USA

The set of multiferroic materials is markedly limited in nature. Many multiferroics only exhibit a coexistence of antiferromagnetic and ferroelectric ordering and therefore their magnetoelectric coupling is small. In type-II multiferroics, the ferroelectric state is induced by a special antiferro- or ferrimagnetic ordering and for that reason the magnetoelectric coupling is large in such materials. Unfortunately, the critical magnetic and ferroelectric temperatures are mostly low in such systems, which so far rule out any practical applications of multiferroics in memory, magnetic sensors and other magnetoelectric devices.

Fennie and Rabe[1] suggested a new route for preparation of multiferroics with a strong magnetoelectric coupling. They proposed the use of biaxial strain in epitaxial thin films to induce the ferroelectric and ferromagnetic state in materials that are typically paraelectric and antiferromagnetic in bulk form. A requirement for such a material is the existence of strong spin-phonon coupling. Fennie and Rabe[1] proposed, based on their first principles calculations, the use $EuTiO_3$ for such a purpose. Recently, some researchers have confirmed their theoretical prediction and revealed ferroelectric and ferromagnetic ordering in tensile strained $EuTiO_3$ thin films deposited on $DyScO_3$ substrates.[2] In this case 1% tensile strain induced ferroelectricity at 250 K and ferromagnetisim at 4.2 K. Unfortunately, the magnetic Curie temperature in $EuTiO_3$ is too low for practical applications, but the new approach for the preparation of artificial multiferroics, which do not exist in bulk form, was demonstrated.

This contribution is devoted to the experimental search for other strain-induced multiferroics, that should have higher critical temperatures than $EuTiO_3$. We will concentrate on the study of EuO, $Ca_3Mn_2O_7$ and $SrMnO_3$ thin films, which were recently predicted to be multiferroic using first principles calculations.[3-5] All the films were grown using reactive molecular-beam epitaxy. Direct low-frequency dielectric measurements are mostly impossible due to the leakage current present in the strained thin films. Therefore we have used contactless infrared (IR) and microwave dielectric measurements, which are affected only slightly or even not at all by conductivity of the films.

Semiconducting binary oxide EuO crystallizes in a simple rocksalt structure and it undergoes a ferromagnetic phase transition at 69 K.[6] Its Curie temperature can be enhanced up to 170 K by proper Gd doping.[7] Bousquet et al.[3] have shown, based on their first-principles density functional calculations, that EuO can become ferroelectric under epitaxial strain and the ferromagnetic Curie temperature can increase with strain. The critical strain predicted for the onset of ferroelectricity is 3.3% compressive and 4.2% tensile.[3] The ferroelectric polarization is anticipated to be rather strong, i.e., comparable to $BaTiO_3$.

We have investigated three kinds of EuO thin films deposited on yttrium-stabilized ZrO_2 (YSZ), $LuAlO_3$ and $YAlO_3$. The 100nm thick film deposited on YSZ is virtually lattice-matched with 0.04% compressive strain. The films deposited on $LuAlO_3$ and $YAlO_3$ had thickness 15 nm and were biaxially strained in an anisotropic way with in-plane strains up to +1.5% and +2.2%, respectively. In all samples only one phonon is IR active in EuO. At room temperature it exhibits frequencies of 177, 168 and 171 cm^{-1} in the films deposited on YSZ, $LuAlO_3$, and $YAlO_3$, respectively. This indicates that only a small shift in frequency with strain is observed. The phonon

frequencies usually slightly increase (harden) on cooling due to thermal contraction. In our case a small (< 3 cm^{-1}) decrease (softening) of the phonon frequency was observed with lowering temperature. This indicates a tendency towards lattice instability in strained EuO thin films. Unfortunately, the strain was too low for the observation of a ferroelectric phase transition; strains at least twice this amount (>4%) are necessary according to theory.[3]

Lee and Rabe[8] predicted that a biaxial tensile strain larger than 3% can simultaneously induce ferroelectric ferromagnetic ordering in $SrMnO_3$ thin films. Cubic $SrMnO_3$ crystallizes with the perovskite $Pm\bar{3}m$ structure and it undergoes a magnetic phase transition at $T_N \approx 230$ K to a G-type antiferromagnetic state. The possibility of strain-induced ferroelectricity requires strong spin-phonon coupling, which was theoretically predicted, but never experimentally confirmed in bulk $SrMnO_3$. We have performed IR reflectivity measurements of bulk $SrMnO_3$ ceramics and found that the lowest polar phonon frequency exhibits strong (17%) hardening on cooling below the Neel temperature resulting in a 32% decrease of static permittivity below T_N. Such a **huge change of permittivity due to antiferromagnetic ordering** was, according to our knowledge, never observed and it **gives evidence for extremely strong spin-phonon coupling in $SrMnO_3$** bulk ceramics. The presence of the strong spin-phonon coupling is very promising for the possibility of stabilizing the ferroelectric phase in strained films of $SrMnO_3$. We have investigated commensurate epitaxial $SrMnO_3$ films grown on $NdGaO_3$, $DyScO_3$ and $TbScO_3$ substrates, which exhibit strains of 1.2%, 3.4% and 3.9%, respectively. Microwave permittivity in the films deposited on $NdGaO_3$ and $DyScO_3$ revealed a monotonic decrease with temperature similar to bulk $SrMnO_3$. The most strained film on $TbScO_3$ showed an increase of ε' on cooling. However, no dielectric anomaly typical for the predicted improper-ferroelectric phase transition was observed. The phonon frequencies observed in all $SrMnO_3$ films also do *not* exhibit any significant anomalies, which would be a signature of a ferroelectric phase transition.

The last system, which we investigated, was $Ca_3Mn_2O_7$. This material exhibits an antiferromagnetic phase transition near 110 K. The Ruddlesden-Popper type crystal structure can be tetragonal or orthorhombic (possible polymorphism). Benedek and Fennie[4] predicted from first-principles calculations that the two modes from the Brillouin zone edge describing rotation of oxygen octahedra are coupled with one polar phonon and therefore should induce ferroelectricity in $Ca_3Mn_2O_7$. The magnetoelectric coupling should be anomalously strong in this system and therefore the thin film with 1.5% compressive strain should allow 180° switching of magnetization and simultaneous switching of ferroelectric polarization in an external electric field. Our IR reflectivity spectra of bulk $Ca_3Mn_2O_7$ revealed no significant changes of phonon frequencies near T_N, i.e., the spin-phonon coupling is smaller than in $SrMnO_3$. We also did not observe any signature of an improper ferroelectric phase transition in the IR spectra, i.e., no new phonons arise on cooling. Nevertheless, the phonon spectra were partially influenced by the free carrier plasma stemming probably from the oxygen non-stoichiometry of the measured ceramics. We have also measured an epitaxial $Ca_3Mn_2O_7$ thin film deposited on $YAlO_3$. Again no signature of a ferroelectric phase transition was revealed in IR or microwave measurements.

1. C.J. Fennie and K. M. Rabe, Phys. Rev. Lett. **97**, 267602 (2006).
2. J.H. Lee et al. Nature, **466**, 954 (2010); ibid **476**, 114 (2011).
3. E. Bousquet, N.A. Spaldin, and P. Ghosez, Phys. Rev. Lett. **104**, 037601 (2010).
4. N.A. Benedek and C.J. Fennie, Phys. Rev. Lett. **106**, 107204 (2011).
5. J.H. Lee and K.M. Rabe, Phys. Rev. Lett. **104**, 207204 (2010).
6. T.R. McGuire and M.W. Shafer, J. Appl. Phys. **35**, 984 (1984).
7. H. Ott et al. Phys. Rev. B **73**, 094407 (2006).
8. J.H. Lee and K.M. Rabe, Phys. Rev. Lett. **104**, 207204 (2010).
9. M.V. Lubanov et al. J. Phys.: Condens. Matter 16, 5339 (2004).

High-pressure synthesis of new ferroelectric and multiferroic perovskite materials

Alexei A. Belik,[1] Takao Furubayashi,[2] Yoshitaka Matsushita,[2] Masahiko Tanaka,[2] Shunichi Hishita,[2] Eiji Takayama-Muromachi[1]

[1]International Center for Materials Nanoarchitectonics (MANA), National Institute for Materials Science (NIMS), 1-1 Namiki, Tsukuba, Ibaraki 305-0044, Japan
[2]NIMS, Sengen 1-2-1, Tsukuba, Ibaraki 305-0047, Japan

Bi-containing perovskites and perovskite-related compounds have received a lot of attention as multiferroic materials and lead-free ferroelectric materials [1]. Bi-based compounds have strong tendency for ion off-centering because a Bi^{3+} ion has the stereochemically active $6s^2$ lone pair. Among simple $BiMO_3$ compounds, only $BiAlO_3$, $BiFeO_3$, $BiCoO_3$, and $BiInO_3$ have polar perovskite-type crystal structures. $BiScO_3$, $BiCrO_3$, $BiMnO_3$, and $BiNiO_3$ crystallize in centrosymmetric perovskite-type crystal structures. $BiAlO_3$ and $BiFeO_3$ are quite promising lead-free ferroelectrics with switchable polarization. Chemical simplicity of $BiMO_3$ makes them ideal systems for materials fabrications, theoretical understanding, and thin-film growths. They can only be prepared at high-pressure high-temperature conditions (except for $BiFeO_3$) in a bulk form.

$BiGaO_3$ was predicted to have the $PbTiO_3$-type perovskite structure with a huge tetragonal distortion [2]. Experimentally, however, $BiGaO_3$ was found to crystallize in a pyroxene-type structure (with tetrahedral coordination of Ga^{3+} ions) compared with other members of the $BiMO_3$ family [3].

In our talk, we will present results on the high-pressure synthesis and properties of Bi-based perovskites. Simple $BiMO_3$ compounds and solid solutions $BiM1_{1-x}M2_xO_3$ will be discussed. In some solid solutions, the existence of a *Cm* phase was found in a wide compositional range. The *Cm* phase exists in solid solutions of $PbTi_xZr_{1-x}O_3$ at a very narrow compositional range of $x = 0.55$ and is believed to be at the origin of excellent piezoelectric properties of this composition [1]. Therefore, thin films of $BiM1_{1-x}M2_xO_3$ may be promising lead-free materials to replace $PbTi_xZr_{1-x}O_3$.

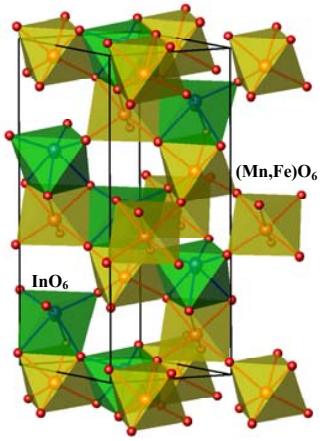

Fig. Crystal structure of $(In_{1-x}M_x)MO_3$ M = $Fe_{0.5}Mn_{0.5}$, $x = 0.176$.

We will also discuss a new class of multiferroic materials: In-based perovskites. We show that $In_{1-x}M_xMO_3$ with $x = 0.112–0.176$ and M = $Fe_{0.5}Mn_{0.5}$ has the same structure with $BiFeO_3$ (Fig.) and high Curie temperature; $In_{1-x}M_xMO_3$ is a canted antiferromagnet with the Néel temperature close to RT [4]. $In_{1-x}M_xMO_3$ presents a new class of perovskite materials (with In^{3+} in the *A* site of a perovskite ABO_3) that is almost completely unexplored. This class of materials is unique because (1) long-range magnetic ordering survives near RT despite of significant disordering in the *A* and *B* sites, (2) the

same transition metals are located in both *A* and *B* sites, and (3) a polar distortion is realized without presence of ions with the lone electron pair. Our results give a significant contribution to the development of RT multiferroics and open wide possibilities for thin-film research and future improvement of In-based perovskites. Our results also show new ways for the preparation of perovskite-type materials.

References:

[1]. N. Izyumskaya, Ya. Alivov, H. Morkoc, Crit. Rev. Solid State Mat. Sci. 34 (2009) 89.
[2]. P. Baettig, C.F. Schelle, R. LeSar, U.V. Waghmare, N.A. Spaldin, Chem. Mater. 17 (2005) 1376.
[3]. A.A. Belik, T. Wuernisha, T. Kamiyama, K. Mori, M. Maie, T. Nagai, Y. Matsui, E. Takayama-Muromachi, Chem. Mater. 18 (2006) 133.
[4]. A.A. Belik, T. Furubayashi, Y. Matsushita, M. Tanaka, S. Hishita, E. Takayama-Muromachi, Angew. Chem. Int. Ed. 48 (2009) 6117.

Session 2
Novel materials: ferroelectrics

Ferroelectricity under applied pressure and applied electric fields

R.E. Cohen,[1] M. Ahart[1] and P. Ganesh[1,2]
[1]Geophysical Laboratory, Carnegie Institution of Washington, Washington DC 20015
[2]Oak Ridge Natl Lab, Ctr Nanophase Mat Sci, Oak Ridge, TN 37830 USA

We have studied $PbTiO_3$ under pressure experimentally and theoretically. We have also studied other systems under applied electric fields (electric displacement field) and will summarize both areas. Pressure was long thought to destroy ferroelectricity until the work of Kornev et al. [1,2] who showed that density functional theory (DFT) predicts reentrant or high-pressure stabilization of ferroelectric distortions. We predicted and found a morphotropic phase boundary (MPB) under pressure *at low temperatures* in $PbTiO_3$ with a sequence of phase transitions, [3,4] but the nature of the highest-pressure region was unclear. At room temperature (Fig. 1) hydrostatic X-ray data seem to show a cubic phase between 12 and 28 GPa. Janolin et al. interpreted their experiments on $PbTiO_3$ to show high-pressure ferroelectricity and no MPB, [5] but since their experiments were at room T no MPB was expected, and the X-ray data do not prove ferroelectricity.

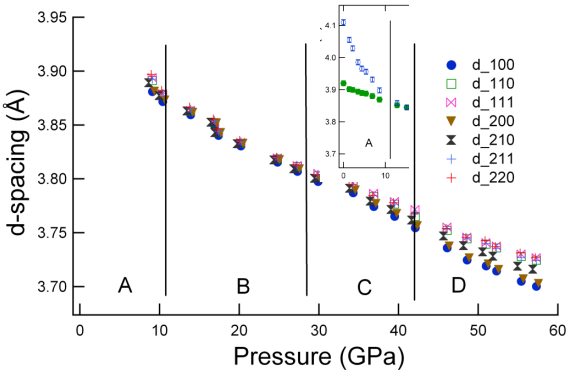

Figure 1. X-ray d-spacings for $PbTiO_3$ versus pressure at room temperature. Region A is tetragonal, B is pseudo-cubic, C is possibly rhombohedral, and D is orthorhombic or lower symmetry.

We have performed DFT computations using structure optimization and density functional perturbation theory (DFPT) with the ABINIT code, and first-principles molecular dynamics (FPMD) using the qbox code up to 100 GPa, and in general find agreement with the work of Kornev, in that there is at least a metastable phase that is ferroelectric at high pressures and zero temperature. However, we disagree with their analysis of the origin of ferroelectricity at zero Kelvin . Kornev et al. attributed the high-pressure ferroelectricity with hybridization with O2s states. However, we do not find any significant hybridization with O2s. We have analyzed the electronic structure by obtaining effective tight-binding matrix elements, and do not find any participation of O2s in the bonding, as expected, since these are deep states in oxides even at extreme pressures. [6] We instead find initial decreases in Pb-O and Ti-O bonding (hybridization) with pressure, followed by increases in bonding at pressures above 60 GPa. This suggests that any ferroelectricity above 60 GPa is likely weak and driven by long-range Coulomb forces.

A different picture from Kornev et al. was proposed by Bousquet and Ghosez, who concluded that it is a change in Ba off-centering that drives the high P ferroelectricity in $BaTiO_3$, [7] whereas Kornev ruled out the importance of the A-site. A reexamination of the formers' results suggests that what they see is mode crossing with pressure, as they said driven by short-range forces, i.e. a crumpling effect that normally leads to rotational rather than ferroelectric instabilities with increasing pressure. In any case, none of the theoretical work done to date proves that there are not one or more lower energy structures that are not polar at high pressures.

We have performed a large set of experiments versus pressure at both room temperature and at 10 K, and find no evidence for polarization or ferroelectricity in ultra-high pressure $PbTiO_3$. X-ray diffraction shows that at high pressures $PbTiO_3$ is not cubic, and is orthorhombic or lower symmetry above 42 GPa. Second harmonic generation shows no polarization in $PbTiO_3$ at high pressures above 25 GPa. We have also looked for dispersion in the Raman modes [8] up to 100 GPa, and it seems the structure is centrosymmetric from 25-100 GPa. At these conditions DFPT computations show that ferroelectric $PbTiO_3$ is metastable under these conditions, but there must be a lower energy state that is centrosymmetric, presumably a distorted perovskite like Pbnm. Under all conditions we find

strong first-order Raman spectra, showing that none of the phases are simple cubic perovskite, which has no first-order Raman.

We are using first-principles molecular dynamics (FPMD) with qbox [9] to try to understand the structural changes with pressure and temperature. We use a 3x3x3 supercell of $PbTiO_3$, corresponding to 135 atoms. An LDA-exchange-correlation functional is used to do the calculations. A 1fs. time-step is used to integrate the equations of motion. The calculations take 4mins./step on 168-cores at the Center for Piezoelectrics by Design, and we are also running on DOD supercomputers. The T_c at zero pressure using LDA is ~ 700 K (Expt. Tc ~ 763 K). Similar simulations were performed at 100GPa, starting form a zero Kelvin optimized *R3c* phase which had a large polarization of ~0.2 C/m^2. The structure/energy equilibrated in about 1 ps, and a further 6ps run was performed. The average rhombohedral angle is slightly above the ideal cubic value of 60° and showed persistent octahedral rotations (Fig 2). A Berry's phase calculation indicated an almost zero value for the polarization, suggesting that $PbTiO_3$ undergoes a ferroelectric to paraelectric phase-transition with temperature. Further work to indentify the T_c as a function of pressure is underway.

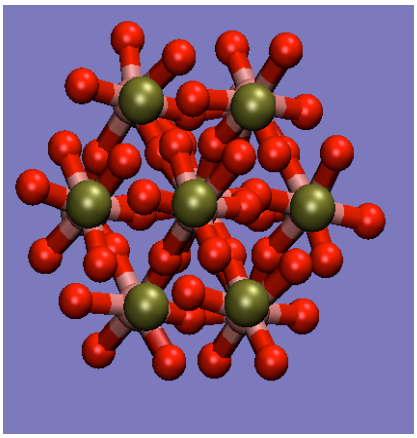

Figure 2: FPMD structure of $PbTiO_3$ viewed along the <111> pseudocubic direction**.** Octahedral rotations persist as temperature is increased to T=700K at 100GPa in $PbTiO_3$ although the ferroelectricity is lost. (O(red), Ti(pink), Pb(tan).).

We are also studying electrostriction in BaO, and ferroelectricity in $(Pb,Sn)TiO_3$, and (Pb,Sn)ZrO3 perovskite ferroelectrics under applied electric field using the constant-D method [10] implemented in the ABINIT code. We have found that the polarization lattice that is intrinsic to the definition of polarization complicates the interpretation of the thermodynamics of polar materials, as the constant D method can jump to different branches of the polarization. This non-physical phenomenon may be ubiquitous in using periodic solids to study the behavior of ferroelectrics, particularly under applied fields.

Acknowledgement:
P. Ganesh would like to thank Eric J. Walter for active computer support on the CPD cluster. This work was supported by the ONR. Computations were performed at CPD, DOD HPC centers, and the Carnegie Institution of Washington.

1. I. A. Kornev, L. Bellaiche, P. Bouvier, P. E. Janolin, B. Dkhil and J. Kreisel, Phys. Rev. Lett. **95** (19), 196804 (2005).
2. I. A. Kornev and L. Bellaiche, Phase Transitions **80** (4-5), 385-413 (2007).
3. Z. Wu and R. E. Cohen, Phys. Rev. Lett. **95**, 037601 (2005).
4. M. Ahart, M. Somayazulu, R. E. Cohen, P. Ganesh, P. Dera, H.-k. Mao, R. J. Hemley, Y. Ren, P. Liermann and Z. Wu, Nature **451** (7178), 545-548 (2008).
5. P. E. Janolin, P. Bouvier, J. Kreisel, P. A. Thomas, I. A. Kornev, L. Bellaiche, W. Crichton, M. Hanfland and B. Dkhil, Phys. Rev. Lett. **101** (23), 237601-237604 (2008).
6. M. J. Mehl, R. E. Cohen and H. Krakauer, J. Geophys. Res. **93** (B7), 8009-8022; Erratum 8094, 1977 (1989). (1988).
7. E. Bousquet and P. Ghosez, Phys. Rev. B **74** (18), 180101 (2006).
8. J. Hlinka, J. Pokorny, S. Karimi and I. M. Reaney, Phys. Rev. B **83** (2), 020101 (2011).
9. F. Gygi, IBM Journal of Research and Development **52** (1/2), 1-8 (2008).
10. M. Stengel, N. A. Spaldin and D. Vanderbilt, Nat Phys (2009).

Ferroelectric $(PbSnTi)O_3$ thin films synthesized by nucleation-mixture depositions and their structural and dielectric properties

Y. Uesu[1*], J. Iwasaki[1], H. Yokota[2], P. E. Janolin[3], J. M. Kiat[3], R. Haumont[4], and R. E. Cohen[5]

[1]*Department of Physics, Waseda University, Tokyo, Japan*

[2] *Department of Physics, Chiba University, Chiba, Japan*

[3]*SPMS, Ecole Centrale Paris, Chatenay-Malabry, France*

[4]*Universite Paris-Sud XI 15, Orsay, France*

[5]*Geophysical Laboratory, Carnegie Institution of Washington, Washington DC, USA*

*uesu93@waseda.jp

This study is motivated by first principles simulations that predict new ferroelectrics with large electromechanical strain and polarization by substituting atoms such as Sn with smaller ionic radii in the Pb sites of $PbTiO_3$ [1, 2]. However few studies concerning the fabrication of these compounds have been reported to date. This is mainly due to the difficulty of realizing Sn^{2+} in perovskite ABO_3 in usual atmospheric environment and Sn ions are apt to occupy B-sites as Sn^{+4}. Therefore we synthesized not pure $SnTiO_3$ or $(PbSn)TiO_3$ but the mixed state of $PbTiO_3$-$SnTiO_3$-$PbSnO_3$ (PST), because the mixture state could assist existences of $PbSnO_3$ and even $SnTiO_3$. For this purpose we adopted nucleation-mixture depositions using three ceramic targets of PbO, SnO and TiO_2 in the pulse laser deposition (PLD) method where PbO, SnO and TiO_2 nucleation islands are mixed in a single layer. To find the most suitable condition for synthesizing these thin films, we changed substrate temperature, O_2 atmospheric gas pressure, the deposition sequence, PbO/SnO/PbO/TiO_2/PbO or TiO_2/PbO/TiO_2/SnO/TiO_2, and laser pulse shots for three targets that make three raw materials on the substrate uniform to promote the solid reaction. Finally we found that the deposition sequence of PbO/SnO/PbO/TiO_2/PbO provides better quality PST films, while TiO_2/PbO/TiO_2/SnO/TiO_2 sequence accelerates mainly $PbTiO_3$ (Fig.1). The optimum condition of the film synthesis is the substrate temperature of 650 ℃, O_2 gas pressure of 30 mTorr and the repetition frequency of laser pulse of 5Hz. For dielectric measurements, $SrRuO_3$ was deposited on the substrate as a bottom electrode and Au was evaporated on the film as top electrodes. The thickness of PST films is 300-500 nm. XRDs with Bragg-Brentano and in-plane geometries reveal that PST films are c-axis oriented and belong to the pseudo-tetragonal system with a~b~ 0.3993 nm and c=0.4051 nm, thereby c/a~1.015.

Temperature dependences of dielectric constant ε_c and tanδ of PST thin film are shown in Fig.2. Around room temperature, ε_c (~700) is almost temperature independent and starts to increase above 100 ℃ due to ferroelectric phase transition taking place at 277 ℃. Dielectric loss (tanδ) is lower than 0.1 below 250 ℃. Fig.3 shows a *D*-*E* hysteresis loops of PST thin film. This result confirms the ferroelectricity of PST thin film. The remnant polarization *P*r is 35 μC/cm^2 at room temperature and

coercive electric field is 100 kV/cm. *P*r value is smaller than the predicted value of 120 μC/cm^2 of $(Pb_{1/2}Sn_{1/2})TiO_3$ [1] due to the three mixed phases and effect of the substrate.

Fig.4 shows temperature dependences of the lattice parameter *c* and FWHM of XRD profiles of PST thin film. Small but distinct change in *c* and a marked change in FWHM are observed at 277 ℃. This fact suggests that ferroelectric phase transition takes place at 277 ℃.

Piezoelectric response was observed at room temperature using PFM. It is interesting to point out that PST thin film appears as an assembly of comparatively large grains and small grains, which exhibit opposite piezoelectric responses.

A result of TEM-EDX of PST film shows that Pb, Sn and Ti atoms in PST films are inhomogeneously distributed forming clusters with Pb rich and Sn rich sites.

References

[1] P.Ganesh, and R.E.Cohen, Extended abstract of Fundamental Phys. of Ferroelectricity, Williamsburg, (2008) p74.

[2] Ahart, M., M. Somayazulu, R.E. Cohen, P. Ganesh, P. Dera, H.-k. Mao, R.J. Hemley, Y. Ren, P. Liermann, and Z. Wu, Nature **451** (2008) 545-548.

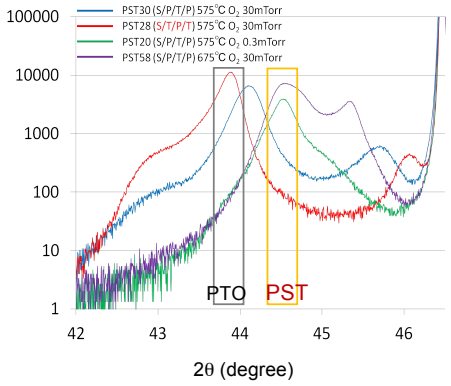

Fig.1. Changes in XRD profile of thin films synthesized under different conditions

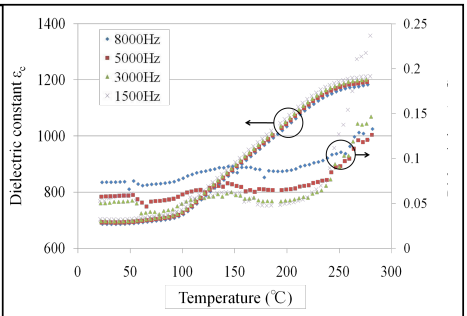

Fig.2. Temperature changes of dielectric constant ε_c and tan(δ) of PST with different frequencies

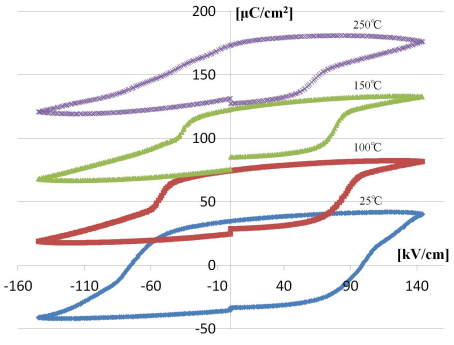

Fig.3. D-E hysteresis loops of PST observed at some temperatures.

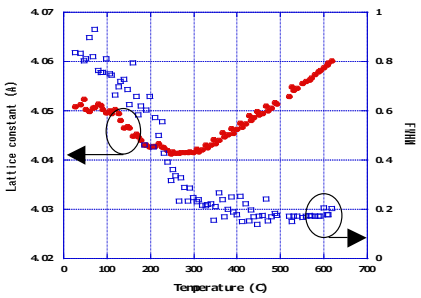

Fig.4. Temperature changes of lattice constant c and FWHM of PST film.

Epitaxial Strain Tunes Polarization and Electronic Band Gap in perovskite $SnTiO_3$

William D. Parker and S. M. Nakhmanson
Materials Science Division, Argonne National Laboratory, Argonne, Illinois 60439, USA

James M. Rondinelli
Department of Materials Science and Engineering, Drexel University, Philadelphia, Pennsylvania 19104, USA

The existence of a polar $SnTiO_3$ has been controversial. By stoichiometry and analogy with $PbTiO_3$, Sn should have a lone electron pair that creates a polar distortion, yet syntesis attempts employing sintering [1] and pulsed-laser deposition [2] with SnO_2 and TiO_2 precursors have failed to produce a clearly polar $SnTiO_3$. While several theoretical investigations [1, 3, 4] have examined the properties of a hypothetical perovskite $SnTiO_3$ utilizing *ab initio* techniques, two other surveys [5, 6] indicate that the ground state is a non-polar ilmenite structure.

We use first-principles density functional calculations to study the structural stability of tin titanate polymorphs with $SnTiO_3$ stoichiometry. We find that the low-energy phases are distorted-perovskite (tetragonal $P4mm$ and monoclinic Cm) and ferroelectric-$LiNbO_3$ ($R3c$), all possessing corner-sharing TiO_6 octahedra and polar cation displacements.

We also evaluate the relative phase stability of the polar perovskite structures under bi-axial strain. We use the theoretical lattice parameter of cubic perovskite ($Pm\bar{3}m$) $SnTiO_3$ to define zero strain ($\varepsilon = a/a_0 - 1$) and show that the elastic strain energy induced by lattice mismatch with the substrate promotes the stereochemical lone-pair activity and simultaneously enables control over the direction and magnitude of the net electric polarization (shown in Figure 1). The growth-direction-oriented polarization in $P4mm$ transforms to an off-growth-axis polarization in Cm under tensile strain. In contrast with $SrTiO_3$, which only produces an in-plane polar distortion under compression, $SnTiO_3$ retains an out-of-plane polarization under all strains between $\pm 2\%$, strongly attesting to the presence of a lone pair.

Additionally, we find that as the polarization moves away from the growth axis under tensile strain, the electronic band gap increases (Figure 2). We attribute this behavior to the broken four-fold symmetry of the Cm

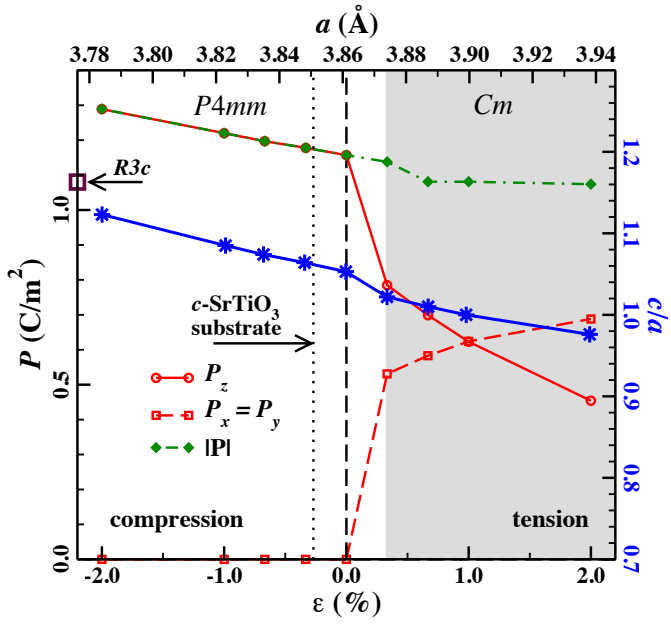

FIG. 1. Polarization [left vertical axis] and tetragonality [right vertical axis, star data points] of epitaxially-strained $P4mm$ and Cm $SnTiO_3$ phases as functions of biaxial misfit strain ε. Polarization of the $R3c$ ferroelectric-$LiNbO_3$-type structure is also marked on the left as an open square for comparison. The shaded area outlines the region of the Cm phase stability.

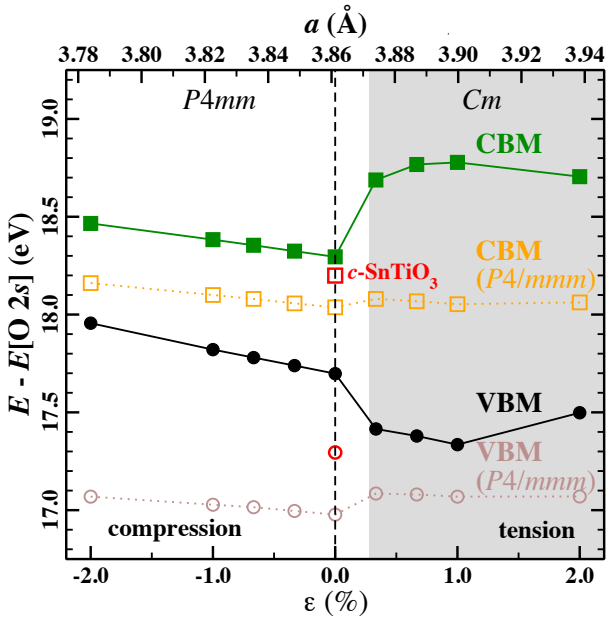

FIG. 2. Valence band maxima (VBM) and conduction band minima (CBM) of epitaxially-strained $P4mm$ and Cm $SnTiO_3$ phases as functions of biaxial strain. Values for the corresponding non-polar $P4/mmm$ structures are also shown in dotted lines. Open square and circle at zero strain mark the VBM and CBM positions in the cubic $Pm\bar{3}m$ structure.

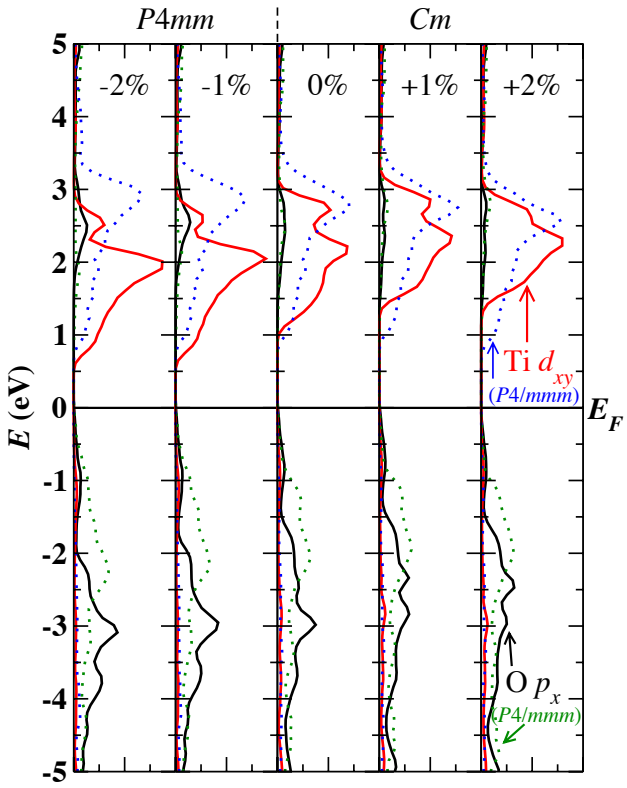

FIG. 3. Evolution of the Ti d_{xy} and O p_x orbital projected density of states (PDOS) in epitaxially-strained $P4mm$ and Cm $SnTiO_3$ with biaxial strain. PDOS for the corresponding non-polar $P4/mmm$ structures is also shown in dotted lines.

structure, which allows the Ti d_{xy} and O p_x, p_y orbitals to hybridize at the Γ-point (Figure 3). The mixing further repels the conduction band minimum and valence band maximum. The dependence of the gap on the direction of the polar distortion presents the opportunity to tune it dynamically, through applied electric field or elastic strain, if $SnTiO_3$ is grown as a thin film close to the phase boundary of $P4mm$ and Cm.

Finally, motivated by the propensity for tin to exist in the 4+ oxidation state, we investigate antisite point defect pairs, namely the substitution of Sn on a Ti site (Sn_{Ti} + Ti_{Sn}). Simulating a 12.5% defect density, we show that antisite substitution leads to metallic behavior from the partial occupation of the formerly empty Ti d bands. The metallic screening decreases the repulsion between the Sn^{2+} lone pairs and oxygen atoms and subsequently reduces the magnitude of but does not quench the cooperative polar distortions.

This project was supported by the U. S. Department of Energy, Office of Science, Office of Basic Energy Sciences and by American Recovery and Reinvestment Act (ARRA) funding through the Office of Advanced Scientific Computing Research under contract no. DE-AC02-06CH11357.

[1] Y. Konishi, M. Ohsawa, Y. Yonezawa, Y. Tanimura, T. Chikyow, H. Koinuma, A. Miyamoto, M. Kubo, and K. Sasata, Mat. Res. Soc. Symp. Proc., **748**, U3.13.1 (2003).

[2] T. Fix, S.-L. Sahonta, V. Garcia, J. L. MacManus-Driscoll, and M. G. Blamire, Crystal Growth & Design, **11**, 1422 (2011).

[3] Y. Uratani, T. Shishidou, and T. Oguchi, Jpn. J. Appl. Phys., **47**, 7735 (2008).

[4] S. Matar, I. Baraille, and M. Subramanian, Chem. Phys., **355**, 43 (2009).

[5] A. Lebedev, Physics of the Solid State, **51**, 362 (2009), ISSN 1063-7834.

[6] G. Hautier, C. C. Fischer, A. Jain, T. Mueller, and G. Ceder, Chem. Mater., **22**, 3762 (2010).

Session 3
Surface/interface compensation

Polarization of Ultrathin $PbTiO_3$ with Controlled Surface Compensation

M.J. Highland,[1,*] T.T. Fister,[2] D.D. Fong,[1] P.H. Fuoss,[1] Carol Thompson,[3] J.A. Eastman,[1] S.K. Streiffer,[4] and G.B. Stephenson[5]

[1]*Materials Science Division, Argonne National Laboratory, Argonne, Illinois 60439, USA*
[2]*Chemical Sciences and Engineering Division, Argonne National Laboratory, Argonne, Illinois 60439, USA*
[3]*Department of Physics, Northern Illinois University, DeKalb, Illinois 60115, USA*
[4]*Physical Sciences and Engineering Directorate, Argonne National Laboratory, Argonne, Illinois 60439, USA*
[5]*Advanced Photon Source, Argonne National Laboratory, Argonne, Illinois 60439, USA*

(Dated: December 16, 2011)

Recent studies on the behavior and stability of ultrathin ferroelectrics have found that the extent of the compensation of the polarization by free charge at interfaces strongly affects the phase transition and switching properties of these materials [1–4]. Incomplete charge compensation due to finite electronic screening lengths in compensating layers results in a residual depolarizing field and a reduction in the Curie temperature T_C [5–7]. Insufficiently compensated interfaces can result in the appearance of equilibrium 180° stripe domain and vortex polarization structures [3, 4, 8–11]. Competitions between energy terms that scale with surface area and those that scale with volume largely dictate the behavior of these system as there size decreases.

Charge compensation of ferroelectric surfaces without electrodes can involve ions arising from the environment of the ferroelectric material [12–19]. Sufficient ionic compensation can occur so that ultrathin films remain polar [13, 14, 21], and their polarization orientation can be altered by changing the chemistry of the environment [15, 18]. When the polarization orientation of a $PbTiO_3$ film is inverted by changing the external oxygen partial pressure controlling ionic compensation, recent experiments [19] have found that, depending upon film thickness and temperature, the transition can occur either through the nucleation and growth of inverted domains or by a continuous mechanism, in which the polarization uniformly decreases to zero and inverts without the formation of domains. This crossover could be explained as an effect of either kinetics (e.g. limited nucleation rate) or thermodynamics (e.g. limited phase stability) in ultrathin films [19]. These considerations motivated efforts to determine the *equilibrium* polarization phase diagrams of ultrathin ferroelectric $PbTiO_3$ films as a function of temperature and the external chemical potential controlling their ionic surface compensation [20] .

The equilibrium phase diagrams in Fig. 1 show the suppression of T_C as a function of pO_2 for three different film thicknesses. Here the color scale represents the net polarization $\langle P \rangle \equiv |P|(2x_{pos} - 1)$, while the symbols show the phase observed at each point measured . In figure 1 triangles pointing up and down indicate monodomain up or down polarization respectively. Square symbols indicate stripe domain formation and circles indicate the paraelectric state. At lower T, the polarization has opposite sign for high and low pO_2 ($x_{pos} = 1$ and 0, respectively). The observed T_C (solid line) is minimum at the pO_2 value where the polarization orientation below T_C changes sign. The degree to which T_C is suppressed at these

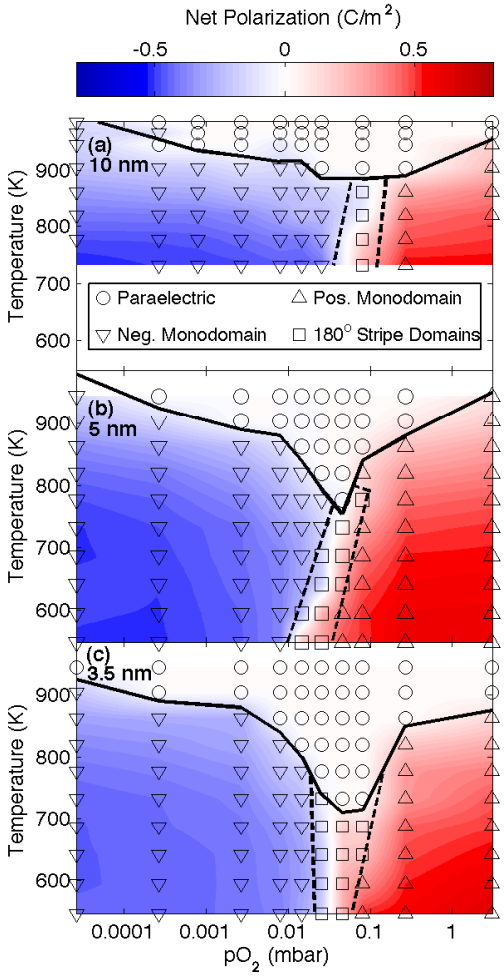

FIG. 1: Temperature vs. pO_2 phase diagrams for three thicknesses of $PbTiO_3$ on $SrRuO_3$ coherently strained to $SrTiO_3$ (001). Color scale indicates net polarization. Symbols show points measured and phase observed. Solid lines indicate T_C, and dashed lines are boundaries of 180° stripe domain regions.

intermediate pO_2 values becomes greater as film thickness decreases. The square symbols show points where the CTR fitting indicates a mixed domain structure. At these points we typically observe diffuse scattering satellite peaks in the in-plane directions around the Bragg peak, indicating formation of equilibrium 180° stripe domains with periods in the range

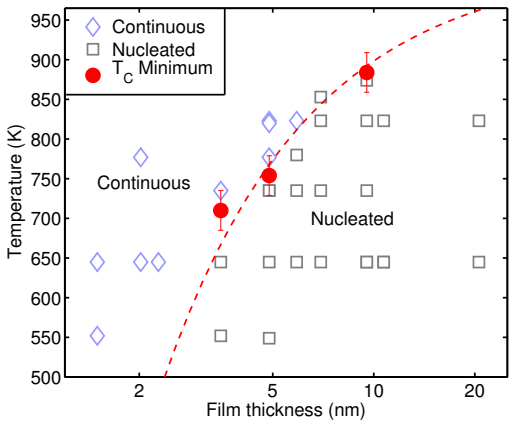

FIG. 2: Correspondence between regions of continuous and nucleated switching mechanisms found previously (open symbols) [19], and the minimum T_C observed in this work (solid circles). Dashed curve is a fit to $T_C^{min} = T_C^{\circ}(1 - t^*/t)$, where $T_C^{\circ} = 1023$ K is the zero-field T_C of $PbTiO_3$ coherently strained to $SrTiO_3$ [29], and $t^* = 1.2$ nm is the best fit value.

12-25 nm [8, 9].

These results provide an explanation for the recent observation [19] of polarization switching without domain formation at the intrinsic coercive field in sufficiently thin $PbTiO_3$ films. Figure 2 shows the observed film thickness and temperature diagram [19] giving the regions for which polarization switching by changing pO_2 at constant temperature occurs by nucleation of oppositely polarized domains, or alternatively by a continuous mechanism in which the local polarization magnitude passes through zero. Superimposed upon this diagram are three points corresponding to the minimum T_C from Fig. 2 for the three film thicknesses studied here.

They correspond well with the boundary between the continuous and nucleated mechanisms of switching. This agreement implies that the change in switching mechanism occurs because of equilibrium behavior rather than simply kinetic effects – the continuous mechanism occurs when the polar phase loses stability with respect to the nonpolar phase rather than the oppositely polarized or stripe phase. On the other hand, the regions of equilibrium 180° stripe domains on the phase diagrams of Fig. 2 indicate that the nucleated switching mechanism observed at these lower temperatures may occur through the initial formation of stripe domains.

These studies show that the chemical environment at the surface of an ultrathin ferroelectric film has strong effects on its phase transition. The nonpolar phase is stabilized and T_C is suppressed at intermediate chemical potentials where the concentrations of surface ions are insufficient to compensate either orientation of the polar phase. Such ionic compensation offers a new tool for tuning ferroelectric properties and a new avenue for devices, and must be considered when comparing studies carried out in different environments, e.g. ambient air or vacuum. Further development of the theory for ionic compensation and its validation through experiment will lay the ground work for fully understanding how a ferroelectric thin film interacts with its environment, and for fully realizing the potential of ferroelectric materials.

This work was supported by the U.S. Department of Energy, Office of Science, Office of Basic Energy Sciences under Contract DE-AC02-06CH11357. The PI's and scientific program were supported by the Materials Sciences and Engineering Division, while use of the Advanced Photon Source was supported by the Scientific User Facilities Division.

* Electronic mail: mhighland@anl.gov

[1] M. F. Chisholm, W. Luo, M. P. Oxley, S. T. Pantelides, and H. N. Lee, *Phys. Rev. Lett.* **105**, 197602 (2010).
[2] A. M. Kolpak *et al.*, *Phys. Rev. Lett.* **105**, 217601 (2010).
[3] P. Zubko, N. Stucki, C. Lichtensteiger, and J.-M. Triscone, *Phys. Rev. Lett.* **104**, 187601 (2010).
[4] M. G. Stachiotti and M. Sepliarsky, *Phys. Rev. Lett.* **106**, 137601 (2011).
[5] I. P. Batra, P. Wurfel, and B. D. Silverman, *Phys. Rev. Lett.* **30**, 384 (1973).
[6] N. Sai, A. M. Kolpak, and A. M. Rappe, *Phys. Rev. B* **72**, 020101(R) (2005).
[7] M. Stengel, D. Vanderbilt, and N. A. Spaldin, *Nature Mater.* **8**, 392 (2009).
[8] S. K. Streiffer *et al.*, *Phys. Rev. Lett.* **89**, 067601 (2002).
[9] D. D. Fong *et al.*, *Science* **304**, 1650 (2004).
[10] B.-K. Lai, I. Ponomareva, I. Kornev, L. Bellaiche, and G. Salamo, *Appl. Phys. Lett.* **91**, 152909 (2007).
[11] C. Thompson *et al.*, *Appl. Phys. Lett.* **93**, 182901 (2008).
[12] S. V. Kalinin and D. A. Bonnell, *Nano Lett.* **4**, 555 (2004).
[13] D. D. Fong *et al.*, *Phys. Rev. Lett.* **96**, 127601 (2006).
[14] R. Takahashi *et al.*, *Appl. Phys. Lett.* **92**, 112901 (2008).
[15] R. V. Wang *et al.*, *Phys. Rev. Lett.* **102**, 047601 (2009).
[16] J. Shin *et al.*, *Nano Lett.* **9**, 3720 (2009).
[17] N. C. Bristowe, M. Stengel, P. B. Littlewood, J. M. Pruneda, and E. Artacho, http://arxiv.org/abs/1108.2208v1.
[18] Y. Kim, I. Vrejoiu, D. Hesse, and M. Alexe, *Appl. Phys. Lett.* **96**, 202902 (2010).
[19] M. J. Highland *et al.*, *Phys. Rev. Lett.* **105**, 167601 (2010).
[20] M. J. Highland *et al. Phys. Rev. Lett.* **107**, 187602 (2011).
[21] C. Lichtensteiger, J.-M. Triscone, J. Junquera, and P. Ghosez, *Phys. Rev. Lett.* **94**, 047603 (2005).
[22] C. Thompson, C. M. Foster, J. A. Eastman, and G. B. Stephenson, *Appl. Phys. Lett.* **71**, 3516 (1997).
[23] D. D. Fong *et al.*, *Phys. Rev. B* **71**, 144112 (2005).
[24] S. V. Kalinin *et al.*, *Phys. Rev. Lett.* **100**, 155703 (2008).
[25] P. Maksymovych *et al.*, *Phys. Rev. Lett.* **102**, 017601 (2009).
[26] M. J. Bedzyk *et al.*, *Phys. Rev. B* **61**, R7873 (2000).
[27] L. Despont *et al.*, *Phys. Rev. B* **73**, 094110 (2006).
[28] N. A. Pertsev, A. G. Zembilgotov, and A. K. Tagantsev, *Phys. Rev. Lett.* **80**, 1988 (1998).
[29] G. B. Stephenson and M. J. Highland, *Phys. Rev. B* **84**, 064107 (2011).

Ferroelectric Surface Chemistry: a first-principles study of the $PbTiO_3$ surface

Kevin Garrity*
Department of Physics & Astronomy, Rutgers University, Piscataway, New Jersey 08854-8019, USA

Alexie Kolpak
Department of Materials Science and Engineering, Massachusetts Institute of Technology, Cambridge, Massachusetts 02139, USA

Arvin Kakekhani and Sohrab Ismail-Beigi
Departments of Physics and Applied Physics, Yale University, New Haven, Connecticut 06520-8120, USA

(Dated: December 2, 2011)

Due to a large, persistent response to electric fields, ferroelectric substrates offer a unique opportunity to tune the properties of a surface via an external field, potentially providing an avenue for advanced surface chemistry. By using an electric field to change the polarization direction of a ferroelectric substrate, one can potentially reversibly modify the surface Fermi level, atomic geometry, or even stoichiometry, all of which can alter the performance of the surface in applications.[1,2] This extra control over surface chemistry could potentially allow one to bind and release molecules from the surface or to turn reaction pathways on and off, enabling a new level of control over surface catalysis.[3,4]

In this work, we use first principles density functional theory to investigate the effects of polarization on the (001) surface of $PbTiO_3$. We both investigate the consequences of changing polarization on stoichiometric surfaces and determine the thermodynamically stable (non-stoichiometric) surface structures as a function of the film polarization. We then consider the adsorption of CO_2 and H_2O to both stoichiometric and non-stoichiometric surfaces. Finally, in addition to looking at the $PbTiO_3$ surface itself, we also consider the effects of adding a single epitaxial surface layer of several different materials in order to combine the high polarization of $PbTiO_3$ with a material that has superior catalytic properties.

We begin by examining the effects of polarization on the stoichiometric TiO_2-terminated surface. We find that both the positively-poled and negatively-poled surfaces compensate the depolarization field with an electronic reconstruction. On the positively-poled surface, electrons move into the conduction band, while on the negatively-poled surface, holes move into the valence band. This screening charge has a large effect on both CO_2 binding modes and binding energies.

While the results for the ideal surface seem promising, our first principles surface thermodynamics calculations indicate that polarized $PbTiO_3$ always prefers to compensate its surface charge by adjusting the surface stoichiometry, rather than through an electronic reconstruction. Over most of the available phase space, the positively-poled surface has a PbO termination with 0.5 ML adsorbed O. The negatively-poled surface is also PbO-terminated, but with 0.5 ML O vacancies. Both of these reconstructions allow the surface to compensate the surface charge while maintaining favorable oxidation states on all surface atoms. These surface reconstructions also modify CO_2 and H_2O binding; however, the total binding tends to be much smaller than on the stoichiometric TiO_2-terminated surface. In particular,

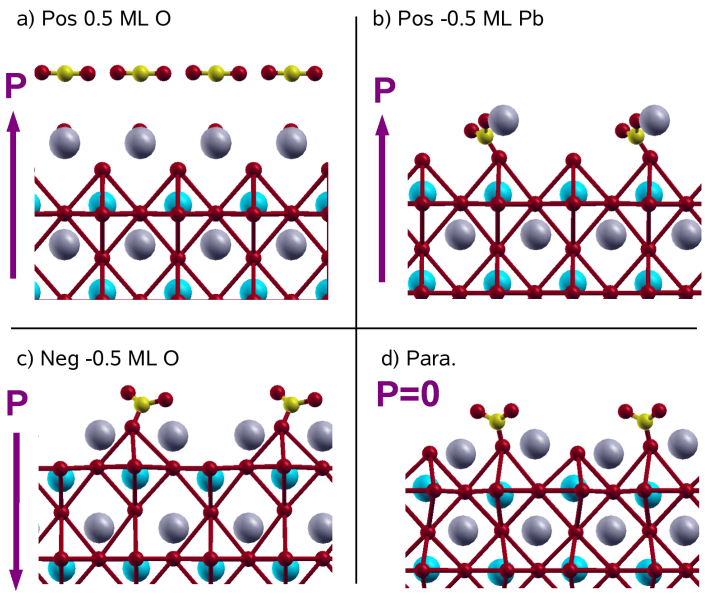

FIG. 1: (Color online) Binding of 0.5 ML CO_2 to selected thermodynamically stable surfaces (see Table **??**). a) Physisorption to positively-poled surface with 0.5 ML O. b) Carbonate bonding to positively-poled surface with 0.5 ML Pb vacancies. c) Carbonate bonding to negatively-poled surface with 0.5 ML oxygen vacancies. d) Carbonate bonding to stoichiometric PbO-terminated paraelectric surface.

we find that the thermodynamically stable negatively-poled surface with oxygen vacancies binds CO_2 in a carbonate geometry with a binding of 0.5 eV, while the stable positively-poled surface only binds CO_2 through physisorbtion (see Fig. 1).

Finally, we attempt to improve binding of CO_2 to the surface by adding a monolayer of a catalytically active material to the surface. Unfortunately, many traditional catalysts (e.g. Pt) are not thermodynamically stable as monolayers on $PbTiO_3$. We do find several oxides and alkali metals which are stable on the surface and which improve CO_2 binding.

In summary, our work demonstrates that ferroelectric polarization can have a large effect on the chemistry of an oxide surface. In particular, our results highlight the importance of considering the effects of polarization on surface stoichiometry, which suggests new avenues for tuning catalytic properties through substrate polarization.

---

* Electronic address: kgarrity@physics.rutgers.edu

[1] K. F. Garrity, A. M. Kolpak, S. Ismail-Beigi, and E. I. Altman, Adv. Mat. **22**, 2969 (2010).

[2] A. M. Kolpak, I. Grinberg, and A. M. Rappe, Phys. Rev. Lett. (2007).

[3] T. Bligaard, J. Nrskov, S. Dahl, J. Matthiesen, C. Christensen, and J. Sehested, Journal of Catalysis **224**, 206 (2004), ISSN 0021-9517.

[4] S. Dahl, A. Logadottir, C. J. H. Jacobsen, and J. K. Nrskov, Applied Catalysis A: General **222**, 19 (2001), ISSN 0926-860X.

Properties of intrinsic ferroelectric surface in extreme clean limit:
Giant 2D conduction on atomically clean surface of stoichiometric $BaTiO_3$ in UHV

Y. Watanabe, D. Matsumoto and S. Kaku

Department of Physics, Kyushu University, Fukuoka, Japan 812-8581

Synopsis We report both nanoscopic and quasi-simultaneous macroscopic multiple-measurements $BaTiO_3$ single crystals in ultrahigh vacuum (UHV), which are fully oxygenated top-seed-solvent-growth (TSSG) having atomically-ordered clean surface realized for the first time. The surface conductance changes 10^5 times by the spontaneous polarization (P_S) and reaches almost metallic one for P_S-up state. Both macroscopic-multiple and UHV-AFM (atomic force microscopy) measurements consistently clearly show intrinsic existence of e^- and h^+ layers on ferroelectric surface, which are favorably compared with ab-initio calculations [1] and GL theory. The result can be interpreted with the aid of ab-initio studies of $BaTiO_3$ surfaces [1,6,7].

Introduction: Surface Ferroelectric is unique among condensed matters, because the macroscopic electrical features reside predominantly at the surface. For example, 180°domains are attributed to the surface charge, i.e, $\nabla \cdot P$; memory and energy conversion uses the screening charge in electrodes, which is determined by charges near the surface; the thickness or size dependence of the properties and, therefore, nano-ferroelectrics are critically controlled by the surface. In particular, in ferro 2010 in Aspen, we have shown that the nanoscopic study of the $BaTiO_3$ domains in UHV, which indicated the intrinsic screening at the surface. The progress of this possibility using TSSG crystal is presented in this presentation.

Aim: Clean free surface In particular, insufficiently screened surface such as free-surface is essential in ferroelectric field effect transistors, energy conversion, nano-ferroelectrics and 180°domains. Here, the surface of ferroelectrics poses a wide variety of puzzles, because its properties critically depend on strain, strain gradient, interdiffusion, stoichiometry, surface relaxation, defects, dislocations, injected carriers, electrical properties of adjacent material and band banding. We believe that a basic approach for these surfaces is to study a simplified limit, e.g., an ideal free-surface of ferroelectrics.

Previous results: Self-field effect Prototypical ferroelectrics such as pure stoichiometric $BaTiO_3$ are considered to be good insulator as confirmed by various experiments. On the other hand, free carrier layer is shown to form at the surface of ferroelectrics $\perp P_S$ for *insufficiently screened* depolarization field E_d because of enormous E_d [1-4]. These theories were supported by all-perovskite ferroelectric FETs [5] and the conductance of poled free surface in ultrahigh vacuum (UHV) [3]. Nonetheless, free-carrier layer on ferroelectric is usually considered due to extrinsic effect such as oxygen vacancies, and therefore not included in the discussions of ferroelectric basics.

Present results: First atomic control of surface & Giant conductance To resolve these controversies, we've recently succeed to obtain atomically ordered clean surface of fully oxygenated top-seed-solvent-growth (TSSG) $BaTiO_3$ single crystals for the first time. We investigated their properties, by quasi-simultaneous macroscopic multiple-measurements of the surface and bulk and multiple-scanning microscopy. All measurements are carried out in UHV.

Atomically ordered surfaces of $BaTiO_3$ single crystals are obtained and are cleaned in UHV so that oxygen vacancy formation is adequately suppressed. These surfaces possess wide well-defined atomic lattice steps, indicating a high surface crystallographic quality. *The surface conduction, the bulk conduction and the linear and nonlinear permittivity were quasi-simultaneously measured* with the electrode having a gap of 10 μm. The P_S-up and down state are formed by application of external field of 100 V between the surface and bottom electrode.

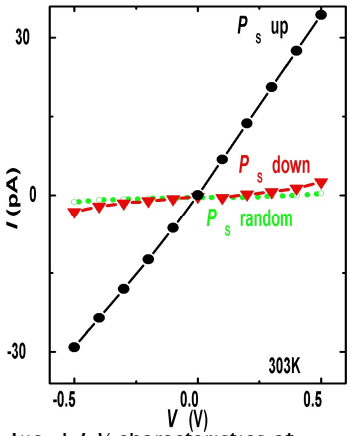

Fig. 1 *I-V* characteristics of surface conductance of $BaTiO_3$ in UHV of P_S-up (e^-), down (h^+) and random(*a*/*c*, *a*) state.

The surface *I-V* characteristics in Fig. 1 show that significantly high conductance for the P_S-up state ($\times 10^5$) and an appreciably enhanced conductance for the P_S-down state, whereas no change in bulk conductance. The P_S direction is confirmed by 2nd harmonic permittivity (Fig.2) and polarization microscopy. The conductance of both P_S-up and down state disappears above Curie temperature where P_S vanishes. The high sensitivity of the surface conductance to the adsorbents indicates that the thickness of the layer is approx. a few lattices in accordance with theories [1,3].

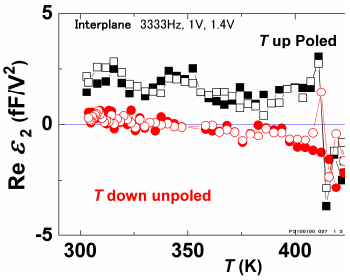

Fig. 2 Temperature dependence of nonlinear permittivity of poled and unpoled states simultaneously measured with conductance.

Ref.

[1] M. Krčmar and C.L. Fu, *Phys. Rev.* B **68**, 115404 (2003)
[2] Y. Watanabe *Phys. Rev.* B 57, 789 (1998).
[3] Y. Watanabe et al., *Phys. Rev. Lett.* 86, 332(2001).
[4] M. Fechner et al., *Phys. Rev.* B 77, 094112 (2008).
[5] Y. Watanabe, *Appl. Phys. Lett.* 66, 1770(1995); *U.S. Patent* 5418389 (1995).
[6] J. Padilla, W. Zhong and D. Vanderbilt, *Phys. Rev.* B, Vol. 53, No.10, R5969 (1996)
[7] B. Meyer and D. Vanderbilt, *Phys. Rev.* B, Vol. 65, No.10,104111 (2002)

Interface Mediated Stabilization of Ferroelectric and Non-Polar Phases of $BiFeO_3$

Young-Min Kim,[1] Alison Hatt,[2] Amit Kumar,[1] Pu Yu,[3] Ying-Hao Chu,[4,3] Ramamoorthy Ramesh,[3] Stephen J. Pennycook,[1] James M. Rondinelli,[5] Sergei V. Kalinin[1], Albina Y. Borisevich[1]

[1]Oak Ridge National Laboratory, Oak Ridge, TN
[2]Lawrence Berkeley National Laboratory, Berkeley, CA
[3]University of California-Berkeley, Berkeley, CA
[4]National Chiao Tung University, Hsinchu, Taiwan
[5]Drexel University, Philadelphia, PA

Atomically-defined interfaces between complex oxides offer a paradigm of novel electronic and coupled functionalities. Among those, devices based on ferroelectric are an attractive option due to possibility of direct control by electric field. Engineering ferroelectric response via coupling with other order parameters enables new device concepts such as Mott transistors and strain coupled electronics; however, realizing such coupling is often difficult. Recently, it was suggested that tilt transitions at interfaces can be used to engineer interface properties.[1,2] A representative multiferroic material, $BiFeO_3$ (BFO) possesses a number of low-laying structurally dissimilar ground states differing in octahedral tilt patterns (see, e.g. [3]). Here, we report the stabilization of the ferroelectric and antiferroelectric phases at the BFO-LSMO interface through termination control and reveal associated atomic-scale mechanisms with the help of quantitative aberration-corrected scanning transmission electron microscopy (STEM) combined with EELS and first-principles theory.

Figure 1 shows annular dark field (ADF) STEM images for the BFO thin film structures with different LSMO interface terminations and their corresponding polarization changes across the interfaces. The terminations of LSMO interface were engineered through the surface termination control of STO substrate. The BFO thin film grown on MnO_2-terminated surface of LSMO exhibits stabilized ferroelectric phase at the interface. The interfacial and bulk polarization are antiparallel, giving rise to a head to head ferroelectric domain wall mostly parallel to the interface. In comparison, the film grown on (Sr/La)O-terminated surface of LSMO exhibits non-polar phase in the vicinity of the interface, with associated ferroelectric-non-polar domain wall in the bulk. Quantitative atomic position mapping and extensive STEM simulations were used to study the octahedral tilt and the cation displacement behavior in the BFO depending on the interface termination. The electronic properties at the interfaces including charged domain walls and FE-non-polar walls, were further probed by energy loss spectroscopy (EELS). These results imply that the structural parameters such as octahedral tilt and ferroelectricity in BFO can be directly controlled by modifying the interface structure. Specifically, this approach allows octahedral tilt induced stabilization of non-polar form in zero fields. The results of related first principles simulations and considerations on the nature of the non-polar phase, as well as considerations on possible device applications will also be reported.

This research is sponsored by the Materials Sciences and Engineering Division (YMK, SJP, SVK, AYB) and Office of BES of the U.S. DOE, and by appointment (YMK) to the ORNL Postoctoral Research Program administered jointly by ORNL and ORISE.

References

[1] A. Borisevich et al., Phys. Rev. Lett., **105**, 087204 (2010).

[2] J.M. Rondinelli and N.A. Spaldin, Phys. Rev. **B 84** 113402 (2010).

[3] O. Dieguez et al., Phys. Rev. **B 83**, 094105 (2011).

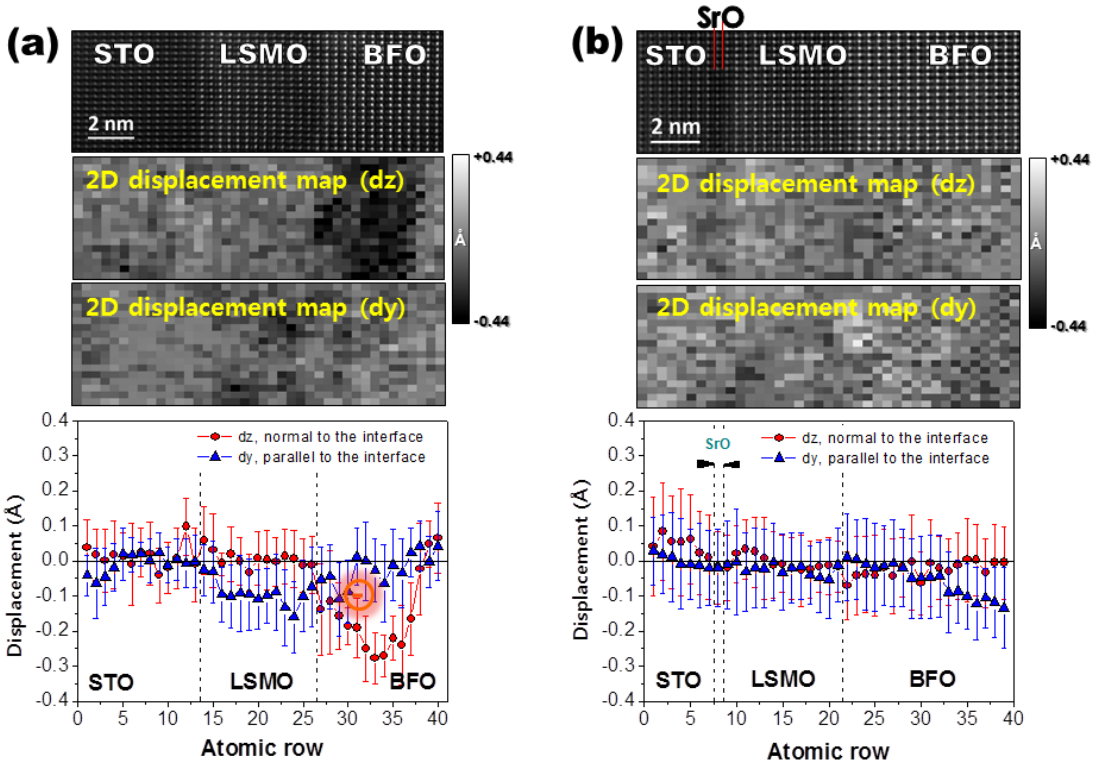

Figure 1. Thin film structures and polarization maps across interface: (a) ADF STEM image for the BFO structure grown on MnO_2-terminated surface of LSMO (topmost panel) and the corresponding two dimensional displacement maps (out-of-plane displacement, dz, and in-plane displacement, dy) of Fe in the pseudo-cubic perovskite structure (two middle panels). Line profiles for the displacement maps are represented in the bottom panel. (b) The same arrangement for the figures applies to the BFO structure grown on (La/Sr)O-terminated surface of LSMO.

Session 4
Topological defects and domains

Binding of Electric Vortices with Electric Antivortices in Ferroelectrics and Multiferroics

L. Bellaiche[1,2], B. Dkhil[2], G. Geneste[3], I. Kornev[2], L. Louis[1,2], S. Prosandeev[1] and W. Ren[1].

[1]*Physics Department, University of Arkansas, Fayetteville, Arkansas 72701, USA*

[2]*Laboratoire Structures, Proprietes et Modelisation des Solides, Ecole Centrale Paris, CNRS-UMR8580, Grande Voie des Vignes, 92295 Chatenay-Malabry Cedex, France*

[3]*CEA, DAM, DIF, F-91297 Arpajon, France*

[*]*e-mail: laurent@uark.edu*

Vortex-antivortex pairing is a fundamental process that has been observed in a variety of materials, such as superfluids, superconductors, and magnets. This pairing of topological defects is often associated with complex phenomena, including nanoscale magnetization dynamics [1-3] or the occurrence of the so-called and intriguing Berezinskii-Kosterlitz-Thouless (BKT) transition [4-7].

Interestingly, pairs of *electric vortices and electric vortices* have just been created in $BiFeO_3$ (BFO) thin films [8-9], which opens the possibility of studying such pairs and their effects on physical properties in ferroelectrics and multiferroics.

The purpose of this Talk is report/discuss phenomena that all involve the binding of electric vortices and antivortices in different ferroelectric and multiferroic nanostructures. Examples of such phenomena (that have been discovered via the use of *ab-initio* and first-principles-based techniques) are:

1) The occurrence of a strain-induced, pure gyrotropic phase transition in BFO thin films grown along the [1-10] direction [10]. Gyrotropic phase transitions are characterized by the appearance of a spontaneous optical activity, and are rare in nature [11-14]. As a matter of fact, we are not aware of any gyrotropic phase transition having been previously reported in any perovskite material.

2) The prediction of the so-called magnetotoroidic effect in BFO nanodots [15]. Such latter effect characterizes the control of magnetic order parameters by the application of curled (rather than homogeneous) electric fields [15,16].

3) The search for a BKT transition happening in a ferroelectric material. BKT transition is an unusual transition that is associated with a change in the response of the system to applied fields and to a diverging correlation length [4,17]. Moreover, some correlation functions decay exponentially with distance above this transition, while they adopt a power law in the low-temperature phase [4,17]. Preliminary results strongly suggest that some specific ferroelectric nanocomposites exhibit all these fingerprints of the BKT transition, which would imply that these nanocomposites can be considered as the ``missing link" that brings ferroelectrics into the realm of materials that have been demonstrated to possess BKT transitions.

These works are supported by ONR Grants N00014-11-1-0384 and N00014-08-1-0915, NSF grants DMR-1066158 and DMR-0701558 and the Department of Energy, Office of Basic Energy Sciences, under contract ER-46612. Some computations were also made possible thanks to the ONR grant N00014-07-1-0825 (DURIP), the MRI grant 0722625 from NSF and a Challenge grant from the Department of Defense.

References:

[1] B. Van Waeyenberge *et al.*, Nature **444**, 461 (2006).
[2] P. E. Roy *et al.*, Physical Review B **79**, 060407 (2009).
[3] J. Li, and C. Rau, Physical Review Letters **97**, 107201 (2006).
[4] V.L. Berezinskii, Soviet Physics JETP **34**, 610 (1972); J.M. Kosterlitz and D.J. Thouless, Journal of Physics C **6**, 1181(1973).
[5] Z. Hadzibabic *et al.*, Nature **441**, 1118 (2006).
[6] A. Yu Galkin and B.A. Ivanov, Journal of Experimental and Theoretical Physics **104**, 775 (2007).
[7] V.B. Eltsov *et al.*, Journal of Low Temperature Physics 162, 212 (2011).
[8] N. Balke *et al*, Nature Nanotechnology **4**, 868 (2009).
[9] N. Balke *et al*, Nature Physics doi:10.1038/nphys2132 (2011).
[10] S. Prosandeev, I. Kornev and L. Bellaiche, Physical Review Letters **107**, 117602 (2011).
[11] S. Hirotsu, Journal of Physics C **8**, L12 (1975).
[12] C. Konak *et al*, Journal of Physics C **11**, 2493 (1978).
[13] H. Wondratschek and W. Jeitschko, Acta. Crystallogr. Sect. A **32**, 664 (1976).
[14] S.V. Akimov and E.F. Dudnik, Phys. Solid. State **51**, 1420 (2009).
[15] W. Ren and L. Bellaiche, Physical Review Letters **107**, 127202 (2011).
[16] H. Schmid, J. Phys. Condens. Matter **20**, 434201 (2008).
[17] R. Gupta *et al*, Physical Review Letters **61**, 1996 (1988).

Static and dynamics conductance of topological defects in ferroelectrics

S.V. Kalinin,[1] P. Maksymovych,[1] N. Balke,[1] A. Borisevich,[1] L.Q. Chen[2] and A N. Morozovska[3]

[1] Oak Ridge National Laboratory, Oak Ridge, TN
[2] Pennsylvania State University, College Park, PA
[2] Ukrainian Academy of Sciences, Ukraine

Domain walls and vortices in ferroelectric and ferroelastic materials have recently attracted much attention as a playground of novel physical phenomena including charge accumulation and associated band bending,[1] ferroelastic transitions,[3] band gap narrowing due to intrinsic symmetry changes,[4] vacancy segregation,[5] and order parameter couplings.[6, 7] While the underpinning theoretical concepts have been explored for several decades, only recently unique functional properties of isolated domain walls have become accessible for direct observations through scanning probe microscopy methods, whereas associated structures including order parameter components are now amenable to atomic resolution electron microscopy techniques.

The recent upsurge of the interest to domain wall phenomena was instigated by the seminal work by Seidel[8] that directly visualized conductive channels at 109° domain walls in $BiFeO_3$. Following this initial report, conductivity was demonstrated for other types of domain walls in $BiFeO_3$ and domain walls in hexagonal manganites, lead zirconate titanate and $LiNbO_3$, suggesting universality of this behaviour. Recently, metallic conductance in ferroelectrics was demonstrated. However, the detailed studies of conductivity at the walls have demonstrated an intriguing set of hysteretic and memory effects and time dynamics.

In this presentation, I will discuss recent studies of hysteretic and memory effects in domain wall and vortex conductance, as well as metallic conductance of ferroelectric nanodomains (P. Maksymovych et al, Nano Lett, AOP). These observations suggest that domain wall conductance is a ***dynamic*** process that is intrinsically linked to slow polarization dynamics (i.e. evolution of wall shape[9]) or slow vacancy segregation processes (e.g. compare to recent studies at metal-ferroelectric junctions[10, 11]). In the former case, as established domain wall has non-equilibrium orientation and associated charge, which then induces conductivity according to Guro-Tagantsev-Morozovska mechanisms.[1, 12, 13] The hysteresis and time dynamics of conductivity is then that of wall geometry. In the second model, the conductivity for the static wall is determined by the kinetics of strain- and field controlled segregation of oxygen vacancies. Realistically, both mechanisms can be active. More generally, these studies suggest that ionic phenomena can provide significant contribution to the physics of transition metal oxides probed by SPM, and potential experiemtnal pathways to decouple these phenomena are discussed.

* This research is sponsored by the Materials Sciences and Engineering Division (SVK, PM, AB) and Scientific User Facilities Division (NB), Office of BES of the U.S. DOE.

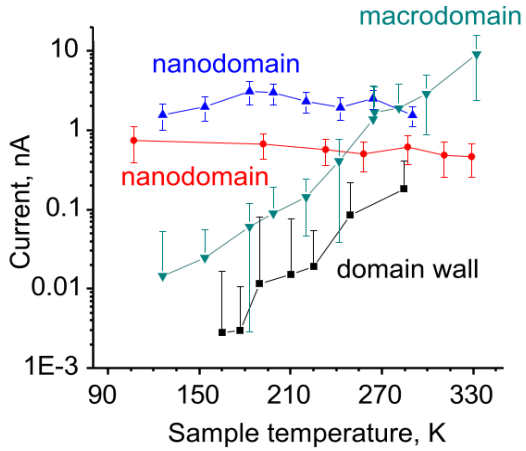

Figure 1. Temperature dependence of conductance in ferroelectric nanodomains

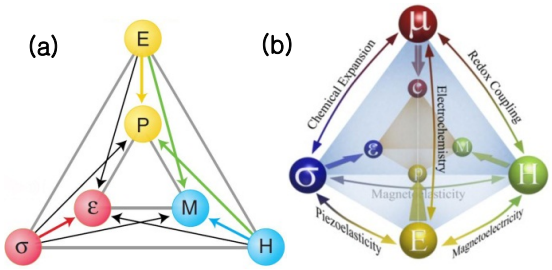

Figure 2. (a) Ferroic coupling diagram [2]. (b) Modified diagram taking into account chemical effects (graphics by S. Jesse, ORNL).

References

1. B. M. Vul, G. M. Guro and Ivanchik, II, Ferroelectrics **6** (1-2), 29-31 (1973).
2. N. A. Spaldin and M. Fiebig, Science **309** (5733), 391-392 (2005).
3. A. Tselev, V. Meunier, E. Strelcov, W. A. Shelton, I. A. Luk'yanchuk, K. Jones, R. Proksch, A. Kolmakov and S. V. Kalinin, Acs Nano **4** (8), 4412-4419 (2010).
4. A. Lubk, S. Gemming and N. A. Spaldin, Physical Review B **80** (10) (2009).
5. L. Goncalves-Ferreira, S. A. T. Redfern, E. Artacho, E. Salje and W. T. Lee, Physical Review B **81** (2) (2010).
6. A. K. Tagantsev, E. Courtens and L. Arzel, Physical Review B **64** (22) (2001).
7. M. Daraktchiev, G. Catalan and J. F. Scott, Physical Review B **81** (22) (2010).
8. J. Seidel, L. W. Martin, Q. He, Q. Zhan, Y. H. Chu, A. Rother, M. E. Hawkridge, P. Maksymovych, P. Yu, M. Gajek, N. Balke, S. V. Kalinin, S. Gemming, F. Wang, G. Catalan, J. F. Scott, N. A. Spaldin, J. Orenstein and R. Ramesh, Nat. Mater. **8** (3), 229-234 (2009).
9. N. Balke, S. Choudhury, S. Jesse, M. Huijben, Y. H. Chu, A. P. Baddorf, L. Q. Chen, R. Ramesh and S. V. Kalinin, Nature Nanotechnology **4** (12), 868-875 (2009).
10. W. Jiang, M. Noman, Y. M. Lu, J. A. Bain, P. A. Salvador and M. Skowronski, Journal of Applied Physics **110** (3) (2011).
11. H. T. Yi, T. Choi, S. G. Choi, Y. S. Oh and S. W. Cheong, Adv. Mater. **23** (30), 3403-+ (2011).
12. M. Y. Gureev, A. K. Tagantsev and N. Setter, Physical Review B **83** (18) (2011).
13. E. A. Eliseev, A. N. Morozovska, G. S. Svechnikov, V. Gopalan and V. Y. Shur, Physical Review B **83** (23) (2011).

Study of ferroelectricity in tetragonal $BaTiO_3$ epitaxial films grown on $SrTiO_3$-buffered Si(001) - Can this system exhibit negative capacitance ?

C. Dubourdieu[1], A. Posadas[2], J. Jordan-Sweet[1], J. Bruley[1], E Cartier[1], D. Frank[1], T. Arruda[3], S. Kalinin[3], M. Choi[2], A. Demkov[2], M.M. Frank[1], V. Narayanan[1]

1. IBM T.J. Watson Research Center, Yorktown Heights, NY 10598, USA
2. Dept of Physics, The University of Texas at Austin, Austin, TX 78712, USA
3. Oak Ridge National Laboratory, Oak Ridge, TN 37831, USA

As the conventional transistor is approaching its ultimate physical limits with a huge power dissipation issue, there is a need for new switches operating at lower voltages [1]. In 2008, it was proposed that introducing a ferroelectric as a gate oxide could decrease the sub-threshold slope below the thermodynamic limit of 60 mV/dec in field-effect transistors (FETs) operating at room temperature [2]. If the thicknesses of the ferroelectric and of the dielectrics (including the silicon substrate contribution) in series are carefully balanced, the ferroelectric may contribute with a negative capacitance to the dielectric stack, increasing its overall capacitance, without causing hysteresis. As a result, a small gate voltage swing would produce a larger swing in the internal potential which gates the device, therefore enabling low-voltage operation. So far, the only experiment providing evidence for this phenomenon in field-effect devices on Si employed an organic material as the ferroelectric [3].

In this work, we study $BaTiO_3$ epitaxially grown on $SrTiO_3$-buffered Si as a candidate for the negative capacitance phenomenon. The perovskite $BaTiO_3$ compound is ferroelectric with a Curie temperature of 120°C and has a crystalline tetragonal structure. A ferroelectric FET requires that the polarization be perpendicular to the Si channel. Thus it is a key milestone to first demonstrate ferroelectricity for $BaTiO_3$ films on silicon, with out-of-plane polarization, in order to eventually optimize the relative thicknesses of each material for the stabilization of negative capacitance. So far, the only demonstration for ferroelectricity in epitaxial $BaTiO_3$ films on Si has been shown by piezoforce microscopy (PFM) with domain write/read experiments [4]. However, no switching of the domains nor piezoelectric hysteresis were demonstrated. In this work, we show a hysteretic behavior of the electromechanical response by PFM pointing to ferroelectricity, at least at a local scale, in films of thickness 8-40 nm.

In a first part, we will discuss the possible occurrence of negative capacitance in $SiO_2/SrTiO_3/BaTiO_3$ stacks based on a 1D modeling of a field-effect transistor device. The inversion charge was calculated as a function of gate voltage for varying SiO_2, $SrTiO_3$ and $BaTiO_3$ thicknesses. We will show that minimizing the low-κ interfacial layer (IL) is a crucial point for allowing negative capacitance stabilization, as illustrated in Fig. 1(a).

In a second part, the structural and microstructural characterization of the heterostructures will be presented. The epitaxial stacks $SrTiO_3/BaTiO_3$ were grown by molecular beam epitaxy on p-type Si(001). A $SrTiO_3$ film (6 to 16 ML) was first deposited at 590°C. $BaTiO_3$ film was then grown at 750°C, with thicknesses in the range 1.2 to 40 nm. The crystalline structure of the stacks was studied by X-ray diffraction at the National Synchrotron Light Source (Fig. 1(b)). The films are found to be tetragonal with the c-axis out of plane. Thicker films (40 nm) consist of a mixture of tetragonal and cubic phases. These results are also confirmed by electron diffraction. The c/a tetragonal distortion decreases with increasing thickness. The TEM images show a high crystalline quality of the films with well defined interfaces. Dislocations are typically observed after 2-3 monolayers, indicating a rapid strain relaxation. An interfacial layer with Si is formed as shown in Fig. 1(c). The elemental distribution within the stack was studied by EDX and EELS and will be discussed. Interdiffusion is observed in the interfacial layer, with the presence of Sr and Ti, which is favorable as it should enhance its dielectric permittivity.

Finally, we will discuss ferroelectricity in these heterostructures. Capacitance versus voltage measurements were performed on MOS capacitors using TiN top electrodes. Stacks of ~ 16 nm $BaTiO_3$ /~6.0 nm $SrTiO_3$ / ~4.5nm IL exhibit a high capacitance density of 1.07 μF/cm^2 (see Fig. 2(a)), which indicates a relative permittivity of the order of 300 for $BaTiO_3$ (assuming 40 for $SrTiO_3$). The corresponding equivalent oxide thickness is 2.8 nm. The flatband voltage (~ -0.60 V) is shifted towards negative values, which is typical for earth-alkaline-based dielectrics. In contrast to many high-κ dielectrics, the CVs show little hysteresis, suggesting limited charge trapping in these films. The CVs response at different frequencies and under different stress conditions including pulsed voltage will be discussed. A ferroelectric hysteresis is not observed in the CVs. This may be due to a significant voltage drop across the Si depletion region and across the conventional dielectric. Ferroelectricity is, however, evidenced locally by PFM. Domains are written and switched under a typical DC voltage of ±10V. The piezoresponse gives hysteresis loops as those shown in Fig 2(b), whose amplitudes depend on the location on the film surface and on the film thickness. In order to shed light on the possible origins of such hysteresis, experiments were also conducted on similar stacks deposited on n-type silicon. Moreover, since partial screening by the silicon substrate may lead to a large depolarization field, the same heterostructures were deposited on n+ and p+ Si substrates. The results obtained for the different Si substrate types and doping levels will be discussed.

1. T.N. Theis and P.M. Solomon, Science 327, 1600 (2010)
2. S. Salahuddin and S. Datta, Nano Letters 8, 405 (2008)
3. A. Rusu, G.A. Salvatore, D. Jimenez, A. Ionescu, IEDM p.16.3.1- 16.3.4 (2010)
4. V. Vaithyanathan *et al*., J. Appl. Phys. 100, 024108 (2006)

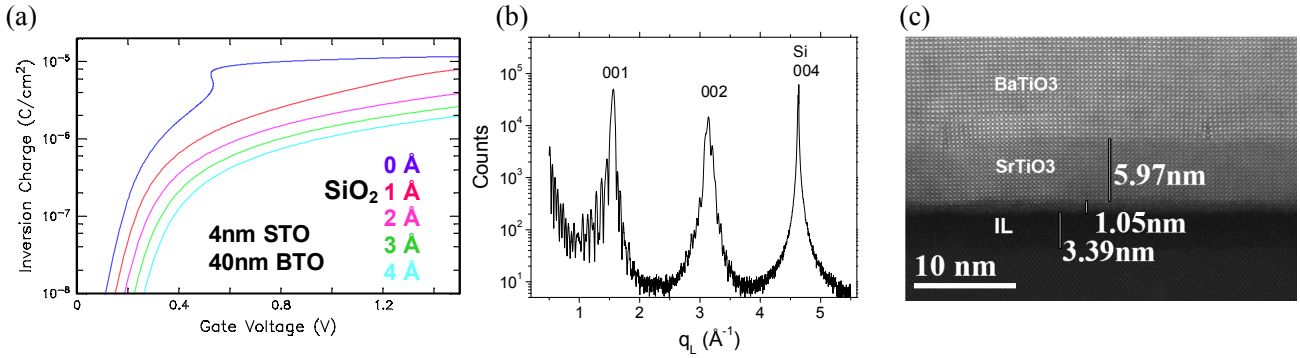

Figure 1: (a) Inversion charge as a function of gate voltage for a field-effect device with $BaTiO_3/SrTiO_3/SiO_2$ as a gate oxide. The $SrTiO_3$ and $BaTiO_3$ film thickness were fixed to 4 and 40 nm respectively while the SiO_2 thickness was varied from 0 to 0.4 nm. (b) X-ray diffraction out-of-plane scan (NSLS) and TEM image for a $BaTiO_3/SrTiO_3/SiO_2$ stack (the TEM shows the presence of an amorphous interfacial layer between Si and STO).

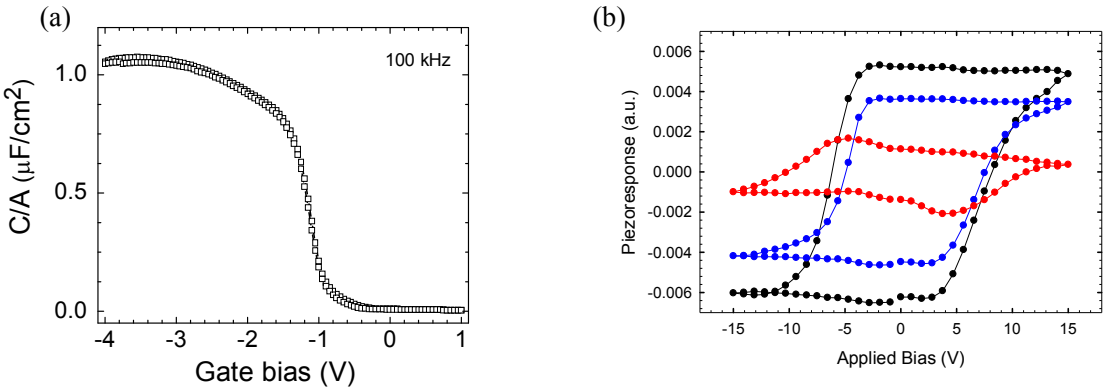

Figure 2: (a) Capacitance density as a function of voltage for 16 nm $BaTiO_3$/ 6 nm $SrTiO_3/SiO_2$ stack – (b) PFM hysteresis loops recorded on a 40 nm $BaTiO_3$/ 6 nm $SrTiO_3/SiO_2$ heterostructure on different location of the surface.

Origin of 90^o Domain Wall Pinning in $Pb(Zr_{0.2}Ti_{0.8})O_3$ Heteroepitaxial Thin Films

Dong Su,[1] Qingping Meng,[2] Myung-Geun Han,[2] C. A. F. Vaz,[3] Yaron Segal,[3] Fred J. Walker,[3] Monica Sawicki,[4] Christine Broadbridge,[4] and Charles H. Ahn[3]

[1]Center for Functional Nanomaterials, Brookhaven National Laboratory, Upton, New York, 11973, USA; [2]Department of Condensed Matter Physics and Materials Science, Brookhaven National Laboratory, Upton, New York, 11973, USA; [3]Department of Applied Physics and Center for Research on Interface Structures and Phenomena, Yale University, New Haven, CT 06520, USA; [4]Department of Physics, Southern Connecticut State University, 501 Crescent Street, New Haven, CT, 06515, USA

Abstract

Researchers have studied the effect of ferroelectric fields in controlling the spin state via electric fields in multiferroic composite structures [1-2]. For instance, in a bilayer system composed of a ferroelectric perovskite ($PbZr_{0.2}Ti_{0.8}O_3$) and a colossal magnetoresistive (CMR) manganite ($La_{0.8}Sr_{0.2}MnO_3$, LSMO), the spin state in the CMR film can be controlled by switching the ferroelectric polarization state, thereby generating a large magnetoelectric coupling [3]. Since switching between the depletion and accumulation states is controlled by the domain switching of the ferroelectric film, the domain's structure and switchability is critically important to the device's performance.

We describe transmission-electron-microscopy study of the ferroelectric domains in a epitaxial $Pb(Zr_{0.2}Ti_{0.8})O_3$(PZT) film grown on $La_{0.8}Sr_{0.2}MnO_3/SrTiO_3$(001)[4]. By applying electric fields in situ, we find that the 90^o domain walls cannot be displaced with electric fields up to 0.40 MV/cm. We directly observe the pinning of 90^o domain walls by pairs of misfit dislocations with Burgers vectors ***a***[100] and ***a***[001]. Electron energy-loss spectroscopy(EELS) measurements show a deficiency of oxygen at the dislocation core which may lead to a surrounding depolarization field. But our model calculations based on the elastic theory suggest that the strain field of misfit dislocation-pair still play the primery role on the formation of 90^o domains and pin it down from possible switching under the applied electric fields. On the other hand, the interficial coupling between PZT and LSMO layer is also demonstrated using EELS line scan. The measurement of Mn valence is in agreement with the suggested change in the valence state of Mn induced by electrostatic charge modulation.

Reference:

[1] W. L. Brown, (1957). U.S. Patent 2, 791, 759.

[2] S. Mathews, R. Ramesh, T. Venkatesan, and J. Benedetto, Science **276**, 238 (1997)

[3] C. A. F. Vaz, J . Hoffman, Y. Segal, J. W. Reiner, R. D. Grober, Z. Zhang, C. H. Ahn, and F. J. Walker, Phys. Rev. Lett. **104**, 127202 (2010)

[4] Dong Su, Qingping Meng, Myung-Geun Han, C. A. F. Vaz, Yaron Segal, Fred J. Walker, Monica Sawicki, Christine Broadbridge, and Charles H. Ahn, Applied Physical Letters, **99**, 102902(2011)

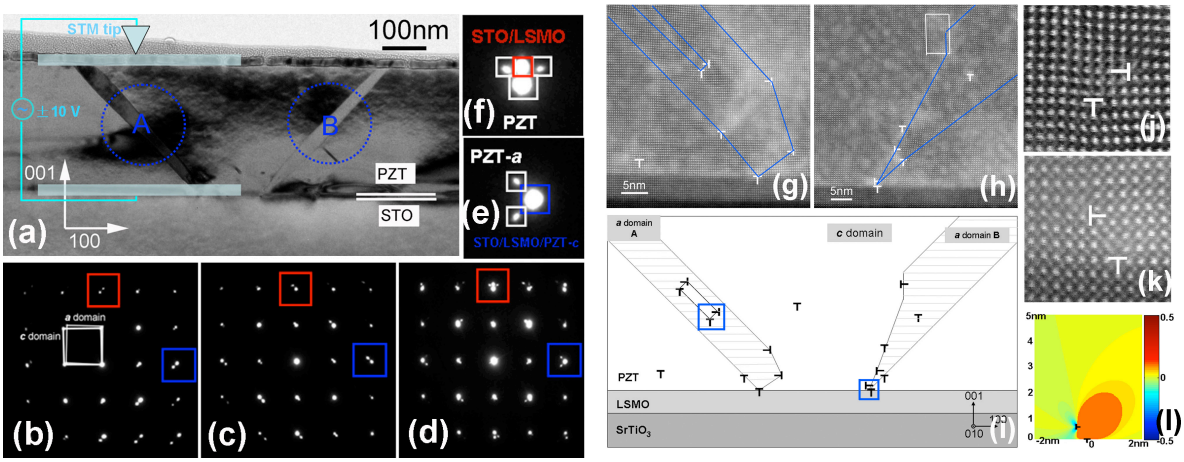

Figure 1: (a) A TEM bright-field image close to [010] zone axis taken with diffraction vector g=00-2. "A" and "B" indicate two a-oriented ferroelectric domains. The inset illustrates the setting of the biasing experiment. (b) and (c) are the corresponding SAED patterns of domain A and B, respectively, while (d) is the SAED pattern taken from the area including both domains and the STO substrate. (e) and (f) are, respectively, the enlarged images of the squares in (d) marked in blue and red. (g) and (h) STEM ADF images along the [010] zone axis of the A and B domains, respectively. Domain walls are marked by the blue lines. (i) Schematic diagram of the pinning of the domains A and B in (g) and (h). (j) and (k) STEM ADF images taken at higher magnifications on the areas marked in (i). (l) Calculated spatial variation of the elastic field $\varepsilon^{c}_{dis/xx}$ in the PZT film. The x and y coordinates are given in Å. The interface between PZT and substrate is at y=0.

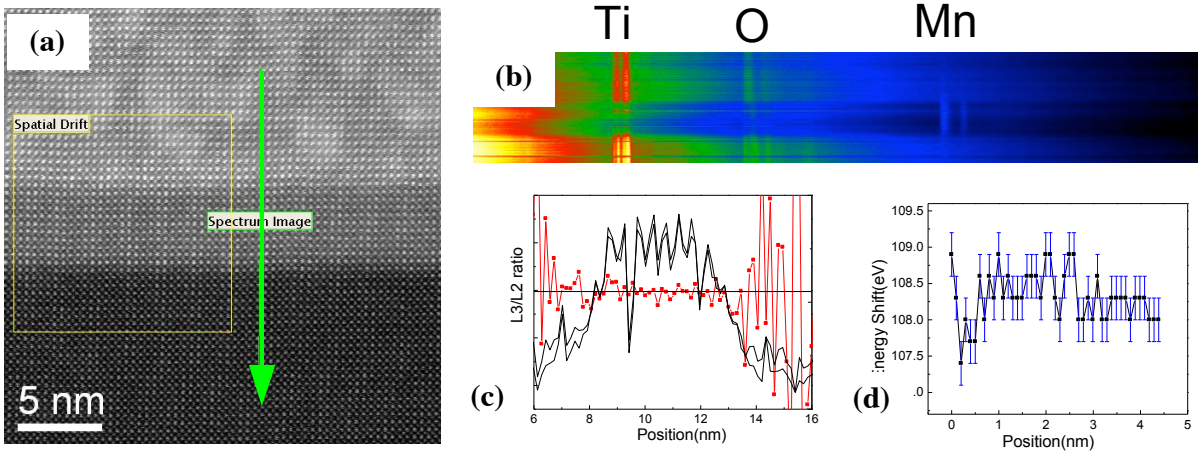

Figure 2, (a) ADF-STEM image showing the interfaces between PZT, LSMO and STO. The scanning-line is indicated by the green line. (b) colorful spectrum-image of the line-scan showing the signals of Ti, O and Mn. (c) Comparison of Mn signal and Mn L_3/L_2 ratio (in red) as a function of position. (d) The energy difference between O-K_a and Mn-L_3 edges crossing the LSMO layer.

Domain Wall Dynamics of Ferroelectric Ultrathin Films

Qingteng Zhang, Ryan Herchig, Inna Ponomareva
Department of Physics, University of South Florida, Tampa, Florida 33620, USA
e-mail: qingteng@mail.usf.edu

Nanosize objects are known to have properties that are very different from their bulk counterparts. As a result, they have become a subject of intense scientific and technological interest recently. One example is that nanoscale ferroelectric films and superlattices can exhibit nanostripes that are nanoscopic regions of "up" and "down" polarizations [1–3], hence forming domain walls which separate nanodomains with different polarization directions. The dynamical properties of domain walls are of technological importance since they are at the heart of ultradense ferroelectric memory technology and may play an important role in nanoscale ferroelectric sensors, actuators, and others.

We take advantage of accurate first-principle-based simulations[4] to reveal the intrinsic dynamics of nanodomains. We used classical molecular dynamics (MD) with the force-field derived from first-principles-based effective Hamiltonian [5–7] to investigate nine ferroelectric ultrathin films made of $PbTi_{0.6}Zr_{0.4}TiO_3$ ferroelectric alloy and with thicknesses ranging from 2 to 20 nm. We simulate films grown along [001] direction subjected to -2.5% epitaxial compressive strain and 84% partial screening of the surface charge. Ground state dipole patterns of these films consist of periodic nanostripe domains of alternating polarization (180° domains), whose morphology is in excellent agreement with experimental findings [2].

To study the oscillatory dynamics of these nanowalls we use non-equilibrium MD [8] and apply sub-switching *ac* electric field with frequencies 1 GHz - 4 THz along the film's out-of-plane direction at $T = 10$ K. Under the electric field, the dipoles near the nanowalls flip to align with the field which leads to a sideways motion of the domain wall. Since the direction of the electric field alternates, so does the direction of the domain wall motion resulting in the oscillatory dynamics of the nanowall. Typically we simulate at least thirty periods of *ac* field to achieve steady state.

We first focus on the oscillatory dynamics in the thinnest film and trace the time evolution of the average nanowall's displacement from its equilibrium position ΔX. This displacement is obtained from the count of dipoles flipped during the simulation. After the first few transient oscillations the dynamics reaches its steady state where the displacement follows the harmonic solution $\Delta X = X\sin(\omega t + \phi)$, indicating that the nanowall moves as an elastic object. Here X is the amplitude of the nanowall's displacement, ω is the *ac* field frequency, t is time, and ϕ is the phase-shift with respect to the electric field. By analyzing the nanowall's response to an electric field of different frequencies we obtain dependence $X(\omega)$ and $\phi(\omega)$ given in Fig.1, and then combine them into a complex response function $\eta(w) = X\cos\phi + iX\sin\phi$. Below 0.3 THz the domain response is independent of the frequency (Fig.1(a)) with the nanowalls oscillating in phase with the electric field (Fig.1(b)). Above 1.5 THz the nanowalls have difficulty following the electric field as indicated by the drastic decrease in the amplitude X and increase in phase-shift ϕ. Surprisingly, there are *two* peaks in the amplitude of nanowall's oscillations that occur at 0.7 THz (low-frequency peak) and at 3.2 THz (high-frequency peak). Existence of these peaks suggests that the nanowalls exhibit a resonance dynamics and must have a mass associated with them.

We will report our computational findings for other films and analyze them using the model of a damped harmonic oscillator. Such analysis reveals intrinsic features of ultrafast nanodomain dynamics that includes: existence of exotic transition from resonance to relaxational dynamics; unusual domain mediated electromechanical coupling and others.

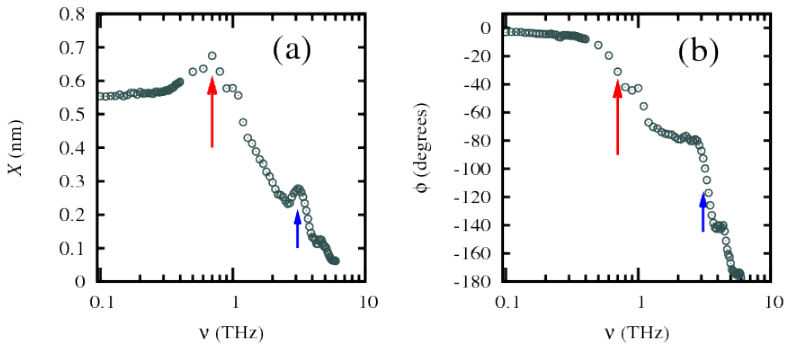

FIG. 1: Frequency dependent response of a nanowall to the electric field in a 0.2 nm thick film. The arrows indicate positions of the peaks.

The present work is supported by the U.S. Department of Energy, Office of Basic Energy Sciences, Division of Materials Sciences and Engineering under award DE-SC0005245 (computational studies) and by USF under Grant No. R070699 (some theoretical developments). The use of services provided by Research Computing, USF is greatly acknowledged.

---

[1] I. Kornev, H. Fu, and L. Bellaiche, Phys. Rev. Lett. **93**, 196104 (2004).
[2] D. Fong et al., Science **304**, 1650 (2004).
[3] S. Lisenkov, I. Ponomareva, and L. Bellaiche, Phys. Rev. B **79**, 024101 (2009).
[4] Q. Zhang, R. Herchig, and I. Ponomareva, Phys. Rev. Lett. **107**, 177601 (2011).
[5] L. Bellaiche, A. Garcia, and D. Vanderbilt, Phys. Rev. Lett. **84**, 5427 (2000).
[6] L. Bellaiche, A. Garcia, and D. Vanderbilt, Ferroelectrics **266**, 41 (2002).
[7] I. Ponomareva, I. I. Naumov, I. Kornev, H. Fu, and L. Bellaiche, Phys. Rev. B **72**, 140102 (2005).
[8] D. Rapaport, *The Art of Molecular Dynamics Simulation* (Cambridge University Press, 2001).

Conduction of topologically-protected charged ferroelectric domain walls

Weida Wu[1], Y. Horibe[1], N. Lee[1], S.-W. Cheong[1] and J.R. Guest[2]

[1]*Department of Physics and Astronomy and Rutgers Center for Emergent Materials, Rutgers University, Piscataway, NJ 08854 USA*

[2]*Center for Nanoscale Materials, Argonne National Laboratory, Argonne, Illinois 60439 USA*

Topology is the foundation for numerous robust phenomena such as topological defects [1], quantum hall effect [2] and topological insulators [3] in condensed matter physics because it is insensitive to continuous deformation or perturbation. Topological defects are pervasive in complex matter such as superfluid, liquid crystals and the early universe [1, 4]. However, little is known about topological defects in systems with coupled order parameters such as multiferroics, where magnetism and ferroelectricity coexist [5, 6]. A unique kind of topological defect, where six interlocked structural antiphase and ferroelectric domain walls merge into a vortex core, was unambiguously identified in multiferroic hexagonal $YMnO_3$ [7]. The intriguing vortex-antivortex network pattern has elegantly been analyzed using graph coloring theory [8]. The band gap of hexagonal (*h*-) *RE*MnO_3 (*RE* = Sc, Y, Ho, … Lu) is relatively small (~1.7 eV) [9], so the conduction properties of ferroelectric vortices may show interesting behavior. In fact, a significant conduction difference between opposite-polarization "domains" has been observed, and this conduction contrast was shown to originate from a polarization modulated Schottky-like barrier [7, 10]. Interestingly, the topology of vortex-antivortex network in 3-dimensional crystal naturally results in the presence of numerous "charged ferroelectric domain walls" where opposite polarizations are facing to each other [8, 11, 12]. Thus, it is imperative to find out the conduction properties of these charged domain walls.

Domain walls are kink solitons that separate domains with different orientations of ferroic order. They may host emergent phases or novel properties such as local conduction in an insulating matrix [13-15]. In conventional ferroelectrics, most studied domain walls are neutral while charged domain walls are rarely observed, which is likely due to unfavorable electrostatic and/or strain energy cost [16, 17]. Experimentally, observed charged domain walls are often associated with defects or needle-shape domains during polarization reversal [18-20]. Theoretically, charged domain walls may be stabilized by charged defects or free charge carriers [21-23]. In contrast to conventional ferroelectrics, the formation of charged domain walls in multiferroic *h-RE*MnO_3 is topologically inevitable because of the presence of highly curved vortex cores [8, 11, 12]. Herein, we report the observation of distinct nanoscale conduction characteristics of charged ferroelectric domain walls in *h*-$HoMnO_3$ (a p-type semiconductor) using *in situ* conductive Atomic Force Microscopy (cAFM), piezo-response force microscopy (PFM), and kelvin-probe force microscopy (KPFM) at low temperatures. Local conduction spectra indicate that the conduction at tail-to-tail (TT) domain walls is significantly (slightly) enhanced at high forward (reverse) bias compared to that of the domains themselves, probably stemming from the accumulation hole-like carriers. In contrast, the conduction of head-to-head (HH) domain walls shows no enhancement at high forward bias and even suppression at high reverse bias, probably due to depletion of hole-like carriers. Our results pave the way for understanding the semiconducting properties of the domains and domain walls in small-gap ferroelectrics.

How vortices propagate along the *c*-axis can be revealed by in-plane PFM with the *c*-axis in the surface plane [11, 12]. As seen in the topography image (shown in fig. 1(a)), we are able to obtain an atomically flat (110) surface of a $HoMnO_3$ single crystal by mechanical cleaving. Fig. 1(b) shows the PFM images taken at room temperature to reveal ferroelectric domain pattern. We aligned the orientation of conductive cantilever so that it was parallel to the *c*-axis, which is along the slow scan axis (vertical direction). In this configuration, the PFM signal (vertical deflection) originates from the buckling of the cantilever caused by shear deformation of in-plane ferroelectric domains in the presence of an out-of-plane electric field [12, 24]. The dark and bright contrasts represent in-plane up and down ferroelectric domains, respectively. The direction of local polarization is determined by the phase of the PFM signal and is further confirmed

by KPFM measurements at 65 K. Fig. 1(c) shows the derivative image of PFM (b) image that highlights the HH (dark) and TT (bright) domain walls, respectively.

In cAFM images with V_{tip}=-10 V, there is no conduction (current) contrast between different domains, as shown in Fig. 1(d). In contrast, there are line features with significant extra current. More interestingly, these lines overlap with the ferroelectric domain walls observed by PFM at the same location. By correlating PFM and cAFM images at the same location, we can identify two vortices in this area, as illustrated in the cartoon sketch in Fig. 1(e). Note that the fast rastering of the cantilever artificially broadens the apparent width of some conduction lines. In the conductance image with very slow rastering the observed width of conduction peaks is ~80-100 nm, which is comparable with the tip radius (~50 nm).

We acknowledge support from NSF DMR-0844807 and DMR-1104484. Use of the CNM was supported by the U. S. DOE, Office of Science, Office of BES, under Contract No. DE-AC02-06CH11357.

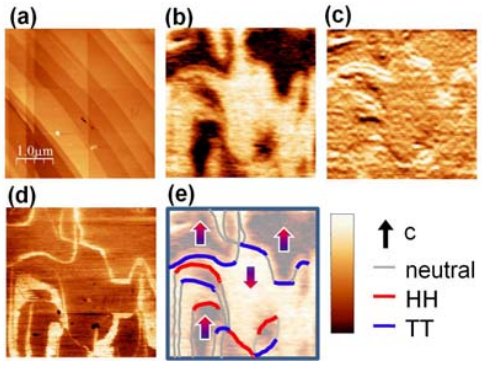

FIG. 1 (a) Topographic and (b), PFM images taken simultaneously at 300 K. (c) derivative map of PFM image along the *c*-axis (vertical) where bright (dark) lines are TT (HH) domain walls. (d) cAFM image taken at the same location as PFM at 300 K with V_{tip}=-10 V. (e) A cartoon sketch of ferroelectric domain walls according to PFM (overlaid) and its derivative images. The arrows indicate in-plane polarization orientation determined from the phase of PFM signal. Color scales are 4.5 nm, 8 pm and 0.4 nA for topography, PFM and cAFM images respectively.

Reference

[1] P. M. Chaikin, and T. C. Lubensky, *Principles of Condensed Matter Physics* (Cambridge University Press, Cambridge, UK, 2000).
[2] J. E. Avron, D. Osadchy, and R. Seiler, Physics Today **56**, 38 (2003).
[3] M. Z. Hasan, and C. L. Kane, Rev. Mod. Phys. **82**, 3045 (2010).
[4] A. A. Fraisse, C. Ringeval, D. N. Spergel, and F. R. Bouchet, Phys. Rev. D **78**, 043535 (2008).
[5] S. W. Cheong, and M. Mostovoy, Nat. Mater. **6**, 13 (2007).
[6] N. A. Spaldin, S.-W. Cheong, and R. Ramesh, Physics Today (2010).
[7] T. Choi *et al*., Nature Materials **9**, 253 (2010).
[8] S. C. Chae *et al*., P. Natl. Acad. Sci. USA **107**, 21366 (2010).
[9] W. S. Choi *et al*., Phys. Rev. B **78**, 054440 (2008).
[10] W. Wu *et al*., Phys. Rev. Lett. **104**, 217601 (2010).
[11] T. Jungk, Á. Hoffmann, M. Fiebig, and E. Soergel, Appl. Phys. Lett. **97**, 012904 (2010).
[12] E. B. Lochocki, S. Park, N. Lee, S.-W. Cheong, and W. Wu, Appl. Phys. Lett. **in press** (2011).
[13] J. Seidel *et al*., Nat. Mater. **8**, 229 (2009).
[14] J. Seidel *et al*., Phys. Rev. Lett. **105**, 197603 (2010).
[15] P. Maksymovych *et al*., Nano Letters **11**, 1906 (2011).
[16] W. Zhong, R. D. King-Smith, and D. Vanderbilt, Phys. Rev. Lett. **72**, 3618 (1994).
[17] M. E. Lines, and A. M. Glass, *Principles and Applications of Ferroelectrics and Related Materials* (Oxford University Press, New York, 2001).
[18] A. Krishnan, M. M. J. Treacy, M. E. Bisher, P. Chandra, and P. B. Littlewood, AIP Conf. Proc. **535**, 191 (2000).
[19] V. Y. Shur, E. L. Rumyantsev, E. V. Nikolaeva, and E. I. Shishkin, Appl. Phys. Lett. **77**, 3636 (2000).
[20] C.-L. Jia *et al*., Nat. Mater. **7**, 57 (2008).
[21] X. Wu, and D. Vanderbilt, Phys. Rev. B **73**, 020103 (2006).
[22] M. Y. Gureev, A. K. Tagantsev, and N. Setter, Phys. Rev. B **83**, 184104 (2011).
[23] E. A. Eliseev, A. N. Morozovska, G. S. Svechnikov, V. Gopalan, and V. Y. Shur, Phys. Rev. B **83**, 235313 (2011).
[24] T. Jungk, Á. Hoffmann, and E. Soergel, New J. Phys. **11**, 033029 (2009).

Elastic Relaxation and Local Strain in $BiFeO_3$ Nanostructures

Martin V. Holt[1], Jeffrey A. Klug[2], Ramesh Nath Premnath[2,3], Alexandra Joshi-Imre[1], Seungbum Hong[2], Ram S. Katiyar[3], Michael J. Bedzyk[4], and Orlando Auciello[1,2]
[1]*Center for Nanoscale Materials, Argonne National Laboratory, Argonne, Illinois 60439 USA*
[2]*Materials Science Division, Argonne National Laboratory, Argonne, Illinois 60439 USA*
[3]*Department of Physics and Institute for Functional Nanomaterials, University of Puerto Rico, San Juan, PR 00931*
[4]*Department of Materials Science and Engineering, Northwestern University, Evanston, Illinois 60208 USA*

We report an elastic relaxation and increase in local strain variation correlated with ferroelectric domains within epitaxial $BiFeO_3$ thin film nanostructures fabricated by combined electron-beam and focused ion-beam nanolithography. Nano-focused x-ray diffraction microscopy provided new insights into the relationship between film strain and ferroelectric domains in nanostructures, namely: i) an out-of-plane (C-axis) elastic relaxation of as much as -1.8% Δc/c in a BFO film-based nanostructure relative to the planar film lattice constant; ii) an out-of-plane rotation trending from the center towards all released edges of the nanostructure; and iii) an increase of inter-domain strain variation within the nanostructure of approximately 10 times the inter-domain variation found within the planar film, correlated with ferroelectric domain boundaries as confirmed by piezoresponse-force microscopy (PFM). These results indicate that the release of in-plane BFO/SRO mismatch strain in a planar film is taken up by the local ferroelectric domain structure after patterning, resulting in greatly increased mechanical strain gradients within the structure.

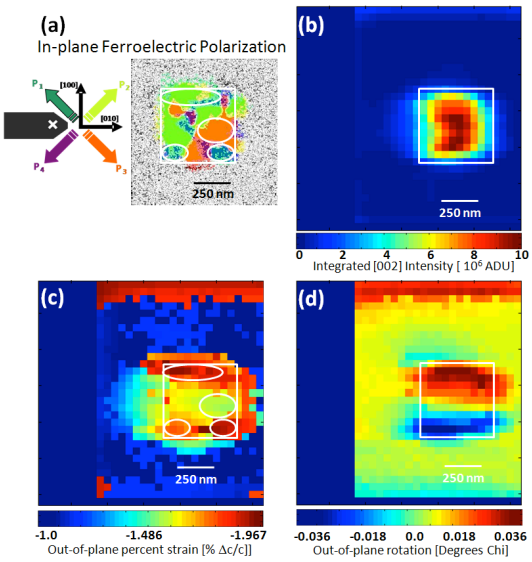

Figure 1. Results of nanofocused x-ray diffraction lattice mapping in a single 500nm BFO nanostructure [(b)-(d)] compared to the ferroelectric domain structure observed via PFM (a). Repeated 2D lateral scans were taken while varying the sample angle across the BFO (002) rocking curve, from which the integrated intensity (b), out-of-plane lattice strain (c), and out-of-plane lattice (C-axis) rotation (d) were extracted. The lattice constant of the film in the nanostructure is relaxed relative to the planar film by a strain value of as much as -1.8% dc/c, with a strain distribution that generally corresponds to the ferroelectric domain structure (from [1]).

[1] "*Elastic relaxation and correlation of local strain gradients with ferroelectric domains in (001) $BiFeO_3$ nanostructures*", J. Klug, M. Holt, R. N. Premnath, A. Joshi-Imre, S. Hong, R. S. Katiyar, M. J. Bedzyk, and O. Auciello, *Appl. Phys. Lett.* **99** 052902 (2011).

Session 5
Superlattices

Nanosecond Dynamics in Ferroelectric/Dielectric Superlattices

J. Y. Jo,[1,2] P. Chen,[1] R. J. Sichel,[1] M. Dawber,[3] H. N. Lee,[4] S. Nakhmanson,[5] E. M. Dufresne,[5] and P. G. Evans[1]

1. Materials Science and Engineering and Materials Science Program, University of Wisconsin, Madison, WI 53706
2. Present address: School of Materials Science and Engineering, Gwangju Institute of Science and Technology, Gwangju 500-712, Korea
3. Physics and Astronomy, Stony Brook University, Stony Brook, NY 11794
4. Oak Ridge National Laboratory, Oak Ridge, TN 37831
5. Argonne National Laboratory, Argonne, IL 60439

Ferroelectric/dielectric superlattices (SLs) have novel properties including the stabilization of two-dimensional nanoscale domain patterns and the extension of remnant polarization into layers with normally dielectric compositions. [1,2] The steady-state and quasi-static properties of these materials are beginning to be understood in both theory and experiment using density functional theory (DFT) calculations and a variety of experimental probes such as x-ray scattering, electron microscopy, and electrical measurements. The effect of the novel electronic and structural phenomena of ferroelectric/dielectric superlattices on their dynamical properties is, however, still less well understood. We will present two recent experimental studies of the nanosecond dynamics of ferroelectric/dielectric superlattices with two compositions. Together these two results show that the dynamics of ferroelectric/dielectric superlattice can provide important insight into fundamental structural and electronic issues in these materials.

Superlattice based on unit-cell-scale layers of $PbTiO_3$ and $SrTiO_3$ exhibit a relatively weak coupling of the polarization between adjacent ferroelectric layers.[3] As a result, the remnant polarization in the $PbTiO_3$ layers self-organizes into a domain pattern with a characteristic repeat length of several nanometers. For the particular composition of the repeating unit of the superlattice in our experiments, 12 unit cells (u.c.) of $PbTiO_3$ and 3 u.c of $SrTiO_3$, the domain period is 6 nm. The modulation of the atomic structure due to the domain pattern leads to a series of diffuse scattering satellite reflections previously reported by Zubko *et al*., ref. 1. Applied fields modify this domain structure and the domain diffuse reflections thus provide insight into the dynamics of the electronic response of the system. We have studied the nanosecond-scale time dependence and electric field dependence of the intensity of the diffuse scattering reflections, as shown in Fig. 1(a). Our approach is based on x-ray microdiffraction, using time resolution provided by the inherently short x-ray bunch duration at synchrotron radiation light sources.[3]

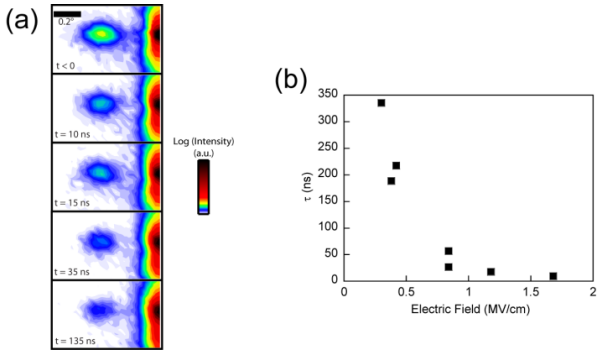

Figure 1 (a) Time evolution of the domain diffuse scattering in a $PbTiO_3/SrTiO_3$ superlattice in an electric field with a magnitude of 0.84 MV/cm starting at t=0(b) Electric-field dependence of the characteristic time of the domain dynamics.

The transition between the initial stripe domain state and the high-electric-field uniform polarization state occurs in a characteristic time that depends on the magnitude of the applied electric field. At the highest electric fields of our study the transition occurs with a characteristic time of several nanoseconds, Fig. 1(b). The transition is reversible, and the stripe pattern is reestablished in the interval between electric-field pulses. The piezoelectric distortion of the superlattice is influenced by the domain dynamics, but exhibits a shifted component even at times at which the stripe pattern is not switched. Based on these observations we have proposed a model for the domain dynamics based on the progressive switching of nanoscale regions of domains.

A second series of experiments probed $BaTiO_3/CaTiO_3$ superlattices in which the dynamics are dramatically slower than the $PbTiO_3/SrTiO_3$ system. The comparatively slow dynamics of a superlattice with a repeating unit of 2 u.c. of $BaTiO_3$ and 4 layers of $CaTiO_3$ is apparent in the piezoelectric distortion shown in Fig. 2. The piezoelectric strain developed at short times is nearly an order of magnitude smaller than the strain eventually reached under longer millisecond-duration pulses.[4] The piezoelectricity observed in longer duration electric fields is qualitatively consistent with the introduction of a large continuous polarization throughout the superlattice, and is also in quantitative agreement with the predictions of DFT calculations with an imposed highly polar tetragonal symmetry. DFT calculations also show, however, that the tetragonal symmetry is likely to be unstable in zero electric field. We thus hypothesize that the applied electric field induces a symmetry transformation between a distorted and comparatively unresponsive zero-field state to a more symmetric state with large piezoelectric coefficients.

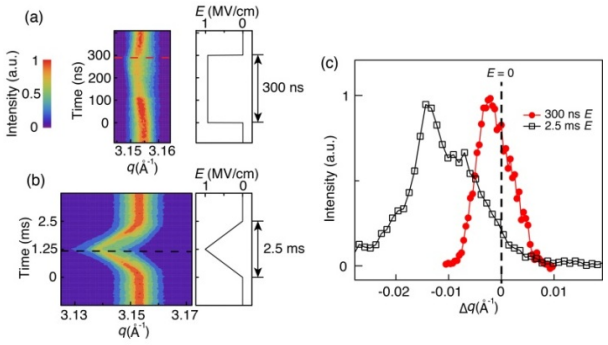

Figure 2 Reflections of the BTO/CTO SL as a function of the elapsed time and wavevector q_z during (a) 300-ns electric field pulses and (b) 2.5-ms triangle-wave electric fields. The intensity scale is normalized to the peak intensity in each plot. Electric field waveforms are shown to the right of the plots. (c) Diffraction patterns acquired at an elapsed time of 291 ns in the plot shown in (a) (circles) and at 1.2 ms in the plot shown in (b) (squares). The electric fields are 0.94 MV/cm and 0.96 MV/cm respectively. The line at $\Delta q=0$ indicates the wavevector of the maximum intensity at zero electric field.

[1] P. Zubko, N. Stucki, C. Lichtensteiger, and J. M. Triscone, Phys. Rev. Lett. **104**, 187601 (2010).
[2] S. M. Nakhmanson, K. M. Rabe, and D. Vanderbilt, Appl. Phys. Lett. **87**, 102906 (2005).
[3] J. Y. Jo, P. Chen, R. J. Sichel, S. J. Callori, J. Sinsheimer, E. M. Dufresne, M. Dawber, and P. G. Evans, Phys. Rev. Lett. **107**, 055501 (2011).
[4] P. Chen, J. Y. Jo, H. N. Lee, E. M. Dufresne, S. M. Nakhmanson, and P. G. Evans, New J. Phys. (in press) (2011).

New $PbTiO_3$ based superlattices with exceptional properties

M. Dawber,[1] S.J. Callori,[1] J. Sinsheimer,[1] J. Gabel,[1] Y. Benkara,[1]
B. Bein,[1] J. Daley,[1] Dong Su,[2] and M.V. Fernandez-Serra[1]

[1] *Department of Physics and Astronomy, Stony Brook University, Stony Brook, NY 11794-3800 USA*
[2] *Center for Functional Nanomaterials, Brookhaven National Laboratory, Upton, NY,USA*

Artificially layered perovskite oxide superlattices present excellent opportunities for the development of tailored materials with intriguing properties. $PbTiO_3$ in particular is a compound which when combined with other perovskite oxides in a finely layered structure enables new phenomena, for example, interfacially driven improper ferroelectricity in $PbTiO_3/SrTiO_3$. Recently we have been studying in detail a broad range of superlattices based on $PbTiO_3$, for example, we have grown series of samples combining $PbTiO_3$ with $BaTiO_3$, $SrTiO_3$ and $CaTiO_3$.

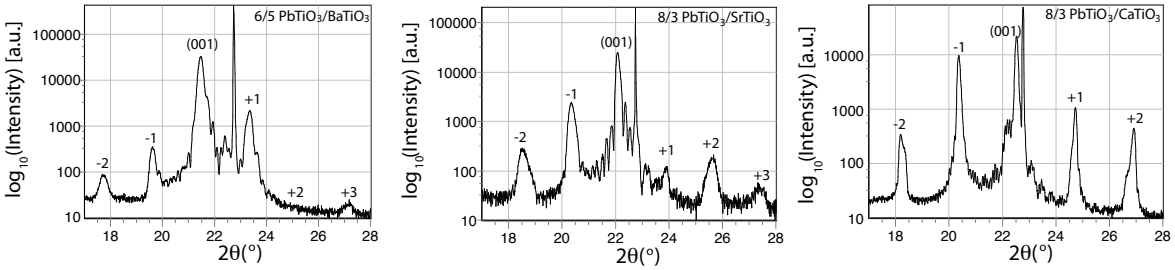

FIG. 1. *$\theta - 2\theta$ x-ray diffraction scans around the (001) peak of $PbTiO_3/BaTiO_3$, $PbTiO_3/SrTiO_3$ and $PbTiO_3/CaTiO_3$ superlattices grown in our laboratory. The superlattices are grown on top of $SrRuO_3$ films on $SrTiO_3$ substrates.*

Through a combination of different experimental techniques, including x-ray diffraction, transmission electron microscopy, electrical measurement and atomic force microscopy our aim is to understand how electrostatics, strain and interactions at layer interfaces can lead to material properties markedly different and superior to those of the parent materials.

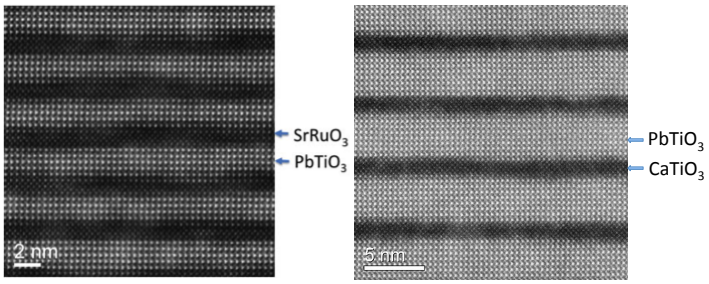

FIG. 2. *TEM images of representative samples of, left, $PbTiO_3/SrRuO_3$ and, right, $PbTiO_3/CaTiO_3$*

In this talk we will focus on two new $PbTiO_3$ based systems we have fabricated and studied. These two systems, $PbTiO_3/SrRuO_3$ and $PbTiO_3/CaTiO_3$ demonstrate quite different, yet equally fascinating, behavior. In the first we use a material normally considered to be a good metal as novel dielectric. In the second we look at the competition between the preference of $PbTiO_3$ for out -of-plane polarization and the preference of $CaTiO_3$ for in-plane polarization when they are grown on $SrTiO_3$ substrates.

In a set of $PbTiO_3/SrRuO_3$ superlattices which contain $SrRuO_3$ layers of single unit cell thickness we measured good polarization hysteresis loops, suggesting the $SrRuO_3$ layers were acting more like dielectrics than metals. Using a combined experiment and theory approach we show that as the $PbTiO_3$ layers are reduced in thickness the conduction properties change markedly and there is an increasingly important effect from compositional inversion symmetry breaking, which arises from the combined A and B site variation in the superlattice.

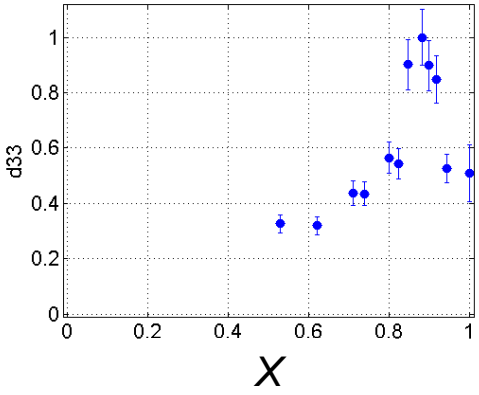

FIG. 4. *d_{33} in $PbTiO_3/CaTiO_3$ superlattices (arbitrary units) as a function of the $PbTiO_3$ volume fraction, $X = \frac{N_{PTO}}{N_{PTO}+N_{CTO}}$. The $CaTiO_3$ layer thickness in each bilayer was held constant at 3 unit cells.*

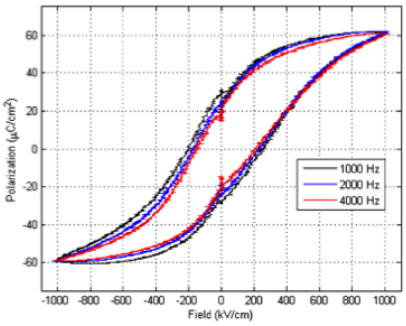

FIG. 3. *Polarization-field hysteresis loop measured on a 5/1$PbTiO_3/SrRuO_3$ superlattice.*

In $PbTiO_3/CaTiO_3$ superlattices we show that changes in the relative thickness of the constituent layers allows rotation of the polarization direction, leading both to fascinating domain structures and a greatly enhanced piezoelectric response when compared to the $PbTiO_3$ parent material. The piezoresponse measured with piezo force microscopy complements electrical measurements that show a related enhancement of dielectric constant and tunability. The structural details of the polarization rotation are revealed by grazing incidence x-ray diffraction performed at X21 and X22 at NSLS, BNL. Our results highlight a route to engineering enhanced piezoresponse through the layering of material with competing desires regarding their polarization direction, even when the entire film is epitaxially constrained to a substrate.

Beyond the exceptional properties of the materials themselves these two new examples serve to highlight the virtually limitless potential of the artificial superlattice approach to materials design.

Highly-confined spin-polarized two-dimensional electron gas in $SrTiO_3/SrRuO_3$ superlattices

J. Junquera,[1] P. García-Fernández,[1] Marcos Verissimo-Alves,[1] Daniel I. Bilc,[2] and Philippe Ghosez [2]

[1]Departamento de Ciencias de la Tierra y Física de la Materia Condensada, Universidad de Cantabria, Cantabria Campus Internacional, Avenida de los Castros s/n, 39005, Santander, Spain

[2]Physique Théorique des Matériaux, Université de Liège, Allée du 6 août 17 (B5), B-4000, Sart Tilman, Belgium

We report first principles characterization of the structural and electronic properties of $(SrTiO_3)_5/(SrRuO_3)_1$ superlattices. We show that the system exhibits a spin-polarized two-dimensional electron gas extremely confined to the 4*d* orbitals of Ru in the $SrRuO_3$ layer. Every interface in the superlattice behaves as minority-spin half-metal ferromagnet, with a magnetic moment of μ= 2.0 $\mu_B/SrRuO_3$ unit. The shape of the electronic density of states, half metallicity and magnetism are explained in terms of a simplified tight-binding model, considering only the t_{2g} orbitals plus (i) the bi-dimensionality of the system, and (ii) strong electron correlations.

As already observed in other confined 2DEG [H. Ohta *et al*., Nature Materials **6**, 129 (2007)], these interfaces exhibit an extremely large Seebeck coefficient S, of the order of 1700 μV/K. However, this enhancement of the Seebeck coefficient does not reflect on the power factor, defined as the numerator of the thermoelectric figure of merit ($S^2\sigma$, where σ is the electrical conductivity). The reason is that, wherever the Seebeck coefficient is large the electrical conductivity is very small or even zero.

Session 6
Phase transitions

Phase Evolution and Stabilization in Highly-Strained Epitaxial $BiFeO_3$ Films: Implications for Enhanced Electromechanical Response

A. R. Damodaran*, S. Lee, K. Jambunathan, and L. W. Martin

Department of Materials Science and Engineering and Materials Research Laboratory, University of Illinois, Urbana-Champaign, Urbana, IL 61801
*rdanoop@illinois.edu

$BiFeO_3$ is a widely studied multiferroic perovskite exhibiting antiferromagnetism that is coupled with ferroelectric order. The bulk ground state of $BiFeO_3$ is a rhombohedrally distorted perovskite structure ($R3c$ symmetry, a ~ 3.96 Å, and α_r ~ 0.6°), but $BiFeO_3$ also exhibits a strain-induced structural phase transition under large compressive strains to a tetragonally-distorted perovskite phase ($P4mm$ symmetry, a ~ 3.665 Å, c ~ 4.655 Å). Moreover at the critical compressive stain level of ~4.5%, as is the case in $BiFeO_3/LaAlO_3$ (001) heterostructures, so-called mixed-phase structures have been observed in which both the tetragonal- and rhombohedral-like phases coexist. It is in these mixed-phase films, that reversible electric field induced strains between 4-5% have been reported. Recent studies suggest that such films exhibit an exotic structural evolution accompanied by exciting properties that could make these materials candidates for future lead-free piezoelectric devices. The enhanced electromechanical response in these films has been attributed to the emergence of the complex mixed-phase structures and the ability for this material to reversibly transform under applied electric fields between these various phases.

In this presentation, we will discuss a number of intriguing aspect of these complex and interesting materials including the structural evolution of these films as a function of strain, thickness, and temperature, the observation of new phases of $BiFeO_3$, the implications of these phases for the observed large electromechanical response, a model for the formation of these structures that builds upon the idea of a spinodal-modulated structure, and routes to stabilize these structure for future applications. We begin by first examining the nanostructural evolution of the strain-induced phase boundaries in $BiFeO_3/LaAlO_3$ (001) heterostructures of varying thickness. Films were produced via pulsed laser deposition and characterized using a combination of high-resolution X-ray diffraction and scanning-probe microscopy-based studies (Fig. 1). We have uniquely identified the numerous phases present at these phase boundaries and their nanoscale spatial arrangement. We show that the mixed-phase regions in these films are made up not of a mixture of tetragonal-and rhombohedral-phases of $BiFeO_3$, but of an intimate mixture of highly distorted, monoclinic phases – one a monoclinic version of the so-called tetragonal-phase ($M_{II,tilt}$-phase, c~ 4.667) tilted 1.6° from the surface normal and the other an intermediate, monoclinic phase (M_I-phase, c ~ 4.168 Å) tilted 2.8° from the surface normal in the opposite direction. We also employ piezoresponse force microscopy (PFM)-based techniques to show that the added complexity associated with the strain-induced structural phase boundaries in $BiFeO_3$ films are

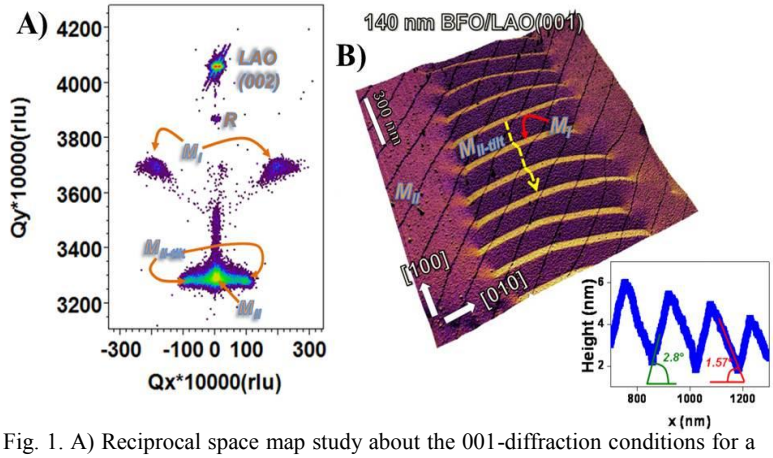

Fig. 1. A) Reciprocal space map study about the 001-diffraction conditions for a 140 nm $BiFeO_3$ / $LaAlO_3$ (001) heterostructure reveals a complex set of phases. B) High-resolution atomic force microscopy image of the so-called mixed-phase structures with areas corresponding to each phase labeled. Inset shows a line trace across the mixed-phase regions and the corresponding surface displacements associated with the tell-tale saw-tooth structure.

key in determining the electric field response of these materials. We will present a detailed model of the nature of the nanoscale structural evolution between the dramatically different phases including evidence of an asymmetric boundary structure and we will discuss PFM-based switching experiments that indicate our ability to reversibly write pure-tetragonal-like and mixed-phase regions with a high degree of spatial control and will end with a proposed model for the enhanced electromechanical coupling observed in these materials.

We will also present the temperature- and thickness-dependent structural and morphological evolution of these strain induced transformations. Using high-resolution X-ray diffraction and temperature-dependent scanning-probe-based studies we have observed a complex temperature- and thickness-dependent evolution of phases in this system. It is observed that the fraction of the mixed-phase regions decreases with increasing temperature and that in 40 nm thick films, all evidence of the mixed-phase structure is removed. Upon cooling the films, the mixed-phase structures are observed to return. This suggests that in some films (i.e., those less than ~250 nm) the mixed-phase structures form via a strain induced spinodal-instability and the resulting mixed-phase structures represent a strain-relaxation mechanism in these films. Details of the thermodynamic landscape and connections with other systems will be discussed. Furthermore, in films > 250 nm, a breakdown of this strain-stabilized metastable mixed-phase structure to non-epitaxial microcrystals of the parent rhombohedral structure of $BiFeO_3$ is observed. By a thickness of 300 nm, the entire film is observed to have experienced epitaxial breakdown. We will discuss a proposed mechanism for this breakdown and present a proposed phase stability map as a function of strain and film thickness at the growth temperature. Such an irreversible transformation of the mixed-phase structure, in turn, limits the magnitude of the net surface displacement associated with these field-induced phase transformations. Therefore, we have investigated chemical alloying routes to further stabilize the mixed-phase structures to greater thicknesses. By alloying the $BiFeO_3$ with Pb (up to 50%) (Fig. 2) we have observed the ability to stabilize the mixed-phase structures in films in excess of 500 nm thick and have demonstrated surface height depressions in excess of 20 nm.

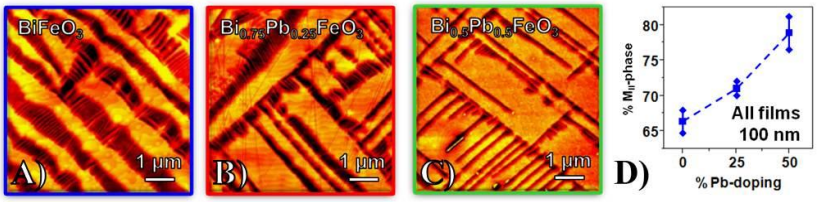

Fig. 2.Atomic force microscopy images of 100 nm thick A) $BiFeO_3$, B) $Bi_{0.75}Pb_{0.25}FeO_3$, and C) $Bi_{0.5}Pb_{0.5}FeO_3$ thin films grown on $LaAlO_3$ (001) substrates. D) Corresponding analysis of the total areal fraction made-up of the highly-distorted M_{II}-phase. Increasing Pb-content stabilizes the highly-distorted M_{II}-phase.

This work adds on to our understanding of the complex and technologically exciting phase boundaries in highly-strained $BiFeO_3$ thin films. Again, we will show that the presence of a variety of polymorphs of the $BiFeO_3$ is essential for the strong electromechanical response in these films.

References:

1) A. R. Damodaran, C.-W. Liang, Q. He, C.-Y. Peng, L. Chang, Y.-H. Chu, L. W. Martin, *Adv. Mater.***23**, 3170 (2011).
2) A. R. Damodaran, S. Lee, J. Karthik, S. MacLaren, L. W. Martin, under review at *Phys. Rev. B* (Nov. 2011).
3) A. R. Damodaran, A. Choquette, L. W. Martin, under review at *Appl. Phys. Lett.* (Nov. 2011).

Novel Properties in $BiFeO_3$ Films

S. Prosandeev, Wei Ren, L. Bellaiche

Institute for Nanoscience and Engineering and Physics Department, University of Arkansas, Fayetteville, Arkansas 72701, USA

B. Dupe, B. Dkhil, I. Kornev

Laboratoire Structures, Proprietes et Modelisation des Solides, CNRS-UMR 8580, Ecole Centrale Paris, Grande Voie des Vignes, 92295 Chatenay-Malabry Cedex, France,

G. Geneste

CEA, DAM, DIF, F-91297 Arpajon, France

Zuhuang Chen, Z. L. Luo, Wei Ren, Yajun Qi, C. W. Huang, Lu You, C. Gao, Tom Wu, Junling Wang, P. Yang, T. Sritharan, and Lang Chen

School of Materials Science and Engineering, Nanyang Technological University, Singapore 639798, Singapore
National Synchrotron Radiation Laboratory, University of Science and Technology of China, Hefei, Anhui 230029,
People's Republic of China
Singapore Synchrotron Light Source (SSLS), National University of Singapore, 5 Research Link, Singapore 117603, Singapore
Division of Physics and Applied Physics, School of Physical and Mathematical Sciences Nanyang Technological University, Singapore, 637371, Singapore

$BiFeO_3$ (BFO) films that are grown along the [001] direction and that are under high compressive strain have recently attracted a lot of attention, mostly because of the occurrence of novel monoclinic phases with giant axial ratio and the prediction of large magnetoelectric coefficients [1-8].

Here, we report the discovery of several other novel features in BFO films [9-11].
More precisely:

1) Density-functional calculations were performed to predict structural and magnetic properties of (001) BFO films under *tensile* epitaxial strain. These films remain monoclinic (Cc space group) for misfit strains between 0% and 8%, with the polarization, tilt axis and magnetization all rotating when varying the strain. At a tensile strain of around 8%, these films undergo a first-order phase transition towards an orthorhombic phase (Ima2 space group). In this novel phase, the polarization and tilt axis lie in the epitaxial plane. An unexpected additional degree of freedom, namely, an antiphase arrangement of Bi atoms, is also found for all tensile strains [9].

2) Two tilted triclinic phases were found via synchrotron x-ray diffractions in the mixed-phase regions of highly strained (001) BFO films. First-principles calculations suggest that these two triclinic phases

originate from a phase separation of a single monoclinic state accompanied by elastic matching between the two phase-separated states and further suggest that the ease of phase transition between these two energetically close phases is responsible for the large piezoelectric responses observed in Zhang et al., Nat. Nano. **6**, 98 (2011) [10].

3) The effect of misfit strain on properties of epitaxial BFO films that are grown along the pseudocubic [-110] direction, rather than along the usual [001] direction, were predicted from density-functional theory. These films adopt the monoclinic Cc space group for compressive misfit strains smaller in magnitude than 1.6% and for any investigated tensile strain. In this Cc phase, both polarization and the axis about which antiphase oxygen octahedra tilt rotate within the epitaxial plane as the strain varies. Surprisingly and unlike in (001) films, for compressive strain larger in magnitude than 1.6%, the polarization vanishes and two orthorhombic phases of Pnma and $P2_12_12_1$ symmetry successively emerge via strain-induced transitions. The Pnma-to- $P2_12_12_1$ transition is a rare example of a so-called pure gyrotropic phase transition, and the $P2_12_12_1$ phase exhibits original interpenetrated arrays of ferroelectric vortices and antivortices [11].

The work in Arkansas is mostly supported by ONR grants N00014-11-1-0384, N00014-08-1-0915 and N00014-07-1-0825 (DURIP). We also acknowledge the Department of Energy, Office of Basic Energy Sciences, under contract ER-46612, and NSF grants DMR-1066158, DMR-0701558 and DMR-0080054 (C-SPIN). Some computations were made possible thanks to a Challenge grant from HPCMO of the U.S. Department of Defense and thanks to the MRI NSF grant 0722625.

References:

1. J. X. Zhang, Q. He, M. Trassin, W. Luo, D. Yi, M. D. Rossell, P. Yu, L. You, C. H. Wang, C.Y. Kuo, J. T. Heron, Z. Hu, R. J. Zeches, H. J. Lin, A. Tanaka, C. T. Chen, L. H. Tjeng, Y.-H. Chu, and R. Ramesh, Phys.Rev. Lett. 107, 147602 (2011).
2. H. Béa, B. Dupé, S. Fusil, R. Mattana, E. Jacquet, B. Warot-Fonrose, F. Wilhelm, A. Rogalev, S. Petit, V. Cros, A. Anane, F. Petroff, K. Bouzehouane, G. Geneste, B. Dkhil, S. Lisenkov, I. Ponomareva, L. Bellaiche, M. Bibes, and A. Barthélémy, Phys. Rev. Lett. 102, 217603 (2009).
3. Alison J. Hatt and Nicola A. Spaldin, Claude Ederer, Phys. Rev. B 81, 054109 (2010).
4. C. Ederer and N. A. Spaldin, Phys. Rev. Lett. 95, 257601 (2005).
5. Oswaldo Diéguez, O.E. González-Vázquez, Jacek C. Wojdeł, Jorge Íñiguez, Phys. Rev. B 83, 094105 (2011).
6. B. Dupé, I. C. Infante, G. Geneste, P.-E. Janolin, M. Bibes, A. Barthélémy, S. Lisenkov, L. Bellaiche, S. Ravy, and B. Dkhil, Phys. Rev. B 81, 144128 (2010).
7. C. J. M. Daumont, S. Farokhipoor, A. Ferri, J. C. Wojdeł, Jorge Íñiguez, B. J. Kooi, and B. Noheda, Phys. Rev. B 81, 144115 (2010).
8. L. Pálová, P. Chandra, and K. M. Rabe, Phys. Rev. B 82, 075432 (2010).
9. B. Dupe, S. Prosandeev, G. Geneste, B. Dkhil, and L. Bellaiche, BiFeO3 Films under Tensile Epitaxial Strain from First Principles, Physical Review Letters **106**, 237601 (2011).
10. Zuhuang Chen, S. Prosandeev, Z. L. Luo, Wei Ren, Yajun Qi, C. W. Huang, Lu You, C. Gao, I. A. Kornev, Tom Wu, Junling Wang, P. Yang, T. Sritharan, L. Bellaiche, and Lang Chen, Coexistence of ferroelectric triclinic phases in highly strained $BiFeO_3$ films Physical Review B **84**, 094116 (2011).
11. S. Prosandeev, Igor A. Kornev, and L. Bellaiche, Phase Transitions in Epitaxial (-110) $BiFeO_3$ Films from First Principles, Physical Review Letters **107**, 117602 (2011).

Stability and Field Induced Response of Heterophase Nanostructures in Constrained Ferroelectrics and Ferroelastics

Alexander Roytburd
University of Maryland, College Park
Department of Materials Science and Engineering

First order transformations under mechanical constraint, particularly in epitaxial films and nanowires with fixed length, can result in formation of heterophase states consisting of two or more coexisting phases (Fig. 1). However, equilibrium two phase areas on theoretically calculated temperature-misfit diagrams are usually absent. The attempt to obtain two phase area using Landau-Devonshire potential renormalized by constraint with fixed domain arrangement does not describe the thermodynamic equilibrium state [1]. This approach takes into account only elastic interaction between the film and substrate, neglecting interaction between the phases. On the other hand, elastic domain theory which considers thermodynamics at relatively small deviation from equilibrium state of phases can correctly describe elastic interaction between incompatible phases [2]. This theory shows that the stability of two phase equilibrium is determined by competition of phase-substrate elastic interaction which initiates mixture formation and phase-phase elastic interaction which opposes phase mixture. If phase-substrate interaction is dominant, formation of polydomain heterophase structure with nonconvex dependence of its free energy on phase (domain) fraction. If phase-phase interaction dominates, the two phase state is unstable and direct and reversible transformations proceed with hysteresis (Fig. 2).

For stable two phase state, changing temperature or external electrical or mechanical fields leads to domain evolution which results in enhanced extrinsic properties, including large electrical susceptibility, piezo effect, or elastic compliance [3]. This enhancement is more pronounced for mixture of incompatible phases than for mixture of compatible phases or twins because non-convex free energy lowers the stability of the two-phase state and makes it more sensitive to influence of external field. Besides that, the elastic distortion of coherent phases decreases the interface energy and the Peierls' barrier for interface movement. The essential elastic distortions, which are uniform in phase domains, can mimic intermediate low-symmetry phases. On the other side, polydomain mixture with small domain thickness can be interpreted as average "polysynthetic" or "adaptive" phases.

The concepts above are all valid for heterophase ferroelastics. For ferroelectrics, additional electrostatic interactions between phases and substrate should be taken into account. However, the electrostatic effect is diminished as a result of formation of 180 degree domains or redistributions of free charges. The presented thermodynamical concept on stability and evolution of heterophase polydomain structure is applied for analysis of recent experimental observations of nanostructure and field induced response of $BiFeO_3$ epitaxial film as well as PZT crystal near morphotropic boundary. Extension of these ideas to constrained nanowires is discussed.

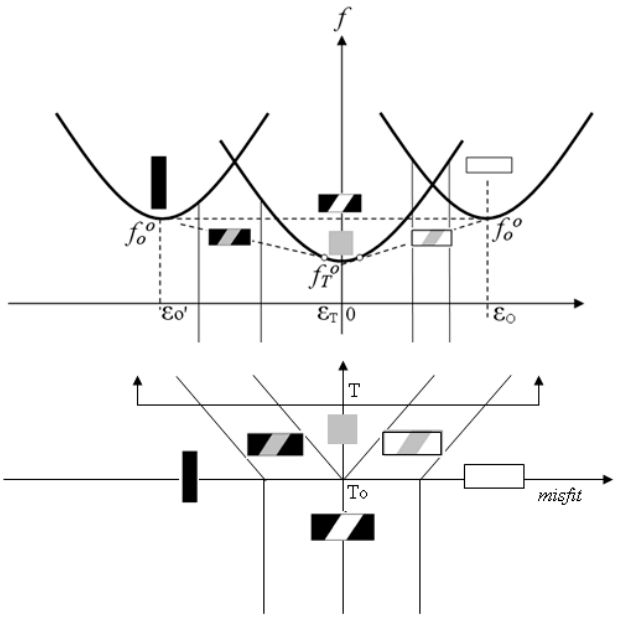

Figure 1: Free energy – misfit and temperature-misfit diagrams for tetragonal-orthogonal transformation of compatible phases.

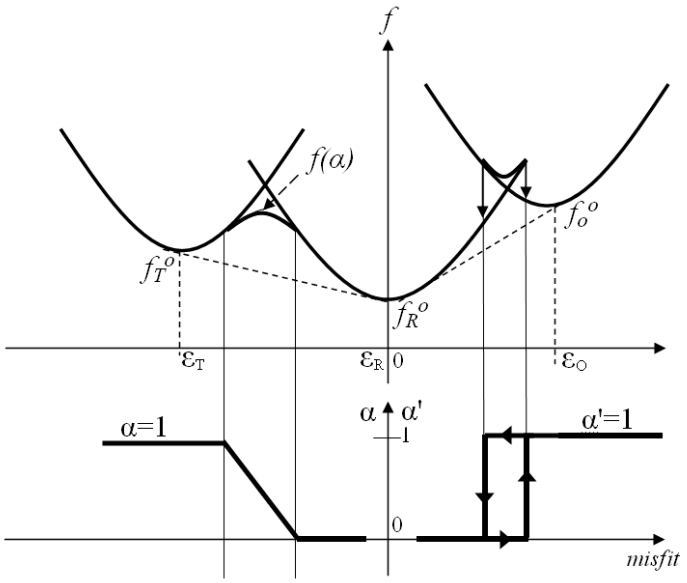

Figure 2: Free energy – misfit and phase fraction – misfit diagrams for rhombohedral-tetragonal and rhombohedral-orthorhombic transformation. ε_T, ε_R, and ε_o are self strains for tetragonal, rhombohedral and orthorhombic phases correspondingly.

REFERENCES

1. N. A. Pertsev, V. G. Koukhar, *Phys. Rev. Let.* **84,** 3722 (2000).

2. A. L. Roytburd, *J. Appl. Phys.* **83,** 228 (1998); **83,** 239 (1998).

3. A. L. Roytburd, J. Ouyang, B. M. Boyerinas, H. A. Bruck, *Appl. Phys. Lett.* **99**, 172902 (2011).

Tricritical Points and Related Properties of $Pb(Zr_{1-x}Ti_x)O_3$ Single Crystals

Alexei A. Bokov, Yujuan Xie, Xifa Long and Zuo-Guang Ye

Department of Chemistry and 4D LABS, Simon Fraser University,

Burnaby, British Columbia, V5A 1S6, Canada

For many years $Pb(Zr_{1-x}Ti_x)O_3$ (PZT) has been a canonical piezoelectric material due to excellent electromechanical properties observed in the solid solution compositions close to the morphotropic phase boundary (MPB). Besides MPB, in the temperature-composition (T-x) phase diagram of PZT, tricritical points are expected to be present, which separate the compositions exhibiting first and second order phase transition at the Curie point (T_C). However, the exact positions of tricritical points have not been verified. Recent investigations suggest that the positions of the tricritical points with respect to MPB can influence the properties significantly and may be at the origin of large piezoelectric effect of PZT and some other high-performance ferroelectric materials [1, 2]. However, the theoretical conclusions are contradictive. It was suggested initially that the high piezoelectricity stems from the composition proximity of the tricritical point to the triple point at which MPB ends [1]. In contrast, other authors [2] found that a single tricritical point coinciding with the triple point does not enhance the piezoelectric response and the response is larger if the two tricritical points exist far apart from one another. To clarify the picture, the experimental investigations are needed which are aimed at determining the tricritical point concentrations and the properties of the crystals at these points. In our previous study of PZT crystals in a wide composition range $0.2 < x < 0.6$ [3], we confirmed the existence of tricritical points at $x_{t1} \approx 0.55$ and $x_{t2} \approx 0.42$ and found another tricritical point at $x_{t3} \approx 0.25$. In the present work we investigate the ferroelectric properties at the tricritical Curie points and compare them with the behaviour at other compositions.

The temperature dependences of the dielectric susceptibility χ and birefringence Δn were measured. The spontaneous polarisation (the transition order parameter) was calculated from $P \propto (\Delta n)^{1/2}$. For tricritical compositions, the scaling relations $\chi \propto (T - T_C)^{-\gamma}$ and $P \propto (T - T_C)^{\beta}$ are valid around T_C (in the fluctuation-dominated critical region) with the non-classical values of critical exponents γ =1.49 and β = 0.33 equal to those observed in the concentration range of the second-order phase transition. The size of the critical region, $\tau \equiv (T\text{-}T_C)/T_C$, is about 0.1. Above and below the critical region, the behaviour predicted by

the mean-field theory is observed, namely, $\gamma = 1$ and $\beta = 1/4$ for the tricritical compositions, and $\gamma = 1$ and $\beta = 1/2$ for the second-order phase transition compositions (see Fig. 1).

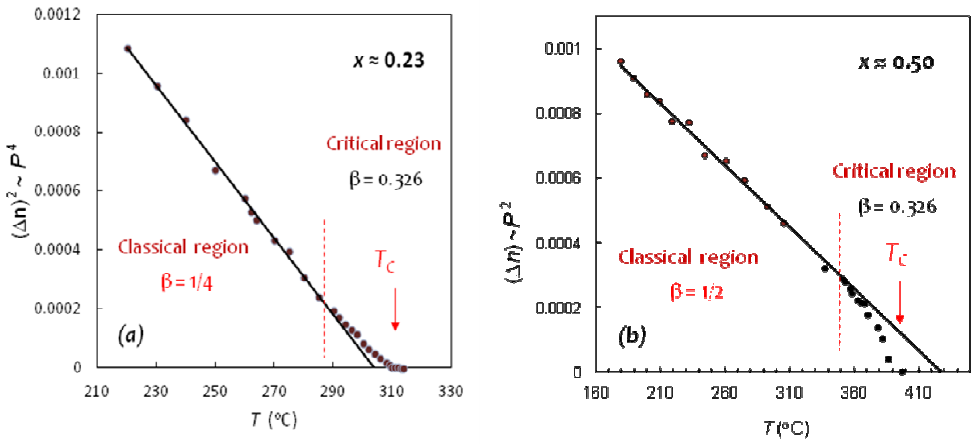

Figure 1. Critical behaviour of the order parameter, $P \propto (\Delta n)^{1/2}$ a) for $Pb(Zr_{0.77}Ti_{0.23})O_3$ crystal with the composition close to tricritical point; b) for $Pb(Zr_{0.50}Ti_{0.50})O_3$ crystal with the composition far from tricritical points. Experimental data are represented by symbols; the lines are the fits to scaling relation.

The work was supported by the U.S. Office of Naval Research (Grants No. N00014-06-1-0166 and No. N00014-11-1-0552).

References:

1. W. Lui and X. Ren, *Phys. Rev. Lett* **103,** 257602 (2009).
2. M. Porta and T. Lookman, *Phys. Rev. B* **83,** 174108 (2011).
3. A. A. Bokov, Y. Xie, X. Long and Z.-G. Ye, *in Fundamental Physics of Ferroelectrics and Related Materials 2011,* Gaithersburg, MD (2011).

Tuning the structural instability of $SrTiO_3$ by Eu doping: the phase diagram of $Sr_{1-x}Eu_xTiO_3$

Zurab Guguchia[1], Alexander Shengelaya[2], Hugo Keller[1], Jürgen Köhler[3], Myung-Hwan Whangbo[4], and Annette Bussmann-Holder[3]

[1]Physik Institut der Universität Zürich, Winterthurerstr. 190, CH-8057 Zürich, Switzerland
[2]Department of Physics, Tbilisi State University, Chavchavadze 3, GE-0128 Tbilisi, Georgia
[3]Max-Planck-Institut für Festkörperforschung, Heisenbergstr. 1, D-70569 Stuttgart, Germany
[4]Department of Chemistry, North Carolina State University, Raleigh, North Carolina 27695-8204, USA

Recently we have shown that the almost multiferroic system $EuTiO_3$ undergoes a structural phase transition at T_S=282K [1]. This transition is analogous to the one of $SrTiO_3$ at T_S=105K, where the oxygen octahedral rotations freeze out caused by the softening of a transverse acoustic zone boundary mode. Besides of this similarity between $SrTiO_3$ and $EuTiO_3$ also others exist, namely strong zone center optic mode softening reminiscent of a ferroelectric instability, however, suppressed by quantum fluctuations [2 – 5]. Both compounds have almost the same lattice constants since the ionic radii of Sr and Eu are the same. As such it is rather amazing that T_S in the Eu compound is more than doubled as compared to the transition temperature of $SrTiO_3$.
In order to explore the origin of this distinction, we have characterized the phase diagram of $Sr_{1-x}Eu_xTiO_3$ as a function of x experimentally by electron paramagnetic resonance (EPR) techniques and resistivity measurements. Theoretically a lattice dynamical study of the phase transitions has been performed and complemented by density functional calculations for the end members of the system.
Both, EPR and resistivity data show distinct anomalies in their temperature dependencies which are related to the structural phase transition. From these anomalies the phase diagram has been constructed which is shown in Fig. 1.

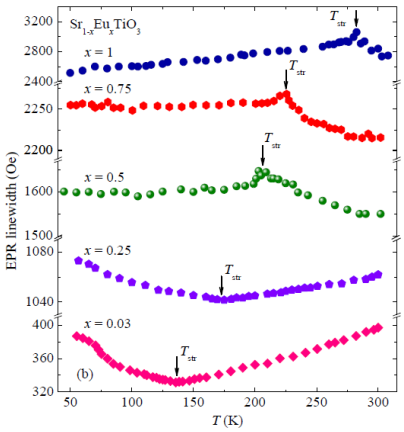

Figure 1) Temperature dependence of the EPR line width for $Sr_{1-x}Eu_xTiO_3$ samples with x=0.03≤x≤1. The arrows indicate the structural phase transition temperature T_S.

Obviously a nonlinear dependence of T_S on x is realized appearing as a kink in the EPR line width for x≥0.5, whereas a minimum in the line width at T_S is seen for x≤0.25. These differences in the temperature dependencies of the line widths are due to a crossover from metallic to semiconducting between x=0.25 and x=0.5 as evidenced by the resistivity measurements (Fig. 2).

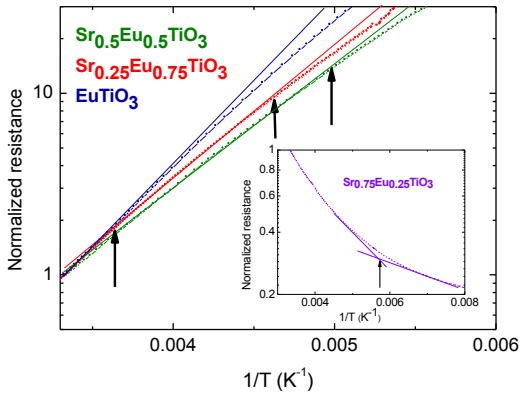

Figure 2 Normalized resistance ρ/ρ_0 as a function of inverse temperature with $\rho_0 = \rho(T = 300K)$ for x ≥ 0.5. The inset shows the same for the sample with x=0.25.

The results from lattice dynamical calculations and density functional theory explain the x-dependent structural phase transitions in terms of a crossover of the dynamics from displacive to order-disorder, since the double-well potentials change from broad and shallow to deep and narrow with increasing x [6]. Simultaneously, the elastic constants are altered from very soft to hard due to optic-acoustic mode-mode coupling for small x and absence of this coupling for x≥0.25. Both theoretical results are mapped onto each other and almost perfect agreement for the double-well potentials is obtained, thus confirming the conclusions about substantial changes in the dynamics. Further implications for the long wave length optic mode frequency are discussed.

References

1. A. Bussmann-Holder, J. Köhler, R. K. Kremer, and J. M. Law, Phys. Rev. B **83**, 212102 (2011).
2. H. Burkhard and K. A. Müller, Helv. Phys. Acta **49**, 725 (1976).
3. W. Cochran, Adv. Phys. **3**, 387 (1960).
4. S. Kamba, D. Nuzhnyy, P. Vaněk, M. Savinov, K. Knížek, Z. Shen, E. Santavá, K. Maca, M. Sadowski, and J. Petzelt, Europhys. Lett. **80**, 27002 (2007).
5. V. Goian, S. Kamba, J. Hlinka, P. Vaněk, A. A. Balik, T. Kolodiazhnyi, and J. Petzelt, Europ. Phys. J. B **71**, 429 (2009).
6. J. L. Lewis, M.-H. Whangbo, J. Köhler, A. Bussmann-Holder, and A.R. Bishop, Phys. Rev. B, in press.

Session 7
Relaxors

Molecular Dynamics Study of Dielectric Response in a Relaxor Ferroelectric

Hiroyuki Takenaka, Ilya Grinberg, and Andrew M. Rappe
The Makineni Theoretical Laboratories, Department of Chemistry
and
Department of Materials Science and Engineering
University of Pennsylvania
Philadelphia, PA 19104-6323 USA

Polar oxides with chemical formula ABO_3 and the perovskite crystal structure offer high electromechanical coupling, leading to their use as piezoelectric materials. In many cases, these systems are solid-state solutions of antiferroelectric and ferroelectric materials. The highest piezoelectric response comes from solutions with one component that is a "relaxor ferroelectric."

Unlike normal ferroelectrics, which exhibit Curie-Weiss behavior and a narrow peak in dielectric constant at the phase transition temperature, relaxor ferroelectrics show elevated dielectric response over hundreds of kelvins, making them extraordinarily useful for real-world applications such as next-generation Naval SONAR. Further exploration of this class of materials is hampered by the complex behavior of relaxors, which is thought to arise from poorly-understood "polar nanoregions."

We use atomistic molecular dynamics simulations to study relaxor behavior in the $0.75[Pb(Mg_{1/3}Nb_{2/3})O_3]$-$0.25[PbTiO_3]$ (PMN-PT) material. Even for a fairly small simulation size of 1000 atoms, the system exhibits frequency dispersion and deviation from the Curie-Weiss law typical of relaxor materials. Analysis of the time autocorrelation functions for individual atoms allows us to identify the Nb atoms with a high concentration of neighboring Ti atoms as the nucleation sites for the relaxor behavior. This is due to the higher coupling between the cation displacements induced by the presence of overbonded oxygen atoms.

To reveal the nature of time-dependent dipolar coupling and relaxation, we employ the dynamical pair distribution function appproach introduced by Dmowski et al. This time-resolved and space-resolved technique provides direct information about the shape and extent of regions with oriented dipoles.

Magnetic and ferroelectric relaxor properties in $PbFe_{1/2}Nb_{1/2}O_3$

C. Stock[1,2], S.R. Dunsiger[3], R. Mole[4], H. Luo[5]
[(1)]NIST Center for Neutron Research, [(2)]Indiana University, [(3)]Munich Technical University, [(4)] FRM2, [(5)]Shanghai Institute of Ceramics

$PbFe_{1/2}Nb_{1/2}O_3$ (PFN) belongs to a class of disordered perovskites, termed relaxors, were the well defined transition present in conventional ferroelectrics (ex. $PbTiO_3$) is replaced by a broad and frequency dependent peak in the dielectric response. These compounds typically have large piezoelectric coefficients and high electromechanical coupling. PFN is unique owing to the presence of a magnetic (Fe^{3+}, S=5/2) ion the B site. Dielectric work has found evidence for coupling between the magnetic and dielectric properties [1]. Neutron diffraction and muon spectroscopy have reported short-range magnetic correlations consistent with a spin-glass [2].

Using neutron scattering, we investigate the relation between ferroelectric and magnetic order in the relaxor $PbFe_{1/2}Nb_{1/2}O_3$. We have measured the temperature dependence of the lowest energy transverse optic phonon mode, sensitive to ferroelectric order, and also the low-energy magnetic scattering characteristic of magnetic ordering with a propagation wave vector of **Q**=(1/2,1/2,1/2). At temperatures ~ 400 K, we observe a recovery in energy of the soft transverse optic mode indicating the presence of ferroelectric order consistent with dielectric measurements and similar to responses observed in prototypical non magnetic relaxors such as $PbMg_{1/3}Nb_{2/3}O_3$ (PMN) and $PbZn_{1/3}Nb_{2/3}O_3$ (PZN). At temperatures ~ 50 K, we observe a gradual slowing of spin correlations with a finite low temperature correlation length of 17 Angstroms and a deviation from linearity of the square of the optic mode frequency.

Figure 1 illustrates a summary of the main results of this study. Panel a) illustrates the soft optic mode frequency squared as a function of temperature in PFN compared to the results in PMN. Panel (b) shows the magnetic linewidth in energy as a function of temperature demonstrating a gradual slowing of the spin fluctuations with decreasing temperature. Panel (c) plots the magnetic susceptibility extracted from constant Q scans at the (1/2,1/2,1/2) position. These results illustrate a deviation from linearity of the soft optic mode at low temperatures where static short-range spin correlations develop. Therefore, PFN displays a coupling between the short-range ferroelectric and magnetic correlations.

References:

[1] Y. Yang, J.-M. Liu, H.B. Huang, W.Q. Zou, P. Bao, Z.G. Liu Phys. Rev. B **70**, 132101 (2004).
[2] G.M. Rotaru, B. Roessli, A. Amato, S.N. Gvasaliya, C. Mudry, S.G. Lushnikov, and T.A. Shaplygina Phys. Rev. B **79**, 184430 (2009).

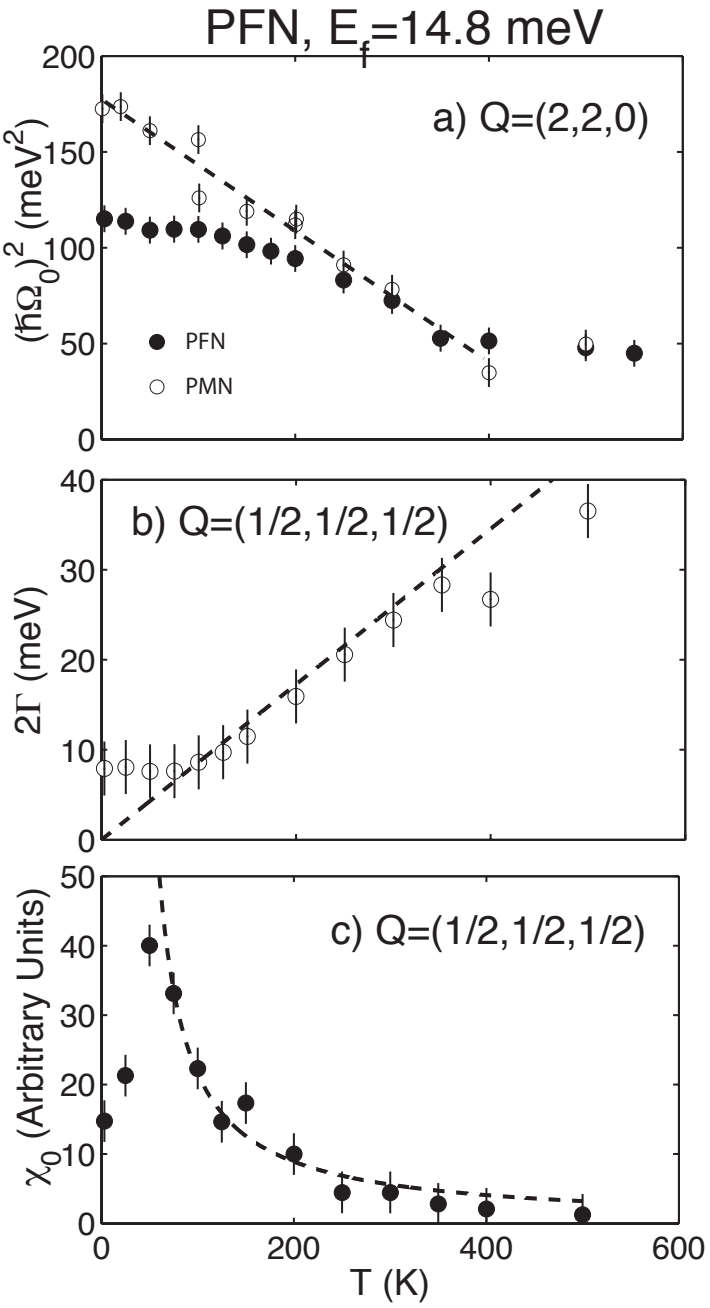

Figure 1: a) The soft transverse optic mode frequency squared, b) the linewidth in energy of the magnetic fluctuations, c) and magnetic susceptibility as a function of temperature.

Diffuse scattering in perovskites: typical features, parameterization and microscopic origin

S.B. Vakhrushev[1,2], R.G. Burkovsky[2], A. Bosak[3], D. Chernyshev[4], D. Damjanovic[5], A. Filimonov[2], A.Tagantsev[5],
[1]Ioffe Institute, St.-Petersburg 194021, Russia.
[2]St.-Petersburg State Technical University, St.-Petersburg 194021, Russia.
[3]European Synchrotron Radiation Facility, Grenoble, France
[4]Swiss-Norwegian Beamlines, ESRF, Grenoble, France
[5]LC, EPFL, Lausanne, Switzerland

Diffuse scattering (DS) in crystals in general is one of the major indications of the existing of different types of disorder. For the first time diffuse scattering in diamond was observed in 1940[1]. This observation was one of the important reasons for the future development of the classic lattice dynamics theory. Later new interest to the diffuse scattering was developed due to the study of different types of the defects in solids.

In perovskites first observation of the X-ray critical diffuse scattering in LaAlO3 at the BZ boundary was reported in 1968 [2] and was considered by W. Cochran as a proof of the soft mode hypothesis. DS in the zone center was described by R. Comes et al. in 1969 [3] and reproduced many times. 3 "shining planes" (SP) perpendicular to principal cubic axes were observed in the cubic (C) phase with one of these (perpendicular to z-axis of the tetragonal (T) phase disappear at C -- T transition and only one (perpendicular to nonpolar axis) kept in the orthorhombic phase. In rhombohedral phase no SP were observed. Appearance of the SP can be considered as a consequence of the static [3] or dynamic [4] (anisotropic phonon branches) short-range correlations between chain-like objects, oriented perpendicular to the chain axis. Disappearance of one of he SP indicates creation of the long-range order with the SP intensity being transformed into the intensity of the Bragg peaks.

In cubic relaxors strong temperature dependent DS was originally reported by Vakhrushev et al., [5] and was interpreted in terms of fluctuations of ferroelectric order parameters. In a large number of later publications (for a brief review see introduction to [6]) this DS was considered as a scattering from anisotropic polar nanoregions in nonpolar matrix. However recently DS in PMNPT10 compound was carefully remeasured and was shown to be inconsistent with such nanoheterogeneous model.

In this report w would like to present new results of the DS measurements in the lead-free Li0.02(k0.5Na0.5)0.98O3 (KNN), PMNPT10 and PZT and to demonstrate possibility of describing generic features of the DS in first 2 compounds using simple dynamic model of Vaks [8], while for the high-temperature diffuse scattering in PMN and DS in PZT at room temperature can be easily described in terms of microscopic elastic lattice distortions (Huang scattering).

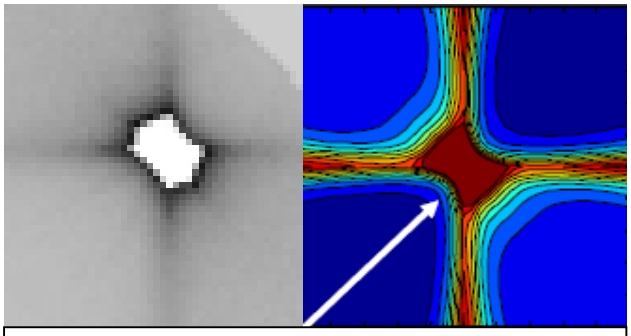

Figure 1 Experimental and simulated DS pattern in cubic phase of KNN

We have carried out DS and inelastic X-ray scattering with small single crystals cleaved from the larger ones and carefully polished and etched. For KNN observed pattern of the DS was similar to that described in [3] and was used to determine the polarization rotation path as it will be discussed. DS was shown to be preliminary dynamic in nature and in not so close vicinity of the Γ-point was determined by the strongly anisotropic TA phonons. We have used a model of

interacting acoustic (both TA and LA) and transverse optic modes to parameterize observed DS. Parameters describing the dispersion of the acoustic mode were taken from elastic tensor, TO unperturbed dispersion and anisotropic acoustic-optic coupling was considered to be the same as in KTaO3. In the Figure 1 experimental and simulated DS patterns around (220) Bragg point are shown demonstrating good agreement. Temperature evolution was easily followed by including of triply degenerated soft mode splitting.

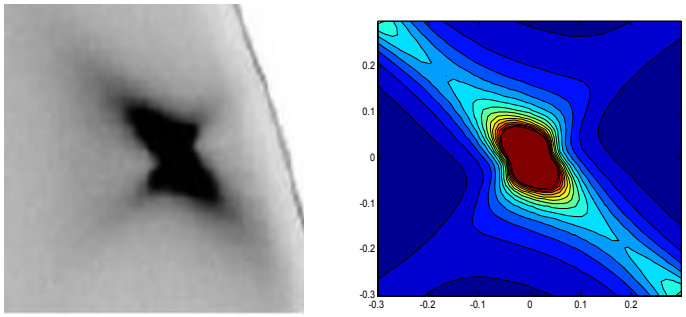

Figure 2 Experimental and simulated DS PMNPT10 near (310) Bragg point

We have attempted to use similar model for describing the DS in PMN related compound. The only essential difference was change of the sign of the parameter describing the TO mode anisotropy. Results of the simulations are presented in the Figure 2. The simulation perfectly reproduces major details of the experimental 2D intensity map including strong suppression of the DS in the direction along the nearest reciprocal lattice vector. This important detail in principle cannot be reproduced by nanoheterogeneous models

Finally we would like discuss 2 other cases, namely high-temperature DS in PMN and DS in PZT. Unlike the situation considered above that are related to the polarization correlations that are suppressed in the longitudinal geometry in the latter cases we saw suppression of the scattering in the transverse geometry. This situation is very typical for the Huang scattering and we have succeeded to describe it using corresponding formalism. More details will be discussed.

Work was supported by RFBR grant 11-02-00687-a

References:

1 – C.V. Raman and P. Nilakantan “Specular reflection of X-rays by high frequency sound waves” *Nature*, **145**, 667 (1940)

2 – V. Plakhty, W. Cochran X-Ray Study of the Phase Transition and Lattice Vibrations of Lanthanum Aluminate” P*hysica Status Solidi (b)* **29**(1) K81-K83 (1968)

3 – Comés, R., Lambert, M. & Guinier, A. *Acta Cryst.* **A26**, 244-253 (1969).

4 – Hüller, A. *Z. Phys* **220**, 145-158 (1969).

5 – Vakhrushev S. B. et al., *Ferroelectrics*, **90**, 173 (1989)

6 – Gehring P. M., “Reassessment of the Burns temperature and its relationship to the diffuse scattering, lattice dynamics, and thermal expansion in relaxor Pb(Mg(1/3)Nb(2/3))O(3)” *Phys. Rev.* **B 79**, 224109 (2009)

7 – A. Bosak, D. Chernyshov, S. Vakhrushev, M. Krisch “Diffuse scattering in relaxor ferroelectrics: true three-dimensional mapping, experimental artefacts and modeling” *Acta Cryst.* **A68** (2012) (available online)

8 – Vaks G., “Introduction to the microscopic theory of ferroelectricity” Moskwa, Nauka (1973) in rusian

Anisotropic Acoustic Lattice Dynamics in $PbMg_{1/3}Nb_{2/3}O_3$

C. Stock,[1, 2] P. M. Gehring,[1] H. Hiraka,[3] I. Swainson,[4] Guangyong Xu,[5] H. Luo,[6] Y. Qiu,[1] J. Li,[7] and D. Viehland[7]

[1] National Institute of Standards and Technology, NCNR, Gaithersburg, MD 20899
[2] Indiana University, Dept of Physics, Bloomington, IN 47404
[3] Tohoku University, Institute for Materials Research, Sendai, 980-8577 Japan
[4] National Research Council, Chalk River Laboratories, ON, Canada, K0J 1J0
[5] Brookhaven National Laboratory, Condensed Matter Physics and Materials Science Dept, Upton, NY 11973
[6] Shanghai Institute of Ceramics, Chinese Academy of Sciences, Shanghai, China, 201800
[7] Virginia Polytechnic Institute and State University, Dept of Materials Science and Engineering, Blacksburg, VA 24061

Using neutron inelastic scattering methods to probe transverse acoustic (TA) phonons in single crystal $PbMg_{1/3}Nb_{2/3}O_3$ (PMN), we demonstrate the presence of a highly anisotropic TA phonon damping mechanism. For temperatures below ~420 K, where truly static, short-range, polar correlations (i.e. polar nanoregions) first appear [1], we find that TA phonons propagating along [1-10] and polarized along [110] (TA_2 phonons) are heavily damped across the entire Brillouin zone, as is shown in the lower left-hand panel of Fig. 1. On the other hand, at the same temperature, the lower right-hand panel of Fig. 1 illustrates that phonons polarized along [001] and propagating along [100] (TA_1 phonons) are only damped for wave vectors close to the zone center. In both cases the damping vanishes at high temperatures as is shown in the two upper panels of Fig. 1.

The anisotropy and temperature dependence of the TA phonon lifetime are directly related to the elastic diffuse scattering cross section [2]; this suggests that the polar nanoregions are the cause of the damping. The anisotropic TA phonon damping further points to polar nanoregions that are highly anisotropic in real space, which would be consistent with the so-called Pancake model [3] previously derived from x-ray and neutron diffraction studies. We emphasize that our data are inconsistent with TA-TO phonon coupling [4] or the existence of an extra, soft "quasi-optic" TO mode [5], and they provide an alternate explanation for the origin of the extra neutron scattering cross section observed at low energies in some Brillouin zones. The strong coupling between the diffuse scattering (polar nanoregions) and the TA phonons may provide an explanation for, or at least a signature of, the unusually large piezoelectric constants that are observed in these and related materials [6].

REFERENCES:

[1] P.M. Gehring *et al*., Phys. Rev. B **79**, 224109 (2009).
[2] C. Stock *et al.*, J. Phys. Soc. Jpn. **74**, 3002 (2005).
[3] G. Xu *et al*., Phys. Rev. B **70**, 174109 (2004).
[4] J. Hlinka *et al*., Phys. Rev. Lett. **91**, 107602 (2003).
[5] A. Naberezhnov *et al*., Eur. J. Phys. B **11**, 13 (1999); S. Vakhrushev and S.M. Shapiro, Phys. Rev. B **66**, 214101 (2002).
[6] M. Matsuura *et al*., Phys. Rev. B **74**, 144107 (2006).

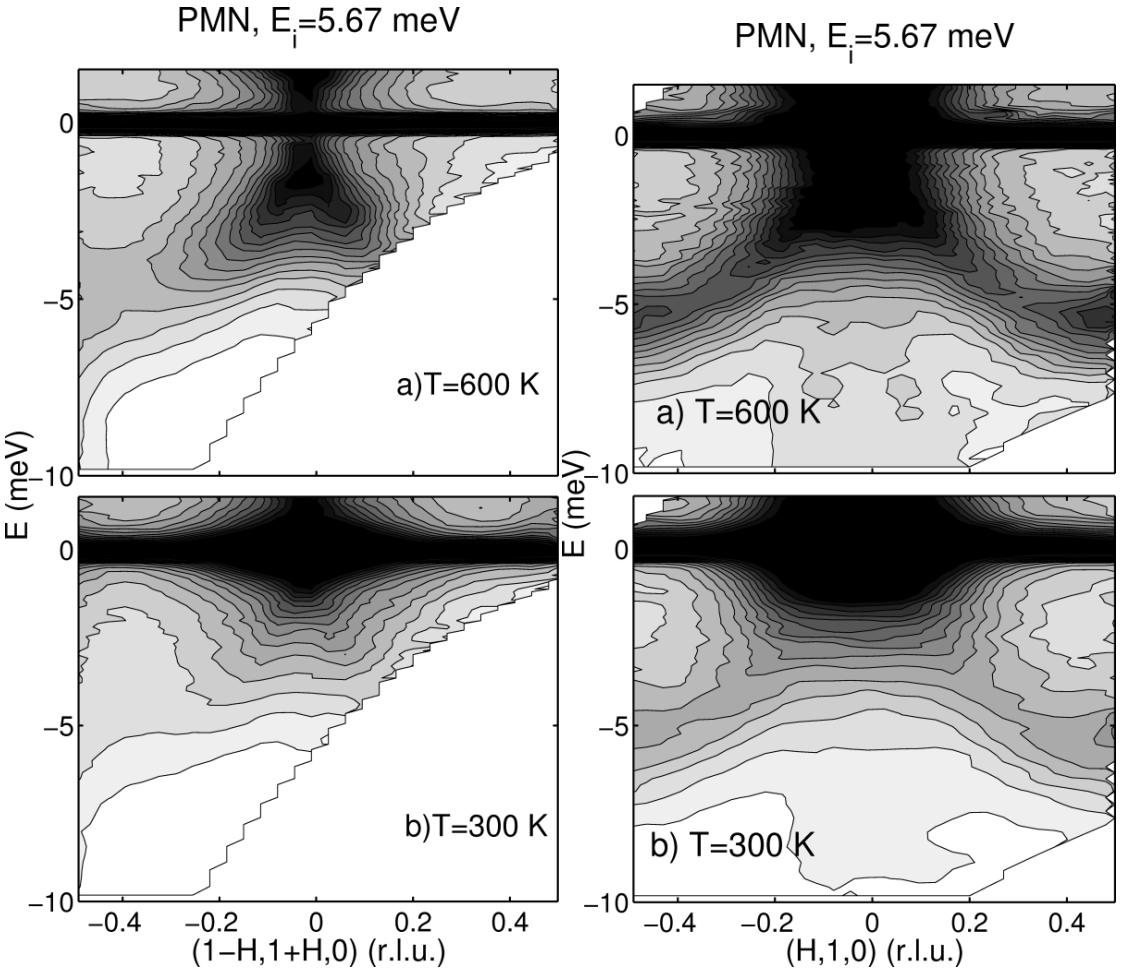

Fig. 1: The left-hand panels show constant-intensity contours of the TA_2 phonon scattering cross section at 600 K and 300 K that illustrate how the TA_2 mode disperses out from the (110) Bragg peak. The right-hand panels show the same for the TA_1 mode near the (010) Bragg peak.

Session 8
Flexoelectricity

First-principles theory of flexoelectricity

David Vanderbilt and Jiawang Hong[1]
[1]*Department of Physics and Astronomy, Rutgers University Piscataway, New Jersey 08854, USA*

Flexoelectricity refers to the linear response of electric polarization to an applied strain gradient. Because a strain gradient breaks inversion symmetry, flexoelectricity is always symmetry-allowed, unlike piezoelectricity which arises only in noncentrosymmetric materials. The flexoelectric effect is normally negligible on conventional length scales, but it may become very strong at the nanoscale, where huge strain gradients can significantly affect the functional properties of dielectric thin films, superlattices, and nanostructures. The possibility of large effects at the nanoscale with application to functional devices has caused a recent explosion of experimental interest in flexoelectricity [1-3].

There have been remarkably few theoretical studies of flexoelectricity, the main difficulty being that strain gradients are inconsistent with translational symmetry. A classical phenomenological theory focused on lattice-mediated contributions was proposed by Tagantsev [4] and later applied to study flexoelectric properties of dielectrics by Maranganti and Sharma [5]. A first attempt at a first-principles calculation of flexoelectricity is due to Hong *et al.* [6]. Recently, Resta [7] developed a first-principles theory of flexoelectricity, extending a previous formulation of Martin [8] for flexoelectricity. Resta's theory was, however, limited to simple elemental insulators such as Si, and was not implemented in practice. Thus, unlike piezoelectricity, which is routinely calculated using modern first-principles methods in a mature theoretical framework, the theory of flexoelectricity has remained in a relatively primitive state.

Just like the piezoelectric coefficient, the flexoelectric coefficient (FEC) can be divided into two contributions: the "frozen-ion" and "lattice" parts. The "frozen-ion response" is the result of atomic coordinates being displaced strictly according to an ideal strain gradient, e.g.,

$$\Delta R_{lix} = \frac{1}{2}\,\nu_{xxx}\,R_{lix}^2\ , \qquad (1)$$

where ΔR_{lix} is the x displacement of atom i in cell l located at $\mathbf{R}_{li}$, and $\nu_{xxx} = d\eta_{xx}/dx$ describes the strength of a gradient of the strain η_{xx} in the x direction The "lattice" response then arises from additional displacements of atoms in response to the strain and its gradient. Previous works, e.g., Refs. [4-5], have focused mainly on the lattice response.

We discuss first the frozen-ion response. A partial formulation of this problem was recently introduced by Resta [7] based on an approach similar to one developed by Martin to treat piezoelectricity [8]. Resta's formulation was, however, limited to elemental solids. Here we present a complete theory of the frozen-ion FEC, appropriate to insulating crystals of any symmetry. Without loss of generality we can assume the gradient of the strain to be along the x direction, and we then adopt *mixed electric boundary conditions* in which D_x, E_y, and E_z are constrained. Note that D_x is a component of the electric *displacement* field, while E_y and E_z refer to the ordinary electric field; the reasons for this choice will be explained. We then demonstrate that the contribution of a given atom to the frozen-ion FEC is just proportional to the third moment of the change in charge density induced by its displacement (or, more precisely, by the simultaneous displacement of a plane of atoms having the same x coordinate). This is true for *all* insulating crystals, from elemental dielectrics to piezoelectrics and ferroelectrics.

Furthermore, we propose several practical supercell-based methods for extracting the FEC from *ab initio* calculations, based on displacing a plane of atoms and computing the induced change in charge density. Three possible geometries for such calculations are shown in Fig. 1. In each case, the system is maintained at fixed electric displacement field D_x in the long direction x of the supercell. In (a), this is done by making equal and opposite displacements of two layers in the supercell; in (b) it is done by controlling a dipole layer in a vacuum region; and in (c) it is done by using a code capable of enforcing fixed-D boundary conditions. We show that all three methods give consistent results, and discuss the relative advantages and disadvantages of each.

We use this supercell approach to compute the frozen-ion FECs for C, Si, MgO, NaCl,

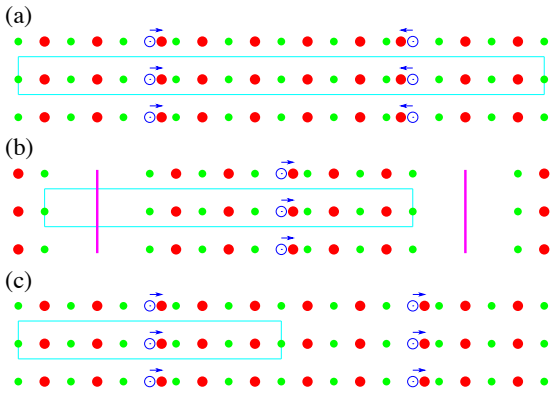

FIG. 1: (Color online) Supercell geometries. Large (red) and small (green) dots are two species of atoms; open dots are atoms before being displaced as shown by arrows. Rectangles indicate supercells. (a) Bulk supercell for Method A. (b) Slab supercell for method B; vertical lines indicate dipole correction layers in vacuum. (c) Bulk supercell for Method C.

$SrTiO_3$, $BaTiO_3$, and $PbTiO_3$, and discuss the trends that emerge from this data. Some of our results are summarized in Table I. We find that all FECs μ_{xxxx} are negative, and surprisingly, they are of roughly comparable magnitude for the rather wide variety of materials shown in Table I, from simple semiconducting elements to dielectric and piezoelectric perovskites. Trends in the data will be discussed.

We will also briefly discuss three important subtleties: (i) the issue of pseudopotential dependence; (ii) the question of "surface contributions" to the flexoelectricity, and (iii) the treatment of transverse components using current-density response.

Finally, in the last part of the talk we will discuss work in progress on a careful formulation of the lattice contribution to the flexoelectric response, based on a long-wave analysis. Previous workers seem not to have noticed that a deep subtlety arises in the very *definition* of the lattice flexoelectric response: what does it mean to relax the atoms in the presence of a strain gradient? It is impossible; if the atoms are allowed to relax fully, the strain gradient will disappear! To put it another way, the presence of a strain gradient implies the presence of a stress gradient, and a stress gradient produces a force density. Thus, in the presence of a general strain gradient, there must be a *net force* acting on the atoms inside each unit cell. How should we partition this force? We demonstrate that the value of the flexoelectric coefficient depends on how this choice is made. One natural choice is to weight the forces by the atomic masses, but no choice can be singled out as fundamentally preferred. Of course, in many situations of physical interest, such as in the interior of a statically loaded bent beam, the force density is zero because the various Fourier components of the strain and stress fields give canceling force densities, and the ambiguity disappears. However, for simple cases like that described by Eq. (1), the difficulty cannot be avoided.

TABLE I: Lattice constants and frozen-ion flexoelectric coefficients computed from first principles.

	a (Bohr)	μ_{xxxx} (pC/m)
C	6.69	−175.4
Si	10.22	−105.7
MgO	7.73	−95.6
NaCl	10.66	−47.9
$SrTiO_3$	7.31	−144.7
$BaTiO_3$	7.52	−141.9
$PbTiO_3$ (PE)	7.43	−156.0
$PbTiO_3$ (FE)	7.35	−148.9

The work was supported by ONR Grant N00014-05-1-0054. Computations were done at the Center for Piezoelectrics by Design.

[1] L.E. Cross, J. Mater. Sci. **41**, 53 (2006).

[2] P. Zubko, *et al.*, Phys. Rev. Lett. **99**, (2007); G. Catalan, *et al.*, Phys. Rev. B **72**, 020102 (2005); G. Catalan,*et al.*, Nat Mater **10**, 963 (2011).

[3] D. Lee, *et al.*, Phys. Rev. Lett. **107**, 057602 (2011).

[4] A. K. Tagantsev, Phys. Rev. B **34**, 5883 (1986); Phase Transitions **35**, 119 (1991).

[5] R. Maranganti and P. Sharma, Phys. Rev. B **80**,054109 (2009).

[6] J. Hong, G. Catalan, J. F. Scott, and E. Artacho, J. of Phys.: Condens. Matter. **22**, 112201 (2010).

[7] R. Resta, Phys. Rev. Lett. **105**, 127601 (2010).

[8] R.M. Martin, Phys. Rev. B **5**, 1607 (1972).

Flexoelectric effect in finite samples

Alexander K. Tagantsev[a] and Alexander S. Yurkov [b]
[a]Ceramics Laboratory, Swiss Federal Institute of Technology (EPFL), CH-1015 Lausanne, Switzerland
[b]644076, Omsk, Russia

The flexoelectric effect consists of a linear response of the dielectric polarization to a strain gradient. This is a high-order electromechanical effect which is expected, in general, to be rather weak. However, some of its features make this effect interesting from both fundamental and applied points of view. This has stimulated recent intensive experimental and theoretical activity in the field.

On the practical side, of first importance is that this effect, in contrast to the piezoelectric effect, is allowed in centro-symmetric material. It is believed that it is the flexoelectric effect that is responsible for the generation of an electric field in acoustic shock waves propagating in centro-symmetric solids. The most applied interest is focused on the "piezoelectric metamaterial" -- composites made of non-piezoelectric components, which exhibit effective piezoelectric response generated due to the flexoelectric effect. The work in this direction was initiated by pioneering experimental studies by Professor Cross with coworkers[1] and was later also supported by theory. Presently, $(Ba,Sr)TiO_3$-based composites have been shown to yield effective piezoelectric coefficients comparable to those of commercial piezoelectric ceramics.

Presently, the analysis of experimental data is customarily performed in terms of the so-called bulk static contribution to the flexoelectric response treated in an infinite medium. The goal of this paper is to show that an adequate treatment of the flexoelectric response under static or quasi-static conditions requires (i) taking into account the finite size effects and (ii) taking into account at least two contributions: the aforementioned static bulk contribution and the contribution of the surface piezoelectricity.

(i) It was argued, based on the constitutive equation for the flexoelectric response, that a mechanical sensor made of the aforementioned metamaterials should exhibit a very unusual property. Specifically, in contrast to piezoelectric based devices, it will not behave as an actuator. There are several reasons to question such statement. First, already in the 60's of the past century, the group of Professor Bursian reported experimental data on $(Ba,Sr)TiO_3$ crystals[2] and gave arguments based on equilibrium thermodynamics[3], which contradict this statement. Second, the existence of a linear sensor-not-actuator may come into conflict with the general principles of thermodynamics.

In this paper we address theoretically this conflict situation to demonstrate that despite an explicit asymmetry of the constitutive equations for the bulk flexoelectric effect, when this effect is characterized in a realistic finite sample the apparent asymmetry of the electromechanical response will vanish. In particular, this implies that the aforementioned piezoelectric metamaterial should exhibit the identical effective

piezoelectric constants when characterized in "direct" and "converse" regimes. These constants are directly calculated for the bending mode of a “flexoelectric sensor/actuator”.

(ii) As was recognized at the first thorough treatment of the flexoelectric response the polarization response to a strain gradient in a finite sample, generally speaking, may not be fully controlled by the contribution of the bulk static flexoelectricity, even in materials with high values of the dielectric constant (high-K materials)[4]. The competing effect that is due to surface piezoelectricity, was not, however, properly addressed theoretically. Thus, it is not clear if it can in fact compete in high-K materials with the static bulk flexoelectricity. In high-K materials, the contribution of the static bulk flexoelectricity is enhanced, since it scales as the dielectric susceptibility[4]. At the same time, the effect associated with surface piezoelectricity originates from the presence of the interface adjacent layers where the piezoelectricity is induced by the inversion-symmetry-breaking effect of the interface. Since the sign of the effective piezoelectric coefficients of the layers on the opposite sides of a plate should be opposite (as controlled by the orientation of the surface normal), bending of the plate should result in dipole moments in these layers, the sign of which are the same. The dipole moment in a layer is proportional to the strain in it, which, in turn, is proportional to the product of the strain gradient and the plate thickness. Having calculated the resulting change of the average polarization of the whole system, this will give rise to a net polarization proportional to the strain gradient. From this reasoning it is not obvious that such response will be enhanced once that the dielectric constant of the bulk of the material is high. However, such reasoning does not provide a proper vision of the whole effect. In this paper, we will show that such enhancement does take place: in high-K materials, surface contribution to the flexoelectric response scales with bulk value of the dielectric constant and can be readily comparable to that of the bulk contribution.

This finding is of a crucial importance for the interpretation of experimental data on the flexoelectric response. This point is that in earlier publications[4] it was hypothesized that these dependences are expected to be different. Based on this hypothesis, the fact that an experimentally measured flexoelectric coefficient scales as the dielectric constant of the material was customarily taken as an indication that the measured flexoelectric response is controlled by the static bulk contribution to the flexoelectric effect. This finding essentially changes the situation. Now one can state that the fact that the experimentally measured flexoelectric coefficient scales as the dielectric constant of the material does not imply that the measured flexoelectric response is controlled by the static bulk contribution to the flexoelectric effect.

1 W. Ma and L. E. Cross, Appl. Phys. Lett. **79**, 4420 (2001).
2 E. V. Bursian and Zaikovskii.O.I, Sov. Phys. Solid State **10**, 1121 (1968).
3 E. V. Bursian and N. N. Trunov, Sov. Phys. Solid State **16**, 760 (1974).
4 A. K. Tagantsev, Phys. Rev. B **34**, 5883 (1986).

Flexoelectric effect in 2D sp^2-bonded crystals or BN for a nanogenerator

Ivan I. Naumov[1], Alexander M. Bratkovsky[1], and V. Ranjan[2]
[1]*Hewlett-Packard Laboratories, Palo Alto, California 94304*
[2]*North Carolina State University, Raleigh, North Carolina 27606*

Flexoelectricity refers to an electromechanical property to generate a voltage either in response to director field gradients $\partial_i n_j$ (in liquid crystals[1, 2]) or to strain gradients $\partial_i \partial_j u_l$ (in insulating solids [3]), where $\mathbf{n}(\boldsymbol{r})$ is the director, $\boldsymbol{u}(\boldsymbol{r})$ the displacement vector, ∂_i the gradient operator, i the Cartesian index. In contrast to the liquid crystals, in bulk three-dimensional (3D) solids the flexoelectric effect is usually small and evades experimental detection unless large strain gradients are externally imposed or artificially designed inhomogeneous metamaterials are used [4, 5].

Contrary to 3D systems, truly two-dimensional (2D) sp^2-bonded crystals, like graphene and boron nitride (BN) [6], are able to sustain huge elastic structural distortions and, thus, exhibit exceptional forms of electromechanical coupling, especially non-centrosymmetric BN, which is our main subject. The BN sheet, for example, becomes pyroelectric when it is wrapped into a chiral or a zigzag nanotube with the macroscopic polarization proportional to the inverse square of the tube radius, $1/R^2$, and directed along the tube [7–9]. Formally, this effect can be considered as a *quadratic* flexoelectric effect, since $(\partial_i \partial_j u_k)^2 \propto 1/R^2$.

Here we show that 2D sp^2-bonded non-centrosymmetric crystals like BN exhibit another unusual flexoelectric effect: generation of a macroscopic in-plane polarization in response to out-of-plane periodic atomic displacements $u_z(\boldsymbol{r}) = A\sin(\boldsymbol{k}\cdot\boldsymbol{r}+\varphi)$. We show further that this phenomenon opens up the way to the development of a novel type nanogenerator.

To describe periodically and commensurately distorted hexagonal BN sheets, we introduce the corrugation wave vector $\boldsymbol{k} = 2\pi\mathbf{e}/\lambda$, where the unit vector $\mathbf{e}$ and the wavelength λ are expressed via the lattice vectors $\boldsymbol{a}_1$ and $\boldsymbol{a}_2$ of a 2D sheet in the following way: $\mathbf{e} = \boldsymbol{\lambda}/\lambda$, with $\boldsymbol{\lambda}(n,m) = n\boldsymbol{a}_1 + m\boldsymbol{a}_2$, $\lambda = a\sqrt{n^2+nm+m^2}$, where n and m are integers, $a_1 = a_2 = a$. The corrugation with the wave-length $\lambda(n,m)$ leads to a rectangular supercell whose translational vectors are $\boldsymbol{\lambda}(n,m)$ and some translation vector $\boldsymbol{T} = N\boldsymbol{a}_1 + M\boldsymbol{a}_2$, which is perpendicular to $\boldsymbol{\lambda}$.

It is also convenient to define the vector $\boldsymbol{k}$ in the polar coordinate system (k, θ), where θ is the angle between the $\boldsymbol{k}$ and $(\boldsymbol{a}_1 + \boldsymbol{a}_2)$. Borrowing the terminology from the theory of nanotubes, we shall call the sine-wave distortions with $\theta = 0 \pm \pi l/3$ the "armchair"-like and with $\theta = \pi/6 \pm \pi l/3$ the "zigzag"-like, where l is an integer. All other distortions falling between the two will be called "chiral".

The corrugation-induced polarization is computed from first principles by using the Berry's phase approach [10] or from the geometrical phases accumulated by the occupied electronic states in the slow (adiabatic) process of corrugation: $\boldsymbol{P} = \boldsymbol{P}^{(u)}$- $\boldsymbol{P}^{(0)}$, where $\boldsymbol{P}^{(0)}$ corresponds to the initial flat sheet. To analyze how the polarization is distributed in real space over the supercell $\lambda \times T$, we also calculate $\boldsymbol{P}$ in terms of the shifts of the Wannier function (WF) centers corresponding to π and σ chemical bonds. Although we used different codes to calculate Berry's phases and WFs (ABINIT [11] and PWSCF [12], respectively), the obtained results are remarkably consistent with each other.

The calculations show that the polarization $\boldsymbol{P}(\boldsymbol{k})$ strongly depends on $\boldsymbol{k}$. The mutual orientation of the $\boldsymbol{P}$ and $\boldsymbol{k}$ evolves as the latter rotates through the angle θ. $\boldsymbol{P}$ becomes purely longitudinal along the armchair $\boldsymbol{k}-$directions and purely transversal along the zigzag directions. Along the chiral $\boldsymbol{k}$-directions, it has both components.

To analyze the relationship between electronic structure and $\boldsymbol{P}(\boldsymbol{k})$, we notice that the WF in a flat BN sheet have roughly the character of the σ- and π-bond orbitals (σ and π WFs.) The $\pi-$like WFs are centered on N atoms exactly, while their σ counterparts are somewhere in the middle of the B-N bonds closer to N atoms (Fig. 1c). The contributions of the π and σ WFs to a 'clamped-ion' polarization induced by an in-plane uniaxial stretching have the *same* sign, with the π WFs dominating and amounting up to as much as 85% of the total (see also Ref. [9]).

Although the corrugation of a flat BN sheet leads to the rehybridization effects like mixing of π and π^* electronic bands due to breaking of the $z \to -z$ mirror symmetry, it is still possible to classify all the WFs into π and σ types, Fig. 1. It might naively appear that in the corrugated structures the main contribution to $\boldsymbol{P}(\boldsymbol{k})$ would also come from the π WFs. In fact, this is not the case. The contribution of σ WFs generally increases, becoming strongly dominant in some special cases in corrugated films.

Consider first the case of zigzag corrugation with $n = 4$, $m = -4$, $A/\lambda = 0.1$ and $\varphi = 0$, Fig. 1. Here, the shifts of π WFs are still dominant but not so apparently, and $|P_\pi/P_\sigma|$ is only about 2.5. In contrast to the flat case, the π and σ WFs have the *opposite* sign contributions to $\boldsymbol{P}(\boldsymbol{k})$ exhibiting inhomogeneous shifts within the two-dimensional supercell $\lambda \times T$. Upon the corrugation, the π WF centers shift relative to the initial positions, as shown in Fig. 1d. Apparently, electron density shifts along the y axis of right-most column of N-atoms exactly cancel each other while the rest shift along the x-axis, which means the appearance of a macroscopic transverse polarization,

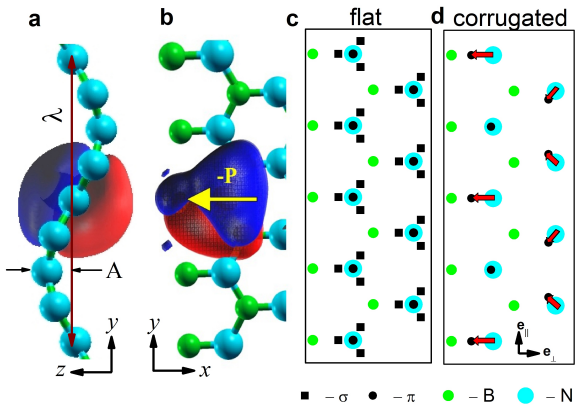

FIG. 1: The Wannier functions (a,b) and their shifts (c,d) in a corrugated BN sheet corresponding to a "zigzag" vector $\boldsymbol{\lambda}(4,-4)$ ($\theta = 90°$), A/λ=0.1 and φ= 0. (a,b) Side and top views of a π-like WF contributing most to the polarization (isosurface = ± 0.9). The yellow arrow indicates the shift of the WF, which is antiparallel to the locally induced polarization $\mathbf{P}$. (c,d) The positions of the centers of the $\pi-$ (black circles) and σ WFs (black squares) in a flat and corrugated BN sheet, respectively. In the flat state, π WFs coincide with N atoms. The red arrows show the (scaled up) shifts of π WFs.

$\boldsymbol{P} \perp \boldsymbol{k}$.

Now, we turn our attention to another case, represented by the armchair undulation with $n = 4$, $m = 4$, $A/\lambda = 0.1$, and $\varphi = 0$. Here again, the π and σ WFs give the *compensating* contributions to the polarization. But now, in contrast to the zigzag case, σ WFs dominate by a wide margin: $|P_\sigma/P_\pi| \sim 4.5$. All the WFs move in such a way that the sum of their shifts along the x axis cancels, so that the induced polarization is purely longitudinal. The dominant σ WFs move towards the N-atoms, thus further increasing the polarity of the σ B-N bonds.

The important characteristic, the voltage drop U between opposite sides of the BN strip, Fig.2, can be estimated as $(P/\pi\epsilon\epsilon_0)\ln(L/b)$, where P is the usual 2D polarization (in units of C/m), L the separation between the charged strip edge states (strip width), and b the effective radius of those states, ϵ_0 the dielectric permittivity of vacuum. Taking b to be on the order of the lattice parameter a, for a reasonable $L = (100 - 1000)a$ and $P = 10^{-2}\ e/a_B$, we obtain $U \lesssim 5 - 8$V for BN strip suspended in vacuo and smaller values for the strip on dielectric substrate like SiO_2 with $\epsilon = 3.9$) (the actual bias U will be limited by a charge transfer between edges to about half-bandgap of BN, so in practice $U \lesssim 2$ V.)

From general considerations it is clear that the thermal ripples in a BN sheet will produce zero net polarization. However, if the ambient wave-like movements have preferential orientation in space, they will induce a macroscopic polarization in the corresponding direction. Many such types of movements, artificial as well as natural, are

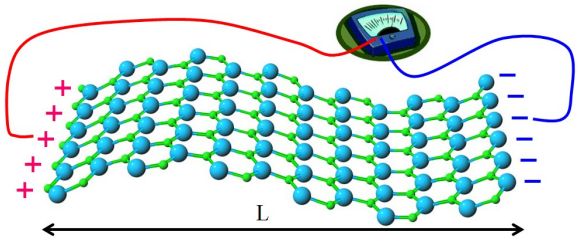

FIG. 2: Schematic showing generation of a bias voltage between the edges of a corrugated BN nanosheet. Note that the induced polarization is longitudinal, because the corrugation is of the armchair type.

likely to be frequently met in practice. The ability of a BN sheet and similar materials to generate electricity from ambient agitation can be used to power small electronic devices like medical implants, remote sensors, etc. A possible realization of such a nanogenerator would be a BN strip suspended between supports and compressed (statically or periodically), or the strip placed on a flexed insulating membrane (e.g. Si_3N_4) with deposited electrodes, etc.

[1] R. B. Meyer, Phys. Rev. Lett **22**, 918 (1969).
[2] P. G. de Gennes and J. Prost, *The Physics of Liquid Crystals* (Clarendon Press, Oxford, 1993).
[3] A. K Tagantsev, Phys. Rev. B **34**, 5883 (1986).
[4] L. E. Cross, J. Mater. Sci. **41**, 53 (2006).
[5] N. D. Sharma, R. Maranganti, and P. Sharma, J. Mech. Phys. Solids **55**, 2328 (2007).
[6] K. S. Novoselov *et al.*, Proc. Natl. Acad. Sci. USA **102**, 10451 (2005).
[7] E.J. Mele and P. Král, Phys. Rev. Lett. **88**, 056803 (2002).
[8] S. M. Nakhmanson, A. Calzolari, V. Meunier, J. Bernholc, and M. Buongiorno Nardelli, Phys. Rev. B **67**, 235406 (2003).
[9] N. Sai and E. J. Mele, Phys. Rev. B **68**, 241405(R) (2003).
[10] R. D. King-Smith and D. Vanderbilt, Phys. Rev. B **47**, 1651 (1993).
[11] X. Gonze et al., Comp. Mater. Sci. 25, 478 (2002).
[12] S. Baroni *et al.*, http://www.pwscf.org.

Session 9
Modeling

Dynamical matrix in magnetoelectrics

Raffaele Resta
Dipartimento di Fisica, Università di Trieste,
and DEMOCRITOS Simulation Center, CNR-IOM, Trieste

In magnetoelectrics (MEs) the fields $\mathbf{E}$ and $\mathbf{H}$ are both coupled to the lattice on the same footing, and both contribute to the dynamical properties in the infrared regime. If the crystal symmetry is high enough (orthorombic or higher) the zone center optical modes are either longitudinal (LO) or transverse (TO); the free energy of the fields $\mathbf{E}$ and $\mathbf{H}$ provide an additional restoring force which accounts for the LO-TO splitting. The field-lattice coupling is also at the root of the difference between the two magnetoelectric response tensors at $\omega = 0$ (static) and $\omega = \infty$ ("static high frequency", a.k.a. "clamped nuclei"). It has been recently shown that a scalar function of these two tensors, together with the zone-center frequencies, fulfill a generalized Lyddane-Sachs-Teller relationship [1]. Notably, the fields $\mathbf{E}$ and $\mathbf{H}$ enter this relationship and its derivation in a very symmetric way.

In ordinary dielectrics the dynamical matrix at the zone center in general is a nonanalytic function of degree zero in the wavevector $\mathbf{q}$. Its expression (for a crystal of arbitrary symmetry) is well known and is routinely implemented in first principle calculations. The nonanalytic behavior occurs in polar crystals and owes to the coupling of the macroscopic electric field $\mathbf{E}$ to the lattice. Here I provide the explicit generalization to ME crystals of arbitrary symmetry. As for ordinary dielectrics, the dynamical matrix is the sum of two contributions: an analytic and a nonanalytic one. The latter term is a homogeneous function of order zero in $\mathbf{q}$. The present expression is exact in the harmonic approximation; once more, the $\mathbf{E}$ and $\mathbf{H}$ couplings are accounted for in a symmetric way.

The next issue to be discussed is: which fields and why? In presence of a long wavelength phonon of wavevector $\mathbf{q}$, the solid is macroscopically homogeneous in the plane normal to $\mathbf{q}$, while all macroscopic properties display a modulation in the direction of $\mathbf{q}$. It is immediate to realize that the components of $\mathbf{D}(\mathbf{q})$ and $\mathbf{B}(\mathbf{q})$ parallel to $\mathbf{q}$ and the component of $\mathbf{E}(\mathbf{q})$ and $\mathbf{H}(\mathbf{q})$ normal to $\mathbf{q}$ vanish: $\mathbf{E}$ and $\mathbf{H}$ are both longitudinal, while $\mathbf{D}$ and $\mathbf{B}$ are both transverse. Therefore the analytic term in the zone-center dynamical matrix corresponds to $\mathbf{E} = \mathbf{H} = 0$. Because of this most of the ME literature, including Refs. [1-3], is formulated in terms of a free energy whose independent variables are $\mathbf{E}$ and $\mathbf{H}$. These are not the fields of choice for a first-principle theorist: the macroscopic fields entering the Kohn-Sham Hamiltonian, in fact, are $\mathbf{E}$ and $\mathbf{B}$ (*not* $\mathbf{H}$). Notice also that the macroscopic fields $\mathbf{E}$ and $\mathbf{B}$ in a crystal are by definition the cell average of their microscopic counterparts $\mathbf{E}^{(\mathrm{micro})}(\mathbf{r})$ and $\mathbf{B}^{(\mathrm{micro})}(\mathbf{r})$. These are the only fields actually measurable (at least in principle) within the material, while a microscopic $\mathbf{H}$ cannot be defined unambiguously. Modern calculations routinely provide the macroscopic polarization in zero $\mathbf{E}$ and the macroscopic magnetization in zero $\mathbf{B}$ (not zero $\mathbf{H}$).

The values of all fields ($\mathbf{D}$, $\mathbf{E}$, $\mathbf{B}$, and $\mathbf{H}$) inside a finite sample depend on the

value of the fields far away outside (generated by external charges and currents), as well as on the sample shape (via the depolarization/demagnetization coefficients). Equivalently, for a long-wavelength phonon in an infinite crystal the fields depend on the wavevector direction. For TO phonons $\mathbf{E} = \mathbf{H} = 0$, but $\mathbf{B} \neq 0$; conversely, for LO phonons $\mathbf{D} = \mathbf{B} = 0$, but $\mathbf{H} \neq 0$. In ordinary dielectrics a straightforward frozen-phonon calculation provides the energy of a TO mode. At variance with this, in MEs a frozen-phonon calculation—or equivalently a second order expansion of the total energy in the sublattice displacements, performed with the usual periodic boundary conditions for Schödinger equation—implies $\mathbf{E} = \mathbf{B} = 0$: it yields therefore the energy of a "bastard" mode, neither transverse nor longitudinal, which does not coincide with the eigenfrequency of any physical mode. The force constants computed in this way include the restoring forces due to nonvanishing $\mathbf{H}$; this contribution must be discounted to get the analytic term in the force-constant matrix: The explicit formula will be given.

The approach of Refs. [1-3] is essentially macroscopic, in the same spirit as the Huang phenomenological theory of lattice dynamics. Next we may ask what is the *microscopic* mechanism responsible for the tensors Z_s^* and ζ_s^*, which couple the lattice to the macroscopic fields.

The answer for Z_s^* in ordinary dielectrics is well known. By definition the force exerted by a macroscopic field $\mathbf{E}$ on the s-th nucleus at its equilibrium position is $\mathbf{f}_s = eZ_s^*\mathbf{E}$. If we adopt an all-electron framework (no pseudopotentials) $\mathbf{f}_s$ can be equivalently expressed as $\mathbf{f}_s = eZ_s\mathbf{E}^{(\mathrm{micro})}(\mathbf{r}_s)$, where Z_s is the bare nuclear charge and $\mathbf{r}_s$ is the nuclear position. Therefore the ratio between the Born charge and the bare charge equals the ratio between the microscopic field at the nuclear site and the macroscopic field.

As for MEs, the microscopic force at site s depends on both macroscopic fields $\mathbf{E}$ and $\mathbf{H}$. The tensor ζ_s^* (magnetic analogue of Z_s^*) is defined via the force exerted by $\mathbf{H}$ (at zero $\mathbf{E}$) as $\mathbf{f}_s = e\zeta_s^*\mathbf{H}$. This is apparently paradoxical, given that a magnetic field cannot exert any force on a classical point charge at rest. Nonetheless ζ_s^* is in general nonzero, and has been actually computed for the paradigmatic ME crystal Cr_2O_3 [3]. The microscopic mechanism behind the magnetic lattice coupling will be discussed.

Work supported by the ONR grant N00014-11-1-0145.

[1] R. Resta, *Lyddane-Sachs-Teller Relationship in Linear Magnetoelectrics*, Phys. Rev. Lett. **106**, 047202 (2011).

[2] R. Resta, *Zone-Center Dynamical Matrix in Magnetoelectrics*, `http://arxiv.org/pdf/1110.3732v2`, submitted to Phys. Rev. B.

[3] J. Ìñiguez, *First-Principles Approach to Lattice-Mediated Magnetoelectric Effects*, Phys. Rev. Lett. **101**, 117201 (2008).

Coexistence of ferroelectricity and octahedral rotations in ABX_3 perovskites

Nicole A. Benedek and Craig J. Fennie
School of Applied and Engineering Physics, Cornell University, Ithaca NY 14853 USA

Nearly all cubic perovskite materials are unstable to energy-lowering structural distortions. The most intensively studied distortions are those that induce ferroelectricity and tilts or rotations of the anion octahedra. The phonon dispersion curves of many perovskites contain both types of instability (for example $CaTiO_3$, see below), although competition between the different types of distortions usually leads to ground-state structures in which one type of instability has been eliminated. Hence, whereas there are many perovskites that are *either* ferroelectric or have rotated octahedra, there are very few perovskites that are *both* ferroelectric and have rotated octahedra. A good understanding of the energetic competition between different structures has been built up from first-principles studies of the lattice dynamics of these materials and it is now generally possible to predict which particular structure a perovskite will adopt in its ground state. However, there is no chemically intuitive picture – one that combines lattice dynamics with a local description of bonding – to explain why, for example, the majority of ferroelectric perovskites with rotated octahedra form in only a select few space groups. Such knowledge is at the foundation of the current materials-by-design effort, which attempts to use design rules, based on both chemical and energetic criteria, to create new materials with desired properties.

We use a combination of Density Functional Theory, group theoretical techniques and crystal chemistry arguments to study the interaction between ferroelectric and octahedral rotation distortions in a family of perovskite fluorides and oxides. By considering both 'long-range' distortions (phonons) and the local bonding environment of each ion in a particular structure, we are able to show that, in contrast to the common assumption, ferroelectricity and octahedral rotations do not always compete. In particular, we examine the interplay between ferroelectricity and octahedral rotations in space group R3c and identify a mechanism whereby octahedral rotations actually promote ferroelectricity.

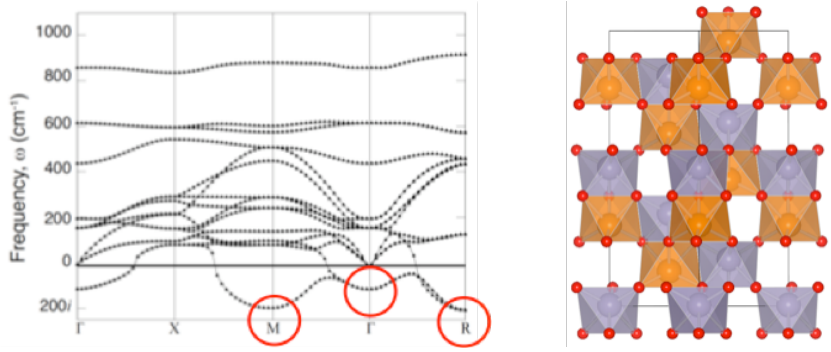

(Left) The phonon dispersion curve of cubic *Pm3m* $CaTiO_3$, showing the zone-boundary instabilities (R and M) and a ferroelectric zone-center instability, the latter of which is suppressed in the non-polar ground state. (Right) The *R3c* structure, in which octahedral rotations can promote ferroelectricity.

Structural analysis of ferroelectric phase of $CdTiO_3$ from first-principles calculations

Hiroki MORIWAKE[1], Craig A. J. FISHER[1], Akihide KUWABARA[1], Hiroki TANIGUCHI[2], Mitsuru ITOH[2], and Isao TANAKA[1,3]
[1] Nanostructures Research Laboratory, Japan Fine Ceramics Center, Nagoya 456-8587, Japan
[2] Materials and Structure Laboratory, Tokyo Institute of Technology 4259 Nagatsuta, Yokohama 226-8503 Japan
[3]Department of Materials Science and Engineering, Kyoto University, Kyoto 606-8501, Japan
E-mail: moriwake@jfcc.or.jp

Extended abstract

$CdTiO_3$ is one of the perovskite titanate, whose ferroelectric phase has been reported to appear at the low-temperature region.[1] The recent rigorous Raman scattering study has revealed an ideal classical displacive-type phase transition, in which the soft mode softens toward zero-frequency at $T_c \sim 85.5$ K obeying conventional Cochran's law.[2] However, the crystal structure in the low-temperature region is still unclear due to the rather small displacement at the phase transition and difficulty in preparation of sufficiently large and high-quality single crystals for the structural analysis.[3] Both of possible ferroelectric structures $Pna2_1$(#33) and $P2_1ma$(#26) are found depending on the samples and experimental conditions. The situation is still controversial. Lebedev[4] reported theoretical phonon calculation only Γ-point of the *Pnma* of $CdTiO_3$. He reported two softmode phonon in *Pnma* phase of $CdTiO_3$, which read to $Pna2_1$(#33) and $P2_1ma$(#26) phase. In the present study, we performed series of a first-principles calculations of $CdTiO_3$, in order to elucidate completely the mechanism of the ferroelectric phase transition and the structure of the low-temperature phase. The result clarifies that the low-temperature symmetry is $Pna2_1$ (#33) with the polarization axis along *b*-axis of the paraelectric *Pnma* phase. The calculated phonon dispersion structure clearly shows the existence of the ferroelectric soft mode in Γ-point of the *Pnma* phase, and it vanishes in the ferroelectric $Pna2_1$ phase, confirming the soft-mode-type phase transition of $CdTiO_3$.(Fig.1) However, energy gain of this ferroelectric phase transition is very tiny, its only 0.2meV/f.u. In addition, the phonon dispersion relation, in another word, soft-modes are strongly depending on the lattice volume. As shown in fig.3(a), in the tensile condition (+2% of theoretical equivalent volume), not only *B*2*u* mode which read to $Pna2_1$(#33) phase but also *B*3*u* mode which reads to $P2_1ma$(#26) phase show imaginary frequency. On the other hand, As shown in fig.3(b), in the compression condition (-2% of theoretical equivalent volume), these soft-modes are vanished. This indicates that ferroelectric phase transition of $CdTiO_3$ *Pnma* phase is very sensitive to pressure/strain. Depending on the stress/pressure both of ferroelectric phase $Pna2_1$(#33) phase and $P2_1ma$(#26) phase can be stabilized. This can be a explanation for controversial experimental results of ferroelectric structure of $CdTiO_3$. [5]

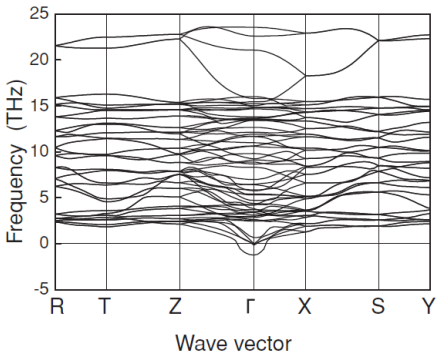

Fig. 1 Theoretical phonon dispersion curves for *Pnma* phases of $CdTiO_3$.

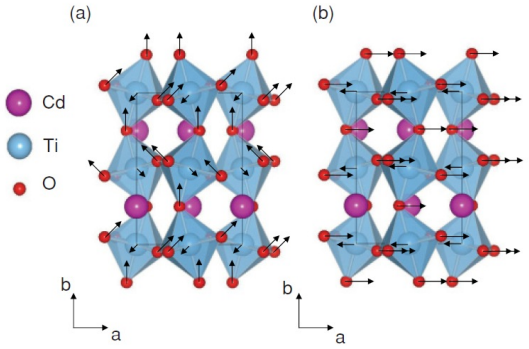

Fig. 2 Directions of ion displacements in the *Pnma* structure corresponding to (a) *B*2*u* and (b) *B*3*u* modes associated with transformations to the $Pna2_1$ and $P2_1ma$ phases, respectively.

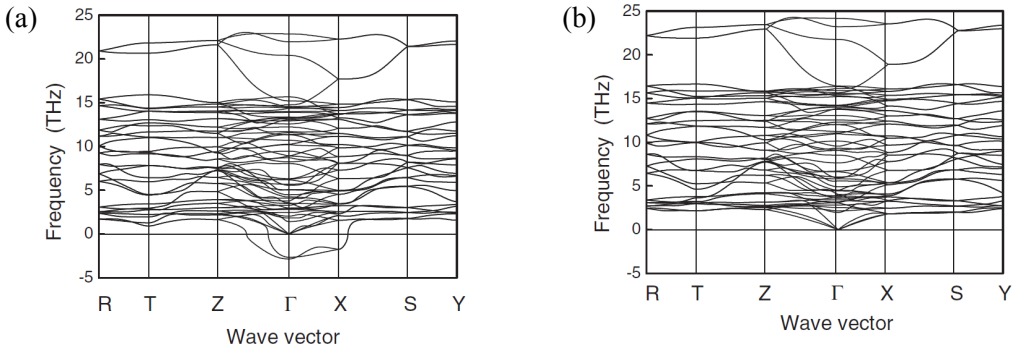

Fig. 3 Theoretical phonon dispersion curves for the *Pnma* phase of $CdTiO_3$ when the volume is uniformly (a) expanded by 2%, and (b) contracted by 2% relative to the equilibrium value.

Acknowledgements

This work was supported by the Ministry of Education, Culture, Sports, Science and Technology of Japan through the Grants-in-Aid for Priority Area "Atomic Scale Modification" (No. 474) and Scientific Research (C) No.21560708.

References

1. G. A. Smolenskii, *Dolk. Akad. Nauk. SSSR* **70** (1950) 405.
2. H. Taniguchi, Y. J. Shan, H. Mori, and M. Itoh, *Phys. Rev.* B **76** (2007) 212103.
3. P. -H Sun, T. Nakamura, Y. J. Shan, Y. Inaguma, M. Itoh. *Ferroelectrics* **217** (1998) 137-145.
4. A. I. Lebedev, *Physics of the Solid State*, **51** (2009) 802–809.
5. H. Moriwake, C. A. J. Fisher, A. Kuwabara, H. Taniguchi, M. Itoh, and I. Tanaka, *Phys. Rev.* B **84** (2011) 104114.

Spin-phonon coupling effects in transition-metal perovskites: a DFT+U and hybrid-functional study

Jiawang Hong,[1] Alessandro Stroppa,[2] Jorge Iniguez,[3] Silvia Picozzi,[2] and David Vanderbilt[1]

[1] *Department of Physics and Astronomy, Rutgers University, Piscataway, NJ 08854-8019, USA*
[2] *CNR-SPIN, L'Aquila, Italy*
[3] *Institut de Ciencia de Materials de Barcelona (ICMAB-CSIC), Campus UAB, 08193 Bellaterra, Spain*

The understanding and control of spin-phonon coupling effects holds promise for the discovery of new multiferroics, as demonstrated recently by Fennie and Rabe [1]. Here we take the frequency shifts $\Delta\omega$ of low-frequency phonons between ferromagnetic (FM) and antiferromagnetic (AFM) configurations as a measure of the spin-phonon coupling, and investigate conditions under which the desirable enhancement of this coupling might be achieved.

In the search for materials with large spin-phonon coupling, first-principles calculations have usually been carried out using the DFT+U method [2], which accounts for correlation effects driven by on-site Hubbard interactions. However, DFT+U suffers from shortcomings associated with the U-dependence of the calculated properties [3]. Even if an appropriate choice of U can accurately reproduce the binding energy of localized d states of transition-metal oxides, it is by no means guaranteed that the same U can accurately reproduce other properties of the same compound, such as the volume, which has a significant effect on the phonons. Another shortcoming of the DFT+U approach is that there is usually no obvious choice of the U value to be adopted. Another paradigmatic approach – that of hybrid functionals – has been widely applied in solid-state materials science, showing improved performance with respect to standard DFT methods. Even when using the more efficient Heyd-Scuseria-Ernzerhof (HSE) hybrid functional [4], however, the use of hybrids entails an increased computational cost which makes the calculation of phonon properties of complex magnetic oxides very difficult.

In this work, we circumvent this bottleneck by combining the DFT+U and HSE approaches, choosing the appropriate U for each material by fitting to the HSE results for frequency shifts. This provides a fairly efficient and affordable strategy that preserves the "HSE accuracy" for lattice constants, spin-phonon related couplings, and related properties, while taking advantage of the computationally inexpensive DFT+U method for the detailed calculations.

We investigate spin-phonon coupling effect in $A\mathrm{MnO_3}$ perovskites with $A=$ Ca, Sr and Ba, which may be good candidates for spin-phonon–coupling driven multiferroicity [5-7], as well as the simple perovskite $\mathrm{La}M\mathrm{O_3}$ materials with $M=$ Cr and Fe and double perovskite $\mathrm{La_2(CrFe)O_6}$, which have Néel temperatures above room temperature [8] and large band gaps. We have performed the DFT+U and HSE calculations using the PBEsol [9] (PBEsol+U) and HSE06 [4] functionals, respectively. The unit cell for simulating the G-type AFM and FM magnetic ordering is doubled along the $\langle 111\rangle$ direction as shown in Fig. 1. The phonon frequencies were calculated using the frozen-phonon method.

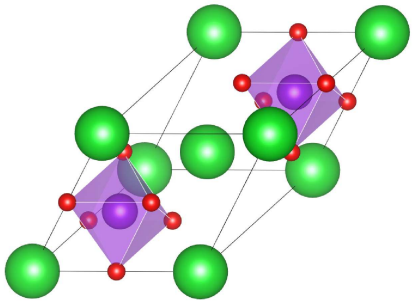

FIG. 1: $AB\mathrm{O_3}$ perovskite structure doubled along the [111] direction. A atoms (largest) shown in green; B atoms shown in violet; O atoms (smallest) shown in red.

We first performed the calculation by varying U and considering the Γ_4^- and R_5^- modes, which are the ones that compete to determine whether a ferroelectric or other instability freezes in. From Fig. 2 we see that the frequencies of the Γ_4^- and R_5^- modes depend strongly on the chosen U. Notably, the frequency shift $\Delta\omega = \omega_{\mathrm{AFM}} - \omega_{\mathrm{FM}}$ of the Slater mode (S-Γ_4^-) can change from 400 cm^{-1} to 0 as U changes from U=0 to 8 eV. The $\Delta\omega$ of the Axe (A-Γ_4^-) and R_5^- modes also depend on the U, although $\Delta\omega$ is nearly insensitive to U for the Last mode (L-Γ_4^-) in this range of U. Clearly, the strong U-dependence of the spin-phonon coupling suggests that it is crucial to choose the appropriate U value in order to avoid artifactual "strong" couplings.

However, the lack of the experimentally available data for our systems prevents us from extracting U directly from experiments. Here, we propose a practical scheme to reduce the computational load while still retaining an accuracy comparable to HSE for the phonons and spin-phonons couplings. The U is extracted from HSE calculations with respect to the frequency shifts between AFM and FM magnetic orders. We have tested that the proposed scheme works well: the calculations of the phonon frequency shifts $\Delta\omega$ based on an estimated U from HSE give almost the same phonon frequency shifts

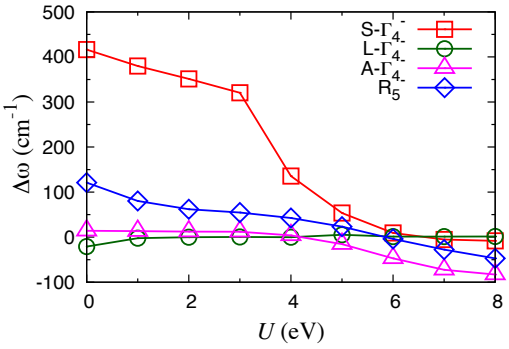

FIG. 2: Effect of U on the spin-phonon coupling in $SrMnO_3$

as obtained by using HSE directly. The fact that HSE works "remarkably well" for transition metal oxides [10] make us confident that the HSE phonon frequency shifts are also reliable, and provides a strict benchmark for our proposed method. By using this method, we obtained U= 3.0, 2.8, 2.7, 3.8, and 5.1 eV for $CaMnO_3$, $SrMnO_3$, $BaMnO_3$, $LaCrO_3$ and $LaFeO_3$, respectively.

Our PBEsol+U method gives good lattice constants and magnetic moments compared with our HSE calculation. As shown in Tables I and II, the phonon frequency shift ($\Delta\omega$) for the PBEsol+U and HSE calculations are in overall good agreement [11], indicating that our PBEsol+U approach can reproduce the same spin-phonon coupling effects as HSE but at a lower computational cost, provided that U is obtained by fitting to energy differences between the two magnetic orders.

Table I shows that the spin-phonon coupling effects are large only for some modes and can be negligible for the others in $AMnO_3$. The frequency shift of the polar Slater mode are anomalously large, which suggests that they may be good candidates for multiferroics under external strain [5-7]. Our phonon calculation also hints that doping Ca or Sr into $BaMnO_3$ may induce ferroelectricity even without external strain. In addition, we can see that $\Delta\omega$ for the R_5^- modes is relatively large for $SrMnO_3$ and $BaMnO_3$. As is well known, oxygen octahedron rotations in perovskites have a strong impact on the magnetism, as they control the metal-O-metal bond angles for the super-exchange paths. Therefore, different spin configurations will couple via the super-exchange and hence can induce a large $\Delta\omega$ for the R_5^- modes.

For the spin-phonon coupling effect in $LaMO_3$, Table II shows that most of the Γ and R frequencies are sensitive to the spin order. However, the Γ phonon frequencies of $LaCrO_3$ and $LaFeO_3$ decrease as the spin order changes from AFM to FM, while the Γ frequencies of the double perovskite $La_2(CrFe)O_6$ increase.

TABLE I: Phonon frequency of $AMnO_3$ with HSE and PBEsol+U (+U) calculation, in units of cm^{-1}. $\Delta\omega$ is the frequency difference between AFM state (ω_{AFM}) and FM state (ω_{FM}), i.e., $\Delta\omega = \omega_{AFM} - \omega_{FM}$.

	$CaMnO_3$		$SrMnO_3$		$BaMnO_3$	
	$\Delta\omega_{HSE}$	$\Delta\omega_{+U}$	$\Delta\omega_{HSE}$	$\Delta\omega_{+U}$	$\Delta\omega_{HSE}$	$\Delta\omega_{+U}$
S-Γ_4^-	206.2	195.9	273.1	329.0	95.1	−14.6
Γ_5^-	57.4	80.9	38.4	54.7	36.1	30.0
L-Γ_4^-	86.6	78.5	9.6	0.2	5.4	5.6
A-Γ_4^-	11.3	6.4	7.1	12.2	18.9	−3.4
R_4^-	3.1	4.1	2.3	2.6	3.3	3.4
R_5^+	−10.2	−7.4	2.8	3.0	27.9	36.4
R_4^-	16.7	18.8	13.7	28.7	18.9	31.1
R_3^-	21.3	20.7	17.5	27.5	16.2	51.6
R_5^-	13.9	16.0	70.1	55.8	21.0	59.9
R_2^-	5.1	8.6	21.0	19.7	39.2	70.3

TABLE II: Phonon frequency of $LaMO_3$ with HSE and PBEsol+U ("+U") calculation, in units of cm^{-1} [11].

	$LaCrO_3$		$LaFeO_3$		$La_2(CrFe)O_6$
	$\Delta\omega_{HSE}$	$\Delta\omega_{+U}$	$\Delta\omega_{HSE}$	$\Delta\omega_{+U}$	$\Delta\omega_{+U}$
Γ_5^-	51.1	61.7	5.5	11.8	−16.8
S-Γ_4^-	44.6	46.0	12.6	12.5	−12.8
L-Γ_4^-	21.2	24.5	10.7	13.5	−39.1
R_4^-	17.6	18.9	11.4	9.9	2.7
A-Γ_4^-	15.1	17.1	14.3	11.9	0.4
R_5^-	14.1	15.0	10.7	11.2	−3.2
R_3^-	14.2	14.3	12.4	10.1	15.0
R_5^+	−16.4	−13.7	−9.5	−8.1	−15.7
R_4^-	8.0	8.7	9.8	9.8	1.9
R_2^-	−3.2	−1.5	−25.9	−23.6	6.5

[1] C. J. Fennie and K. M. Rabe, Phys. Rev. Lett. **97** 267602 (2006).

[2] C. Loschen, J. Carrasco, K. M. Neyman, and F. Illas, Phys. Rev. B **75**, 035115 (2007).

[3] A. Rohrbach, J. Hafner and G. Kresse, J. Phys. Cond. Mat. 15, 979 (2003).

[4] J. Heyd, G. E. Scuseria, and M. Ernzerhof, J. Chem. Phys. **124**, 219906 (2006)

[5] S. Bhattacharjee, E. Bousquet, and P. Ghosez, Phys. Rev. Lett. **102**, 117602 (2009).

[6] J. M. Rondinelli, Aaron S. Eidelson, and Nicola A. Spaldin, Phys. Rev. B **79**, 205119 (2009).

[7] Jun Hee Lee and Karin M. Rabe, Phys. Rev. Lett. **104**, 207204 (2010).

[8] J. B. Goodenough, Phys. Rev. **164**, 785 (1967).

[9] J.P. Perdew, *et al.*, Phys. Rev. Lett. **100**, 136406 (2008).

[10] T. Archer, *et al.*, Phys. Rev. B **84**, 115114 (2011)

[11] The HSE calculation for $La_2(CrFe)O_6$ is not carried out due to its low symmerty which requires enormous computational cost.

First-principles calculations of finite temperature Sc NMR parameters in $Pb(Sc_{2/3}W_{1/3})O_3$

Eric J. Walter and H. Krakauer
Department of Physics, College of William and Mary, Williamsburg, VA, 23187-8795

High performance solid solution ferroelectrics, based on the ideal ABO_3 perovskite structure, are widely used in technological applications such as ultrasonic transducers, sensors, actuators, and thin film applications. The strong electromechanical coupling in these materials is related to a balance of competing instabilities, such as cation off-centerings and oxygen octahedral rotations. The perovskite structure offers many ways to fine tune these interactions through chemical substitutions, such as alloying on the A and/or B sites, and through epitaxial control in layered and thin film geometries. Solid state nuclear magnetic resonance (NMR) is one of the few experimental techniques, which can directly probe the local structure and dynamics of targeted nuclei in these complex perovskites [1, 2, 3, 4], probing the coupling of nuclear magnetic dipole and electric quadrupole moments with the local magnetic field and electric field gradient, respectively. How these NMR observables change as a function of temperature is also acessible to experiment and can greatly increase our understanding of the local ordering and structure. The interpretation of NMR spectra in complex solid solution perovskites is complicated, however, by the presence of broad spectral features due to disorder. First-principles calculations of electric field gradient [5] and chemical shielding [6, 7] tensors can play an important role interpreting NMR spectra in these materials.

Here, we present a first-principles study of the NMR chemical shift tensors and quadrupole interaction parameters for $Pb(Sc_{2/3}W_{1/3})O_3$ (PSW). Recent NMR measurements of Sc quadrupole parameters show a three-fold change in Sc quadrupole coupling over a temperature range of $T = 250 - 330$ K[8]. We are investigating the temperature dependence of the Sc quadrupole coupling and chemical shifts in order to see if thermal disorder could be responsible for these measurements.

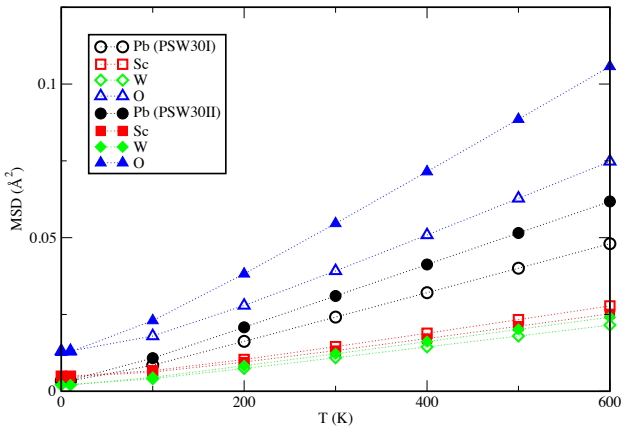

Figure 1: Mean square atomic displacements for PSW, as a function of temperature. Results for the two 30 atom supercells are shown.

Calculations were carried out using the GIPAW method [9] within the QuantumESPRESSO package [10]. Three structural models for PSW are considered: two 30 atom unit cells as well as one 15 atom system. The 15 atom is a simple 2:1 stacking of Sc:W along the [111] direction. The structure of the two 30 atom cells is consistent with the random site model. This constraint yields two unique supercells, hereafter designated as "PSW30I" and "PSW30II" and are distinguished by the symmetry of their ideal (unrelaxed) structures ($I4/mmm$ and $Immm$, respectively). For all of the PSW structural models, the experimentally measured unit cell volume[11] was used.

Figure 1 shows a plot of the average atomic mean-square displacement (MSD) vs. temperature for each of the PSW unit cells. These values are computed using the phonon frequencies and eigenvectors for each system. From these, the atomic MSD can be derived using the quasi-harmonic approximation [12]. These curves show that there are significant changes in the atomic positions

over the in the range of 250-330K in both PSW structural models.

Table 1 shows our preliminary ^{45}Sc quadrupole and chemical shift results for PSW. To validate the GIPAW pseudopotentials and other aspects of the methodology, results are also presented for the simpler Sc_2O_3 and $ScVO_4$ systems (experimental results from Ref [13] are shown in parenthesis). For both Sc_2O_3 and $ScVO_4$ there is good agreement for C_Q and η. Using the measured isotropic shift results for Sc_2O_3, we have computed a theoretical shielding reference of 773 ppm. Using this reference, we find good agreement for $\delta_{\rm iso}$(Sc) in $ScVO_4$. This 773 ppm reference is also used to determine the PSW chemical shifts in Table 1 from the calculated chemical shielding. The PSW results in Table 1 are for structures with relaxed atomic positions and do not include thermal effects.

To model the effects of thermal disorder, we will use an ensemble of frozen-in thermal structures, sampled from the thermal distribution obtained from the quasiharmonic approximation (as reflected by the mean-square displacements in Fig. 1). First-principles calculations will be performed for each sampled structure, and the results for $C_{\rm Q}$ and chemical shielding tensors will be averaged over the ensemble and compared with the NMR measurements.

Table 1: ^{45}Sc quadrupole and chemical shift results for Sc_2O_3, $ScVO_4$, and PSW. Experimental results from Ref [13]

	$C_{\rm Q}$	η	$\delta_{\rm iso}$
Sc_2O_3	-26(23.37)	0 (0)	105(108.0)
	18(15.37)	0.54 (0.63)	131(128.7)
$ScVO_4$	-26 (21.6)	0 ($\leq$ 0.03)	-48 (-34.0)
PSW15	-23	0	202
	-22	0	201
PSW30I	-13	0.88	179
	-43	0.12	188
	25	0.66	150
	23	0.57	165
PSW30II	-11	0.41	195
	-14	0.35	169
	-17	0.52	167
2001.	32	0.33	174

Acknowledgments: This work was supported by ONR grants N00014-08-1-1235 and N00014-09-1-0300. Calculations were performed at the Center for Piezoelectric by Design.

References

[1] D. H. Zhou, G. L. Hoatson, R. L. Vold, and F. Fayon *Phys. Rev. B*, vol. 69, p. 134104, 2004.

[2] A. Baldwin, P. A. Thomas, and R. Dupree *J. Phys.: Condens. Matter*, vol. 17, p. 7159, 2005.

[3] M. Vijayakumar, G. L. Hoatson, and R. L. Vold *Phys. Rev. B*, vol. 75, p. 104104, 2007.

[4] R. Blinc, V. V. Laguta, B. Zalar, M. Itoh, and H. Krakauer *J. Phys.: Condens. Matter*, vol. 20, p. 085204, 2008.

[5] D. Mao, E. J. Walter, H. Krakauer, and Z. Wu *Phys. Rev. B*, vol. 76, p. 014105, 2007.

[6] D. L. Pechkis, E. J. Walter, and H. Krakauer *J. Chem. Phys.*, vol. 131, p. 184511, 2009.

[7] D. L. Pechkis, E. J. Walter, and H. Krakauer *J. Chem. Phys.*, vol. 135, p. 114507, 2011.

[8] J. Ellden, G. L. Hoatson, and R. L. Vold private communication, 2011.

[9] C. J. Pickard and F. Mauri *Phys. Rev. B*, vol. 63, p. 245101,

[10] P. Giannozzi *et al. J. Phys.: Condens. Matter*, vol. 21, p. 395502, 2009.

[11] P. Juhas, I. Grinberg, A. M. Rappe, W. Dmowski, T. Egami, and P. K. Davies *Phys. Rev. B*, vol. 69, p. 214101, 2004.

[12] S. Rossano, F. Mauri, C. J. Pickard, and I. Farnan *J. Phys. Chem. B*, vol. 109, p. 7245, 2005.

[13] M. D. Alba, P. Chain, P. Florian, and D. Massiot *J. Phys. Chem. C*, vol. 114, p. 12125, 2010.

All-atom *ab-initio* models for perovskite ferroelectrics and lattice mode interactions in $PbTiO_3$

Jacek C. Wojdeł, Mathias Ljungberg, Jorge Íñiguez
Institut de Ciència de Materials de Barcelona (ICMAB-CSIC), Campus UAB, 08193 Bellaterra, Spain

Patrick Hermet, Philippe Ghosez
Physique Théorique des Matériaux, Université de Liège, Allée du 6 Août 17 (B5), 4000 Sart Tilman, Belgium

Temperature dependent properties of perovskite ferroelectric materials play an important role in their applications in devices [1, 2] and are of major interest from the fundamental physical point of view [3]. It is therefore highly desirable to be able to model such properties in atomistic simulations. Unfortunately, direct *ab-initio* access to these phenomena is not yet possible due to the high computational cost associated with running simulations potentially involving (tens of) thousands of atoms. This computational constraint has led to the development of *ab-initio* based model approaches in which the atomic system is simplified to a model which captures the essential features of potential energy surface (PES). The parameters for such models are obtained from a limited set of *ab-initio* electronic structure calculations [4, 5, 6]. The major simplifying assumption for such models is that not all structural degrees of freedom are retained, which changes the phonon dispersion spectrum of the system. If only a few important phonon branches remain in the model, they need to be chosen carefully which requires a priori insight in the dynamics of the system. This latter can be especially difficult in case of more complex nanostructured materials (such as superlattices of perovskite layers).

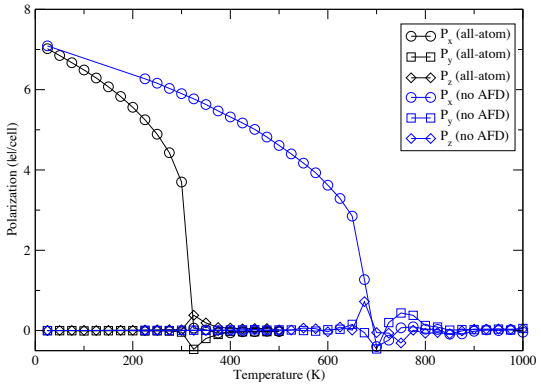

Figure 1: Spontaneous polarization of $PbTiO_3$ in Monte Carlo simulation with or without AFD degrees of freedom

We present an all-atom model Hamiltonian method, in which all structural degrees of freedom are explicitly retained, with all the parameters obtained from the *ab-initio* calculations. Our method is based on a rigorous expansion of the PES in Taylor series around the high symmetry perovskite structure. In the presented approach the terms up to second order are by construction equivalent to the *ab-initio* calculated quantities. Phonon spectra, Born charges and elastic constants are calculated using perturbational scheme, as implemented in ABINIT code [7, 8]. Higher order terms of our model Hamiltonian are properly symmetrized and adjusted to correctly represent the energetics and the phonon spectra of several selected structures with lower symmetry. Efficient calculation of the total energy of such a model for arbitrary supercell sizes is possible thanks to the fact that the interatomic interactions can be divided into long-range (electrostatic) and short-range parts [9], which can be evaluated independently. In the presented approach, we find that the the anharmonic contributions to the energy landscape are of short-ranged nature, which allows us to limit the number of independent parameters considerably.

In the calculations of the $PbTiO_3$ (PTO) lattice dynamics, we use a model which expands PES up to a fourth order with respect to atomic displacements. This allows us to correctly represent the double-well potential shape of the PES in the subspace of polar distortions. We have found that non-polar distortion energetics is well represented at this order of expansion as well. Our calculations show that without considering the strain-phonon coupling terms, the PTO model exhibits a groundstate in which both ferroelectric (FE) and anti-ferro-distortive modes (AFDs – oxygen octahedra rotations) are present. The cubic perovskite structure is distorted rhombohedrally with the polarization pointing in [111] direction. At the same time the oxygen octahedra undergo anti-phase rotations along all three axes and the symmetry of the groundstate resulting from these two types of distortions is R3c.

From our *ab-initio* calculations we extract also strain-phonon coupling terms, which proved to be significantly non-linear in the strain range of interest. For that reason, these coupling terms are calculated from *ab-initio* values using finite-difference scheme at the linear (w.r.t. strain) level, while the higher order coupling terms are fit to the tetragonally distorted groundstate properties (structural distortions, energy and phonon spectrum). As expected, the introduction of these terms leads to the proper description of the fully relaxed structure, in which only a FE distortion is present and all AFD modes are absent. We found, however, that contrary to the previous model approaches [5] the higher order terms of the strain-phonon coupling are essential for describing properly the groundstate structure, and also that they strongly influence the character of the phase transition observed in this material.

Using a constrained dynamics simulations, we can also quantify the extent of the effect that inclusion of all structural degrees of freedom has on the resulting properties of the model. We show that neglecting the AFD motion of oxygen octahedra in the model leads to a large differences in the transition temperature for the FE-PE phase transition (see Figure 1). Notably, this transition is found to be very close to the experimentally measured temperature (and also to the result presented in ref. [5]) only in case the AFD modes are not allowed to contribute to the dynamics of the material. We have found that this effect is essentially independent from the details of the model Hamiltonian parametrization, provided that it fits properly the *ab-initio* energetics. This result shows that new physical insights can be gained from the all-atom simulations as compared to previous model approaches.

References

[1] P. Muralt. Ferroelectric thin films for micro-sensors and actuators: a review. *Journal of Micromechanics and Microengineering*, 10(2):136, 2000.

[2] J. F. Scott and C. A. Paz de Araujo. Ferroelectric memories. *Science*, 246:1400, 1989.

[3] K. Rabe, Ch. H. Ahn, and J.-M. Triscone, editors. *Physics of Ferroelectrics. A modern Perspective*, volume 105 of *Topics in Applied Physics*. Springer, 2007.

[4] W. Zhong, D. Vanderbilt, and K.M. Rabe. Phase transitions in BaTiO3 from first principles. *Physical Review Letters*, 73(13):1861, 1994.

[5] U. V. Waghmare and K. M. Rabe. Ab initio statistical mechanics of the ferroelectric phase transition in PbTiO3. *Physical Review B*, 55(10):6161, 1997.

[6] I. Kornev et al. Finite-temperature properties of multiferroic $bifeo_3$. *Phys. Rev. Lett.*, 99:227602, 2007.

[7] X. Gonze et al. Abinit : First-principles approach of materials and nanosystem properties. *Computer Phys. Commun.*, 180:2582–2615, 2009.

[8] X. Gonze et al. A brief introduction to the abinit software package. *Zeit. Kristallogr.*, 220:558–562, 2005.

[9] X. Gonze and C. Lee. Dynamical matrices, born effective charges, dielectric permittivity tensors, and interatomic force constants from density-functional perturbation theory. *Physical Review B*, 55(16):10355, 1997.

Session 10
Techniques

Full field electron spectromicroscopy of ferroelectric materials

N. Barrett[1], J. Rault[1], G. Niu[2], B. Vilquin[2], B. Gautier[3], D. Albertini[3], S. Fusil[4,5], M. Bibes[4,6], K. Winkler[7], B. Kroemker[7], A. Locatelli[8], T.O. Mentes[8], G. Geneste[9]

[1] CEA, DSM/IRAMIS/SPCSI, F- 91191 Gif sur Yvette cedex, France
[2] Université de Lyon, Ecole Centrale de Lyon, Institut des Nanotechnologies de Lyon, F- 69134 Ecully cedex, France
[3] Université de Lyon, INSA Lyon, Institut des Nanotechnologies de Lyon, F- 69621 Villeurbanne cedex, France
[4] Unité Mixte de Physique CNRS/Thales, 1 Av. Augustin Fresnel, Campus de l'Ecole Polytechnique, 91767 Palaiseau, France
[5] Université d'Evry-Val d'Essonne, Boulevard François Mitterrand, 91025 Evry cedex, France,
[6] Université Paris-Sud, 91405 Orsay, France
[7] Omicron NanoTechnology GmbH, Limburger Str. 75, 65232 Taunusstein, GERMANY
[8] Sincrotrone Trieste S.C.p.A., S.S. 14 Km 163.5, I-34149 Basovizza, Italy
[9] CEA, DAM, DIF, F-91297 Arpajon, France

At a boundary of a ferroelectric material, the surface charge creates a depolarizing electric field opposite to the FE polarization. It may be screened by charge carriers or defects in the bulk or by external charges from adsorbate species. In nanoscale films, the charge state of a FE surface can dominate the film properties even in deeper layers and impose ultimate limits on polarization and thickness. [1] Screening of the fixed polarization charge at the surface will result in a change in the surface potential. However, the full electronic and chemical structure underlying the surface domain ordering and the electrical properties of these materials remains a challenge for experimentalists. Optical, electrical and X-ray diffraction techniques have provided invaluable information on the domain structure at the surface of ferroelectric materials and near field scanning probe microscopy complements these techniques with high spatial resolution.

The analysis of chemical and electronic states in complex and nanostructured material systems requires electron spectroscopy to be carried out with high lateral resolution. Here we present two examples of electron spectromicroscopy applied to the study of ferroelectric domain surfaces.

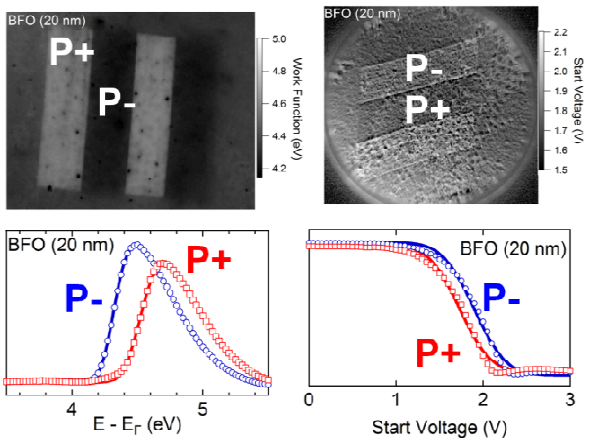

Figure 1 Above, work function and electrostatic potential maps of 10 μm PFM written P^+/P^- domain structures obtained from threshold PEEM and MEM-LEEM transitions. Below, threshold and electron reflectivity extracted from the data sets showing clear contrast due to polarization.

The electrostatic potential above the surface and the work function were studied using low energy electron microscopy (LEEM) and energy filtered photoelectron emission microscopy (PEEM), providing insights into the ferroelectric polarization of ultra-thin epitaxial $BiFeO_3$ films as a function of film thickness. Electrical characterization of these films is made difficult in the tunnel regime due

to the high leakage current. Detrimental tip-surface interactions inherent to scanning probe microscopy may be avoided by using mirror electron microscopy (MEM), [2] which allows full-field imaging of the surface topography and potential [3] and has recently been applied to FE domains. [4] By using reflected electrons, MEM minimizes possible surface charging and low energy electron induced oxygen desorption. [5] It is highly sensitive to the local variations of the surface potential, as small differences in the latter determine large differences in the electron reflectivity. [6] Thus, the energy of the MEM-LEEM transition provides an accurate nondestructive map of the charge state or screening of the surface of FE domains.

The second example presents an energy filtered PEEM study of the band structure of a micron scale region in a strained $BaTiO_3$ epitaxial thin film. Energy-filtered PEEM with similar electron optics to LEEM provides the full photoemission spectrum with high spatial resolution, giving access to surface properties via the work function, chemistry from core level imaging and electron structure in the valence band region. [7,8] Using suitable electron optical configuration the diffraction plane can be projected onto the detector providing a spatially resolved reciprocal space image of the electron dispersion relations in the first Brillouin zones. [9]

The dispersion relations as a function of electron wave vector parallel to the surface are mapped compared with first principles calculations, revealing subtle differences in the dispersion relations with respect to those obtained on a relaxed bulk $BaTiO_3$ single crystal.

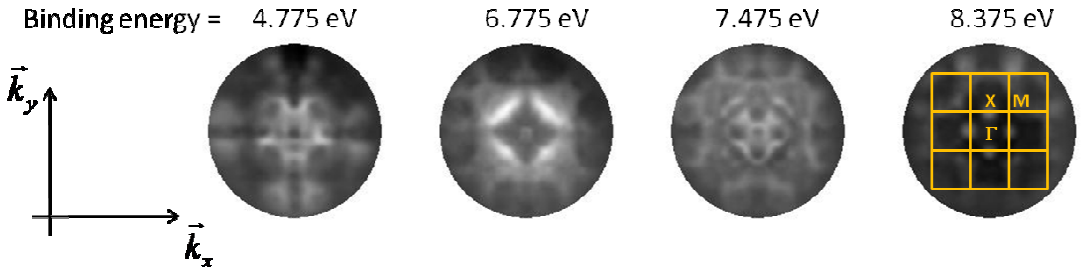

Figure 2 Four constant energy cuts in reciprocal space of the mainly O 2p valence band region of 12 nm BTO on Nb:STO substrate. Experiment performed on the Nanospectroscopy beamline at the ELETTRA synchrotron, photon energy 52 eV, the energy resolution is 0.3 eV, the wave-vector resolution 0.05 $Å^{-1}$. In-plane strain as measured by X-ray diffraction ~ 1%.

The examples show that the combination of real and reciprocal space imaging of ferroelectric surfaces using full field electron spectromicroscopy is potentially a powerful new tool for unraveling the electronic structure responsible for ferroelectric order, screening and switching.

[1] J. Junquera and P. Ghosez, *Nature* **422**, 506 (2003).
[2] G. Bartz, G. Weissenberg and D. Wiskott, *Proc. of the Fourth Int. Conf. on Electron Microscopy*, London, 1954, p. 395.
[3] W. Swiech, B. Rausenberger, W. Engel, A. M. Bradshaw and E. Zeitler, *Surf. Sci.* **294**, 297 (1993).
[4] S. Cherifi, R. Hertel, S. Fusil, H. Béa, K. Bouzehouane, J. Allibe, M. Bibes and A. Barthélémy, *Phys. Stat Solidi.* RRL **4**, 22 (2010).
[5] O. Dulub, M. Batzilln, S. Solovev, E. Loginova, A. Alchagirov, T. E. Madey, and U. Diebold, *Science* **317**, 1052 (2007).
[6] S. A. Nepijko, N. Sedov, and G. Schönhense, *J. Microsc.* **203**, 269 (2001).
[7] A. Locatelli and E. Bauer, *J. Phys. Condens. Matter* **20** 093002 (2008).
[8] M. Escher, K. Winkler, O. Renault and N. Barrett, *J. Electron Spectrosc. Relat. Phenom.* **178–179**, 303 (2010).
[9] C. Mathieu, J. Rault, Y. Mi, B. Zhang, W. A. de Heer, C. Berger, E. Conrad, O. Renault and N. Barrett. *Phys. Rev. B* **83**, 235436 (2011).

Structural Control of Magnetic Anisotropy in a Multiferroic $EuTiO_3$ Thin Film

J.W. Freeland[1], X. Ke[2], P. Ryan[1], J.W. Kim[1], R. Misra[3], J.H. Lee[1], T. Birol, C.J. Fennie[4], P. Schiffer[3], and D.G. Schlom[4]
[1]Advanced Photon Source, Argonne National Laboratory, Argonnne, IL 60439, USA
[2]Neutron Scattering Science Division, Oak Ridge National Laboratory, Oak Ridge, TN 37831
[3]*Department of Physics and Materials Research Institute, Pennsylvania State University, University Park, Pennsylvania 16802, USA*
[4]*Department of Applied and Engineering Physics, Cornell University, Ithaca, New York 14853, USA*

The use of strain in complex oxides has been demonstrated as a unique route to activate novel properties in strongly correlated systems. Our previous work on EuTiO3 showed that under tensile strain the system converts from an antiferromagnetic paraelectric to a multiferroic groundstate with ferromagnetic and ferroelectric order[1]. Here we present a study of the uniaxial magnetic anisotropy which is connect to a unaxial octahedral tilt pattern that emerges under strain.

Stoichiometric EuTiO3 was grown on orthorhombic DyScO3(110) substrates by reactive molecular-beam epitaxy (MBE). Neutron scattering and magnetic measurements show the magnetic moment orders with an easy axis along only one of the (110) pseudocubic axis of the unit cell (see Figure 1). Using synchrotron based x-ray diffraction uncovers a coubling of the unit cell due to the development of octahedral tilts under strain. The tetragonal structure agrees well with recent theoretically predicted structure under biaxial strain (see Figure 2). Such an easy axis is connected to the uniaxial crystal structure that evolves from cubic to tetragonal with octahedral tilting. The magnetic anisotropy for Eu is attributed to an asymmetric crystal field due to the uniaxial symmetry of the Eu-O coordination that results from the octahedral tilt pattern.

Work at Argonne, including the Advanced Photon, is supported by the U.S. Department of Energy, Office of Science, and Office of Basic Energy Sciences, under Contract No. DE-AC02-06CH11357.

[1] J.-H. Lee et al. Nature **466**, 954 (2010).

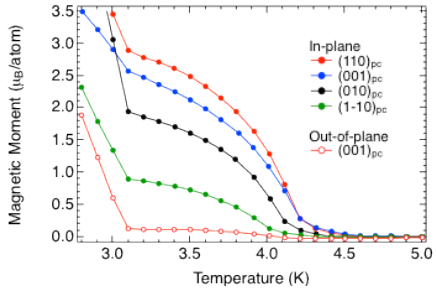

Figure 1 Zero field cooled magnetic moment data measured in an applied field of 100 Oe. The response shows a magnetic easy axis which favors the (110) pseudocubic axis.

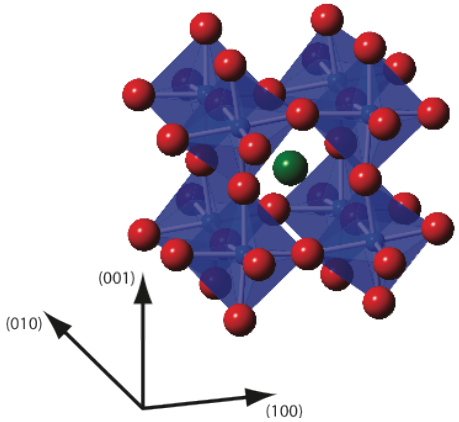

Figure 2 Theoretically predicted and experimentally confirmed tetragonal structure with strain -induced octahedral rotations.

Ultrafast optical manipulation of the ferroelectric order in multiferroic bismuth ferrite

Haidan Wen[1], Pice Chen[2], Donald Walko[1], June Hyuk Lee[1], Carolina Adamo[3], Richard D. Schaller[4], Jon Ihlefeld[5], Eric Dufresne[1], Darrell Schlom[3], John Freeland[1], Paul Evans[2], and Yuelin Li[1*]

[1] *X-ray Science Division, Argonne National Laboratory, Argonne, Illinois 60439*
[2] *Department of Materials Science and Engineering and Materials Science Program, University of Wisconsin–Madison, Madison, Wisconsin 53706*
[3] *Department of Materials Science and Engineering, Cornell University, Ithaca, New York 14853-1501*
[4] *Center for Nanoscale Materials, Argonne National Laboratory, Argonne, Illinois 60439*
[5] *Sandia National Laboratories, Albuquerque, New Mexico 87185*
**ylli@aps.anl.gov*

Ultrafast lattice dynamics in an epitaxial thin film of bismuth ferrite can be driven by ultrafast laser-generated photocarriers. We report a structural study of these dynamics conducted with a temporal resolution of 100 ps. Multiferroics exhibit simultaneous magnetic and ferroelectric (FE) degrees of freedom [1, 2]. The coupling between these degrees of freedom and their interaction with excitations is beginning to be understood in a static sense [3, 4], but the timescales of the interaction of polarization and magnetism with strain and excited carriers are not yet known. Understanding these interactions is important to testing theoretical prediction of the coupling among strain, magnetism, and polarization as well as in eventual applications of multiferroics in electronics and optics.

We report a laser pump/x-ray probe experiment performed at the 7ID beam line at the Advanced Photon Source (APS) that reveals ultrafast variation of the FE order in epitaxial BFO thin film. The optical pump pulses had durations of 50 fs and a wavelength of 400 nm. This photon energy is above the BFO band gap and results in the creation of carriers in an absorption depth of approximately 32 nm. X-ray pulses with 10 keV photon energy and duration of ~100 ps are used to probe the lattice dynamics at variable delays from the pump pulse. The BFO layer was 35 nm thick, prepared by molecular beam epitaxy on [001] $SrTiO_3$. We report a study of the dynamics of the BFO layer based on an analysis on the dynamics of the (002) diffraction peak.

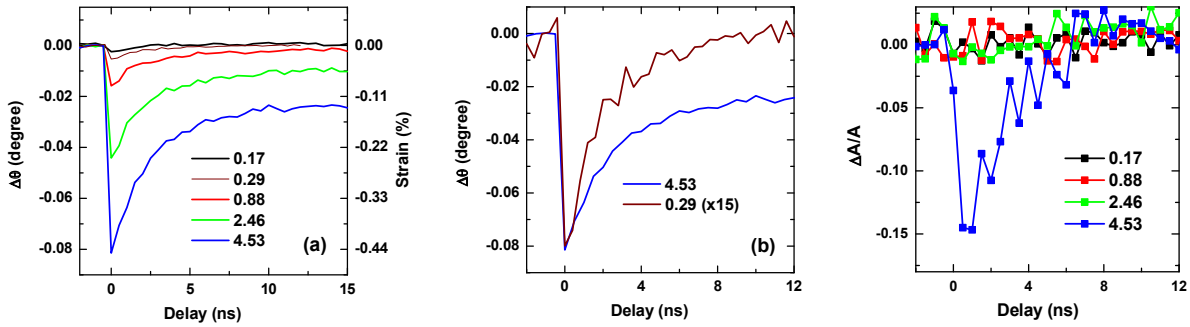

Figure 1Time dependent (a) (b) strain and (c) change in diffraction intensity as a function of delay between the laser pulse and the x-ray probe at different laser fluence. Comparison in (b) highlights the different strain dynamics at different laser fluence. The fluence is corrected for sample reflection, in mJ/cm^{-2}.

Figure 1 depicts the time dependence of the Bragg angle of the 002 reflection, the strain computed from this angular shift, and the change in the peak intensity of the 002 diffraction peak at several laser fluences. The strain displays a fast rise of less than 100 ps, followed by a decay characterized by two timescales. The faster timescales depends on the laser fluence. The slower decay does not show an obvious laser fluence dependence. Figure 2 shows the variation of strain and diffraction intensity as a function of the laser pump fluence at fixed time delays of 100 ps and 15 ns. The strain has a clear linear dependence on the laser fluence. The intensity drops at fluences higher than a threshold of ~1.5 mJ/cm^2.

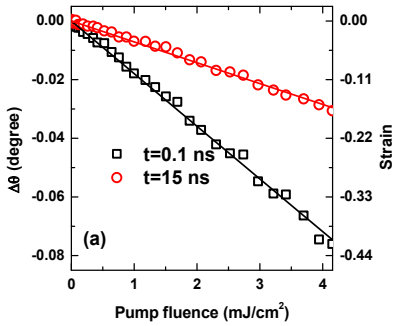

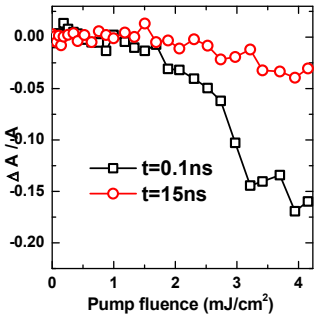

Figure 2 (a) Laser-induced shift in the 002 Bragg angle and strain for time delays of 100 ps (black squares) and 15 ns (red circles). (b) Fractional change in the peak intensity of the 002 reflection as a function of laser fluence at these delays. The laser fluence is corrected for sample reflection.

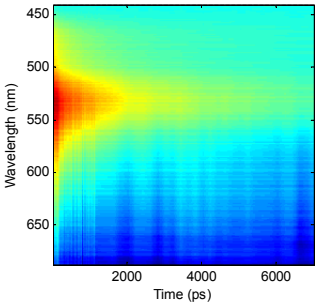

Figure 3 Optical absorption spectrum as a function delay between the 400 nm pump and the continuum probe.

An estimate based on the thermal properties of BFO shows that the maximum strain due to the instantaneous temperature rise is lower than the strains shown in Figure 2 by factors of 10 and 5 at 0.1 and 15 ns, respectively. At short delay times, the laser-induced strain is due to the interaction of the FE order with photo-carriers via screening the depolarization field. Based on a piezoelectric constant of d_{33}~50 pm/V [1], the observed strain of 0.2% corresponds to a screened field of 40 MV/m. A photostriction effect with a similar magnitude has been observed in BFO single crystals [5], and we hypothesize that the photocarrier screening mechanism is also responsible in that case. We also note that the increase of the out-of-plane lattice parameter yields a rotation of the FE polarization in BFO, different from the case of tetragonal $PbTiO_3$ [6].

The fluence dependence of the strain can be explained via a model involving the formation of piezoelectric polarons [7]. Free carriers induce a local lattice distortion via the piezoelectric effect which in turn leads to a self-trapping of the carriers and formation of polarons. The trapping or localization reduces the mobility of the carriers, leading to significant change of their dynamics, effectively slowing the response of the lattice. The reduced mobility of polarons is consistent with the smaller than expected THz response of free carriers in BFO and the abrupt formation of a long lasting absorption band (see Figure 3) in a separate optical pump probe experiments, similar to observations in $LiNbO_3$ [8]. The photocarrier screening effect dominates lattice dynamics at low laser fluences. At higher fluences, however, heating due to polaron recombination begins to have an important role. The lattice distortion associated with the formation of polarons increases the intensity of diffuse scattering and reduces the intensity of Bragg reflections. Localized lattice distortion due to polarons broadens diffraction peaks and is observable when the broadening exceeds the angular width of the Bragg reflection, e.g. as in a manganite bilayer [9].

Our experiment opens the door for studying the real time, ultrafast electromagnetic coupling dynamics in multiferroics, a significant step beyond previous studies under static conditions [3, 4].

Work at Argonne is supported by the U.S Department of Energy, Office of Science, and Office of Basic Energy Sciences, under Contract No. DE-AC02-06CH11357.

1. G. Catlan and J. F. Scott, *Advanced Mat.* **21**, 2463 (2009).
2. J. Wang et al., *Science* **299**, 1719 (2003).
3. T. Zhao et al, *Nat Mat.* **5**, 823 (2006).
4. D. Lebeugle, et al., *Phys. Rev. Lett.* **100**, 227602 (2008).
5. B. Kundys et al, *Nat. Mat.* **9**, 803 (2010).
6. D.Daranciang et al., *Phys. Rev. Lett.*, submitted.
7. W.E. Tefft, *Phys. Rev.* **164**, 1032 (1967).
8. S. Sasamoto, et al, *J. Appl. Phys.* **105**, 083102 (2009).
9. L. Vasiliu-Doloc, et al., *Phys. Rev. Lett.* **83**, 4393 (1999).

Ultrafast terahertz and x-ray probes of ferroelectric structural and electronic dynamics

D. Daranciang[1,2], J. Goodfellow[2,3] M. Highland[4], H. Wen[4], S. Young[5], P. Fuoss[4], A. Rappe[5], G.B. Stephenson[4], and A.M. Lindenberg[2,3]

[1]*Department of Chemistry, Stanford University, Stanford, CA 94305*
[2]*Department of Materials Science and Engineering, Stanford University, Stanford, CA 94305*
[3]*PULSE Institute for Ultrafast Energy Science, SLAC National Accelerator Laboratory, Menlo Park, CA 94025*
[4]*Materials Science Division, Argonne National Laboratory, Argonne, IL 604595*
[5]*The Makeni Theoretical Laboratories, University of Pennsylvania, Philadelphia, PA 19104*
E-mail: aaronl@stanford.edu

The interaction of light with ferroelectric materials has seen renewed interest in recent years associated with both electronic and structural responses [1-5]. Here we report femtosecond time-resolved x-ray diffraction and ultrafast terahertz (THz) spectroscopic measurements that probe the coupled lattice and electronic degrees of freedom following above-band-gap photoexcitation in $PbTiO_3$ and $BiFeO_3$ thin films. X-ray measurements [6] were carried out at the Linac Coherent Light Source and at the Advanced Photon Source probing ferroelectric polarization dynamics under above-band-gap visible light excitation,

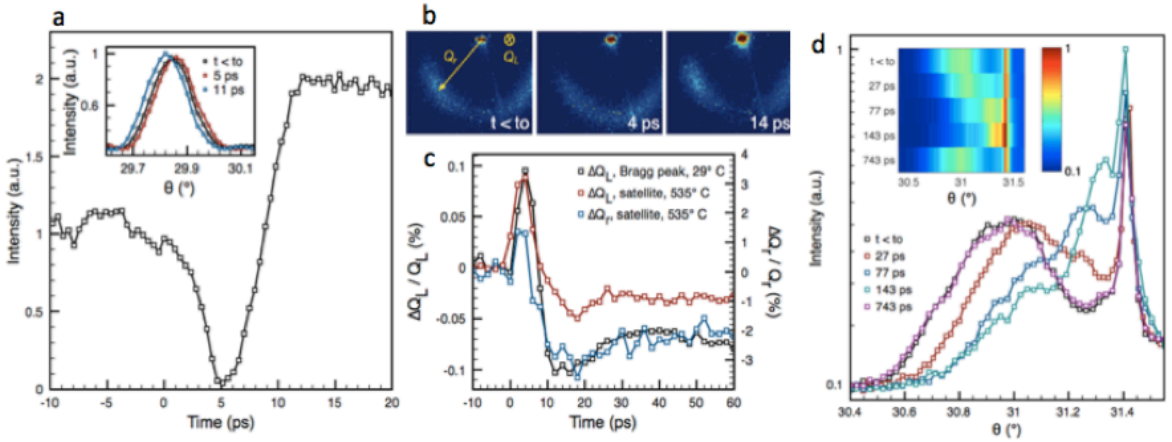

Figure 1. (a) (003) time-resolved diffracted intensity. (b) X-ray diffuse scattering snapshots of stripe phase dynamical response. (c) Analysis showing optically-induced changes in polarization and domain period. (d) Reversible optically-induced switching between ferroelectric and paraelectric phase.

probing $PbTiO_3$ nanolayers deposited on both $SrTiO_3$ and $DyScO_3$. Femtosecond x-ray pulses were scattered from the films and collected with either a point detector or an area detector as a function of laser delay and x-ray incidence angle in order to directly probe the time-dependent polarization and strain within the sample. Time-dependent rocking curve traces taken at room temperature (Fig. 1a) for 20 nm PTO on STO samples with polarization pointing out of the film indicate a symmetric shift of the Bragg peak to higher Q (where $Q = 4\pi \sin\theta/\lambda$) within 5 ps, corresponding to a uniform contraction of the unit cell in the out-of-plane direction and an associated decrease in the ferroelectric polarization. Subsequently, we observe a long-lived, uniform polarization enhancement of the entire nanolayer developing after 10 ps, evidenced by the symmetric shift of the diffraction peak to lower Q, in contrast to what would be expected from simple heating of a ferroelectric. High temperature diffuse scattering measurements probing dynamics in a nanoscale stripe phase are displayed in Fig. 1b,c showing dynamics consistent with the room temperature response, in which the sample is initially depolarized followed by a long-lived polarization increase as well as indications of ultrafast changes in the period of the stripe

domains. We also observe reversible switching between the ferroelectric and paraelectric phases associated with simple heating of the thin films (Fig. 1d). The above effects can be described by a model for the photovoltaic response of the thin films, according to a step-wise process in which electrons undergo a coherent shift first towards the free surface and then away, associated with both a shift current response [7] and a screening of the internal depolarizing field. This is supported by first principles calculations of the expected shift current response, by the observed saturation response as a function of incident laser fluence, by LGD model calculations of the expected changes in the c-axis lattice parameters associated with a screening of the depolarization field, and by the observed response of the thin films in the centrosymmetric paraelectric phase.

We have also carried out complimentary THz emission measurements in which the emitted field from an unbiased PTO or BFO film is directly measured using photoconductive switch techniques to coherently sample the radiated field. The magnitude, time-structure, and polarization of the emitted field then provides complimentary information about the internal photo-currents in the sample, including their crystallographic direction and time-dependence, supporting as well the above interpretations. Fig. 2 shows measurements for the case of in-plane-polarized BFO/DSO samples, showing that the THz polarity switches on rotation of the orientation of the ferroelectric polarization. Also shown is the emitted signal from PTO/STO samples.

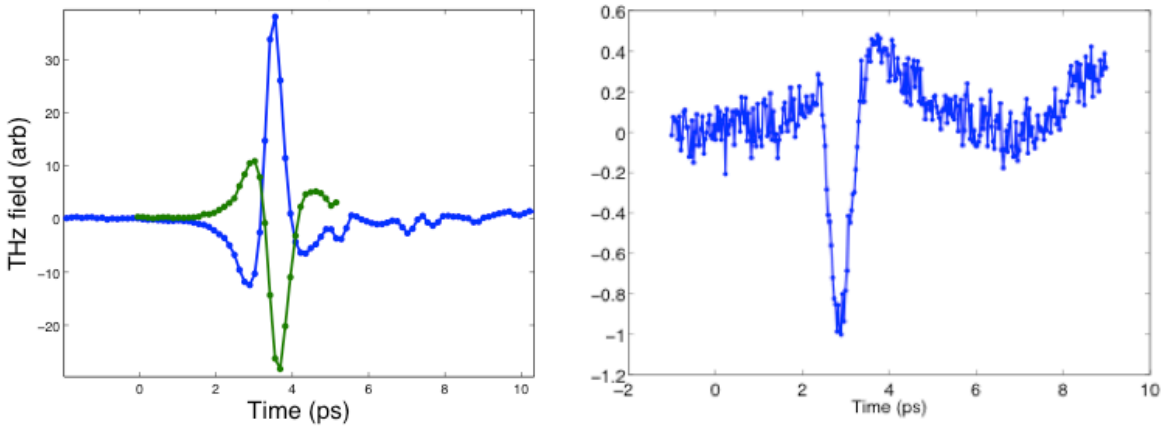

Fig. 2. (left) THz emission from 100 nm BFO sample on DSO with in-plane polarization. Blue and green curves show comparison of emitted waveforms when sample is rotated azimuthally by 180 degrees. (right) THz emission from 40 nm PTO on STO.

References.

[1]. S. Yang, J. Seidel, S. Byrnes, P. Shafer, C.-H. Yang, M. Rossell, P. Yu, Y.-H. Chu, J. Scott, J. Ager, III, L. Martin, R. Ramesh. *Nat. Nanotechnol.* **5,** 143 (2010).

[2] T. Choi et al., Science **324**, 63 (2009).

[3] A.M. Glass, D. von der Linde, T.J. Negran, Appl. Phys. Lett., **25,** 233 (1974).

[4]. C. Korff Schmising, M. Bargheer, M. Kiel, N. Zhavoronkov, M. Woerner, T. Elsaesser, I. Vrejoiu, D. Hesse, M. Alexe. *Phys. Rev. Lett.* **98,** 257601 (2007).

[5]. B. Kundys, M. Viret, D. Colson, D.O. Kundys, *Nat. Mat.*, **9**, 803 (2010).

[6]. D. Daranciang et al. *Submitted* (2011).

[7]. D. Cote, N. Laman, H.M. van Driel, Appl. Phys. Lett. **80**, 905 (2002).

Abstracts for Poster Presentations

The Influence of Phase Coexistence and Ferroelastic Domain Texture on the Performance in $Ba(Zr_{0.2}Ti_{0.8})O_3$-$x(Ba_{0.7}Ca_{0.3})TiO_3$ Piezoceramics

Matthias C. Ehmke[1], John E. Blendell[1], Keith J. Bowman[1,2]
[1]School of Materials Engineering, Purdue University, West Lafayette, Indiana 47907, USA
[2]Mechanical, Materials & Aerospace Engineering, Illinois Institute of Technology, Chicago, Illinois 60616, USA

The motivation to find an alternative for widely used lead-based piezoelectric materials, such as lead zirconate titanate (PZT), has been intensified by current legislation[1]. The challenge is to find a lead-free material system that demonstrates properties that are comparable to those in the hazardous PZT system. Especially findings by Saito et al.[3] and recently by Liu et al.[4], in the barium zirconate titanate barium calcium titanate (BZT-BCT) system, have drawn a lot of attention. Piezoelectric constants with values up to 620 pm/V have been reported for BZT-50BCT that even exceed those values of most PZT materials[4].

In our research we discuss the influence of poling, phase coexistence and ferroelastic domain texture on the properties in $(1\text{-}x)Ba(Zr_{0.2}Ti_{0.8})O_3$-$x(Ba_{0.7}Ca_{0.3})TiO_3$ (100xBCT). It has been demonstrated that higher piezoelectric performance can be achieved by poling at high fields and temperatures exploiting the field cooling poling method. The results can be discussed using an internal bias field[5].

We investigated compositions from 40BCT to 50BCT and found that there is a relatively large composition and temperature region, in which rhombohedral and tetragonal phases coexist. 45BCT through 50BCT exhibit a mixed phase at room temperature that prevails up to 60°C. These findings were supported by temperature dependent *in-situ* X-ray diffraction experiments carried out at the National Synchrotron Light Source at Brookhaven National Laboratories. Figure 1 shows the pseudocubic $(200)_{pc}$ and $(222)_{pc}$ reflections for 45BCT and 50BCT at room temperature (25°C), 60°C and 100°C. At room temperature both, 45BCT and 50BCT, show peak splitting in both $(200)_{pc}$ and $(222)_{pc}$ reflections. This suggests a phase mixture between rhombohedral and tetragonal that prevails up to 60°C. At 100°C both compositions are purely cubic. Due to the proximity of the tricritical point[4] in 45 BCT and the shape of the reflections it is likely that the peaks not only feature a rhombohedral and tetragonal phase coexistence but also an additional cubic phase as suggested elsewhere[6]. This can facilitate the extraordinarily high piezoelectric performance through polarization rotation and extension mechanisms[6].

The stability of electric field induced ferroelastic domain texture is probed by transitioning from the rhombohdral to tetragonal phase field and back, as depicted in Figure 1. Figure 2, $(200)_{pc}$ and $(222)_{pc}$ reflections from *in-situ* temperature dependent X-ray diffraction for a poled 50BCT sample at 25°C, after heating to 70°C and after cooling, again at 25°C are shown in Figure 2. The low angle contribution of both reflections is enhanced due to the ferroelastic domain texture in both coexisting phases. Heating to 70°C brings the material to a purely tetragonal state and letting it cool down to 25°C shows that large parts of the ferroelastic domain texture have been removed, which suggests limitations to the applicability of materials near the high performing compositions in this material system.

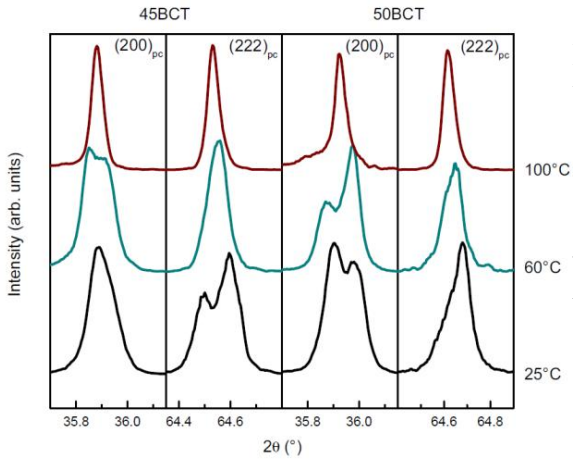

Figure 1: $(200)_{pc}$ and $(222)_{pc}$ reflections from *in-situ* temperature dependent X-ray diffraction for 45BCT and 50BCT at room temperature (25°C), 60°C and 100°C. At room temperature both, 45BCT and 50BCT, show peak splitting in both $(200)_{pc}$ and $(222)_{pc}$ reflections. This indicates a phase mixture between rhombohedral and tetragonal that prevails up to 60°C. At 100°C both compositions are purely cubic. Data taken from ref[2].

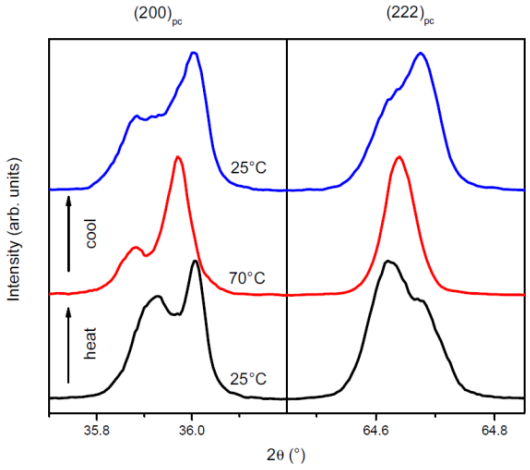

Figure 2: $(200)_{pc}$ and $(222)_{pc}$ reflections from *in-situ* temperature dependent X-ray diffraction for a poled 50BCT sample at 25°C, after heating to 70°C and after cooling, again at 25°C. The low angle contribution of both reflections is enhanced due to electric field induced ferroelastic domain texture in both coexisting phases. Heating to 70°C brings the material to a purely tetragonal state and letting it cool down to 25°C shows that large parts of the ferroelastic domain texture have been removed. Data taken from ref[2].

References

1 J. Rödel, W. Jo, K. T. P. Seifert, E.-M. Anton, T. Granzow, and D. Damjanovic, J. Am. Ceram. Soc. **92,** 1153 (2009).

2 M. Ehmke, S. Ehrlich, J. E. Blendell, and K. J. Bowman, Submitted to J. Appl. Phys. (2011).

3 Y. Saito, H. Takao, T. Tani, T. Nonoyama, K. Takatori, T. Homma, T. Nagaya, and M. Nakamura, Nature **432,** 84 (2004).

4 W. Liu and X. Ren, Phys. Rev. Lett. **103,** 257602 (2009).

5 B. Li, J. E. Blendell, and K. J. Bowman, J. Am. Ceram. Soc. **94,** 3192 (2011).

6 D. Damjanovic, N. Klein, J. Li, and V. Porokhonskyy, Funct. Mater. Lett. **3,** 5 (2010).

Effect of 90° domain walls on the dielectric and pyroelectric susceptibilities of epitaxial ferroelectric thin films

J. Karthik*, A. R. Damodaran, and L. W. Martin
Department of Materials Science and Engineering and Materials Research Laboratory, University of Illinois, Urbana-Champaign, Urbana, IL 61801
*kjambun2@illinois.edu

Domains walls are known to dramatically impact the properties of ferroic materials. In ferroelectrics, such domain structures can have a profound effect on the dielectric, piezoelectric, and pyroelectric susceptibilities. This is due to the reversible displacement of domain walls under external stimuli (e.g., electric field, stress, and temperature) that modifies the relative fraction of the domains and gives rise to an extrinsic contribution to the susceptibilities in addition to the intrinsic response of the polarization. These extrinsic contributions have been theoretically predicted to give rise to large responses near strain- and thickness-induced phase transformations. Such effects are known to contribute significantly to the observed dielectric properties at room temperature. Prior experimental studies, particularly focused on bulk ceramic and polycrystalline film samples, have shown that extrinsic effects contribute nearly 25-50% of the observed room temperature response. Even though 90° domain walls are expected to play a significant role theoretically, quantitative investigation of the effect of 90° domain walls to the susceptibilities has proven difficult to obtain due to the presence of grain boundaries and a mixture of domain wall types in typical ferroelectric samples. Likewise, while dielectric properties are known to be increased due to the presence of such domain walls, the overall effect of domain walls on the temperature susceptibility (i.e., pyroelectric response) is less well understood.

In this work, we present a combination of theoretical and experimental approaches that directly probe the effect of 90° domain walls on the room temperature dielectric and pyroelectric susceptibilities of $PbZr_{0.2}Ti_{0.8}O_3$ thin films and will unequivocally demonstrate how these domain walls can affect give rise to enhanced responses. Using epitaxial thin film strain, we have tuned the domain structure and the resulting properties in $PbZr_{0.2}Ti_{0.8}O_3$ films. Comparisons to polydomain Ginzburg-Landau-Devonshire (GLD) models reveal strong similarities and in-depth experimental analysis enables us to extract the domain wall contribution to the susceptibilities and relate the measured effects to the microscopic details of the domain wall response to the applied stimuli. This work sheds light on the importance of 90° domain walls to the room temperature susceptibilities and provides a realistic comparison between models and experiment.

In order to understand the effect of these domain walls on the physical properties, we use GLD models for polydomain structures to calculate the dielectric and pyroelectric susceptibilities. From such calculations at 300 K for $PbZr_{0.2}Ti_{0.8}O_3$, we see that the film undergoes a transformation from $c \rightarrow c/a/c/a \rightarrow a_1/a_2/a_1/a_2$ domain structures with increasing tensile strain. In the $c/a/c/a$ phase, which possesses 90° domain walls, an increasing fraction of *a*-domains with tensile strain is accompanied by an increase in the out-of-plane dielectric permittivity and the pyroelectric coefficient (Fig. 1). While the domain wall contribution to the dielectric permittivity is always positive, we see a different behavior in the pyroelectric coefficient. Unlike the dielectric response, the effect of domain walls on the pyroelectric properties depends

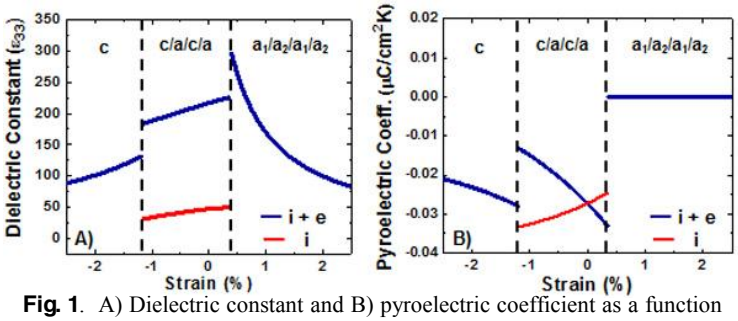

Fig. 1. A) Dielectric constant and B) pyroelectric coefficient as a function of strain for $PbZr_{0.2}Ti_{0.8}O_3$ thin films at 300K showing the extrinsic + intrinsic contributions (blue) and the intrinsic contributions only (red).

on the magnitude of strain. While a tensile strain increases the intrinsic pyroelectric coefficient, a compressive strain decreases it.

In order to investigate the effect of 90° domain walls on the susceptibilities, we have grown 150 nm $PbZr_{0.2}Ti_{0.8}O_3$ / 20 nm $SrRuO_3$ heterostructures on $SrTiO_3$ (001), $DyScO_3$ (110), $TbScO_3$ (110), and $GdScO_3$ (110) substrates using pulsed laser deposition. These substrates provide a lattice mismatch with $PbZr_{0.2}Ti_{0.8}O_3$ that ranges from -0.8 to 0.9% and corresponds to the $c/a/c/a$ domain state. As we increase the lattice mismatch, we can effectively increase the fractions of *a*-domains. Detailed X-ray diffraction studies reveal single-phase, fully epitaxial thin films and off-axis reciprocal space maps about the 103-pseudocubic diffraction condition revealed that the *c*-domain portion of the heterostructures are coherently strained to the underlying substrate in all cases (directly matching the models). X-ray diffraction and piezoresponse force microscopy were used to measure the average domain periodicity and fraction of *a*-domains in these films. These films serve as model systems to observe the domain wall contributions to the dielectric and pyroelectric susceptibilites.

The measured dielectric constants show that the 90° domains do indeed contribute significantly to the permittivity at room temperature and the values match well with the predictions of the GLD model (Fig. 2). Coupled with an independent experimental measurement of the domain fractions and remnant polarization, this enables a direct comparison to microscopic models of domain wall interaction with electric field and enables us to extract the experimentally measured values of force constants for these interactions. The measured pyroelectric coefficients also show good agreement with the predictions of the GLD models. The pyroelectric response, however, shows larger deviations from the GLD model. The non-linearities in the interaction of the domain walls with temperature and the trapped defect charges at domain walls could be important factors in determining the susceptibility to temperature. The measured values of pyroelectric coefficient help us understand the temperature response of ferroelectrics and provides the foundation for the development of a microscopic treatment of domain wall response to changes in temperature.

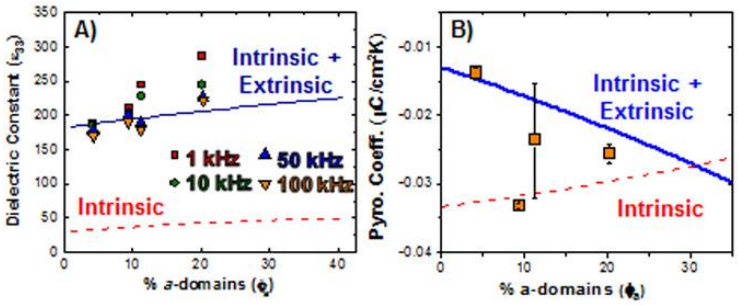

Fig. 2. A) Dielectric constant as a function of percent *a*-domains for $PbZr_{0.2}Ti_{0.8}O_3$ thin films at 300K at various frequencies compared with the predictions of the GLD model. B) Measured pyroelectric coefficient as a function of percent *a*-domains for $PbZr_{0.2}Ti_{0.8}O_3$ thin films compared along with the predictions of the GLD model. The predictions of the GLD model are marked as extrinsic + intrinsic (blue) and intrinsic only (dashed red).

In conclusion, this work offers unique insight into the microscopic coupling between domain walls and external stimuli such as electric field and temperature in ferroelectrics. We have fabricated a model set of epitaxial thin films that closely match polydomain GLD models and have observed the unambiguous contribution of 90° domain walls to response at room temperature. This enables the first realistic comparison to theory and is essential to the optimization of ferroelectric materials for various applications which utilize their susceptibility to electric fields and temperature.

References:

1. J. Karthik, A. R. Damodaran, L. W. Martin, under review at *Phys. Rev. Lett.* (Nov. 2011).
2. J. Karthik, L. W. Martin, *Appl. Phys. Lett.* **99**, 032904 (2011).
3. J. Karthik, L. W. Martin, *Phys. Rev. B* **84**, 024102 (2011).

Heating-up and cooling-down molecular-dynamics simulations of 90-degree domain structures in $PbTiO_3$

Takeshi Nishimatsu[1], Kenta Aoyagi[1], Takanori Kiguchi[1], Toyohiko J. Konno[1], Yoshiyuki Kawazoe[1],Anil Kumar[2,3], Umesh V. Waghmare[2]

[1]Institute for Materials Research (IMR), Tohoku University, Sendai 980-8577, Japan
[2]Theoretical Sciences Unit, Jawaharlal Nehru Centre for Advanced Scienti c Research (JNCASR), Jakkur, Bangalore, 560 064, India
[3]Department of Physics and Astronomy, Rutgers University, 136 Frelinghuysen Road, Piscataway, NJ 08544-8019

While lead titanate $PbTiO_3$ has wide-range of applications, dynamics of domain structures and their temperature dependence has not been understood due to the di culty of *in situ* experiments. Moreover, it makes experiments rather di cult that the sample needs to be heated over its transition temperature $T_C = 763$ K and this heating process leads to the evaporation of Pb ions and changes the composition of the sample[1].

Here, heating-up and cooling-down molecular-dynamics (MD) simulations of $PbTiO_3$ are performed with our original fast MD code named `feram` (`http://loto.sourceforge.net/feram/`)[2]. The code is based on rst-principles e ective Hamiltonian[3, 4, 5] and the set of parameters of the Hamiltonian is transported from [6]. One of the advantages of MD simulations compared to Monte Carlo simulations is the ability to simulate time-dependent dynamical phenomena, e.g. the MD simulator can perform heating-up and cooling-down simulations.

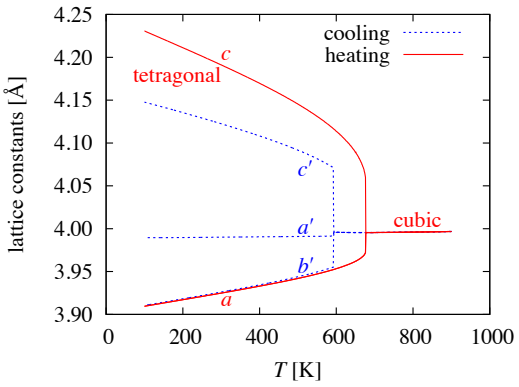

Figure 1: (Color online) Simulated temperature dependence of lattice constants of $PbTiO_3$ in heating-up (red solid lines) and cooling-down (blue dashed lines) molecular-dynamics simulations.

Temperature is kept constant in each temperature step in the canonical ensemble using the Nosé-Poincaré thermostat. This simplectic thermostat is so e cient that we can set the time step to $t = 2$ fs. In our present MD simulations, we thermalize the system for 20,000 time steps, after which we average the properties for 20,000 time steps. We used a supercell of system size $N = L_x \times L_y \times L_z = 32 \times 32 \times 32$ and small temperature steps in heating-up (+1 K/step) and cooling-down (−1 K/step) simulations. The heating-up simulation from 100 K to 900 K is started from an z-polarized initial con guration generated randomly. The cooling-down one from 900 K to 100 K is started from random paraelectric initial con guration. Temperature dependence of averaged lattice constants is shown in Fig. 1. While the tetragonal-to-cubic ferroelectric-to-paraelectric phase transition is clearly observed in the heating-up simulation at 677 K, strange behaviors in lattice constants is found with transition temperature 592 K in the cooling-down simulation. The averaged value 634 K of these two transition temperature is slightly lower but in good agreement with the experimental value $T_C = 763$ K.

By taking a snapshot of dipoles in the supercell as shown in Fig. 3, we found that this is due to a 90° domain structure, though 4 unit cell = 1.6 nm of the domain size is much smaller than experimentally observed ones 50–200 nm[7]. Each domain may have the $a = b < c$ tetragonal structure of $PbTiO_3$, but average in whole crystal gives smaller c' than c and larger a' than a. The lattice constant b' have almost same values to a, because polar directions of two kind of domains are perpendicular to the b'-axis. It should be note that this 90° domain structure is frozen and found in MD simulations in bulk under in nite periodic boundary condition (PBC), not in thin lms. Under PBC, there is no depolarization eld inside the bulk. Moreover, this domain structure can be easily reproduced in cooling-down

simulations from any random paraelectric initial con gurations and any seeds for the pseudo random number generator. We have never seen such strange behavior in bulk $BaTiO_3$ simulations[2, 8].

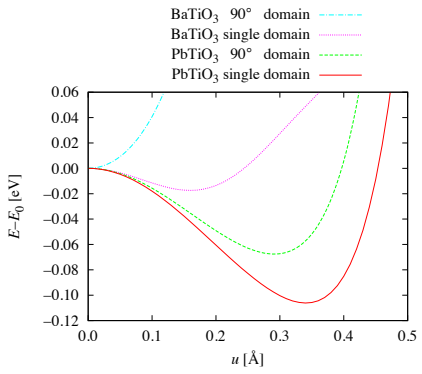

Figure 2: (Color online) Calculated total energy surfaces.

To understand the reason of stability of the 90° domain structure even in bulk $PbTiO_3$, we compared "total energy surfaces" between single and 90° domain structures. The total energy surface of single domain structure with [001] polarization is same as that de ned in Ref. [2, 8]. For the total energy surface of 90° domain structure, we sample a snapshot of the supercell at 300K, which is shown in Fig. 3. Calculated total energy surfaces of single and 90° domain structures for $PbTiO_3$ are plotted in Fig. 2 with solid and dashed lines, respectively. For comparison, those for $BaTiO_3$ are also plotted assuming the same 90° domain structure by using the set of parameters listed in [8]. It is contrastive that while the 90° domain structure of $PbTiO_3$ has $u \neq 0$ minimum, that of $BaTiO_3$ does not. It is why the 90° domain structures can be found in simple cooling-down simulations in $PbTiO_3$, but cannot in $BaTiO_3$. To simulate 90° domains of $BaTiO_3$, more realistic conditions for simulations such as larger system sizes, depolarization eld coming from nite system or some defects may be required.

References

[1] R. Gerson: J. Appl. Phys. **31** (1960) 188.

[2] T. Nishimatsu, U. V. Waghmare, Y. Kawazoe and D. Vanderbilt: Phys. Rev. B **78** (2008) 104104.

[3] R. D. King-Smith and D. Vanderbilt: Phys. Rev. B **49** (1994) 5828.

[4] W. Zhong, D. Vanderbilt and K. M. Rabe: Phys. Rev. B **52** (1995) 6301.

[5] U. V. Waghmare, E. J. Cockayne and B. P. Burton: Ferroelectrics **291** (2003) 187.

[6] U. V. Waghmare and K. M. Rabe: Phys. Rev. B **55** (1997) 6161.

[7] K. Aoyagi, T. Kiguchi, Y. Ehara, T. Yamada, H. Funakubo and T. J. Konno: Sci. Technol. Adv. Mater. **12** (2011) 034403.

[8] T. Nishimatsu, M. Iwamoto, Y. Kawazoe and U. V. Waghmare: Phys. Rev. B **82** (2010) 134106.

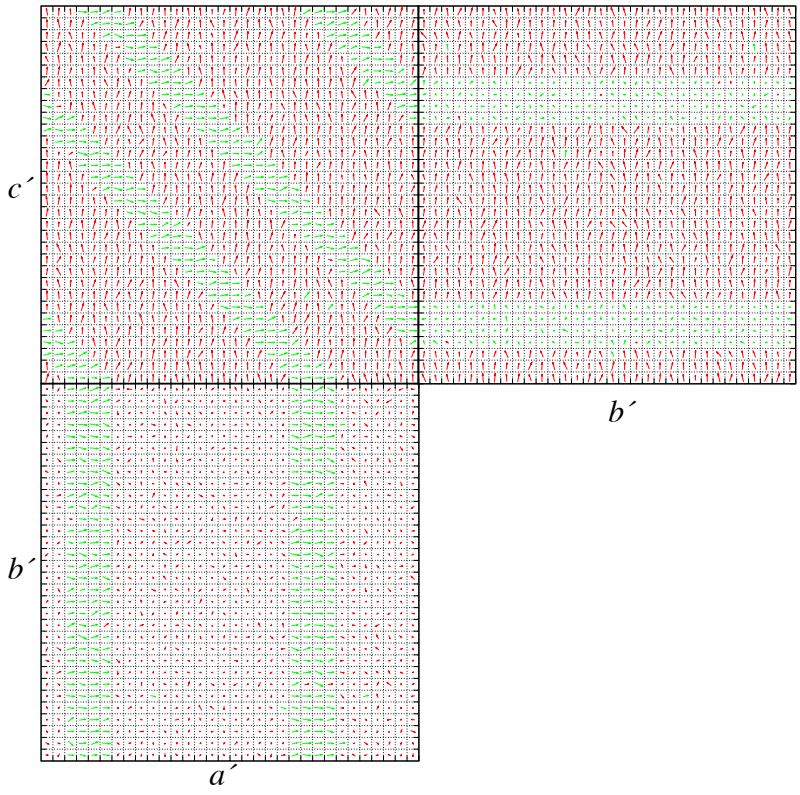

Figure 3: (Color online) Snapshot of three "sides" of the $32 \times 32 \times 32$ supercell at $T = 300$K in a cooling-down simulation of $PbTiO_3$. Dipole moments of each site are projected onto the side planes and indicated with arrows. Dipoles of $u_z > 0.2$Å are indicated with red color. Dipoles of $u_z \leq 0.2$Å are indicated with green. Crystalline directions are indicated with a', b', and c' as indicated in Fig. 1.

Stripe domain evolution in ultrathin $BiFeO_3$ films grown on $TbScO_3(110)$

Christian M. Schlepütz[1], Yongsoo Yang[2], Carolina Adamo[3], Darrell G. Schlom[3] and Roy Clarke[2]

[1] *X-ray Science Division, Argonne National Laboratory, Argonne, IL 60439, USA*
[2] *Department of Physics, University of Michigan, Ann Arbor, MI 48109, USA*
[3] *Department of Materials Science and Engineering, Cornell University, Ithaca, NY 14853, USA*

We report on x-ray scattering studies on thin films of bismuth ferrite ($BiFeO_3$: BFO) grown heteroepitaxially on (110)-oriented orthorhombic $TbScO_3$ (TSO) perovskite substrates. Folkman et. al. [Appl. Phys. Lett. 94, 251911 (2009)] have observed the formation of ordered BFO stripe domains for thick films (200-800 nm) grown on TSO. Our work confirms the existence of such domains also for very thin films (4 – 50 unit cells) on TSO(110), and shows that the lateral domain sizes are strongly thickness-dependent.

The presence of these ordered domains manifests itself in the appearance of satellite peaks along only one of the in-plane directions and close to the film Bragg peaks. By using a pixel area detector, on can obtain scattering volume data sets with a single reciprocal space scan [Schlepütz et. al., J. Appl. Crystallogr. 44, 73 (2011)], which can be processed to yield 3-dimensional reciprocal space maps (RSMs).
Figure 1 shows the intensity distribution in these RSMs as a function of the K- and L-coordinates around the (404) peak [measured in surface coordinates of TSO(110), which corresponds to the (202) in pseudo-cubic coordinates] for four different film thicknesses. The satellite peaks due to the domain formation are clearly visible up to the third order for most films, indicative of a very narrow domain size distribution. The domain size evolution as a function of thickness is shown in Figure 2.

So far, it remains an open question what the exact structural nature of these domains is in the case of these very thin films. Specifically, it is unclear, whether the monoclinic rhombohedral-like structure observed for the thicker films is already formed in the thin film limit, or if the strong substrate interaction results in yet another phase. The RSMs in Figure 1 show the transition from a pure satellite signal for the 4 unit cell (UC) thick film to a much more feature-rich diffraction intensity distribution for the sample with 50 UCs of BFO. This may be indicative of a phase transition occurring in the film structure. We are presently conducting additional diffraction measurements to address these questions in more detail and to add information for a few more intermediate film thicknesses, which will be presented during the meeting.

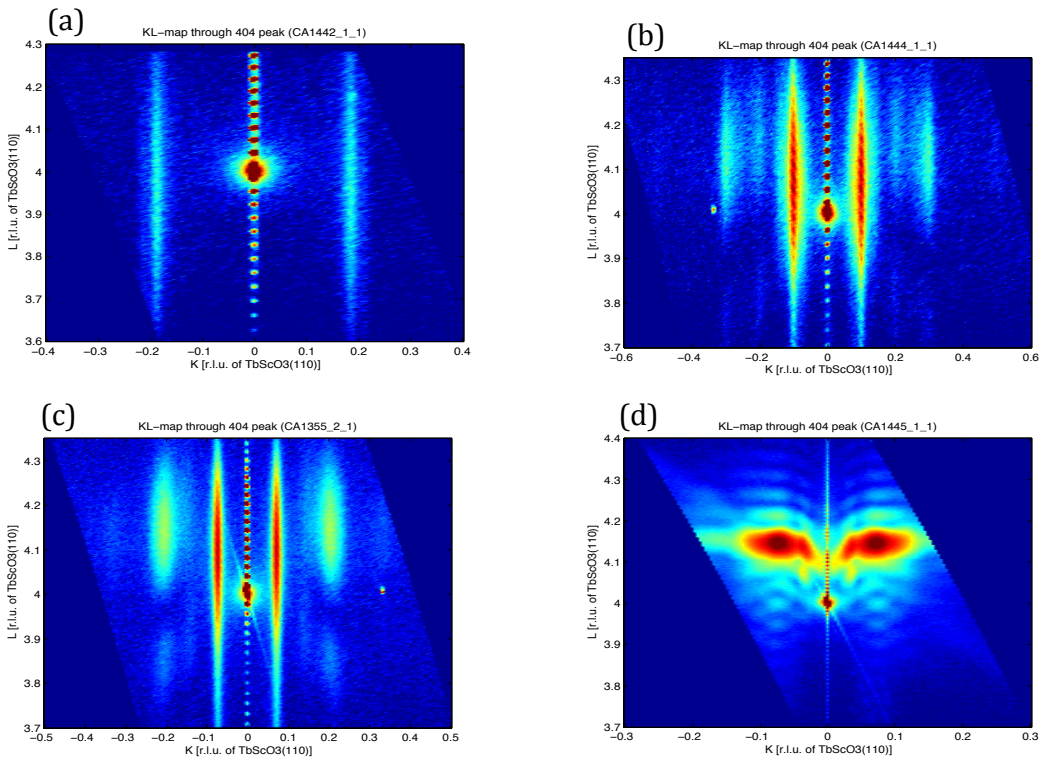

Figure 1: Reciprocal space maps of the HL-plane around the (404) reflection for film thicknesses of (a) 4 UC, (b) 8 UC, (c) 10 UC, and (d) 50 UC.

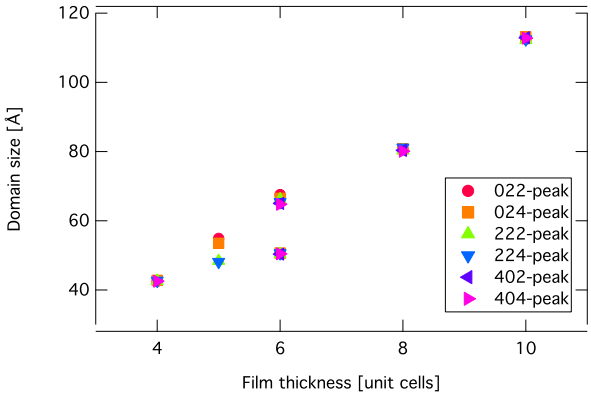

Figure 2: BFO stripe domain widths as a function of film thickness, calculated based on the satellite peak spacing measurements around several diffraction peaks.

Enhanced Electromechanical Response of Ferroelectrics Due to Charged Domain Walls

Tomas Sluka,* Alexander K. Tagantsev, Dragan Damjanovic, Maxim Gureev, and Nava Setter
Ceramics Laboratory, Swiss Federal Institute of Technology, Lausanne, CH-1015 Switzerland
(Dated: November 29, 2011)

Charged domain-walls in ferroelectrics are considered inactive with regards to the piezoelectric response and therefore are largely ignored in the search for high performance ferroelectrics. In direct contrast, we demonstrate here a mechanism that leads to a strong enhancement of the dielectric and piezoelectric properties in ferroelectrics with increasing density of charged domain walls.

In the past, it has been found that in the classical lead-free perovskite ferroelectric $BaTiO_3$, a high density of domain walls with spacing in the micrometer range can result in up to a four-fold enhancement of functional properties [1], while it was established that the enhancement is not associated with the domain wall motion. However, the body of available experimental data is insufficient to clearly relate the observed effects to features of the domain patterns in the samples. This experimental activity has drawn much attention by theorists [2–6] who were unable to explain the experimental observations unless unrealistic assumptions were taken. Thus, despite intriguing experimental findings, the future of fine-scale domain patterns as systems with enhanced electromechanical properties remains obscure.

In the experimental reports on enhanced properties due to engineered domain structures, the authors recognized that head-to-head and tail-to-tail domain configurations, such as those shown in Fig. 1**b**, must have been formed during the frustrated poling process of $BaTiO_3$ [7, 8]. However, the significance of this formation of charged domain walls passed entirely un-noticed.

Here we show an analysis, based on Landau-Ginzburg-Devonsire theory and the theory of semiconductors, which establishes that the dielectric and piezoelectric response of such systems with charged domain-walls increase strongly upon the reduction of the domain period. This is expected to happen under two conditions: (i) the ferroelectric phase transition in the material should be of first order and (ii) a strong dielectric anisotropy must exist.

We show that an incomplete compensation of bound polarization charge at these walls creates a stable built-in depolarizing field across each domain (Fig. 1) leading to increased electromechanical response (Fig. 2) which is qualitatively in good agreement with experimental observations of domain wall density effects on macroscopic properties of $[111]_c$ poled $BaTiO_3$ crystals [1, 7–9]. Our model clarifies a long-standing unexplained effect of domain wall density on macroscopic properties of domain engineered ferroelectrics.

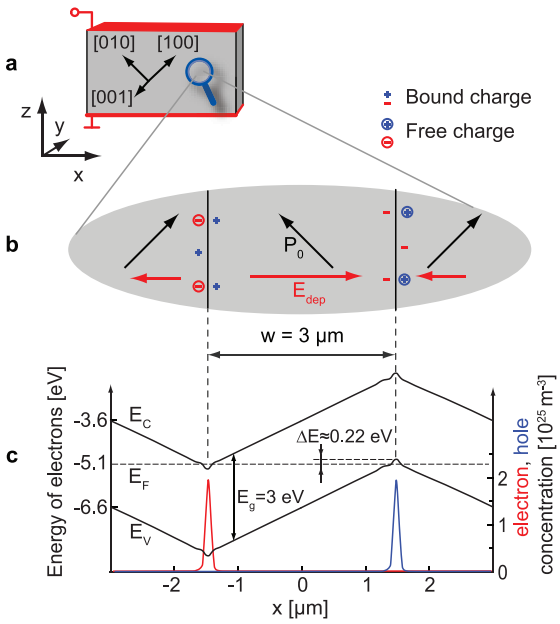

FIG. 1: **Free charge concentration and band bending in $(110)_c$ plate of a tetragonal ferroelectric with charged domain walls.** **a**, An electroded $(110)_c$ plate of $BaTiO_3$. **b**, A periodic structure of charged 90° domain walls where bound polarization charge (+, -) induced by divergence of polarization, P_0, is almost perfectly compensated by free charge ($\oplus$, $\ominus$) while the imperfection of compensation creates built-in depolarizing field E_{dep}. **c**, Phase field simulation-calculated band bending induced by E_{dep}. The bending causes the edges of the conduction E_C or valence E_V bands to approach the Fermi level E_F where high concentration of free electrons or holes are generated and become available for compensation of the bound charge.

*Electronic address: tomas.sluka@epfl.ch

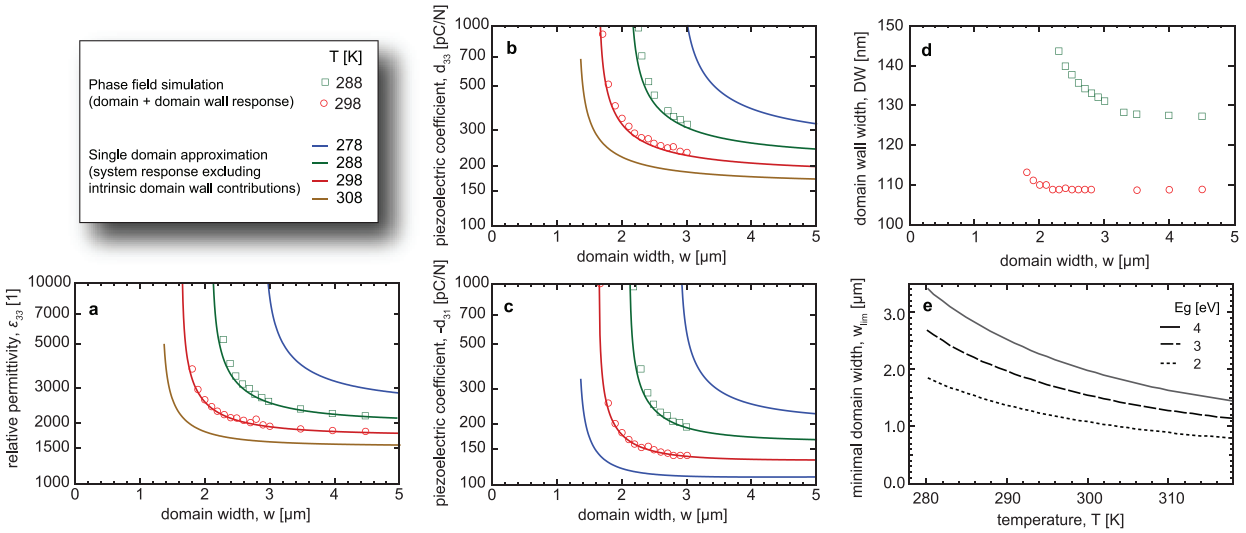

FIG. 2: **Enhancement of dielectric and piezoelectric properties against domain size in a** $(110)_c$ **plate of** $BaTiO_3$**with charged domain walls.** Permittivity ε_{33}, **c**, and piezoelectric coefficients d_{33}, **a**, and d_{31}, **b**, are plotted as a function of domain width w. The solid lines represent the inner response of a domain which is exposed to built-in depolarizing field due to imperfectly compensated charged domain walls. Circles and rectangles represent phase field simulation results that include intrinsic contributions of charged domain walls at temperatures 288 and 298 K. Domain wall width DW against domain width w, **d**, shows small domain wall broadening when critical domain width is approached. **e**, The critical (minimal) domain width w_{lim} against temperature T is shown for bandgap $E_g = 2, 3, 4$ eV.

[1] Wada, S., Yako, K., Kakemoto, H., Tsurumi, T., and Kiguchi, T. Enhanced piezoelectric properties of barium titanate single crystals with different engineered-domain sizes. *Journal of Applied Physics* **98**(1), 014109 (2005).

[2] Ahluwalia, R., Lookman, T., Saxena, A., and Cao, W. W. Domain-size dependence of piezoelectric properties of ferroelectrics. *Physical Review B* **72**(1) (2005).

[3] Rao, W. F. and Wang, Y. U. Domain wall broadening mechanism for domain size effect of enhanced piezoelectricity in crystallographically engineered ferroelectric single crystals. *Applied Physics Letters* **90**(4) (2007).

[4] Hlinka, J., Ondrejkovic, P., and Marton, P. The piezoelectric response of nanotwinned $BaTiO_3$. *Nanotechnology* **20**(10) (2009).

[5] Xiang, Y., Zhang, R., and Cao, W. W. Piezoelectric properties of domain engineered barium titanate single crystals with different volume fractions of domain walls. *Journal of Applied Physics* **106**(6) (2009).

[6] Sluka, T., Damjanovic, D., Tagantsev, A., Colla, E., Mtebwa, M., and Setter, N. The stress-assisted enhancement of piezoelectric properties due to mechanically incompatible domain structures in $BaTiO_3$, (2010). Times Cited: 0 IEEE International Symposium on the Applications of Ferroelectrics (ISAF) AUG 09-12, 2010 Edinburgh, SCOTLAND.

[7] Wada, S. and Tsurumi, T. Enhanced piezoelectricity of barium titanate single crystals with engineered domain configuration. *British Ceramic Transactions* **103**(2), 93–96 (2004).

[8] Wada, S., Muraishi, T., Yokoh, K., Yako, K., Kamemoto, H., and Tsurumi, T. Domain wall engineering in lead-free piezoelectric crystals. *Ferroelectrics* **355**(1), 37 – 49 (2007).

[9] Wada, S., Yako, K., Kakemoto, H., Erhart, J., and Tsurumi, T. Enhanced piezoelectric property of $BaTiO_3$single crystals with the different domain sizes. *Electroceramics in Japan VII* **269**, 19–22 (2004).

Modeling Domain Dynamics in Single- and Polycrystalline Ferroelectrics

Zizhao Zhao, J. Blendell, K. Bowman, R. Edwin García

School of Materials Engineering, Purdue University,

West Lafayette, IN 47907 USA

December 1, 2011

Abstract

Ferroelectric materials are extensively used in a variety of electromechanical applications, owing their performance to their underlying piezoelectric properties. Current challenges include an ever increasing demand of actuation strain output, a less pronounced ferreoelctric and mechanical fatigue. In this context, the effect of bipolar, sesquipolar, and unipolar electric load is studied through a numerical implementation of Landau-Ginzburg-Devonshire phenomenological theory. Simulation results prove that three polarization populations, represented in terms of four Gaussian polarization distributions, describe the microscopic switching mechanisms of ferroelectric domains. Results also show that in the sesquipolar regime, tensile stresses are minimized by 33% and compressive stress minimized by 38%, while maximum strain output decreases by only 1%, Furthermore, an analytical and numerical method is developed to investigate the effect of compressive mechanical loads on the macroscopic hysteretic response of single-crystal and polycrystalline ferroelectric materials. Stress analyses show that the domain mobility and remnant polarization show an exponential dependence to the externally applied mechanical stress in good agreement with experimental observations. Furthermore, numerical simulations for untextured polycrystals predict that the built-in electric field increases quadratically as the increase of applied stress fields, also in agreement with experiments. Such a trend is a result of thermal expansion and piezoelectric contributions for small compressive stresses, and a result of electrostrictive contributions and stress-induced phase transformations for large stresses.

Electronic structure of LaO doped $SrTiO_3$

R. Adhikari, Huaxiang Fu

Department of Physics, University of Arkansas, Fayetteville, AR 72701 USA

Abstract

By using density functional calculations within the LDA+U formalism we have investigated the electronic properties of LaO δ-doped $SrTiO_3$. We found that the system is metallic, with Fermi energy located inside the conduction bands. Our band structure calculations show that different conduction bands near the Fermi energy have very different dispersions. The bands with large dispersions produce high-mobility electrons on the xy plane, while other bands with small dispersions generate low-mobility electrons. The theoretical results are consistent with, and provide explanations for, the phenomenon observed in experiments. We have further examined the wave functions close to the Fermi energy. We found that the conduction states have very different localizations along the direction perpendicular to the doped plane, which include interfacial, bulk, and mixed states of Ti d-orbitals. Finally, we have also applied the inplane strain and determined how the electron states are affected by strain.

First-principles study of structural and vibrational properties of $SrZrO_3$

Safari Amisi[1,2] , Eric Bousquet[1,3] , Karume Katcho[2] , and Philippe Ghosez[1]
[1] Physique Théorique des Matériaux, Université de Liège, B-4000 Sart Tilman, Belgium
[2] Département de Physique-Technologie, ISP/Bukavu, RD Congo and
[3]Department of Materials, ETH Zurich, Wolfgang-Pauli-Strasse 27, CH-8093 Zurich, Switzerland

Argonne, USA, 29/01 – 01/02/2012

Abstract:
Using first-principles calculations, we investigate the electronic, structural and vibrational properties of SrZrO3. We start from the high-symmetry cubic perovskite phase, for which the phonon dispersion curves are reported. We point out the coexistence of antiferrodistortive instabilities at the R and M zone-boundary points and a ferroelectric instability at the zone center.
We show that the strong antiferrodistortive motions suppress ferroelectricity and are responsible for the orthorhombic ground state in a way similar to what was previously reported for CaTiO3. The structural properties of the intermediate phases and of the orthorhombic Pnma ground-state phase are reported and, for the latter, an assignment of IR and Raman zone-center phonon modes is proposed. The main features of the ferroelectric instability are also discussed and we show that a ferroelectric ground state can even be induced by strain engineering.

Keywords: Ab initio calculations, Lattice dynamics, Ferroelectrics, Phonons modes.

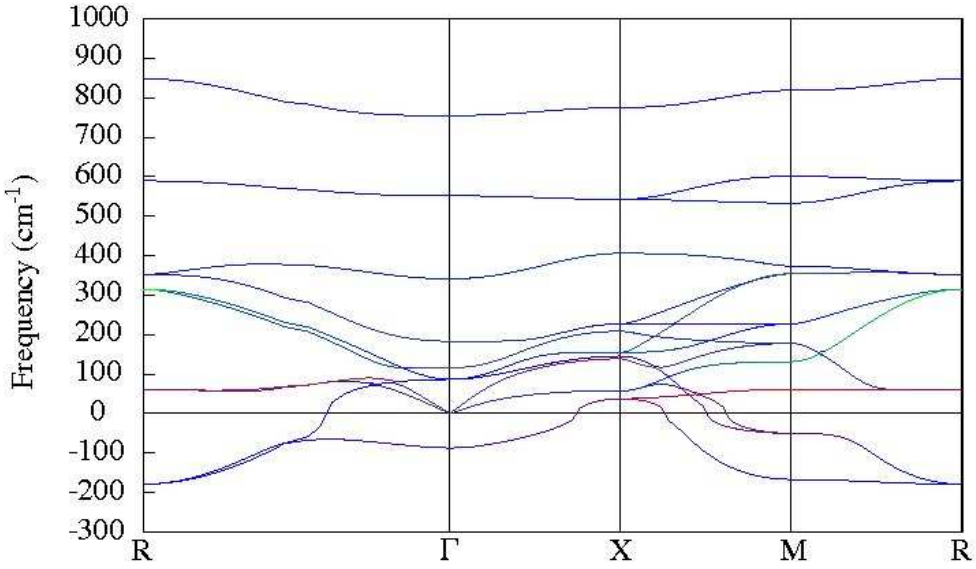

Calculated phonon dispersion curves of cubic $SrZrO_3$ along the path R-Γ-X-M-R of the cubic Brillouin zone.

Phase-field modeling of resistance degradation and I-V characteristics in perovskite-based ferroelectric oxides

Y. Cao, S. Bhattacharya, C. A. Randall, and L.Q. Chen

Department of Materials Science and Engineering, Penn State University, University Park, PA 16802, United States

Perovskite based material such as strontium titanate ($SrTiO_3$) and barium titanate ($BaTiO_3$) have been widely utilized in a variety of electronic devices such as sensors, actuators and capacitors. [1] In semiconductor industry, modern technology has made thousands of capacitors highly integrated in even smaller electronic devices, and the dielectric layers in multilayer ceramic capacitors (MLCC) thinner for high capacitance. Therefore a higher electric field is expected under constant voltage load. As a result, the reliability of ceramic capacitors of reduced sizes has become a major concern. Under high dc field stress, the long-term resistance degradation, i.e. increasing leakage current under a constant voltage stress will eventually occur and the lead to the breakdown of the capacitor.

Dielectric capacitors in real service usually take tens of years before the degradation happens. To speed up the test, the highly accelerated lifetime tests (HALTS) have been widely used. It has been well understood that the defect chemistry and defect transport play an important role in the resistance degradation behavior. Baiatu and Waser et al. studied the electrocoloration of Fe-doped $SrTiO_3$ single crystal and compared them with the numerical simulation showing the oxygen vacancy migration as a key mechanism to the degradation. [2] A small adiabatic polaron hopping conduction has also been suggested as possible explanation to the degradation phenomenon in both $SrTiO_3$ and PMN-PT compound [3, 4]. On the other hand, several models have been proposed to investigate into the problem. In Waser's well accepted demixing model [5], an increase of leakage current is attributed to the oxygen vacancy segregation near cathode and the compensating charge from electrons $n \approx 2[V_O^{\bullet\bullet}]$ in cathode region. Meyer et. al. further studied the leakage current evolution in $Ba_{0.3}Sr_{0.7}TiO_3$ by taking into consideration the effect of metal electrode acting as blocking barriers for oxygen vacancy and as an ideal Schottky contact for free electron exchange between electrodes and thin film. [6]

Although a number of theoretical and experimental works have been done in the study of degradation mechanism, almost all the works are conducted at elevated temperature (150^{o}C or higher). On the other hand, the capacitors in-service are working at much lower temperature in the ferroelectric state with complex domain structures. It is reasonable to expect that the polarization and the associated electrostrictive and piezoelectric induced strains have a significant influence on the degradation. Therefore the degradation behavior and mechanism for dielectric capacitors obtained in HALTS may not be representative for ferroelectric materials such as $BaTiO_3$ at room temperature because the polarization contribution is missing.

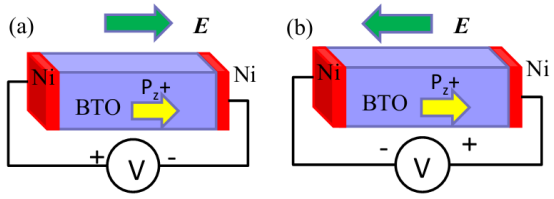

FIG.1. Schematic plot of single domain BaTiO3 under forward load (a) and reverse load (b)

In this work, we developed a computational model based on phase-field approach as well as thermodynamic and transport theories to study the resistance degradation behavior of single crystal $BaTiO_3$ at room temperature with artificially assigned single domain in terms of defect migration, polarization change, space charge distribution and current density evolution. The evolutions of leakage current with time under both forward and reverse dc load have been studied and compared with each other.

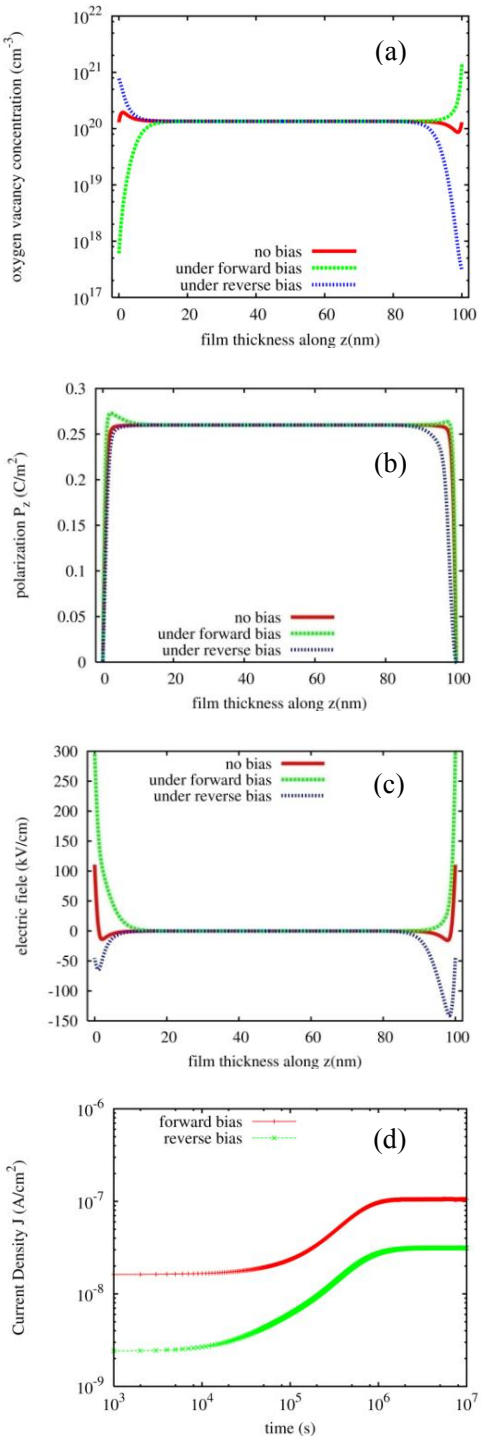

FIG. 2. Evolution of (a) oxygen vacancy, (b) polarization, (c) electric field and (d) current density under forward and reverse bias in $BaTiO_3$ single crystal of 100 nm thickness assuming (001) single tetragonal domain under 0.1V bias and at room temperature (25^{o}C)

The I-V characteristics of single crystal $BaTiO_3$ have also been investigated and a non-linear I-V curve for $BaTiO_3$ single crystal at different degradation stage indicate the possibility of electron trapping due to oxygen vacancy segregation near the electrode. Our simulation results provide some insight in the study of resistance degradation phenomenon in ferroelectric materials.

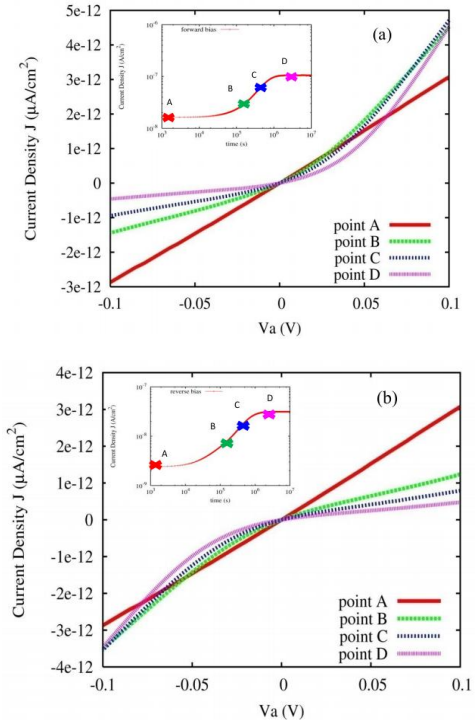

FIG. 3. I-V characteristics of $BaTiO_3$ single crystal at different degradation stages under forward load (a) and reverse load (b)

References:

[1] O. Auciello et. al., Phys Today **51**, 22 (1998)

[2] R. Waser et. Al., J. Am. Ceram. Soc. **73**, 1654, (1990)

[3] W. Liu et. al. J. J. Appl Phys, **48**, 051404, (2009)

[4] S. Zhao et. al., J. Appl Phys, **105**, 053705, (2009)

[5] R. Waser et. Al., J. Am. Ceram. Soc. **73**, 1663, (1990)

[6] R. Meyer et. al., Appl. Phys. Lett. **86**, 112904 (2005)

Dynamics of Relaxation Times in the Three-Dimensional Ising Model

R. Grigalaitis[1], S. Lapinskas[1], J. Banys[1] and E. E. Tornau[2]

[1] *Faculty of Physics, Vilnius University, Sauletekio 9, LT-10222 Vilnius, Lithuania*

[2] *Semiconductor Physics Institute, Center for Physical Sciences and Technology, Gostauto 11, LT-01108 Vilnius, Lithuania.*

The static critical properties of 3D Ising model are well-known, and the corresponding critical exponents are numerically well estimated both above and below the phase transition point. The dependence of the dynamical properties of this model on finite size effects was studied numerically in [1-3] mostly above the phase transition point. However the most interesting results are expected to occur below the phase transition point, where the response functions and the relaxation times of the magnetization [4] are extremely sensitive to finite-size effects. Thus, the problems dealing with occurrence of the, so-called, "ergodic relaxation time"[1], which is related to magnetization reversals of a spin cluster below the phase transition point, might still be of considerable interest.

Here we present the results of a relaxation dynamics performed by Monte Carlo calculations of three-dimensional polar nanoclusters consisting of Ising-type spins. Main attention is paid to the studies of the relaxation time at $T<T_c=T_c(L\to\infty)$, where L the linear size of a cube-cluster. Both periodic (PBC) and open (OBC) boundary conditions have been used in the calculations. To explore how the type of dynamics affects the dynamic properties of the Ising model we used two types of spin flip (or particle jump) dynamics for their mutual comparison. The first type considered here is usual Glauber-type dynamics, where spin flip probability $\omega(E_{\text{initial}} \to E_{\text{final}}) = 1/[1 + \exp(\Delta E/k_BT)]$ depends on a difference of energies after (E_{final}) and before (E_{initial}) the local change of state. The second type is related to the fact that in some cases the particle has no *a priori* knowledge of its final energy - the depth of minimum to which it is hopping. Then it is reasonable to assume the jump probability to be proportional just to $\exp(-E_{\text{initial}}/k_BT)$, since the final energy might be important only when the particle overcomes the barrier, i.e. for the next jump of the particle. We calculated the time-delayed autocorrelation function of magnetization in a following form: $\psi(t) = \frac{d}{dt}\left\langle\left(\sigma(\text{t}) - \langle\sigma\rangle\right)\left(\sigma(0) - \langle\sigma\rangle\right)\right\rangle$, where $\langle\sigma\rangle$ denotes spin average and $\sigma(t)$ time-dependent value of the spin variable. We registered time dependence of spin operator and its variation over a chosen time-span which is equal to the maximum chosen correlation delay $t_{\max}$.

Temperature dependence of the autocorrelation functions above and below $T_c(L)$ have the forms presented in Fig.1. Characteristic long time behavior is related to ergodic relaxation time τ_e and is caused by flips of clusters. The intrinsic relaxation time τ_e is probably caused by the short range fluctuations inside the cluster. We have found that below the phase transition temperature $T_c(L)$ the obtained autocorrelation function (3) is best described by 4 single exponential decaying functions ($\exp(-t/\tau)$) superposition. The function with longest relaxation time describes the ergodic relaxation process quite well, while the other ones – correspond to intrinsic relaxation time.

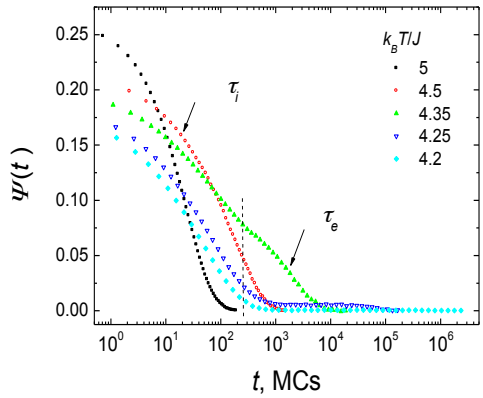

Fig. 1 The autocorrelation decay function for L = 20 at different temperatures. The dotted line shows the appearance of ergodic relaxation time.

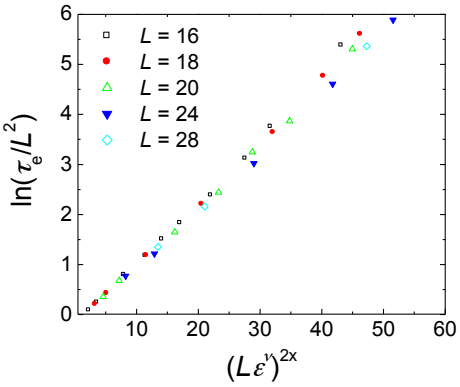

Fig. 2 The linearization of $\ln(\tau_e/L^z)$ curves (z=2) using x^{2k} dependence.

Below the phase transition point the ergodic relaxation time scales with the scaling argument $x = L\varepsilon^{\nu}$, where $\varepsilon = 1 - T/Tc$ and ν is the critical exponent of the correlation length ξ. the value of ν for 3D Ising model was numerically found to be between 0.62 and 0.64 (see e.g.[3]). Assuming $z = 2$ and using PBC we obtain that τ_e is proportional to $L^z \exp(const\ x^2)$, i.e. the same result which was obtained by Binder [1,2] from calculations of interface free energy between two coexisting magnetization domains. At the same time the function $\ln(L^{-z}\ \tau_e)$ obtained using OBC demonstrates non-linearity with respect to x^2 and linearizes only with respect to x^{2k} with k = 1.6. It should be noted that our results does not depend on a type of dynamics used. The scaling results are summarized in Fig. 2. It should be noted that we performed also a indirect calculation of scaling behavior of ergodic relaxation time proposed by Binder [1,2] and based on the calculation of interface tension from magnetization distribution curves. The obtained results confirms our previous findings quite well.

References

[1] K. Binder and D. W. Heermann, Monte Carlo simulations in statistical physics (Springer-Verlag, Berlin, Heidelberg, 1988, p. 42-54.
[2] K. Binder, Phys. Rev. A 25, 1699 (1982).
[3] S. Wansleben and D. P. Landau, Phys. Rev. B 43, 6006 (1991).
[4] W. Koch, V. Dohm, and D. Stauffer, Phys. Rev. Lett. 77, 1789 (1996).

Terahertz Frequency Dynamics of Ferrolectric Nanowires

Ryan Herchig[1], K. Schultz[2], K. McCash[1], Inna Ponomareva[1]
[1]*Department of Physics, University of South Florida, Tampa, Florida 33620, USA*
[2]*Department of Physics and Astronomy, Carthage College, Kenosha, Wisconsin 53140, USA*
e-mail: rch@mail.usf.edu

Ferroelectric nanowires are exceptional candidates for nanoscale multifunctional devices thanks to their many unique properties, such as existence of electric polarization at nanoscale, multiple dipole patterns, strong dependence of electrical properties on the boundary and growth conditions [1–3]. Many of such features are unique to nanoscale and could potentially lead to development of new or drastically improved device concepts. For example, such nanowires are very promising for ultrahigh density nonvolatile memory, ultrafast sensing, and efficient energy converting devices.

Here we design and conduct computational experiments to reveal the unique properties of ferroelectric nanowires in the terahertz frequency range. This frequency range is underutilized nowadays and is often called "THz gap" due to very limited applications that take advantage of this part of the electromagnetic spectrum [4]. Ferroelectric nanowires are very promising candidates for developing multifucntional applications in the "THz gap" since the intrinsic dynamics of such nanowires is in the THz frequency range. In our computational experiments we subject two ferroelectric nanowires made of $Pb(Zr_{0.4}Ti_{0.6})O_3$ alloy to THz frequency radiation.

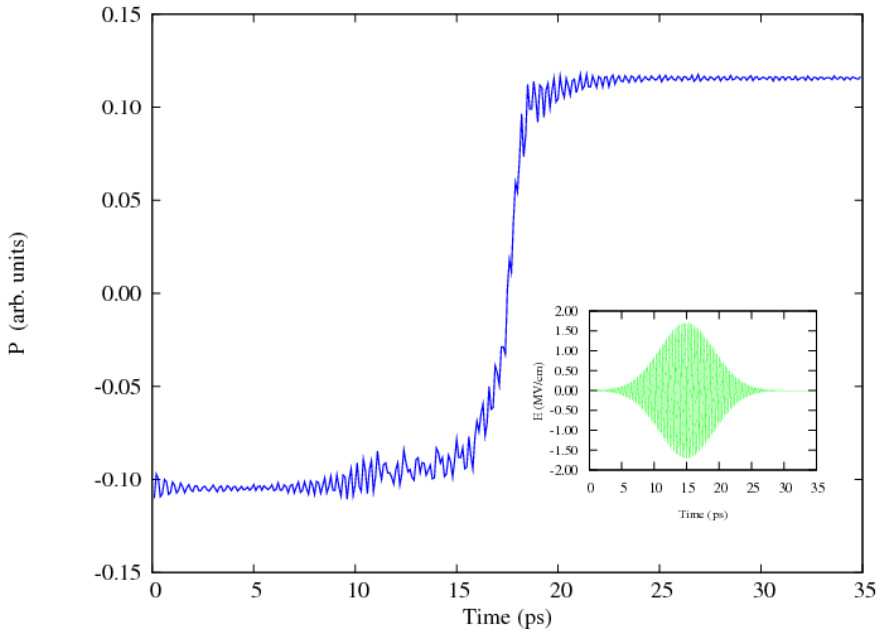

FIG. 1: The polarization P along the nanowire axis as a function of time in response to the THz pulse shown in the inset.

We consider both continuous-wave THz radiation and THz pulses of different shapes. Technically the study is carried out in the frame of classical molecular dynamics [5] with

the force field derived from first-principles-based effective Hamiltonian [6]. The nanowire is under open circuit boundary conditions and, therefore, at equilibrium develops polarization along the axial direction [7]. The interaction of a nanowire with THz radiation is modeled via the term that couples electric field with individual electric dipoles in the nanowire. The nanowires have square cross section of 4.8 and 6.4 nm^2. To simulate continuous-wave radiation we apply THz *ac* electric field with the amplitudes in the range 0.05 - 2.0 MV/cm and with the frequencies of 1.0 - 5.0 THz. The THz pulses are modeled via Gaussian envelopes (see inset to figure).

We found that some particular THz pulses lead to polarization reversal that could be used in remote THz switchers, while some other pulses could induce metastable nanodomain configuration. Example of polarization reversal induced by a THz pulse is given in the figure. The corresponding pulse is shown in the inset to the figure. Interestingly the polarization reversal is ultrafast and completes within 20 picoseconds. The possibility to control nanowire temperature via application of THz radiation is also explored and the energy dissipation mechanism is investigated at an atomistic level.

Acknowledgments: The present work is supported by the U.S. Department of Energy, Office of Basic Energy Sciences, Division of Materials Sciences and Engineering under award DE-SC0005245 (THz continuous-wave radiation modeling) and by the Army Research Office under contract 57787-EL.

---

[1] B.-K. Lai, I. Ponomareva, I. Naumov, I. Kornev, H. Fu, L. Bellaiche, and G. Salamo, Phys. Rev. Lett. **96**, 137602 (2006).

[2] I. Ponomareva and L. Bellaiche, Phys. Rev. B **74**, 064102 (2006).

[3] P. Rorvik, T. Grande, and M.-A. Einarsrud, Adv. Materials **23**, 4007 (2011).

[4] Y.-S. Lee, *Principles of Terahertz Science and Technology* (Springer Science, 2009).

[5] D. Rapaport, *The Art of Molecular Dynamics Simulation* (Cambridge University Press, 2001).

[6] L. Bellaiche, A. Garcia, and D. Vanderbilt, Phys. Rev. Lett. **84**, 5427 (2000).

[7] I. Ponomareva, I. I. Naumov, and L. Bellaiche, Phys. Rev. B **72**, 214118 (2005).

Development of Classical Potential for $PbTiO_3$

Shi Liu, Takenaka Hiroyuki, Ilya Grinberg, and Andrew M. Rappe
The Makineni Theoretical Laboratories, Department of Chemistry,
University of Pennsylvania, Philadelphia, PA, 19104-6323

Ferroelectric perovskite oxides have been extensively investigated, in part due to their applications in information storage and SONAR devices. First-principles density functional calculations (DFT) have played an important role in enhancing the microscopic understanding of the relationships between composition, structure and properties. Despite the success of first-principles methods, the great computational expense and restriction to studying zero-temperature properties necessitate the development of efficient, yet accurate atomistic models for use in large-scale molecular dynamical (MD) simulations.

The shell model has been extensively used in atomistic simulations of oxides[3, 4]. In the shell model, each ion is consisted of a positively charged massive core and negatively charged massless shell. The core-shell interaction of the same ion is described by a harmonic spring and the core-shell displacement reflects the ionic polarizability. Two different shell models for $PbTiO_3$ have been developed by Sepliarsky *et al*[6] and Shimada *et al*[5], respectively. These two potentials differ mainly in their description of the short-range interactions. For the shell model parameterized by Sepliarsky *et al* , the short-range interactions for the O-O shells are described by the Buckingham potential and the Pb-Ti, Pb-O and Ti-O short-range interactions are described by the Rydberg potential. In Shimada's shell model, the Buckingham potential is used for all the short-range interactions. Both potentials are capable of reproducing equilibrium crystals structures in both the cubic and tetragonal phases under constant stress MD simulations[5, 6].

An alternative atomistic model has been developed on the basis of bond-valence theory[8, 12]. The bond-valence theory, or bond-valence summation rule, states that each atom i has a desire to fulfill a preferred atomic valence, $V_{0,i}$, in a crystal structure. The actual atomic valence,V_i, for atom i can be obtained by summing over the bond valences,V_{ij}, which can be calculated from the empirical inverse power-law relationship between the bond length and bond valence[13, 14].The energy contribution of the bond-valence can be written as

$$E_{BV} = \sum_i (V_i - V_{0,i})^2 \tag{1}$$

This model potential has been successfully applied in canonical-ensemble MD simulations to study the phase transiton and movement of domain walls in $PbTiO_3$[7–10] as well as dynamics in $Pb(Mg,Nb)O_3$-$PbTiO_3$[11].

To compare the computational efficiencies of the two models, we carried out a benchmark study with the shell model (parameters taken from Ref. 5) and the bond-valence model. All the simulations were performed under constant volume with a 0.1fs timestep for 30ps. The CPU time of the bond-valence model is 590s and that of the shell model is 18398s for a $2 \times 2 \times 2$ supercell. For a $4 \times 4 \times 4$ supercell, the speed of bond-valence mode (4304s) is about 18 times faster than the shell model (78422s). This suggests that the bond-valence model is a more promising approach for an efficient atomistic potential that will be capable of reproducing accurate full dynamical properties, ferroelectric instabilities and phase transitions of ferroelectric perovskites under constant-pressure MD simulations.

To determine how the accuracy of the bond-valence model can be improved, we performed a detailed analysis of the physics that give rise to the bond-valence conservation principle. We found that the bond-valence energy can be naturally derived from the second-moment bond-order potential, such as the well-known Finnis-Sinclair potential[15, 16].

Within the frame work of tight-binding model[17], the Finnis-Sinclair potential can be expressed as:

$$U_{FS} = \sum_i \left[\sum_j \phi(r_{ij}) - \gamma_i (\mu_i^{(2)})^{\frac{1}{2}} \right] \tag{2}$$

where $\phi(r_{ij})$ is a pair-wise repulsive potential and $\mu_i^{(2)}$ is the second-moment of local density of state (LDOS), which specifies the width of the LDOS distribution and can be evaluated from summation over all the nearest-neighbor hopping paths that start and end on atom i:

$$\mu_i^{(2)} = \sum_j \beta_{ij}\beta_{ji} = \sum_j \beta_{ij}^2 \tag{3}$$

where β_{ij} is the averaged hopping integral between atom i and j. By assuming the atomic orbital has a decay as $exp(-k_{ij}r_{ij})$, Eqn. 2 can be written as

$$U_{FS} = \sum_i [\frac{1}{2} \sum_j a_{ij} n_i^e n_j^e e^{-2k_{ij}r_{ij}} - \gamma_i (\sum_j b_{ij} n_i^e n_j^e e^{-2k_{ij}r_{rj}})^{\frac{1}{2}}] \tag{4}$$

where n_i^e is the number of electrons at atom i, a_{ij} is

a constant scaling the strength of the repulsive interactions, and b_{ij} scales the bonding interaction. The total energy will be minimized when following equation is satisfied:

$$\sum_j b_{ij} n_i^e n_j^e e^{-2k_{ij}x_{ij}} = \frac{\gamma_i^2 b_{ij}^2}{a_{ij}^2}. \quad (5)$$

Note that for a two component system, b_{ij}/a_{ij} would be the same for all the atomic pairs,and we can then rigorously define the interatomic bond-valence V_{ij} as

$$V_{ij} = \frac{V_{0,i} b n_i^e n_j^e}{C\gamma_i^2} e^{-2k_{ij}r_{ij}} \quad (6)$$

where $C = a^2/b^2$. It is evident that the energy minimization condition becomes

$$\sum_j V_{ij} = V_{0,i} \quad (7)$$

which is just the bond-valence summation rule. This means that the valence of an individual bond V_{ij} corresponds to the hopping integral with $V_{ij} \propto \beta_{ij}^2$. After substituting Eqn. 6 to Eqn. 2 and Taylor expanding V_i around $V_{0,i}$, we get:

$$U_{FS} = \sum_i \left[-\frac{1}{2} C^{\frac{1}{2}} \gamma_i^2 + \frac{1}{8} \frac{\gamma_i^2 C^{\frac{1}{2}}}{V_0^2} (V_i - V_0)^2 \right] \quad (8)$$

which has identical form to Eqn. 1.

Given that bond-valence model is intrinsically a second-moment bond-order potential, we expect that the limitations on the BV model accuracy are due to the fact that the second-moment only accounting for the LDOS width does not reflect the LDOS shape. Within the framework of bond-valence theory, this limitation can be stated as the bond-valence energy is not sensitive to structure changes during which the bond-valence summation rule is held. It has been generally accepted that higher moments are important for determining the relative stability of competing crystal structures[16]. Therefore, a systematic approach to improve the accuracy of the bond-valence model is to include contributions of higher moments (e.g. fourth moment) to the total energy[18, 19]. We suggest that two observables, bond-valence vector summation and standard deviation of bond-valence, can reflect the changes in the fourth moment and the resulting energy difference for different perovskite structures. An atomistic potential including these new terms is now under development.

[1] R.C. Miller and G. Weinreich, Phys, Rev. **117**, 1460 (1960).

[2] M. E. Lines and A. M. Glass, *Principles and Applications of Ferroelectrics and Related Materials* (Clarendon Press, Oxford, 1977).

[3] B. G. Dick and A. W. Overhauser, Phys. Rev. **112**, 90 (1958).

[4] M. Sepliarsky and R. E. Cohen, AIP Conf. Proc. **626**, 36 (2002).

[5] T. Shimada, K. Wakahara, Y. Umeno, and T. Kitamura, J. Phys.: Condens. Matter, **20**, 325225 (2008).

[6] M. Sepliarsky, A. Asthagiri, S. R. Phillpot, M. G. Stachiotti, and R. L. Migoni, Curr. Opin. Solid State Mater. Sci. **9**, 107 (2005).

[7] I. Grinberg, V. R. Cooper and A. M. Rappe, Nature **419**, 909 (2002).

[8] Y.-H. Shin, V. R. Cooper, I. Grinberg and A. M. Rappe, Phys. Rev. B **71**, 054104 (2005).

[9] Y.-H. Shin, I. Grinberg, I.-W. Chen and A. M. Rappe,Nature **449**, 881 (2007).

[10] Y.-H. Shin, J.-Y. Son, B.-J. Lee, I. Grinberg, and A. M. Rappe, J. Phys.: Cond. Matt. **20**, 0152241 (2008).

[11] I. Grinberg, Y.-H. Shin, and A. M. Rappe, Phys. Rev. Lett. **103**, 197601 (2009).

[12] I. D. Brown, Chem. Rev. **109**, 6858 (2009).

[13] I. Brown and R. Shannon, Acta Cryst. A **29**, 266 (1973).

[14] I. Brown and K. K. Wu, Acta. Cryst. B **32**, 1957 (1976).

[15] M. W. Finnis and J. E. Sinclair, Philos. Mag. A, **50**, 45 (1984).

[16] A. P. Sutton, *Electronic structure of materials* (Oxford University Press, 2004).

[17] A. P. Horsfield, A. M. Bratkovsky, M. Fearn, D. G. Pettifor, and M. Aoki, Phys. Rev. B **53**, 12694 (1996).

[18] A. E. Carlsson, and N. W. Ashcroft, Phys. Rev. B **27**, 2101 (1983).

[19] L. Hansen, P. Stoltze, K. W. Jacobsen, and J. K. Nϕrskov, Phys. Rev. B **44**, 6523 (1991).

Multiphysics model of semiconducting ferroelectrics and its application to memory devices

Nathaniel Ng and Kaushik Bhattacharya
Division of Engineering and Applied Science
California Institute of Technology
Pasadena CA 91125, USA

Ferroelectric transistors and capacitors are important components in many electronic devices, in particular there is considerable interest in their use for nonvolatile memory applications. The behavior of ferroelectrics are commonly described via the time-dependent Ginzburg Landau equations. In this classical model, however, ferroelectrics are treated as insulators. On the other hand, it is well known that ferroelectrics are in fact wide band-gap semiconductors. It then follows that capturing the key aspects of semiconductor physics—band bending at the interface, Fermi levels, depletion layers, require ferroelectrics to be treated as semiconductors. Recent progress has been made in describing such behavior; in particular, there are methods that make no a priori assumptions on the space charge or polarization distributions [1]. However, these methods are often restricted to equilibrium profiles and may not necessarily bridge the time scales between the dynamics of the mobile charge and domain wall motion. Recent progress has been made with a 1D model [2] and in this work, a full 2D model has been developed. Here, we introduce a model that addresses these difficulties, yet at the same time is consistent with both the time-dependent Ginzburg Landau model and the classic drift-diffusion model for semiconductors. Via this model, we first demonstrate that charge carriers migrate to neutralize electric fields across 90° domain walls (Fig 1). Next, we attempt a full simulation of a ferroelectric transistor with a configuration consisting of a ferroelectric placed on top of a silicon substrate. From our model, we calculate the current flow, as well as the electric field and polarization distributions.

References:
[1] Y. Xiao, V. B. Shenoy and K. Bhattacharya, PRL 95, 247603 (2005).
[2] P. Suryanarayana and K. Bhattacharya (submitted).

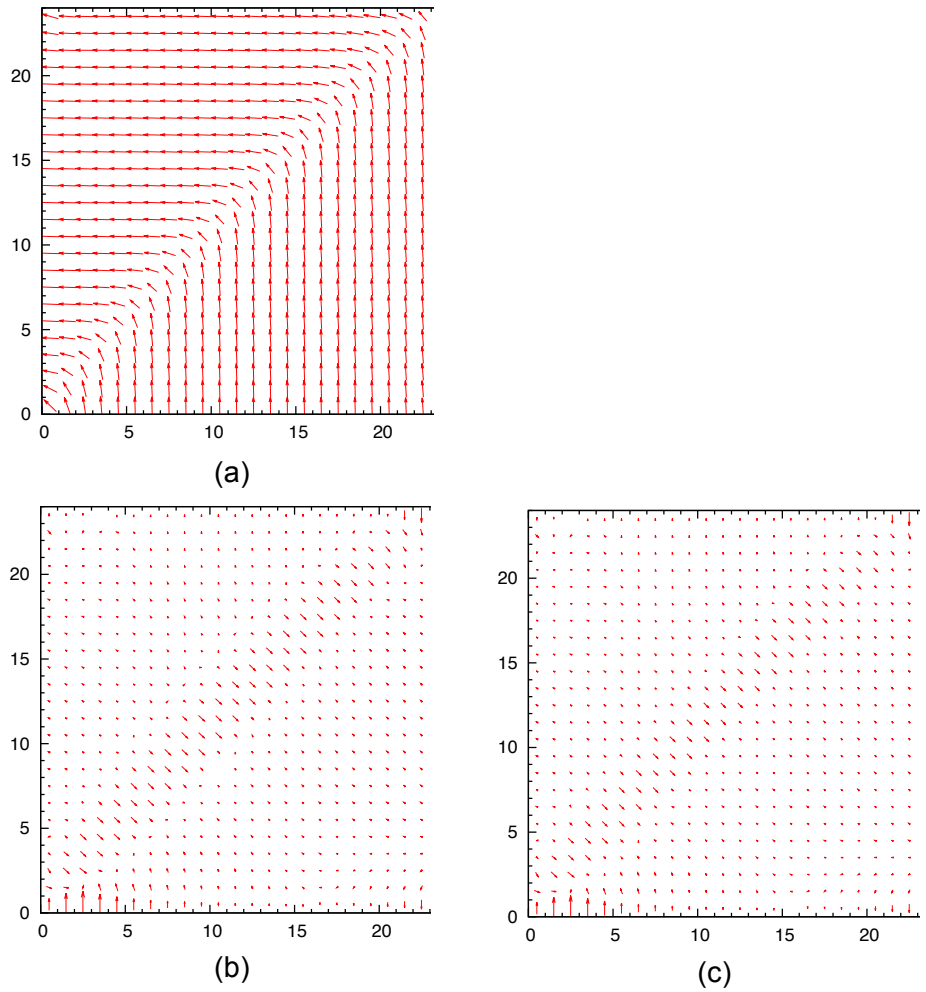

Fig 1: (a) Polarization distribution across a 90° domain wall, (b) Initial electric field distribution across the domain wall, (c) Equilibriated electric field distribution across the domain wall.

Role of electrical and mechanical boundary conditions on the ferroelectric properties of $YMnO_3$ epitaxial thin films

Alina Prikockytė[1,2], Catherine Dubourdieu[2], and Philippe Ghosez[1]

[1] *Physique Théorique des Matériaux, Université de Liège, B5, 4000 Sart Tilman, Belgium*
[2] *Laboratoire des Matériaux et du Génie Physique, CNRS, Grenoble INP, 38016 Grenoble, France*

Hexagonal $YMnO_3$ is one of the most studied magneto-electric multiferroic materials and also a prototypical improper ferroelectric compound.[1,2] Its structural phase transition from the *P6₃/mmc* paraelectric phase to the *P6₃cm* ferroelectric ground state arises from the condensation of a unstable zone-boundary K_3 mode driving the concomitant condensation of a stable Γ_2^- mode, which couples linearly with it.[1]

Using first-principles density functional theory within the LSDA+*U* approximation, we first study the structural, dielectric and dynamical properties of the paraelectric and ferroelectric phases of bulk $YMnO_3$. Our results are in agreement with previous calculations and experimental data. In particular, we report the whole spectrum of zone-center phonon modes and discuss the reassignment of different Raman peaks of the ferroelectric phase.[3]

Then a simple effective Hamiltonian is proposed, describing the energy landscape around the paraelectric and ferroelectric phases in terms of relevant ionic and strain degrees of freedom. Our first-principles calculations confirm that the ferroelectric distortion is mainly coming from the unstable zone-boundary K_3 mode of the paraelectric phase, at a frequency of $153i$ cm^{-1} and the stable zone-center Γ_2^- mode, at a frequency of 85 cm^{-1} However, the inclusion of these only two ionic degrees of freedom is not sufficient to properly account of the strain relaxation, which requires the additional explicit treatment of the coupling with Γ_1^+ mode. Our effective Hamiltonian properly reproduces the bulk ferroelectric ground-state and allows us to predict the evolution (at T = 0 K) of the ferroelectric properties of $YMnO_3$ epitaxial films between metallic electrodes in terms of (i) the epitaxial strain imposed by the substrate and (ii) the electrical boundary conditions (open-circuit, short-circuit, finite bias), taking into account the quality of screening provided by the electrodes through an effective screening length parameter, λ_{eff}.

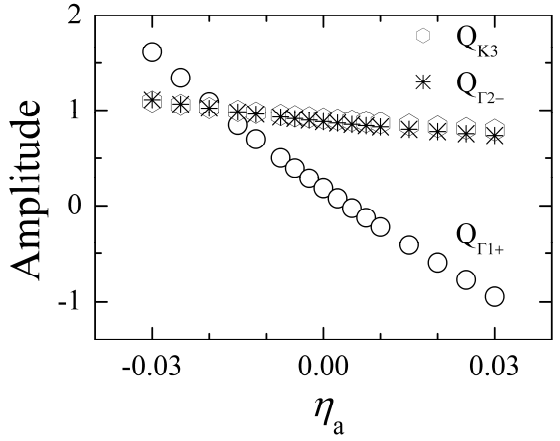

FIG 1. Evolution of the amplitudes of K_3, Γ_2^- and Γ_1^+ distortions in the $P6_3cm$ ground state of epitaxial $YMnO_3$ films under short-circuit (λ_{eff} = 0) in terms of the in-plane epitaxial strain η_a imposed by the substrate (at T = 0 K).

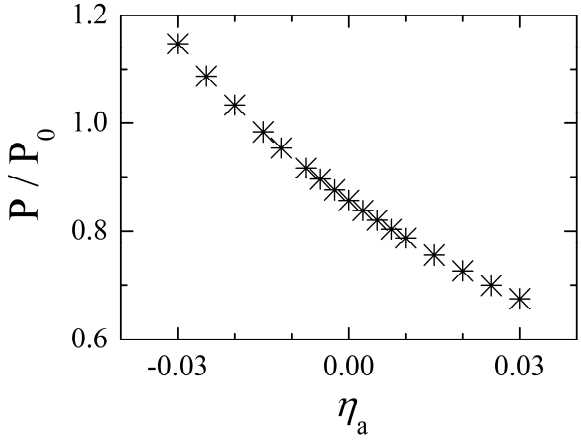

FIG 2. Evolution of the spontaneous polarization P (relative to the bulk polarization P_0) of the $P6_3cm$ ground-state of epitaxial $YMnO_3$ films under short-circuit (λ_{eff} = 0) in terms of the in-plane epitaxial strain η_a imposed by the substrate (at T = 0 K).

[1] C. J. Fennie and K. M. Rabe, Phys. Rev. B 72, 100103 (R) (2005).
[2] Alexandra S. Gibbs, Kevin S. Knight, and Philip Lightfoot, Phys. Rev. B 83, 094111 (2011).
[3] A. Prikockytė, D. Bilc, P. Hermet, C. Dubourdieu and Ph. Ghosez, Phys. Rev. B 84, 214301 (2011).

Response of zone-center phonon structure to epitaxial strain in $BaTiO_3$

Aldo Raeliarijaona and Huaxiang Fu
Department of Physics, University of Arkansas, Fayetteville, AR 72701, USA

Using Density Functional Perturbation Theory we investigate the effect of epitaxial strain on the phonon frequencies and the infrared intensities at the zone-center. We have considered both the tetragonal and the rhombohedral $BaTiO_3$. The in-plane compressive strain ranges from $\eta = 0\%$ to $\eta = 3\%$. By analyzing the overlap of phonon eigenmodes between different in-plane strains, we determined the evolution of individual phonon mode.

We found that some of the phonon modes increase their frequencies with the increasing compressive strain, in both the tetragonal and rhombohedral phases (see **Figure 1** and **Figure 2**). We also found that in the rhombohedral phase the frequency shift curves of two modes, namely: $A_1(TO_1)$ and $E(TO_1)$, show an interesting non-monotonous behavior (see **Figure 2**). This behavior was absent for the modes in the tetragonal phase. The behaviors of the phonon mode frequency shift are explained by examining the eigendisplacements of the modes.

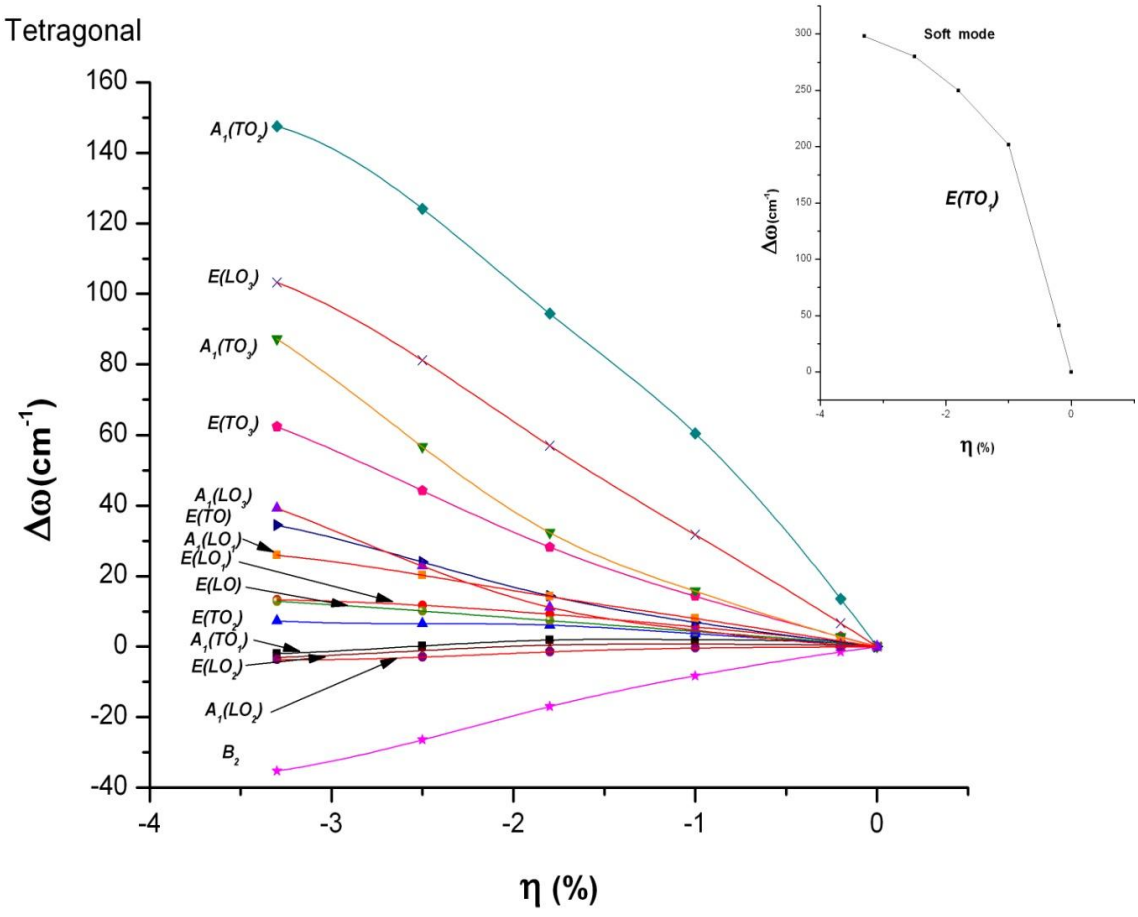

Figure 1: *Frequency shifts in the tetragonal phase.*

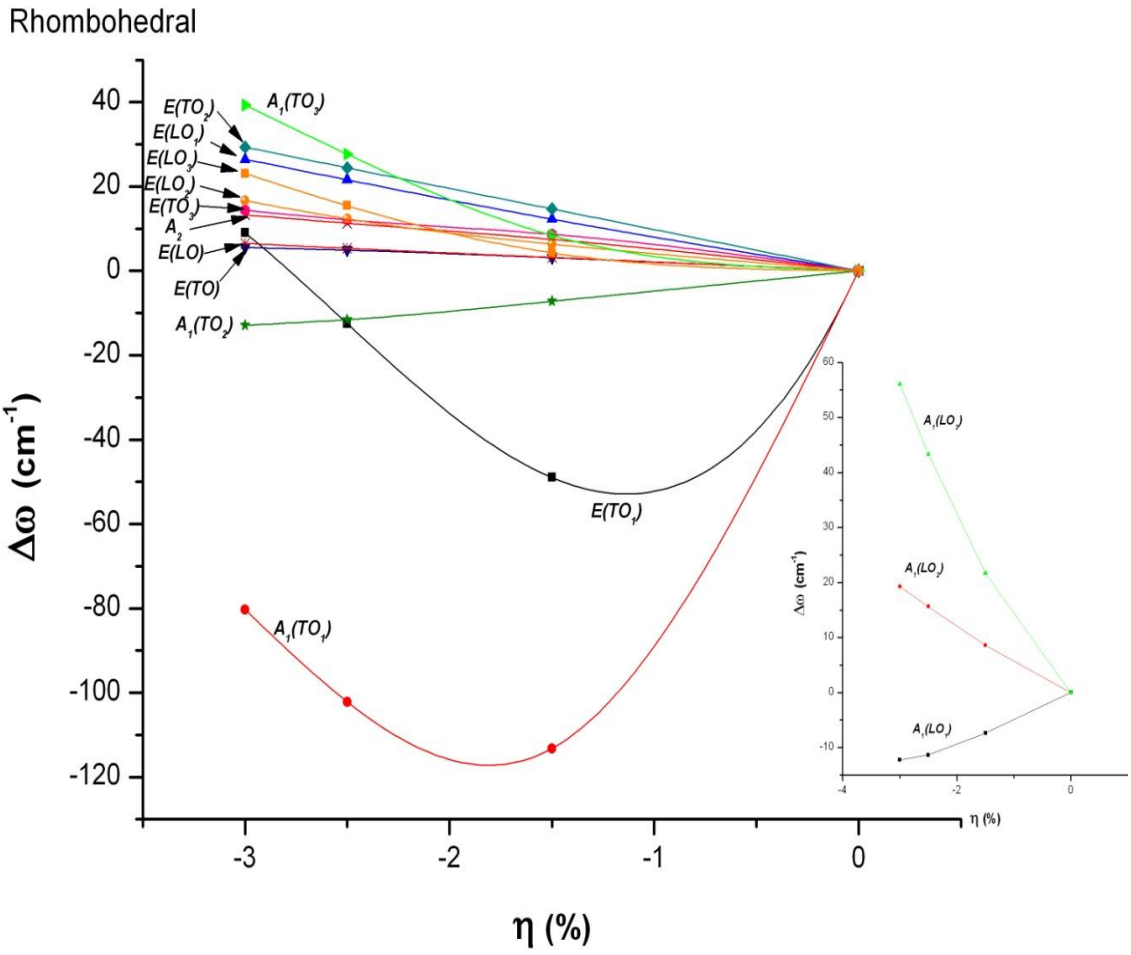

Figure 2: *Frequency shifts in the rhombohedral phase.*

Magnetic cycloid of $BiFeO_3$ from atomistic simulations

D. Rahmedov and L. Bellaiche

Physics Department, University of Arkansas, Fayetteville, AR 72701

D. Wang

Electronic Materials Research Laboratory,

Key Laboratory of the Ministry of Education and International Center for Dielectric Research,

Xian Jiaotong University, Xían 710049, China

J. Íñiguez

Institut de Ci`encia de Materials de Barcelona (ICMAB-CSIC), Campus UAB, 08193 Bellaterra, Spain

The understanding of magnetic and electric properties of materials is a crucial step towards development in information and device technology. Some devices take advantages of materials possessing a magnetic ordering while others are based on materials exhibiting electric order parameters. Recently, an intensive effort has been made to combine advantages of both properties in a single material. Such single phase materials with these two different order parameters are multiferroics [1, 2]. Among different multiferroics, $BiFeO_3$(BFO) occupies a central role, mostly because it is one of the few materials that exhibit both long-range electric and magnetic orderings at room temperature [3, 4].

In fact, the magnetic order of this material is rather peculiar and interesting since the magnetic structure of BFO can be described as a cycloidal structure superimposed on a G-type antiferromagnetic structure [5, 6]. This cycloid is very delicate, as demonstrated by the facts that magnetic fields or epitaxial strain can destroy it in favor of a spin-canted structure possessing a weak ferromagnetic vector. Surprisingly, the details of this cycloid structure are still a subject of debates, and very recent experiments played an important role in resolving this issue [7, 8]. However, a microscopic model that would reproduce the peculiar details of this magnetic structure and will help in understanding its microscopic origins is still absent. In this work, we present a simple microscopic model that fully reproduces all the details of very recent experiments, and provide important information about the roles of different subtle interactions on the magnetic cycloid of BFO.

This work is supported by ONR Grants N00014-11-1-0384 and N00014-08-1-0915, NSF grant DMR-0701558 and the Department of Energy, Office of Basic Energy Sciences, under contract ER-46612. Some computations were also made possible thanks to the MRI grant 0959124 from NSF, N00014-07-1-0825 (DURIP) from ONR and a Challenge grant from HPCMO of the U.S. Department of Defense.

[1] W. Eerenstein *et al*, *Nature (London)* **442**, 759 (2006).

[2] R. Ramesh and N. A. Spaldin, *Nature Mater.* **6**, 21 (2007).

[3] G. Catalan and J. F. Scott, *Adv. Mater.* **21**, 2463 (2009).

[4] G.A. Smolenskii, I.E. Chupis, *Sov. Phys. Usp.* **25**, 475 (1982).

[5] I. Sosnowska *et al*, *J. Phys. C* **15**, 4835 (1982).

[6] D. Lebeugle *et al*, *Phys. Rev. Lett.* **100**, 227602 (2008).

[7] M. Ramazanoglu *et al*, *Phys. Rev. Lett.* **107**,207206 (2011)

[8] M. Ramazanoglu *et al*, *Phys. Rev. B* **83**, 174434 (2011)

The Electrocaloric Effect and the Relationship Between Homogenous Polarization Switching and Phase Transitions in Ferroelectrics

Maimon Rose and R. E. Cohen[1]

[1] Carnegie Institution of Washington, Washington, D.C. 20015

The thermodynamic inverse of the pyroelectric effect, the electrocaloric effect is the reversible temperature change of a polarizable material under the application and/or removal of an electric field. Previous studies have focused on temperatures strictly below the critical temperature (T_c) defining the transition from the ferroelectric state to the paraelectric state. These studies have also kept their focus on applied fields strictly in the same direction as the spontaneous polarization of the ferroelectric state.

In our simulations we employ the same first-principles based shell model used previously to study the pyroelectric effect at zero field in $LiNbO_3$ {Peng, 2011 #7071}. The model uses a three dimensional, surface-free, single domain perfect crystal infinitely repeated with parallelepiped boundary conditions. The crystal super-cell is made up of 8x8x8 unit cells, with a total of 5210 atoms. All simulations are performed using the *DL_POLY* package using the Nosé-Hoover thermostat coupled with the Melchionna modification of the Hoover barostat algorithm in an $N\bar{\sigma}T$ ensemble.

To investigate the electrocaloric effect we took advantage of the thermodynamic relation:

$$\Delta T = -\frac{TV}{C_V}\left(\frac{\partial P}{\partial T}\right)_E \Delta E$$

to calculate the change in the temperature. Applying this relation to various temperatures and electric fields, we see from Figure 2 that the maximum ΔT is found at progressively higher temperatures as the strength of the field is increased. This trend corresponds to the phenomenon in which a ferroelectric with an applied electric field no longer has a well-defined T_c. From our simulations we find the transition from the ferroelectric to the paraelectric state of LiNbO3 without an applied electric field to occur at 1506K, which slightly overestimates the reported value in the literature of ~1480K. However, as can be seen from Figure 1a, the polarization of the material does not drop to zero with an applied positive field. There is an inflection point, and a minimum of the first derivative of the polarization with respect to temperature as can be seen in Figure 1b. This corresponds to the Widom line.

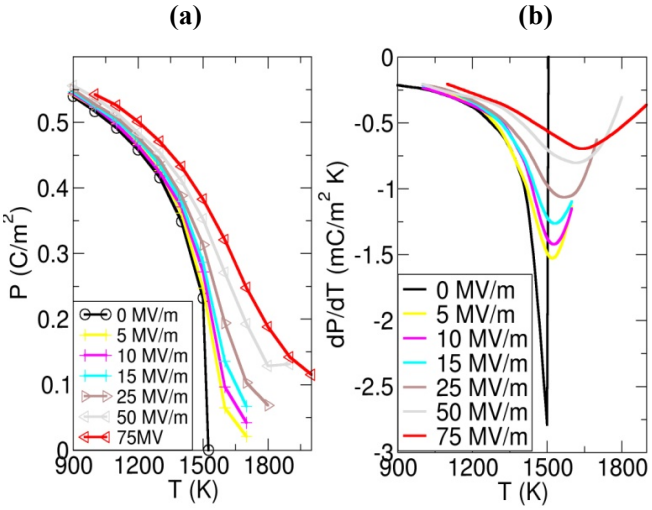

Figure 1 *(a) Average polarization of $LiNbO_3$ with applied field along the same direction as the spontaneous polarization and (b) derivative of polarization with respect to temperature.*

Along the Widom line the electrocaloric effect is the greatest. Note that these temperatures and fields cannot be attained in $LiNbO_3$ since they are above the melting point (1526K) or breakdown fields. Nevertheless they are instructive, as this should be universal behavior.

In our study we employ the convention defining fields applied in the same direction as the spontaneous polarization as 'positive' and the fields applied in the direction opposite that of the spontaneous polarization as 'negative.' We find that with an applied negative electric field, the material homogenous switches polarization direction so that the direction of the polarization of the crystal becomes the same as the direction of the

applied field. We recently studied homogeneous switching in detail in $PbTiO_3$ {Zeng, 2011 #6659}. This switching occurs, depending on the strength of the applied negative field, at a temperature below T_c as is evident from Figure 3.

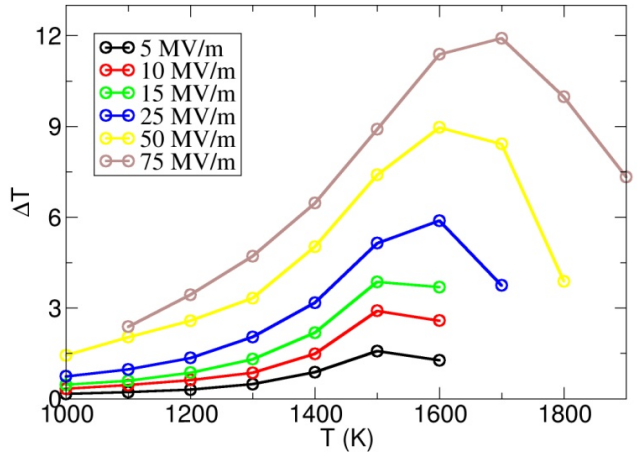

Figure 2. *Calculated change in temperature as a function of temperature for various applied electric fields.*

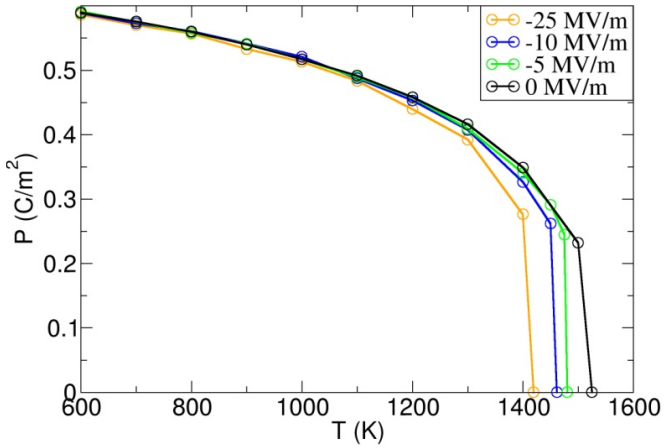

Figure 3. *Average polarization for $LiNbO_3$ with applied electric field in the opposite direction to spontaneous polarization.*

We find that these three aforementioned phenomena (polarization switching with an applied negative field, neutral T_c, and minima of $\partial P/\partial T$ with an applied positive field), collectively T*, all fall on a single line. This result is shown in Figure 4b. In order to explain this finding we invoke the concept of the Widom-Line as a parallel phenomenon. The Widom- Line is defined as the line formed by the locus of the specific heat maxima on a P-T phase diagram emanating from the critical point.

This work supported as part of the EFree, an Energy Frontier Research Center funded by the U.S. Department of Energy, Office of Science, Office of Basic Energy Sciences under Award Number DE-SC0001057. We thank Q. Peng and I. Naumov for useful discussions.

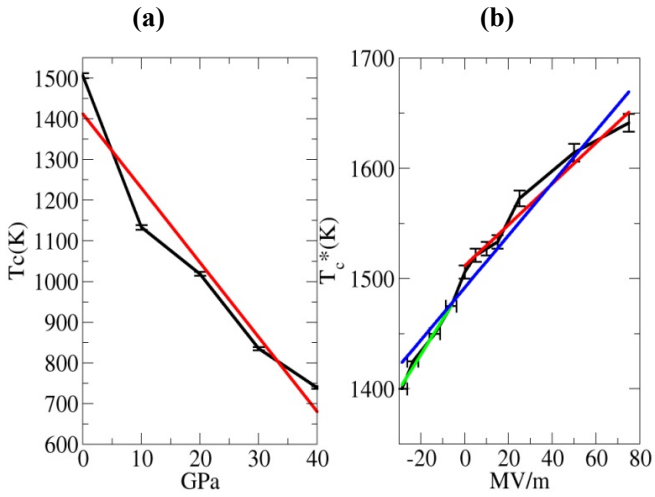

Figure 4. *Illustration of the linear dependence of (a) T_c on pressure and (b) T^*_c on the magnitude of the applied electric field. Red line corresponds to linear fit of positive fields; green to negative fields; blue for entire range.*

A first principle structure dynamics study of doping lone pair A cations to $HoMnO_3$

Sathya Sheela S[1,2], Taisuke Ozaki[1], Kunihiko Yamauchi[3,4], Tamio Oguchi[4] and N. Baskaran[2]

[1] Research Center for Integrated Science (RCIS), Japan Advanced Institute of Science and Technology (JAIST), 1-1 Asahidai, Nomi, Ishikawa 923-1292

[2] Department of Physics, National Institute of Technology, Tiruchirapalli, India-620015

[3]Consiglio Nazionale delle Ricerche-Istituto Nazionale per la Fisica della Materia (CNR-INFM), CASTI Regional Laboratory, 67100 L'Aquila, Italy

[4]ISIR-SANKEN, Osaka University, Japan

Rare earth manganites ($RMnO_3$) with a smaller R radius (R=Ho-Lu) have a non-perovskitic hexagonal ground state structure in contrast to the large radius (R=La-Dy) manganites, which crystallize in the orthorhombic phase [1]. Thus, $HoMnO_3$ being a small radii rare earth manganite, has a $P6_3cm$ hexagonal ground state structure but under high temperatures and pressure, it can be synthesized as an orthorhombic Pbnm perovskite. Both experimental and theoretical findings have predicted that ortho-$HoMnO_3$ has an AFM E ground state and its electric polarization is found to arise due to this specific magnetic ordering [2,3,4].

In this work, a first principle attempt has been made to study the structure and properties of 50% doping lone pair cations to $HoMnO_3$. Electronic structure calculations were carried out to study $Ho_{0.5}A_{0.5}MnO_3$ (A=Ge, Sn, Pb, As, Sb, Bi, Se, Te) under the Generalized Gradient Approximation (GGA) to the density functional theory (DFT). This attempt has been made to analyze the effect of the lone pair cations towards electric polarization and thus to predict new multiferroics.

Full optimization was carried out for the series of compounds in different magnetic ordering (AFM A, C, G, E and FM) to predict the most stable ground state structure for each compound. The total energy calculations are shown in fig. 1.

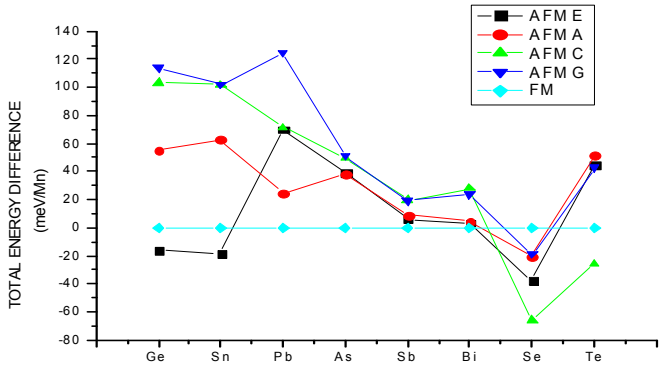

Fig. 1 Total energy GGA calculations for the full optimized layered $Ho_{0.5}A_{0.5}MnO_3$

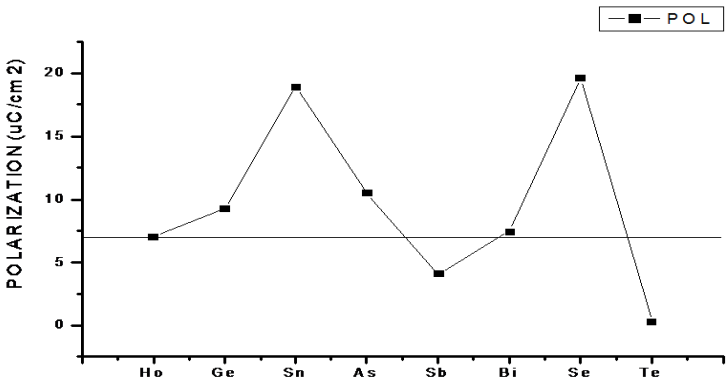

Fig. 2 Electric polarization of $Ho_{0.5}A_{0.5}MnO_3$ (A=(Ge, Sn, As, Sb, Bi, Se, Te)using GGA. Polarization of $HoMnO_3$ is taken as the reference.

$Ho_{0.5}Ge_{0.5}MnO_3$ and $Ho_{0.5}Sn_{0.5}MnO_3$ have an AFM E ground state structure while $Ho_{0.5}A_{0.5}MnO_3$ (A=Pb, As, Sb, Bi) are found to ferromagnetic. $Ho_{0.5}Se_{0.5}MnO_3$ and $Ho_{0.5}Sn_{0.5}MnO_3$ are found to have an AFM C ground state. All the doped compounds showed electric polarization (Fig.2) with the exception of Pb which was found to be metallic under GGA and GGA+U. The reason for the metallic behavior can be attributed to introduction of holes due to the addition of divalent Pb to $HoMnO_3$. $Ho_{0.5}Sn_{0.5}MnO_3$ and $Ho_{0.5}Se_{0.5}MnO_3$ was found to have a very high polarization as compared to the parent $HoMnO_3$. Density of states studies revealed that O 2p - A cation valence p orbitals hybridization is found to strongly influence the electric polarization. Polarization is found to increase with increased p-p hybridization. This p-p hybridization is dependent on the energy of the p orbital of A. An interesting observation is the position of s states of the A cation. The 5s states are found to be more low lying in energy(i.e closer to the Fermi level) as compared to the 4s and 6s states. This is due to relativistic effects. Similarly the 5p states are also low lying as compared to 4p or 6p states thus causing more mixing of states with the O 2p orbitals.

A trend, with respect to the A cation size, is seen in the comparative study of the Mn-O bond distances and Mn-O-Mn bond lengths, revealing the distortions of the Mn-O octahedra. Point charge model calculations for electric polarization were also done and were found to be analogous to the berry phase calculations.

Thus a first principle attempt has been made to perform an extensive search for new multiferroics having a high electric polarization and to provide a pathway for experimentalists to synthesis new promising multiferroic compounds.

[1] H.L. Yakel, W.D. Koehler, E.F. Bertaut, and F. Forrat, Acta Crystallogr.16, 957(1963)
[2] H.W. Brinks et al, PRB, Vol 63, 094411(2001).
[3]K. Yamauchi et al, PRB 78, 014403(2008).
[4]N. Lee et al, PRB 84, 020101® (2011).

The piezoelectric tensor components of the known phases of $KNbO_3$ calculated by first-principle methods

L.F. Wan, [1] T. Nishimatsu, [2] and S.P. Beckman[1,2]

[1] *Department of Material Science and Engineering, Iowa State University, Ames, IA 50010*
[2] *Institute for Materials Research (IMR), Tohoku University, Sendai, 980-8577, Japan*

The ferroelectric nature of $KNbO_3$, (KNO) was first discovered in 1951,[1] and since then KNO single crystals have been incorporated into ultrasonic and acoustic wave transducers due to their excellent piezoelectric coupling at high operating temperatures.[2] The high temperature performance of these crystals is also the origin of the challenges to experimentally study them. It is difficult to fabricate high density single-crystal KNO samples.[3-5] First-principles methods provide an accurate and effective way to explore the complex relationship between the atomic structure and the macroscopic properties that are difficult to investigate experimentally. In this presentation the dielectric, piezoelectric, and elastic tensors for all four of the experimental known phases are calculated and reported. The calculated results are compared with existing measurements when possible, although there are many physical constants that have not been reported until here. In this extended abstract only the piezoelectric constants are presented.

The electronic structure calculations presented here are conducted using the density functional theory (DFT) formalism that is implemented in the ABINIT software package.[6] The exchange-correlation functional are parameterized using the Wu-Cohen expression of the generalized gradient approximation (GGA), which is expected to give better estimations of the properties of ferroelectric oxides compared to LDA and PBE-type GGA.[7] The wavefunction is represented as a plane wave expansion that is truncated at a cut-off energy of 1700 eV and the Brillouin zone is sampled using an 8 × 8 × 8 Monkhorst-Pack grid. The calculations are sufficiently converged to allow the atomic structures to be optimized until the residual forces on the atoms are less than 5 meV/Å. In addition, density functional perturbation theory is used to extract physical properties as the second derivatives of total internal energy.[8] In this work, three types of perturbation are combined to predict the property tensors essential to characterizing the physical behavior of relaxed crystals: electric field, strain, and atomic displacement.[9] The calculated piezoelectric components are presented in table 1 along with experimentally determined components. It is noteworthy that the reported coefficients from refs. [10] and [11] are from direct measurement whereas the values from refs. [12] and [13] fit the coefficients from other experimental data.

For the tetragonal phase, the most significant piezoelectric coefficient is d_{33}, which corresponds to applying a uniaxial stress parallel to the spontaneous polarization direction. The d_{31} components are smaller than d_{33} because they correspond to the uniaxial stresses in the directions orthogonal to the strong Nb–O bonds. When the stress, as associated strain, distorts the Nb–O bonds a large change in the polarization is anticipated because in KNO the ferroelectric behavior is due primarily to the hybridized bond between the Nb and O atoms.

The orthorhombic unit cell also has a moderate magnitude d_{33} component that corresponds to a uniaxial stress parallel to the polarization, and slightly smaller d_{31} and d_{32}. More interestingly the d_{15} and d_{24} components are approximately one order of magnitude larger than the d_{33}. The d_{15} coefficient gives the change in polarization in the P_1 direction when the shear stress σ_{13} is applied, and d_{24} gives the change in P_2 direction when the shear stress σ_{23} is applied. Physically, these coefficients express the rotation of the electric dipole from the z-direction when shears are applied that skew the cell. The shear σ_{13} stretches and tilts the strong covalent bonds between the Nb atom at the O at site O_{II}. As a result the polarization vector rotates slightly into the x-direction causing a large change in the electric dipole in this direction. Hence the tensor component d_{15} is large. The d_{24} tensor component is also large, but is approximately half that of d_{15}. The σ_{23} stress does not directly bond. Instead all of the O sites are skewed relative to the Nb, which rotates the polarization vector into the P_2 direction; however the net change in polarization due to the σ_{23} shear is less than the σ_{13}.

For the rhombohedral phase both the d_{33} and d_{31} components again have a modest magnitude. They express the change in the polarization parallel to the existing, spontaneous dipole, P_3, when a uniaxial uniaxial stress is applied parallel to the polarization, σ_{33}, and perpendicular, σ_{11}, respectively. Neither of these stresses substantially changes the Nb and O bonds along the z-direction. By comparison

Table 1: The piezoelectric tensor components, d_{ij}, for KNO with units of pC/N.

Phase	d_{15}	d_{22}	d_{24}	d_{31}	d_{32}	d_{33}
Tetragonal	-15.90	-	-	-7.421	-	39.89
Orthorhombic	175.0	-	-91.07	12.66	-10.04	20.07
Orthorhombic Exp. [10]	215	-	159	-	-	-
Orthorhombic Exp. [11]	-	-	-	9.8	-19.5	24.5
Orthorhombic Exp. [12]	19.2	-	15.5	2.7 to 4.8	-8.5 to -2.3	-2.5 to +1.5
Orthorhombic Exp. [13]	103	-	78	9.9	-19.2	30.5
Rhombohedral	388.7	111.5	-	5.024	-	10.81

the d_{22} component is large, and it corresponds to the change in the polarization perpendicular to spontaneous polarization, in the P_2 direction, when a uniaxial stress is applied in that direction, σ_{22}. The σ_{22} stress breaks the symmetry of the three fold-degenerate Nb–O bonds and effectively rotates the electric dipole off the body diagonal and creates a polarization component in the P_2 direction. The largest piezoelectric coefficient of any of the phases is the rhombohedral d_{15} component, which has a magnitude of 388 pC/N. This component relates an applied shear along the surface of the rhombohedral in the σ_{13} direction. The shear directly stretches and tilts the Nb–O bond and induces a large change in the dipole in the P_1 direction.

The calculated and measured piezoelectric coefficients are directly compared in table 1. It is observed that the predicted and measured values can differ by as large as 50% of the measured values. Certainly the use of the local density approximation can result in errors when determining the second derivatives of the energy, but it is unclear that this alone is responsible for the disagreement between the theoretical and experimental coefficients. Consider for example the d_{24} coefficient in which the experimental and theoretical results have a similar magnitude but different sign. The sign of the theoretical results can be intuitively understood by visualizing the atomic displacements and the impact of strain. It is unclear why the experimental measurements have a different sign, but it is certainly possible that intrinsic crystal defects, such as vacancies, may impact the experimental results. Due to the high processing temperatures these intrinsic defects are likely to be omnipresent in the experimental specimen.

Acknowledgements

This work was supported in part by the National Science Foundation (NSF) through Grant DMR-1037898 and Japan Society for the Promotion of Science (JSPS) KAKENHI 23740230. Beckman would like to thank the International Collaboration Center (ICC) at the Tohoku University, Institute for Materials Research (IMR), for their support summer 2011.

References

[1] B. T. Matthias and J. P. Remeika, Phys. Rev. 82, 727 (1951).
[2] M. Davis, N. Klein, D. Damjanovic, N. Setter, A. Gross, V. Wesemann, S. Vernay, and D. Rytz, Appl. Phys. Lett. 90, 062904 (2007).
[3] T. Takenaka, H. Nagata, and Y. Hiruma, Jpn. J. Appl. Phys. 47, 3787 (2008).
[4] N. Kumada, T. Kyoda, Y. Yonesaki, T. Takei, and N. Kinomura, Mater. Res. Bull. 42, 1856 (2007).
[5] T. Yoshida, Y. Hiruma, R. Aoyagi, H. Nagata, and T. Takenaka, Key Eng. Mat. 301, 19 (2006).
[6] X. Gonze and et al., Computer Phys. Commun. 180, 2582 (2009).
[7] Z. Wu, R. E. Cohen, and D. J. Singh, Phys. Rev. B 70, 104112 (2004).
[8] X. Gonze and C. Lee, Phys. Rev. B 55, 10355 (1997).
[9] D. R. Hamann, X. Wu, K. M. Rabe, and D. Vanderbilt, Phys. Rev. B 71, 035117 (2005).
[10] E. Wiesendanger, Ferroelectrics 6, 263 (1974).
[11] P. Günter, Jpn. J. Appl. Phys. 16, 1727 (1977).
[12] A. G. Kalinichev, J. D. Bass, C. S. Zha, P. D. Han, and D. A. Payne, J. Appl. Phys. 74, 6603 (1993).
[13] M. Zgonik, R. Schlesser, I. Biaggio, E. Voit, J. Tscherry, and P. Gunter, J. Appl. Phys. 74, 1287 (1993).

Ferroelectricity in Quasi-Amorphous $BaTiO_3$ Ultra-thin Film

J. L. Wang[1], A. Pancotti[1], P. Jégou[1], G. Niu[2], B. Gautier[3], Y. Y. Mi[1], L. Tortech[1,4], S. Yin[2], B. Vilquin[2], N. Barrett[1]

[1] *CEA, IRAMIS, SPCSI, F- 91191 Gif sur Yvette cedex, France*
[2] *Université de Lyon, Ecole Centrale de Lyon, Institut des Nanotechnologies de Lyon, F- 69134 Ecully cedex, France*
[3] *Université de Lyon, INSA Lyon, Institut des Nanotechnologies de Lyon, F- 69621 Villeurbanne cedex, France*
[4] *Institut Parisien de Chimie Moléculaire (UMR CNRS 7201), UPMC Université Paris 06, 4 Place Jussieu, C. 229, 75005 Paris, France*

Until now, the quasi-amorphous (QA) phase in $BaTiO_3$ (BTO), $SrTiO_3$ (STO) and $BaZrO_3$ was achieved by pulling a thick film through a steep temperature gradient. [1,2] Here we show that a room temperature deposited ultra-thin film, subsequently annealed in O_2 can also produce a QA phase. [3] The atomic, electronic and ferroelectric (FE) structure of a QA, ultra-thin BTO grown on STO were studied by X-ray diffraction (XRD), X-ray photoelectron diffraction (XPD), X-ray photoelectron spectroscopy (XPS) and piezo-force microscopy (PFM). The absence of long range order is confirmed by in and out of plane XRD, as well as Ti 2p XPD. FE polarized domains with good retention have been successfully written into the QA film and exhibit a clear P-E hysteresis loop. Substrate clamping frustrates volume expansion during annealing, leading to a QA film. Photoelectron spectroscopy confirms a similar overall electronic structure as for thicker films but with some significant differences. Simple charge transfer arguments are not sufficient to explain the high resolution core level spectra. Ba, Ti and O all show components associated with a surface region. The observation of such a component in the Ti 2p spectrum is most likely linked with the high dynamic charge tensor induced by the large off center displacement of the Ti ion. Thus, local atomic distortion rather than long wavelength soft phonon modes appears to be responsible for the ferroelectricity. [4]

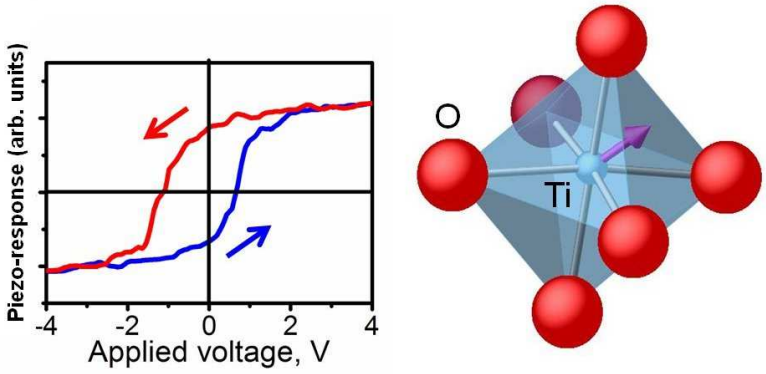

Figure 1 (left) P-E hysteresis curve obtained by PFM 24 hours after domain writing. (right) schematic of local off-centre Ti atom displacement.

The key factor in the production of such a QA film seems to be the appropriate growth rate followed by clamping control during annealing in oxygen. We think that this is the reason why we can anneal the whole STO substrate-supported film directly rather than using a pull through a narrow hot zone. The observed phenomenon may turn out to be more generally applicable in the case of ultrathin amorphous films, offering some interesting new physics.

[1] E. Wachtel and I. Lubomirsky, *Adv. Mater.* **22**, 2485 (2010).
[2] D. Ehre, H. Cohen, V. Lyahovitskaya, and I. Lubomirsky, *Phys. Rev. B* **77**, 184106 (2008).

[3] J. L. Wang, A. Pancotti, P. Jégou, G. Niu, B. Gautier, Y.Y. Mi, L. Tortech, S. Yin, B. Vilquin and N. Barrett, *Phys. Rev. B* **84**, 205426 (2011).
[4] Q. Zhang, T. Cagin, and W. A. Goddard III, *Proc. Natl. Acad. Sci. (USA)* **103**, 14695 (2006).

Switchable polarization in stuffed wurtzite compounds, a new class of ferroelectrics

Joseph W. Bennett, Kevin F. Garrity, Karin M. Rabe and David Vanderbilt
Department of Physics and Astronomy, Rutgers University
Piscataway, NJ 08854

(Dated: November 30, 2011)

One of the challenges in modern materials science is the development of new types of ferroelectric materials, in which a response is produced by an applied field or stress. Because of their many technological applications, including transducers and information storage, the discovery of new ferroelectric materials continues to be of great importance. For a material to be ferroelectric, it must be insulating and have a nonzero polarization that can switched by an external electric field. The wurtzite structure type, including a number of technologically important materials such as ZnO, CdSe (II-VI) and GaN (III-V), is generally considered to be the result of directional sp^3 bonding, with all atoms in tetrahedral coordination. These compounds thus satisfy the first two conditions, but not the third, as the switching of the polarization by 180° would require breaking and reforming the strong sp^3 bonds, and the energy barrier is far too high. Indeed, in the well-known ABO_3 perovskite oxide ferroelectrics, displacements of a B-site within an octahedral O_6 environment and an A-site within a dodecahedral O_{12} environment do not involve the breaking and reforming of chemical bonds, only changes in bond length. However, if the wurtzite structural parameters are not close to ideal tetrahedral sp^3 coordination, but rather have values that correspond to a small buckling of the planes, then similarly the barrier to polarization switching can become small. The barrier to polarization for KSnAs is shown in Figure 1.

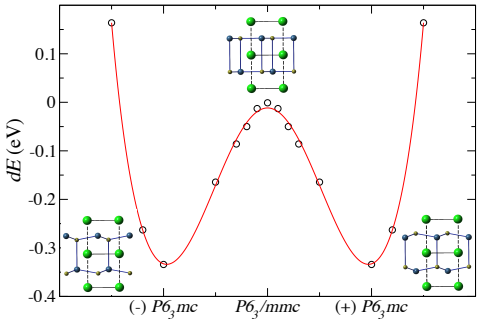

FIG. 1: The difference in energy between the low ($P6_3mc$) and high ($P6_3/mmc$) symmetry ABC structures for KSnAs is 0.34 eV. Also shown are the distortions at either polarization.

This type of wurtzite structure can be found as a substructure of the ternary LiGaGe structure type, where the third "stuffing" atom controls the size of the buckling. A total electron count of 8 or 18 electrons favors insulating char-

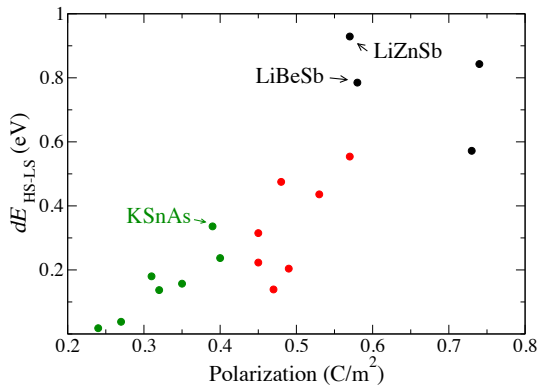

FIG. 2: Difference in energy between the low ($P6_3mc$) and high ($P6_3/mmc$) symmetry ABC structures for all insulating combinations. Combinations with A=Li (black circles) are less likely to be ferroelectric than those with A=Na (red circles) or A=K (green circles). Labeled are the three experimental compositions, LiBeSb, LiZnSb and KSnAs.

acter, and thus we focus on families of compounds that can be classified as I-III-IV (LiGaGe), I-XII-V (LiZnSb), etc. In this talk, using first-principles methods, we investigate about fifty members of this structure type, and find that both the polarization and barrier to switching depend upon the stuffing atom. Moreover, we demonstrate that the members of the family with a large stuffing atom have barriers to polarization switching on the order of those calculated for the perovskite family. This is demonstrated in Figure 2, where the ABC combinations with the larger stuffing cation have the smallest barrier to polarization switching. Information is presented that will be useful in experimental investigation of this proposed new class of ferroelectrics.

First principles prediction of morphotropic phase boundaries in Bi-based ferroelectrics

Valentino R. Cooper,[1] Shigeyuki Takagi,[2] David J. Singh[1]

[1]Materials Science and Technology Division, Oak Ridge National Laboratory, Oak Ridge, TN, USA
[2]Institute for Materials Research, Tohoku University, Sendai, Japan

During the past few decades, the toxicity of lead has made the discovery of Pb free ferroelectrics the subject of much research. One fruitful avenue has been the exploration of Bi-based ferroelectrics. Similar to Pb, Bi has stereochemically active lone pairs and a small ionic radius, resulting in compounds with relatively large *A*-site cation displacements and Born effective charges in a small volume, producing high polarization, ***P***.[1] For piezoelectric applications, one approach to maximizing electromechanical response has been to alloy tetragonal and rhombohedral ferroelectrics. It has been demonstrated that the combination of two such compounds often results in a compositionally dependent region, the morphotropic phase boundary (MPB), where the crystal structure abruptly undergoes a transition between the macroscopic phases of the parent compounds.[2] In general, ferroelectric alloys near MPBs exhibit enhanced electromechanical responses when the parent compounds have high ***P***.[3]

We use density functional theory to study Bi-based ferroelectrics with the goal of exploring the possibility of discovering MPBs through alloying between rhombohedrally and tetragonally ordered ferroelectrics. Unfortunately, the majority of Bi containing compounds are either rhombohedrally distorted or inferior to $PbTiO_3$. For example, we predict that the pseudocubic, double perovskites like $Bi_{1/2}M_{1/2}Zn_{1/2}Nb_{1/2}O_3$ (B*M*ZN; M=Pb,Sr) have relatively high, (111) oriented, remnant polarizations of ≈80 μC/cm.[4, 5] However, it should be noted that, there is recent experimental evidence for supertetragonal Bi-based ferroelectrics, such as appropriately strained $BiFeO_3$.[6] Also, significantly enhanced tetragonality (with ***P*** 50% greater than that of PT) was observed in $BiZn_{1/2}Ti_{1/2}O_3$ both experimentally and by first-priniciples calculations, making it a good candidate for a tetragonal end member for piezoelectrics.[7, 8] (Of course, the supertetragonality of these materials limits their usefulness as ferroelectrics as they require strong electric fields to switch the polarization.)

Consequently, we examine the polarization as a function of composition for alloys of BZT with B. For the structures studied, we show that by alloying with other rhombohedrally oriented Bi-based materials that it is indeed possible to find MBPs (see Fig. 1), hinting at the possibility of high piezeoelectric responses.[9] Another benefit of alloying is that the lower polarization in the monoclinic phase near the cross-over region may foster switchable polarizations and thus these materials may be useful for ferroelectric/piezoelectric applications.

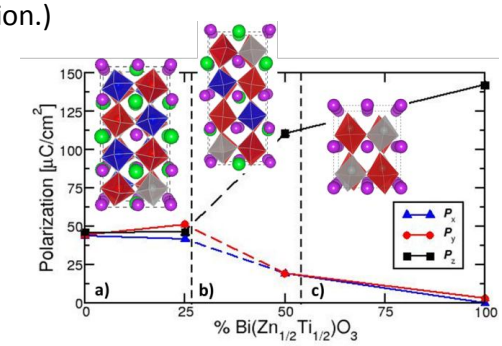

Figure 1 x-, y- and z-components of the of the polarization as a function of BZT concentration for alloys with $Bi_{1/2}Sr_{1/2}Zn_{1/2}Nb_{1/2}O_3$. The inset show the calculated structures which give rise to a) rhombohedral, b) monoclinic and c) tetragonal polarizations.

This work was supported by the Department of Energy, Office of Basic Energy Sciences, Materials Sciences and Engineering Division.

1. J. B. Neaton et al., Phys. Rev. B 71, 014113 (2005).
2. H. Fu, R. E. Cohen, Nature 402, 281 (2000).
3. R. Guo et al., Phys. Rev. Lett. 84, 5423 (2000).
4. S. Takagi, A. Subedi, D. J. Singh, V. R. Cooper, Phys. Rev. B 81, 134106 (2010).
5. S. Takagi, V. R. Cooper, D. J. Singh, Phys. Rev. B, (2011).
6. R. J. Zeches et al., Science 326, 977 (November 13, 2009, 2009).
7. M. R. Suchomel et al., Chem. Mater. 18, 4987 (2006).
8. T. Qi, I. Grinberg, A. M. Rappe, Phys. Rev. B 79, 094114 (2009).
9. V. R. Cooper, A. S. Henry, S. Takagi, D. J. Singh, (2011).

APPLICATIONS OF FERROELECTRIC POLYMER AND OLIGOMER THIN FILMS

Stephen Ducharme

Department of Physics and Astronomy, Nebraska Center for Materials and Nanoscience, University of Nebraska, Lincoln, NE 68588-0299, USA

Ferroelectric polymers and oligomers based on vinylidene fluoride (VDF) have received much attention in recent years for integration into a variety of functional devices. Among the reasons for this interest are the large spontaneous polarization, chemical stability, varied methods deposition and processing, and compatibility with commonly used functional materials. Many of these applications can be highly integrated because the polarization can be patterned by fabrication of nanostructures [1, 2], or by nanoscale control of polarization [3-7].

Integration with inorganic and organic semiconductors affords a wide range of devices, most exploiting the large polarization to control carrier type and density in a field-effect configuration, e.g., to make nonvolatile memory elements when integrated with silicon [8, 9], organic semiconductors [10, 11], or graphene, or to reduce energy dissipation by decreasing the device operating voltage [12]. Heterostructures incorporating ferroelectric polymers and oligomers have the potential to increase the efficiency of organic photovoltaic devices [13], and to make multiferroic transducers with metallic [14, 15] and semiconductor ferromagnets [16]. They can be incorporated into functional nanocomposites for use in electrostrictive transducers [17], as electrocaloric materials for refrigeration or energy harvesting [18], and in dielectrics for high-energy-density capacitors [19].

This research was supported by the National Science Foundation, the Department of Energy, and the Nebraska Research Initiative.

References

[1] M. Bai and S. Ducharme, "Ferroelectric Nanomesa Formation from Polymer Langmuir-Blodgett Films," *Applied Physics Letters,* vol. 85, pp. 3528-30, 2004.

[2] Z. Hu, M. Tian, B. Nysten, A. M. Jonas, "Regular arrays of highly ordered ferroelectric polymer nanostructures for non-volatile low-voltage memories," *Nature Materials,* vol. 8, pp. 62-66, 2009.

[3] K. Noda, K. Ishida, A. Kubono, T. Horiuchi, H. Yamada, and K. Matsushige, "Molecular ferroelectricity of vinylidene fluoride oligomer investigated by atomic force microscopy," *Japanese Journal of Applied Physics,* vol. 40, pp. 4361-4, 2001.

[4] K. Kimura, K. Kobayashi, H. Yamada, T. Horiuchi, K. Ishida, and K. Matsushige, "Orientation control of poly(vinylidenefluoride-trifluoroethylene) crystals and molecules using atomic force microscopy," *Applied Physics Letters,* vol. 82, pp. 4050-4052, 2003.

[5] B. J. Rodriguez, S. Jesse, S. V. Kalinin, J. Kim, and S. Ducharme, "Nanoscale polarization manipulation and imaging of ferroelectric Langmuir-Blodgett polymer films," *Applied Physics Letters,* vol. 90, p. 122904, 2007.

[6] R. V. Gaynutdinov, O. A. Lysova, S. G. Yudin, A. L. Tolstikhina, A. L. Kholkin, V. M. Fridkin, and S. Ducharme, "Polarization switching kinetics of ferroelectric nanomesas of vinylidene fluoride-trifluoroethylene copolymer," *Applied Physics Letters,* vol. 95, p. 023303, July 2009.

[7] P. Sharma, T. J. Reece, S. Ducharme, and A. Gruverman, "High-Resolution Studies of Domain Switching Behavior in Nanostructured Ferroelectric Polymers," *Nano Letters,* vol. 11, pp. 1970-1975, 2011.

[8] S. Fujisaki, H. Ishiwara, and Y. Fujisaki, "Low-voltage operation of ferroelectric poly(vinylidene fluoride-trifluoroethylene) copolymer capacitors and metal-ferroelectric-insulator-semiconductor diodes," *Applied Physics Letters,* vol. 90, p. 162902, 2007.
[9] A. Gerber, M. Fitsilis, H. Kohlstedt, R. Waser, T. J. Reece, S. Ducharme, and E. Rije, "Ferroelectric field effect transistor using very thin ferroelectric polyvinylidene fluoride copolymer Langmuir-Blodgett films as gate dielectrics," *Journal of Applied Physics,* vol. 107, p. 124119, 2010.
[10] G. H. Gelinck, A. W. Marsman, F. J. Touwslager, S. Setayesh, D. M. de Leeuw, R. C. G. Naber, and P. W. M. Blom, "All-Polymer Ferroelectric Transistors," *Applied Physics Letters,* vol. 87, p. 092903, March 2005.
[11] R. C. G. Naber, K. Asadi, P. W. M. Blom, D. M. d. Leeuw, and B. d. Boer, "Organic Nonvolatile Memory Devices Based on Ferroelectricity," *Advanced Materials,* vol. 21, pp. 1-13, 2009.
[12] G. A. Salvatore, D. Bouvet, and A. M. Ionescu, "Demonstration of subthrehold swing smaller than 60 mV/decade in Fe-FET with P(VDF-TrFE)/SiO_2 gate stack," in *Electron Devices Meeting, 2008. IEDM 2008. IEEE International*, San Francisco, 2008, pp. 1-4.
[13] Y. Yuan, T. J. Reece, P. Sharma, S. Poddar, S. Ducharme, A. Gruverman, Y. Yang, and J. Huang, "Efficiency enhancement in organic solar cells with ferroelectric polymers," *Nature Materials,* vol. 10, pp. 296-302, April 2011 2011.
[14] Ce W. Nan, M. Li, X. Feng, and S. Yu, "Possible Giant Magnetoelectric Effect of Ferromagnetic Rare-earth-iron-alloys-filled Ferroelectric Polymers," *Applied Physics Letters,* vol. 78, pp. 2527-2529, 23 April 2001.
[15] A. Mardana, M. Bai, A. Baruth, S. Ducharme, and S. Adenwalla, "Magneto-Electric Effects In Ferromagnetic Cobalt / Ferroelectric Copolymer Multilayer Films," *Applied Physics Letters,* vol. 97, p. 112904, 2010.
[16] I. Stolichnov, S. W. E. Riester, H. J. Trodahl, N. Setter, A. W. Rushforth, K. W. Edmonds, R. P. Campion, C. T. Foxon, B. L. Gallagher, and T. Jungwirth, "Non-volatile ferroelectric control of ferromagnetism in (Ga,Mn)As," *Nature Materials,* vol. 7, pp. 464-7, June 2008.
[17] V. Bharti and Q. M. Zhang, "Dielectric study of the relaxor ferroelectric poly(vinylidene fluoride-trifluoroethylene) copolymer system," *Physical Review B (Condensed Matter and Materials Physics),* vol. 63, p. 184103, 2001.
[18] B. Neese, B. Chu, S.-G. Lu, Y. Wang, E. Furman, and Q. M. Zhang, "Large Electrocaloric Effect in Ferroelectric Polymers Near Room Temperature," *Science (Washington, D. C., 1883-),* vol. 321, pp. 821-3, 8 August 2008.
[19] P. Kim, N. M. Doss, J. P. Tillotson, P. J. Hotchkiss, M.-J. Pan, S. R. Marder, J. Li, J. P. Calame, and J. W. Perry, "High Energy Density Nanocomposites Based on Surface-Modified $BaTiO_3$ and a Ferroelectric Polymer," *ACS Nano,* vol. 3, pp. 2581-92, 2009.

Poling Induced Fatigue in <100> Textured Lead-Free Piezoelectric $Na_{0.5}Bi_{0.5}TiO_3$ (NBT)

Chris Fancher[a], John E. Blendell[a], and Keith J. Bowman[b]

a School of Materials Engineering, Purdue University
b Department of Mechanical, Materials & Aerospace Engineering, Illinois Institute of Technology

$Na_{0.5}Bi_{0.5}TiO_3$ (NBT) is a promising piezoelectric material being investigated as a replacement for PZT in a variety of consumer electronics and actuator applications. NBT materials processed using conventional powder processing techniques do not achieve the piezoelectric performance of PZT; however, inducing a preferred orientation (texture) is one route to enhance the piezoelectric performance of NBT. Textured NBT samples were processed using the tape casting method with a 5wt% template fraction. The crystallographic texture was determined using the software package Materials Analysis Using Diffraction (MAUD)[1]. In this study, the fatigue of <100> oriented NBT was investigated as a function of poling temperature and time.

Textured NBT samples were prepared by tape casting calcined NBT powered with 5wt% template particles. Template particles were prepared using a double molten salt synthesis previously reported by Saito, Zhao, and Zeng et al. [2-4]. Tape cast samples were heated to 600°C to removed organics then fired at 1200°C. Figure 1 compares the XRD spectra of templated NBT and randomly oriented NBT. Sintered ceramics containing a 5wt% template fraction show a strong <100> preferred orientation. In the NBT system, the fraction of oriented material has typically been evaluated by measuring the relative peak intensities. In this study, the orientation distribution function (ODF) was described using both a discrete and harmonic methods. Texture refinement with the harmonic and discreet methods predicts significantly different texture levels, with the discreet model, E-WIMV, reached a maximum of 18.6 MRD, while a spherical harmonic method predicted a maximum texture of 34.4 MRD. This discrepancy suggests the exponential harmonic is ill suited to describe the ODF of highly oriented materials.

During poling, NBT develops both an internal bias field and a reduction in remnant polarization with increased poling time. This phenomenon was explored by poling samples for up to 1 hr in 5 minute increments at room temperature (RT), 50°C, 75°C, and 100°C. At RT, ferroelectric and piezoelectric loops were measured, while at elevated temperature only ferroelectric loops were measured. Figure 2 compares the ferroelectric and piezoelectric response: 1) prior to poling, 2) after poling for 15 minutes, and 3) after poling for 30 minutes. Prior to applying a poling field, textured NBT has a remnant polarization of 25 uC/cm^2. After applying a poling field for 30 minutes at RT, the remnant polarization has degraded to 18 uC/cm^2. Luo and Emkes et al. [5,6] proposed that near surface cracks is a mechanism for polarization degradation in the NBT-Barium Titanate material. The piezoelectric response shows the development of a greater asymmetry after poling for 30 minutes. In addition to an asymmetry, the strain crossover point shifts from ~0 MV/m to 1.2MV/m after poling for 30 min. Poling textured NBT at

60°C induced a 2.5 MV/m bias. This result is similar to work by Balke et al. [7] that concluded asymmetric strain could result from charge build up near domain/grain boundaries in PZT. Charge build up at domain boundaries could decrease their mobility and decrease the total ferroelectric response. However, microcracking may play a role in the polarization degradation.

[1] L. Lutterotti, S. Matthies, H.-R. Wenk, A.J. Schultz and J. Richardson, J. Appl. Phys., 81[2], 594-600, 1997

[2] Y. Saito and H. Takao, Journal of the Korean Physical Society, 51(2):790–797, 2007.

[3] W. Zhao, H. P. Zhou, Y. Yan, and D. Liu, J. Am. Ceram. Soc, 91(4):1322–1325, 2008.

[4] J. T. Zeng, K. W. Kwok, W. K. Tam, H. Y. Tian, X. P. Jiang, and H. L. W. Chan, J. Am. Ceram. Soc, 89(12):3850–3853, 2006.

[5] Z. Luo, J. Glaum, T. Granzow, W.Jo, R. Dittmer, M. Hoffman, J. Rodel, J. Am. Ceram. Soc., 94 [2] 529–535 (2011)

[6] M. Ehmke, J. Glaum, W. Jo, T. Granzow, and J.Rodel J. Am. Ceram. Soc., 94 [8] 2473–2478 (2011)

[7] N. Balke, D. C. Lupascu, T. Granzow, and J. Rodel, J. Am. Ceram. Soc., 90 [4] 1081–7 (2007).

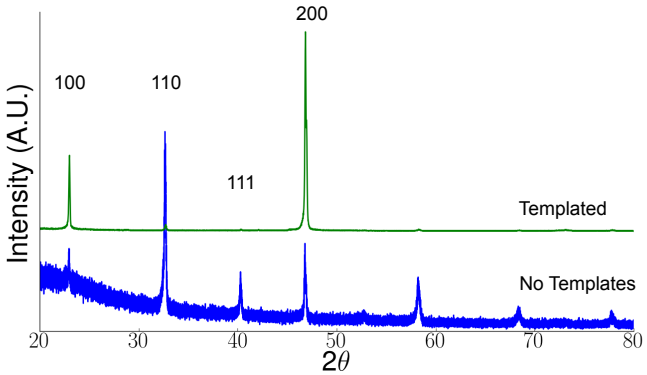

Figure 1 - XRD pattern of randomly oriented NBT and NBT tape cast with a 5 wt% template fraction.

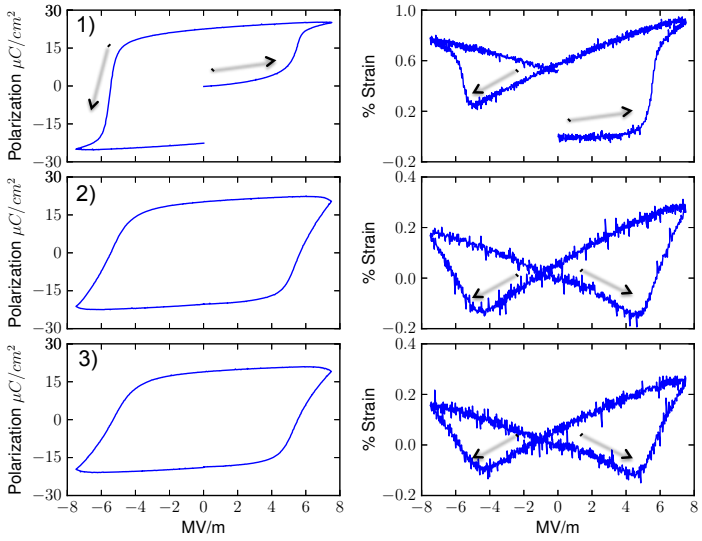

Figure 2 - Ferroelectric and piezoelectric response after: 1) virgin sample, 2) poling for 15 minutes, and 3) poling for 30 minutes.

Crossover between hybrid improper ferroelectricity and proper ferroelectricity in layered perovskites

Andrew T. Mulder, Nicole A. Benedek, Craig J. Fennie
School of Applied & Engineering Physics, Cornell University

Recent progress in designing materials with unconventional mechanisms of ferroelectricity has shown that nominally non-polar octahedral rotations can induce an electrical polarization in certain layered perovskites, e.g., the n=2 Ruddlesden-Popper $Ca_3Mn_2O_7$, and certain A-site ordered $AA'B_2O_6$ double perovskites. In these (what have recently been termed) hybrid improper ferroelectrics, two unstable octahedral rotations of different symmetries couple trilinearly with the polarization. We develop simple criteria for realizing this novel form of ferroelectricity in $A_3B_2O_7$ layered perovskites based solely on the properties of the ABO_3 parent. Then we explore how composition and epitaxial strain lead to different ferroelectric behaviors arising from the same rotation-polarization coupling. Finally we show how strain can tune a single material (Figure 1) between rotation-driven hybrid improper ferroelectricity and conventional proper ferroelectricity.

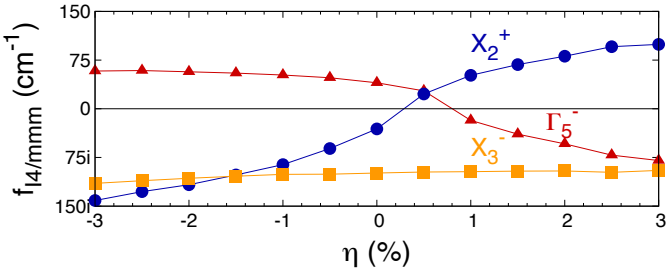

Figure 1: Calculated phonon frequencies of the improper rotational distortions (labeled X_2^+,X_3^-) and proper polar distortion (Γ_5^-) in the layered perovskite $Ba_3Zr_2O_7$ for different in-plane biaxial strains. Under compressive strain $Ba_3Zr_2O_7$ exhibits rotation-driven hybrid improper ferroelectricity, while under tensile strain $Ba_3Zr_2O_7$ exhibits conventional proper ferroelectricity.

Sm-doped $BiFeO_3$ films under compressive strain

Wei Ren,[1] Yurong Yang,[1,2] Weigang Chen,[3] Lu You,[3] Zuhuang Chen,[3] Yajun Qi,[3] Xi Zou,[3] Junling Wang,[3] Thirumany Sritharan,[3] Ping Yang,[4] Lang Chen,[3] and L. Bellaiche [1]

[1] *Institute for Nanoscience and Engineering and Physics Department, University of Arkansas, Fayetteville, Arkansas 72701, USA*
[2] *Physics Department, Nanjing University of Aeronautics and Astronautics, Nanjing 210016, China*
[3] *School of Materials Science and Engineering, Nanyang Technological University, Singapore 639798, Singapore*
[4] *Singapore Synchrotron Light Source (SSLS), National University of Singapore, 5 Research Link, Singapore 117603, Singapore*

(Dated: November 21, 2011)

Single-phase $BiFeO_3$ (BFO) bulk of rhombohedral structure has been intensively investigated. It exhibits a large spontaneous polarization that is oriented along the diagonal direction of the pseudocubic perovskite unit cell, as well as, oxygen octahedral tilting about this [111] direction. Moreover, a G-type antiferromagnetic ordering of magnetic moments on Fe^{3+} ions appears on the plane perpendicular to this direction. Properties of this important material can be widely modified through chemical substitution. For instance, Bi-substitution by rare earth elements (such as Sm) can give rise to a useful morphotropic phase boundary (MPB) separating rhombohedral and orthorhombic phases in *bulk solid solutions*[1].

Moreover, due to the strong coupling between polarization and strain, a rotation of polarization from the [111] to nearly [001] direction can be realized in highly strained BFO *films*[2]. Such strain engineering leads to a very large c/a tetragonality ratio, and an increased magnitude of polarization by 50%. The two phases, namely rhombohedral-like and tetragonal-like, can coexist and lead to the recent experimental observation of strain-driven MPB in pure BFO films[3].

Furthermore, in a recent work, we studied the interesting *interplay* of epitaxial strain and substitution of Bi by Sm atoms, by investigating highly strained Sm-doped BFO (BSFO) films and by comparing their properties with those of pure BFO films[4]. In particular,

structural and ferroelectric properties, as well as domain switching of a 10% Sm-substituted BFO thin film grown on a $LaAlO_3$ (LAO) substrate were revealed. Here, we will discuss these latter findings, as well as, report the energetics and properties of BSFO films for a large variety of epitaxial strains and also for different overall Sm compositions.

These works are supported by ONR Grants N00014-11-1-0384 and N00014-08-1-0915, NSF grants DMR-1066158 and DMR-0701558 and the Department of Energy, Office of Basic Energy Sciences, under contract ER-46612. Some computations were also made possible thanks to the ONR grant N00014-07-1-0825 (DURIP), the MRI grant 0722625 from NSF and a Challenge grant from the Department of Defense. MINDEF-NTU-JPP 10/12, NRF CREATE HUJ-BGU-NTU, and SSLS via NUS Core Support C-380-003-003-001 are also gratefully acknowledged.

References

1. Emery, S. B.; Cheng, C.; Kan, D.; Rueckert, F. J.; Alpay, S. P.; Nagarajan, V.; Takeuchi, I.; Wells, B. O., Phase coexistence near a morphotropic phase boundary in Sm-doped BiFeO3 films. *Appl. Phys. Lett.* **2010,** *97*, 152902.

2. Chen, Z.; Prosandeev, S.; Luo, Z. L.; Ren, W.; Qi, Y.; Huang, C. W.; You, L.; Gao, C.; Kornev, I. A.; Wu, T.; Wang, J.; Yang, P.; Sritharan, T.; Bellaiche, L.; Chen, L., Coexistence of ferroelectric triclinic phases in highly strained $BiFeO_3$ films. *Physical Review B* **2011,** *84* (9), 094116.

3. Zeches, R. J.; Rossell, M. D.; Zhang, J. X.; Hatt, A. J.; He, Q.; Yang, C.-H.; Kumar, A.; Wang, C. H.; Melville, A.; Adamo, C.; Sheng, G.; Chu, Y.-H.; Ihlefeld, J. F.; Erni, R.; Ederer, C.; Gopalan, V.; Chen, L. Q.; Schlom, D. G.; Spaldin, N. A.; Martin, L. W.; Ramesh, R., A Strain-Driven Morphotropic Phase Boundary in BiFeO3. *Science* **2009,** *326* (5955), 977-980.

4. Chen, W.; Ren, W.; You, L.; Yang, Y.; Chen, Z.; Qi, Y.; Zou, X.; Wang, J.; Sritharan, T.; Yang, P.; Bellaiche, L.; Chen, L., Domain structure and in-plane switching in a highly strained $Bi_{0.9}Sm_{0.1}FeO_3$ film. *Appl. Phys. Lett.* **2011,** *99*.

Structural, electronic, and vibrational properties of chloride-based perovskites : A first-principles study

Srijan Kumar Saha, and Philippe Ghosez[1]

[1] *Physique Théorique des Matériaux, Université de Liège, B-4000 Sart Tilman, Belgium*

Using first-principles density functional theory, we determine the structural, electronic and vibrational properties of various chloride-based perovskites of the family CsBCl$_3$ with B = Eu, Hg, Si, Ge, Sn, Pb, Mg, Ca, Sr, Ba.

We start from the high-symmetry cubic phase, for which electronic band structures, charge-density plots, Born effective charges and phonon dispersion curves are reported. In many of these compounds, we find the coexistence of structural antiferrodistortive instabilities at the zone-boundary points and a ferroelectric instability at the zone center. In particular, for $CsEuCl_3$, from the inspection of the unstable modes in the phonon dispersion curves, various possible types of lattice distortions are determined and the energies of the corresponding phases are calculated. Even though, a long time back $CsEuCl_3$ was experimentally reported to be a ferroelectric material, we here find that the strong antiferrodistortive motions suppress ferroelectricity and are responsible for a non-polar orthorhombic ground state. We nevertheless find that some members of the family such as $CsSiCl_3$ or $CsGeCl_3$ exhibit giant anomalous Born effective charges and phonon dispersion curves similar to $BaTiO_3$ and display a ferroelectric ground state. The tendency to ferroelectricity in terms of the type and size of the B cation will be discussed.

Properties of epitaxial (110) $BaTiO_3$ films from first principles

Zhigang Gui, S. Prosandeev and L. Bellaiche

Physics Department and Institute for Nanoscience and Engineering, University of Arkansas, Fayetteville, Arkansas 72701, USA

Epitaxial ferroelectric (FE) thin films have been intensively investigated since the last decade due to improved or original properties compared to their bulk counterparts. Examples include enhanced spontaneous polarizations, significant electromechanical responses associated with low-symmetry phases, and large sensitivity of Curie temperature with misfit strain[1-4]. All the aforementioned novel features concern FE thin films that are grown along the [001] pseudo-cubic direction. On the other hand, studies aimed at determining and understanding the effects of the *growth direction* on properties of FE epitaxial films are rather scarce[5-9].

Here, we investigate epitaxial (110) $BaTiO_3$ (BTO) films. Figure 1 reveals its temperature-versus-misfit strain phase diagram, as predicted by the use of an effective Hamiltonian approach.

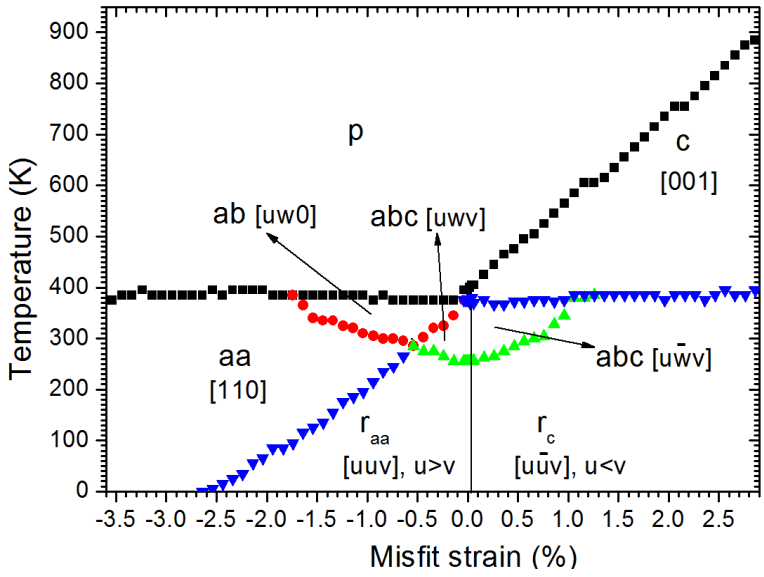

Figure 1: Predicted temperature-*versus*-misfit-strain diagram in epitaxial (110) BTO film. The direction of the polarization for each phase is indicated in the (xyz) coordinate frame near the phases' names.

Our simulations yield some unusual features. For instance, the Curie temperature, T_C, is nearly independent of compressive strain, unlike in (001) BTO films. It has a value of 385K, which is our predicted T_C of BTO bulk – which is very close to its

experimental value[10]. The microscopic origin of this insensitivity will be revealed. Moreover, low-symmetry phases are found near room temperature: an unexpected triclinic phase and three distinct monoclinic phases emerge in the temperature-*versus*-misfit strain diagram for relatively small strains. Such latter phases allow (i) the polarization to easily rotate with strain, which generates large piezoelectric and dielectric responses near room temperature; and (ii) the (110) BTO film to easily switch its polarization's direction via a transition between different low-in-symmetry phases, by applying in-plane and out-of-plane electric fields. Items (i) and (ii) are promising to design miniaturized and lead-free devices.

This work is supported by ONR Grants N00014-11-1-0384 and N00014-08-1-0915, NSF grant DMR-0701558 and the Department of Energy, Office of Basic Energy Sciences, under contract ER-46612. Some computations were also made possible thanks to the MRI grant 0959124 from NSF, N00014-07-1-0825 (DURIP) from ONR and a Challenge grant from HPCMO of the U.S. Department of Defense.

References

1. B.-K. Lai, I. Kornev, L. Bellaiche, and G. Salamo, Appl. Phys. Lett. **86**, 132904 (2005).
2. O. Dieguez *et al*, Phys. Rev. B **69**, 212101 (2004).
3. N. A. Pertsev, A. G. Zembilgotov, and A. K. Tagantsev, Phys. Rev. Lett. **80**, 1988 (1998).
4. J. H. Haeni *et al.,* Nature (London) **430**, 758−761 (2004).
5. N. A. Pertsev, A. K. Tagantsev, and N. Setter, Phys. Rev. B **61**, 825(R) (2000).
6. I. Ponomareva and L. Bellaiche, Phys. Rev. B **74**, 064102 (2006).
7. R. Oja, K. Johnston, J. Frantti and R. M. Nieminen, Phys. Rev. B **78**, 094102 (2008).
8. K. Sone *et al*, Jpn. J. Appl. Phys. **49**, 09MB03 (2010).
9. S. Prosandeev, Igor A. Kornev, and L. Bellaiche, Phys. Rev. Lett. **107**, 117602 (2011).
10. K. J. Choi *et al.,* Science **306**, 1005 (2004).

"Temperature evolution of the linear birefringence in striated single crystals of $KTa_{1-x}Nb_xO_3$ (KTN)"

Daniel K. Jackson[1], Radha Pattnaik[2], and Jean Toulouse[1]
[1]Department of Physics, Lehigh University, Bethlehem, PA 18015, USA
[2]Department of Physics, Lafayette College, Easton, PA 18042, USA

We report the temperature evolution of a special linear birefringence in 3 crystals of $KTa_{1-x}Nb_xO_3$ (KTN), with x=0.155, 0.27 and 0.36 respectively, upon approaching the cubic-tetragonal phase transition. This birefringence, which is not expected in the cubic phase, is caused by growth striations in the crystal which give rise to local strain and, due to the photoelastic effect, result in an effective uniaxial behavior. The set of parallel striations also acts as a volume phase grating that can produce diffracted beams. Upon approaching the phase transition, the measured birefringence displays a rapid temperature dependence which is due to the formation of polar nano-domains (PND's). These are incipient tetragonal uniaxial domains preferentially oriented with their c-axis perpendicular to the plane of the striations. As the birefringence increases, the diffraction efficiency unexpectedly decreases, indicating that the phase grating amplitude is diminished by the PND formation. The striation pattern is well defined in the 15.5% crystal, more diffuse in the 36% crystal, and there are no obvious striations in the 27% crystal. Experimental results are presented and a simple phenomenological model for the birefringence behavior is proposed and discussed. The results for KLTN 15.5% (2.3% Li doped) are shown below. The experimental arrangement was a standard Kerr cell with polarizer, analyser, collimating lenses, photodiode and a beam splitter to reduce the 633 nm laser intensity to ~ 1 microW. The laser was propagated approximately parallel to the striations along a plane of incidence that included the normal vector of the crystal striations. This geometry predicts no birefringence from the coupled wave theory of volume phase gratings.

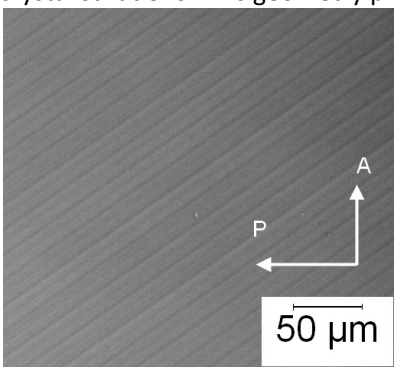

Figure 1: Striations of KLTN-15% with deliberately patterned striations as seen through crossed polarizers at room temperature. The striations are oriented at ~45 degrees to the polarizer. The KLTN15.5 was grown by an off-center TSSG method using periodic air flow to regulate the growth rate

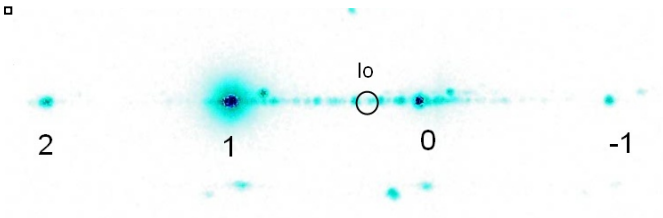

Figure 2: KLTN-15% has 4 observable diffraction spots, 0.0424 radians apart. 97% of the transmitted intensity is contained in the spots labeled 0 and 1. The zeroth order beam is the closest beam to the undiffracted incident beam location shown as Io, and the cause of the shift of this beam is the lack of parallelism between the entrance and exit surfaces of the crystal.

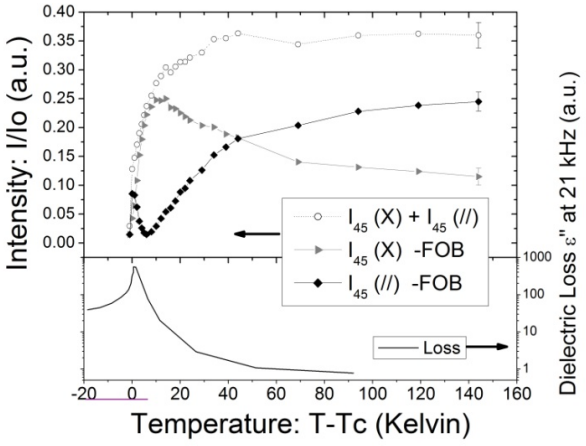

Figure 3:Normalized output intensity for first order beam (FOB) with laser polarization oriented at 45 degrees relative to the striation axes. Dielectric loss data is shown.

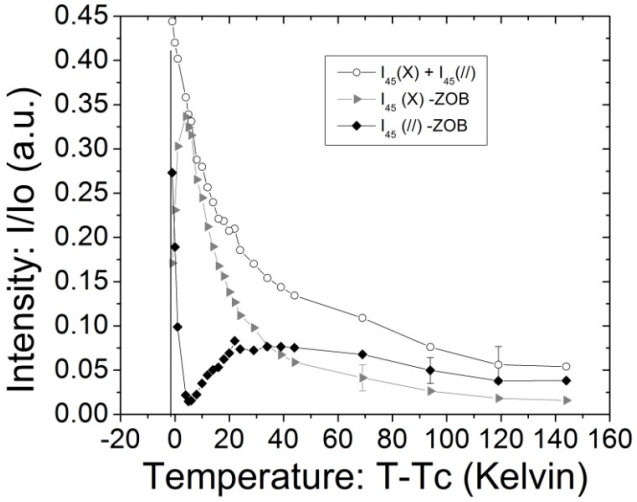

Figure 4: Normalized output intensity for zeroth order beam (ZOB) with laser polarization oriented at 45 degrees to the striation axes.

The optical transmission through a birefringent crystal between crossed polarizers is given by

$$I = I_o\left[\cos^2\chi - \sin 2\phi \sin\left(2\phi - 2\chi\right)\sin^2\left(\frac{\Gamma}{2}\right)\right]; \qquad \Gamma = \frac{2\pi}{\lambda} L\delta n; \qquad \delta n = \left[\frac{a}{\left(T - Tc\right)^{\alpha}} + c\right]$$

where I_o is the light intensity incident on the crystal, $\cos^2\chi$ comes from Malus's law for the output intensity transmitted through two polarizers with their principal axes (PA) aligned at an angle χ with respect to each other. The second term in the left bracket describes the output through a uniaxial crystal with ϕ being the angle between the input polarization vector and one of the principal axes of the material. Γ is the phase difference between the ordinary and extraordinary beam paths in the crystal and is a function of crystal length, L, laser wavelength, λ, and the effective birefringence is estimated by the authors as δn. The exponent α, with constants a and c, were varied to identify the best fit to the data and the results for 3 crystals are shown in table 1 and figure 5.

The data in figure 3 shows the change in intensity of the first order diffracted beam in the KLTN-15.5% sample with a dielectric loss measurement at 21 kHz. The increase of the dielectric loss in KTN is regarded as the energy loss due to the re-orientation of the PND's at low frequency ac voltages and is thus a key indicator of their formation. The dielectric loss profile also shows broadening with increasing Nb concentration (comparison not shown). The peak in the dielectric loss reveals the temperature of the phase transition and these values are shown table 1. The intensity through crossed (I_{45}(X)) and parallel (I_{45}(//)) polarizers are also shown with their sum, which decreases upon approach to the transition. This decrease can be understood as a loss of diffraction efficiency, which is confirmed by the rapid increase in the zeroth order beam intensity seen in figure 4. There was an abrupt loss of intensity below the transition due to critical opalescence, which occurred for all 3 samples. Above T_c +40 K, the effective birefringence caused by the strain is slowly varying with temperature, but a change of slope in these curves occurs near T_c +40 K, and the birefringence begins to vary more rapidly upon approach to the transition. This rapid change is due to the PND's which are oriented along the strain field and thus the larger inherent uniaxial birefringence of the tetragonal domains begins to dominate the strain induced birefringence. The loss of diffraction efficiency must be due to a change in the pattern or modulation strength of the striations, such as would be caused by the formation of PND's. The birefringence shown in figure 5 includes all 3 of the crystals studied. All crystals have a critical behavior upon approach to the transition which is consistent with the Landau-like phenomenological model used, but a good fit to the KTN-27% sample was not possible due to the plateau seen near 20 K. The strength of the high temperature strain birefringence is apparently dependent on both the Nb concentration as well as the strain modulation amplitude.

In conclusion, niobium concentration modulations are responsible for diffraction and a volume birefringence at high temperature, in the cubic phase of KTN or KLTN. Our results suggest that future investigations of KTN materials, particularly refractive index and elastic constants, should refer to the striation orientation as these may produce a substantial modification to bulk values.

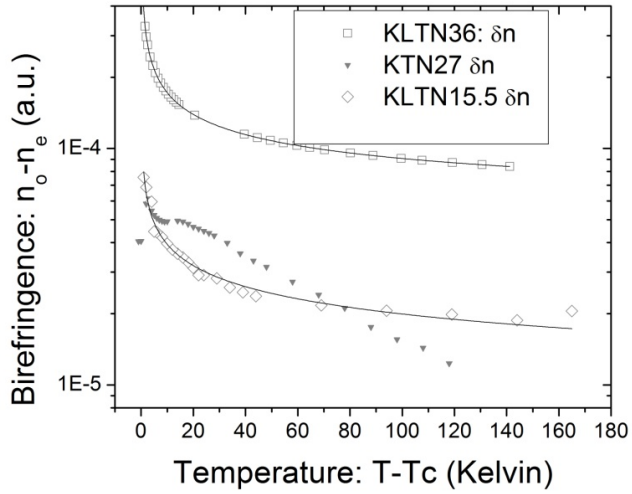

Figure 5: The effective birefringence fits as calculated from equation 1. The Semi-Log plot was chosen for visual clarity, the lines are best fit solutions using equation 1 and parameters from table 1.

Table 1: parameters for best fit of δn given above to the measured birefringence curves shown in Fig.5

Parameter	KLTN36	KLTN 15.5	KTN 27
a (K^{α})	3.42E-4	7.76E-5	
c	3.84E-5	1.74E-6	
α	0.408	0.315	
Tc (K)	275	131	213

Ferroelectric phase transition in GeTe studied by time-domain THz spectroscopy

F. Kadlec, C. Kadlec, P. Kužel, and J. Petzelt

Institute of Physics, Academy of Sciences of the Czech Republic, Na Slovance 2, 182 21 Prague 8, Czech Republic

Germanium telluride (GeTe) is a narrow-gap semiconductor with conducting properties important for applications. Like the related ternary chalkogenide alloys $Ge_xSb_yTe_z$, which have similar properties, it belongs to so-called phase change materials, which are convenient for use in current and future memory and data storage applications [1]. Amorphous GeTe thin films have an electrical conductivity orders of magnitude lower than the crystalline state. GeTe has only two atoms in the unit cell, and thus it is the simplest known ferroelectric (FE); upon heating, it becomes paraelectric (PE) at $T_c \approx 350\,^\circ$C.

While Raman spectra showed phonon softening in the FE phase [2] upon heating and suggested a displacive character of the PT, there is no such evidence above T_c which would represent a clear proof in this sense. Recent XANES data [3] revealed no anomaly of the Ge-Te bond length at T_c, which may indicate an order-disorder behavior. Thus, a controversy persists about the character of its FE phase transition (PT); one of the main reasons is the impossibility to perform standard low-frequency dielectric spectroscopy measurements because of the high conductivity. The question about the PT character appears to be of fundamental interest.

We have studied high-temperature THz transmittance spectra of GeTe films. These were deposited as amorphous on fused silica glass substrates, then crystallized by annealing at 300 °C and covered by a ZnS-SiO_2 capping layer. Special care was taken of the substrate choice and characterization, which is necessary because the films have an optical thickness much lower than the substrates; even a small relative error in the knowledge of the substrate thickness brings a very high error in the optical constants of the film.

The complex permittivity spectra $\hat{\varepsilon}(\omega)$ were determined numerically from the complex transmittance. The imaginary part spectra $\varepsilon''(\omega)$ feature a $\propto 1/\omega$ rise at low frequencies, matching the Drude theory. Therefore, to simplify further analysis, we converted them to real conductivity, $\sigma'(\omega) = \omega\varepsilon''(\omega)$.

In the FE phase, the spectra of the real parts $\varepsilon'(\omega)$ and $\sigma'(\omega)$ are essentially flat. Upon heating, in agreement with the Van-der-Pauw measurements, the THz conductivity monotonically decreases up to the PT temperature, $T_c \approx 350\,^\circ$C where it reaches a flat minimum. This value of T_c is in agreement with earlier observations [2].

To simulate the spectra, we set up models of $\hat{\varepsilon}(\omega)$. For the FE phase, we used terms describing the high-frequency limit ε_∞, a harmonic oscillator, and free carriers conductivity σ_{DC}:

$$\hat{\varepsilon}_{FE}(\omega) = \varepsilon_\infty + \frac{\Delta\varepsilon\omega_0^2}{\omega_0^2 - \omega^2 - i\omega\Gamma} + \frac{i\sigma_{DC}}{\varepsilon_0\omega} \tag{1}$$

where ε_0 represents the vacuum permittivity, ω_0 is the oscillator frequency, Γ denotes its damping and $\Delta\varepsilon$ its contribution to $\varepsilon'(\omega)$. The phonon mode has to be included since it was observed in Raman spectra [2]; owing to high

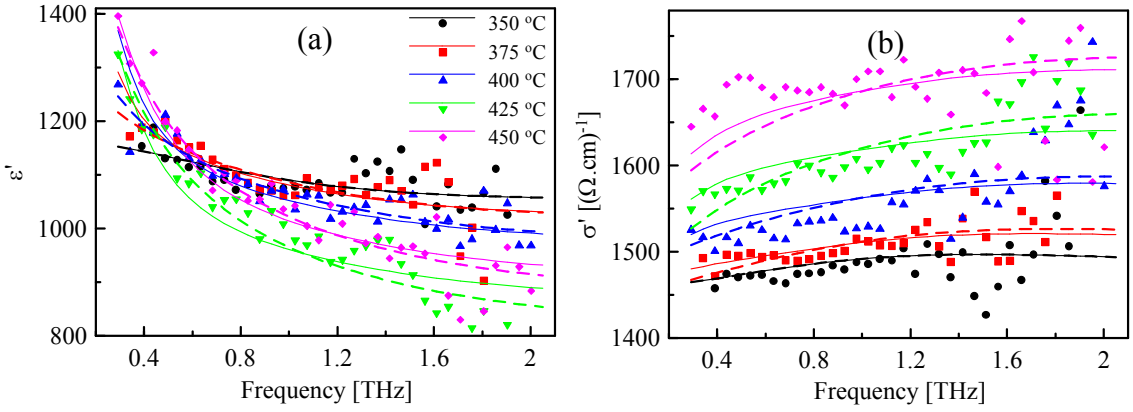

Figure 1: THz spectra of (a) real permittivity and (b) real conductivity of GeTe in the PE phase. Symbols: experimental data, solid and dashed lines: fits using Eqs. 2 and 3.

damping Γ, it gives rise to broad features in our spectra. We therefore fixed $\omega_0(T)$ according to values obtained from the Raman spectra. The calculated spectra are in good agreement with the measured ones. Only limited softening (to 1.5 THz) is seen, less than what is expected for a purely displacive PT.

In the PE phase, the THz conductivity rises with T; a marked curvature appears at low frequencies in the ε' spectra (see Fig. 1). This feature can be explained in two ways. In relation with the unknown nature of the PT, a critical relaxation mode, typical for a order-disorder PT, can be included to the model:

$$\hat{\varepsilon}_{\mathrm{PE}}(\omega) = \hat{\varepsilon}_{\mathrm{FE}}(\omega) + \frac{\Delta\varepsilon_{\mathrm{r}}\omega_{\mathrm{r}}}{\omega_{\mathrm{r}} - \mathrm{i}\omega} \tag{2}$$

where $\Delta\varepsilon_{\mathrm{r}}$ is its contribution to $\varepsilon'(\omega)$ and ω_{r} denotes its relaxation frequency. For order-disorder ferroelectrics, one would assume the Curie-Weiss law to be valid, $\Delta\varepsilon_{\mathrm{r}} = C/(T - T_{\mathrm{c}})$. Then, the relaxation frequency would increase linearly as $\omega_{\mathrm{r}} = a(T - T_{\mathrm{c}})$ and $\Delta\varepsilon_{\mathrm{r}}\omega_{\mathrm{r}}$ would be constant with T. The curves resulting from modeling based on Eq. 2 are shown in Fig. 1 by solid lines; they show a very good agreement with the experimental data. The proportionality constant has then the value of $a \approx 2.7 \times 10^{-3}\,\mathrm{THz\,K^{-1}}$ and the Curie-Weiss constant $C = (1.0 \pm 0.2) \times 10^5\,\mathrm{K}$.

Although the hypothesis of a relaxation mode is able to explain correctly the measured spectra, it is not the only possible one. In view of the relatively high conductivity of GeTe, one can equally assume the low-frequency shape of the spectra to be due to hopping. The films are polycrystalline and, as other phase-change materials, they consist of grains with a typical size of the order of 20 nm. We may therefore apply a hopping model, e.g. the one derived by Dyre [4]. This model was used to describe very similar conductivity spectra of photoexcited amorphous and microcrystalline silicon [5]. The model assumes an inhomogeneous material with a distribution of barrier energies; the probability of occurrence of all values for these energies is supposed to be the same. The relation for the complex permittivity can then be written as

$$\hat{\varepsilon}_{\mathrm{PE}}(\omega) = \hat{\varepsilon}_{\mathrm{FE}}(\omega) + \frac{\sigma_{\mathrm{H}}}{\varepsilon_0}\tau_{\min}\ln[1 + \mathrm{i}/(\omega\tau_{\min})] \tag{3}$$

where σ_{H} is the contribution of the hopping to the high-frequency conductivity and $\tau_{\min}$ is the minimum time that the free carriers need to hop from one site to another. We fitted our experimental data using Eq. 3, assuming $\tau_{\min}$ to be temperature-independent, since the local structure should not change on heating. The curves provided by the fit are shown by dashed lines in Fig. 1 and are also in a good accord with our data. The fit then yields a value of $\tau_{\min} = 190 \pm 30\,\mathrm{fs}$; as for the hopping conductivity σ_{H}, its values provided by the fit show a marked increase with T, which would be a rather unusual behavior.

We performed the first time-domain THz spectroscopy study of the FE PT in GeTe thin films. In the PE phase, we observed a new low-frequency feature which may be either a sign of an order-disorder behavior, or, less probably, due to hopping of charge carriers. As the phonon softening is limited, the PT seems to be of a mixed (displacive and order-disorder) nature.

Financial support by the Funding Agency of the Czech Republic (project No. 202/09/J045) is acknowledged.

References

[1] M. Wuttig, D. Lüsebrink, D. Wamwangi, W. Welnic, M. Gilleßen, and R. Dronskowski, "The role of vacancies and local distortions in the design of new phase-change materials," *Nature Materials*, vol. 6, pp. 122–128, 2007.

[2] E. Steigmeier and G. Harbeke, "Soft phonon mode and ferroelectricity in GeTe," *Solid State Communications*, vol. 8, no. 16, pp. 1275–1279, 1970.

[3] P. Fons, A. Kolobov, M. Krbal, J. Tominaga, K. Andrikopoulos, S. Yannopoulos, G. Voyiatzis, and T. Uruga, "Phase transition in crystalline GeTe: Pitfalls of averaging effects," *Physical Review B*, vol. 82, no. 15, p. 155209, 2010.

[4] J. C. Dyre, "The random free-energy barrier model for ac conduction in disordered solids," *Journal of Applied Physics*, vol. 64, no. 5, pp. 2456–2468, 1988.

[5] L. Fekete, P. Kužel, H. Němec, F. Kadlec, A. Dejneka, J. Stuchlík, and A. Fejfar, "Ultrafast carrier dynamics in microcrystalline silicon probed by time-resolved terahertz spectroscopy," *Physical Review B*, vol. 79, no. 11, p. 115306, 2009.

Can we trust the temperature - misfit strain thin film phase diagrams?

Alexander Kvasov and Alexander Tagantsev
Ceramics Laboratory
École Polytechnique Fédérale de Lausanne
CH-1015 Lausanne, Switzerland

Strain engineering is a modern strategy to control material properties. It represents a technique which deals with semiconductor and ferroelectric thin films strained by a substrate. Such strain can be tensile or compressive and occurs due to the difference in lattice parameters of a film and an underlying substrate; it shifts a paraelectric-to-ferroelectric transition temperature or can even induce ferroelectricity in the material [1].

To describe the strained thin film behavior, it was found convenient to use temperature - misfit strain phase diagrams. First introduced by Pertsev et al. [2], such diagrams present polarization state depending on temperature and parent misfit strain appeared in the film after deposition it on the substrate.

Theoretical study of temperature - misfit strain phase diagrams can provide strain engineering with guide lines. Calculations of such diagrams involve Landau-Ginzburg-Devonshire theory or *ab initio* microscopic approach. First principle calculations [3] are sufficient and powerful, but require a lot of computations. Phenomenological approach based on Landau thermodynamic theory is much simpler and can be valuable. Phenomenology is widely used for phase field modeling [4], for calculations of single-domain [2] and poly-domain [5] thin film diagrams. However there is a considerable difference of results obtained by first-principle calculations and by calculations based on Landau phenomenological theory. What is the reason of such disparity? Is this a problem with an exploited scheme or we simply don't know the coefficients of thermodynamic energy expansion precisely enough? If we suppose that we know the coefficients quite precisely can we trust our thermodynamic description of a strained system, i.e. our phase diagram? This problem was already mentioned [6] and it seems the answer is rather "not always".

An existing issue with the standard description of strained systems can be demonstrated qualitatively by a simple scalar model. Let us describe a system with a Gibbs thermodynamic potential energy expansion keeping only one component of polarization P and stress σ:

$$G = \underbrace{\frac{\alpha}{2}P^2 + \frac{\beta}{4}P^4 + \frac{\gamma}{6}P^6 - \frac{s}{2}\sigma^2 - Q\sigma P^2}_{\text{"ordinary"}} \underbrace{- M\sigma^2 P^2 - R\sigma P^4 - \frac{N}{3}\sigma^3}_{\text{"high-order"}}, \tag{1}$$

where "ordinary" part represents Gibbs energy commonly used to describe ferroelectric systems and "high-order" terms (M, R - high-order electrostrictive coefficients and N - non-linear compliance) which are customarily neglected, because considerable effects were not expected, which is reasonable, for example, for bulk crystal. The situation for a clamped system is different. We can show this considering ferroelectricity in a clamped system, i.e. where the strain ϵ equals the misfit strain ϵ_0. To obtain an effective potential $\widetilde{G}$ for a clamped system we use the mechanical equation of state

$$\epsilon = -\frac{\partial G}{\partial \sigma} = s\sigma + N\sigma^2 + QP^2 + RP^4 + 2M\sigma P^2, \tag{2}$$

and exclude stress σ from (1). The $\widetilde{G}$ will be:

$$\widetilde{G} = G + \epsilon\sigma = \frac{\alpha^*}{2}P^2 + \frac{\beta^*}{4}P^4 + \frac{\gamma^*}{6}P^6 + \frac{\epsilon_0^2}{2s}, \tag{3}$$

where $\epsilon\sigma$ represents a work required to maintain a constant strain. Electro-mechanical interactions in such system lead to renormalization of α, β and γ:

$$\alpha^* = \alpha - \epsilon_0\frac{Q}{s} - \underbrace{\epsilon_0^2\left(\frac{M}{s^2} + \frac{QN}{s^3}\right)}_{\text{A}}, \tag{4}$$

$$\beta^* = \beta + 2\frac{Q^2}{s} + \underbrace{\epsilon_0\left(\frac{2MQ}{s^2} - \frac{R}{s} - \frac{NQ^2}{s^3}\right)}_{\text{B}}, \tag{5}$$

$$\gamma^* = \gamma - \underbrace{6M\frac{Q^2}{s^2} + 6R\frac{Q}{s} + 2N\frac{Q^3}{s^3}}_{\text{C}}. \tag{6}$$

Atomic order of magnitude estimates show that the corrections due to of high-order coefficients A and B are usually small for α, β (except the cases when low-order coefficients are unusually small) whereas C correction may be of the

same order of magnitude as γ (6). In this way the high-order coefficients, which are customarily neglected in majority of problems, should be included into thermodynamic energy expansion as far as γ is important for a description of a problem.

To illustrate this phenomena quantitatively we would like to show the influence of high-order terms on the temperature - misfit strain phase diagram for a single-domain (001)-oriented $BaTiO_3$ (BTO) thin film. Since the high-order coefficients are unknown we calculated them using *ab initio* methods namely "VASP" package. Further we took original coefficients set from [2], supplemented it with calculated high-order coefficients and recalculated the classical Pertsev's diagram from [2] (Fig. 1).

Figure 1 illustrates that high-order coefficients, which were usually neglected may introduce considerable changes to strained system. One should also notice that the inclusion of any of these coefficients leads to the disappearance of ac-phase which was not observed from the first principles [3] (Fig. 1b - 1d) and thus removes the existing contradiction.

Our analysis shows that an adequate Landau theory treatment of the thermodynamics of ferroelectric thin films (single-domain and poly-domain thin films calculations and phase field modeling) requires taking into account high-order electromechanical couplings and non-linear elasticity.

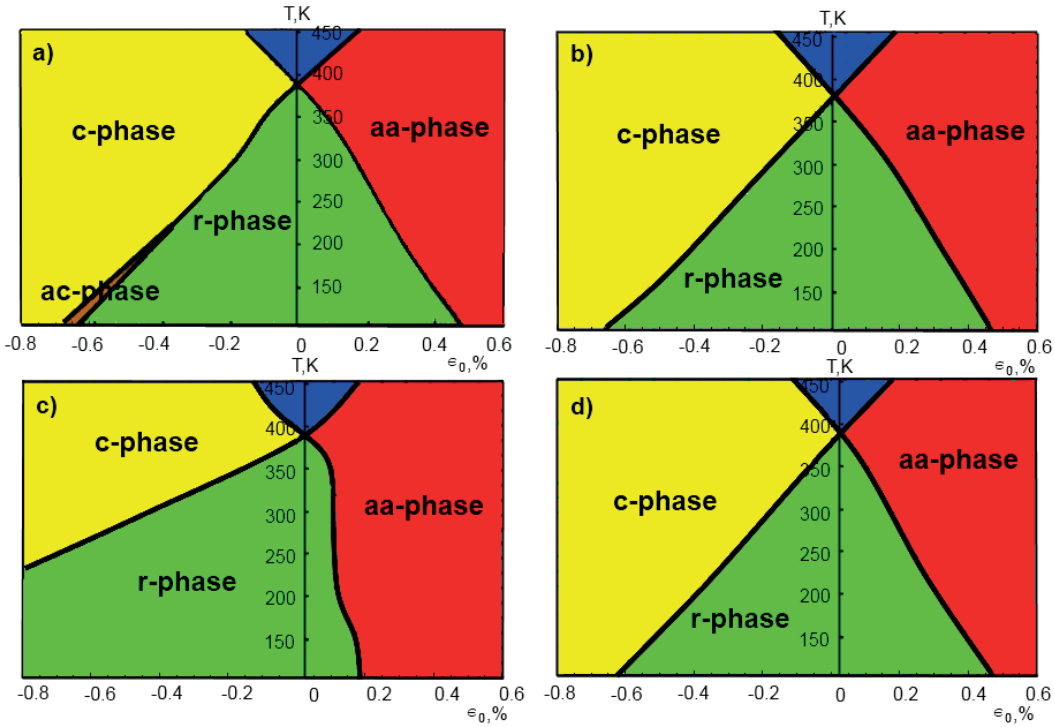

FIG. 1: Temperature - misfit strain phase diagrams of a single-domain (001)-oriented BTO thin film. ϵ_0 - biaxial parent misfit strain, T - temperature of the film. The phases are denoted as (i) the c-phase (yellow), polarization is out-of-plane ($P_1 = P_2 = 0, P_3 \neq 0$); (ii) the aa-phase (red), where polarization is in-plane ($P_1 \neq 0, P_2 \neq 0, P_3 = 0$); (iii) the ac-phase (brown) where $P_1 \neq 0, P_2 = 0, P_3 \neq 0$; (iv) r-phase (red), where all components of polarization are non-zero; and (v) paraphrase (blue), polarization is 0. (a) Original Pertsev's diagrams built with coefficients from [2]. (b) Phase diagram corrected with high-order M_{ijklmn} coefficients. (c) Phase diagram corrected with high-order R_{ijklmn} coefficients. (d) Phase diagram corrected with high-order N_{ijklmn} coefficients.

[1] J. H. Haeni, P. Irvin, W. Chang, R. Uecker, P. Reiche, Y. L. Li, S. Choudhury, W. Tian, M. E. Hawley, B. Craigo, et al., Nature **430**, 758 (2004).
[2] N. A. Pertsev, Z. G. Zembilgotov, and A. K. Tagantsev, Ferroelectrics **223**, 79 (1999).
[3] O. Dieguez, S. Tinte, A. Antons, C. Bungaro, J. B. Neaton, K. M. Rabe, and D. Vanderbilt, Physical Review B **69**, 4 (2004).
[4] Y. L. Li, S. Y. Hu, Z. K. Liu, and L. Q. Chen, Applied Physics Letters **78**, 3878 (2001).
[5] V. G. Koukhar, N. A. Pertsev, and R. Waser, Physical Review B **64** (2001).
[6] A. K. Tagantsev, N. A. Pertsev, P. Muralt, and N. Setter, Physical Review B **65**, 4 (2002).

Polarization Reversal in Ultrathin Ferroelectric Nanowires under High Electric Fields

Kevin McCash[1], Arvind Srikanth[2], Inna Ponomareva[1]
[1]*Department of Physics, University of South Florida, Tampa, Florida 33620, USA*
[2]*Department of Material Science and Engineering, University of Illinois at Urbana-Champaign, Champaign, Illinois 61820, USA*
e-mail: kmccash@mail.usf.edu

Ferroelectric nanostructures have attracted a lot of attention recently, thanks to their ability to develop electric polarization at the nanoscale [1–3]. Such a unique feature could potentially lead to the use of ferroelectric nanowires in nanoscale ultra fast, high-density memory elements.

Here we take advantage of accurate first-principles-based simulations to study ultra fast polarization reversal in ultrathin ferroelectric nanowires. We simulate seven nanowires made of $PbTi_{0.6}Zr_{0.4}O_3$ disordered alloy with the nanowire axis aligned along [001] pseudocubic direction. The nanowires have square cross sections with the lateral size in the range of 3.2-8.0 nm. Under open circuit conditions and below the Curie temperature such nanowires develop an electric polarization along the axial direction. To reverse the polarization direction we apply a *dc* electric field in the direction opposite to that of the polarization with the magnitude in the range of 0.1-7.9 MV/cm. Technically we use classical molecular dynamics simulations [4] with the force-field derived from the first-principles-based effective Hamiltonian [5–7] which allows us to trace the polarization evolution in response to such an electric field. To quantitatively characterize the polarization reversal we plot the inverse switching time as a function of the applied electric field (see Fig.1).

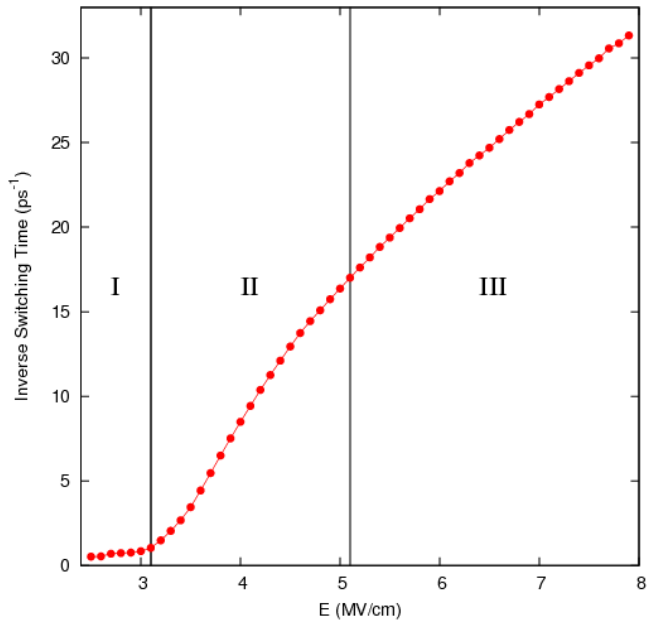

FIG. 1: Inverse switching time as a function of electric field strength for a wire with an 8x8 nm cross section at T=100K. Regions of different slope are separated by vertical lines.

This figure indicates that there exists three regions described by a different slope for the dependence of the inverse switching time on the electric field. We have identified that such regions are associated with the creep mechanism (region I), polarization reversal dominated by the dipole's flip along the nanowire radial direction (region II), and the polarization reversal dominated by the dipole's flip along the nanowire axial direction (region III).

We will report, analyze and compare the dependence of the switching time on the electric field for all studied nanowires obtained at two different temperatures.

The present work is supported by the U.S. Department of Energy, Office of Basic Energy Sciences, Division of Materials Sciences and Engineering under award DE-SC0005245. The use of services provided by Research Computing, USF is greatly acknowledged.

---

[1] H. Fu and L. Bellaiche, Phys. Rev. Lett **91**, 257601 (2003).
[2] P. Rorvik, T. Grande, and M.-A. Einarsrud, Adv. Materials **23**, 4007 (2011).
[3] A. Schilling, D. Byrne, G. Catalan, et al., Nano Letters **9**, 3359 (2009).
[4] D. Rapaport, *The Art of Molecular Dynamics Simulation* (Cambridge University Press, 2001).
[5] W. Zhong, D. Vanderbilt, and K. Rabe, Phys. Rev. B **52**, 6301 (1995).
[6] W. Zhong, D. Vanderbilt, and K. Rabe, Phys. Rev. Lett. **73**, 1861 (1994).
[7] L. Bellaiche, A. Garcia, and D. Vanderbilt, Phys. Rev. Lett. **84**, 5427 (2000).

Studies of Domain Structure and Phase Transitions in $PbZr_{1-x}Ti_xO_3$ Single Crystals

Yujuan Xie, Alexei A. Bokov, Xifa Long and Zuo-Guang Ye

Department of Chemistry and 4D LABS, Simon Fraser University, Burnaby, British Columbia, V5A 1S6, Canada

$PbZr_{1-x}Ti_xO_3$ (PZT) solid solution has been studied extensively over the past decades for both industrial application and fundamental research. Single crystals of PZT are highly demanded for the characterization of the anisotropic properties, and thereby for the understanding of the origin of high piezoelectric response in morphotropic phase boundary (MPB) compositions.

In this work $PbZr_{1-x}Ti_xO_3$ single crystal with composition x=0.21, x=0.42 and x=0.46 were grown by top-seeded solution growth (TSSG) technique. Domain structure and phase transitions have been studied on the $(110)_{cub}$ cut platelets by polarized light microscopy (PLM) combined with dielectric spectroscopy. At room temperature both x=0.21 and x=0.42 exhibit extinction at 35.3°, indicating a rhombohedral (R) symmetry. For the composition x=0.21 only one ferroelectric to paraelectric phase transition is observed at T_C=300 °C, as expected for the R region of PZT. The crystal with composition x=0.42, however, behaves differently upon heating. A change of extinction angle from 35.3° to 65° was observed in the temperature range of 300 °C to 372 °C (T_C). In addition, the temperature dependence of dielectric permittivity shows an anomaly at 335 °C. The intermediate phase above 300 °C could be assigned to the monoclinic phase of M_A symmetry according to the high resolution X-ray diffraction study on PZT ceramics by Noheda *et al.*[1]. The gradual change in the extinction angle to some extent supports the polarization rotation theory[2]. At room temperature the crystal with MPB composition x=0.46 shows an extinction at 68°, indicating an M_A symmetry, consistent with what was previously observed optically on the $(100)_{cub}$ crystal of the same composition[3]. Upon further heating an M_A to tetragonal (T) phase transition occurs with the extinction angle changing from 68° to 90° in the temperature range between 200 and 280 °C. The close free energy of the M_A and T phases makes it possible for the polarization to rotate in the (110) plane, which is experimentally observed in this study, providing a better understanding of the mechanism of high piezoelectric response in the MPB compositions. Based on these results, a revised PZT phase diagram with an extended area of MPB is proposed.

This work is supported by the U.S. Office of Naval Research (Grants No. N00014-06-1-0166 and No. N00014-11-1-0552).

References

1 B. Noheda, D. E. Cox, G. Shirane, R. Guo, B. Jones, and L. E. Cross, Phys. Rev. B **63**, 014103 (2001).

2 Huaxiang Fu and Ronald E. Cohen, Nature **403**, 281 (2000).

3 A. A. Bokov, X. F. Long, and Z. G. Ye, Phys. Rev. B **81**, 172103 (2010).

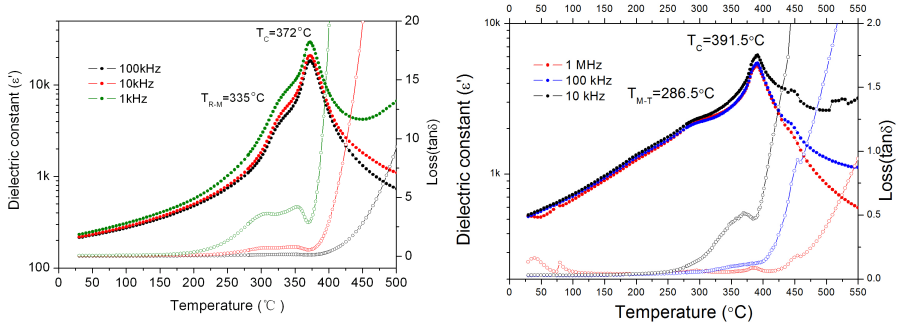

(a) (b)

Fig. 1. Temperature dependence of dielectric constant in (a) $Pb(Zr_{0.58}Ti_{0.42})O_3$ and (b) $Pb(Zr_{0.54}Ti_{0.46})O_3$ single crystals

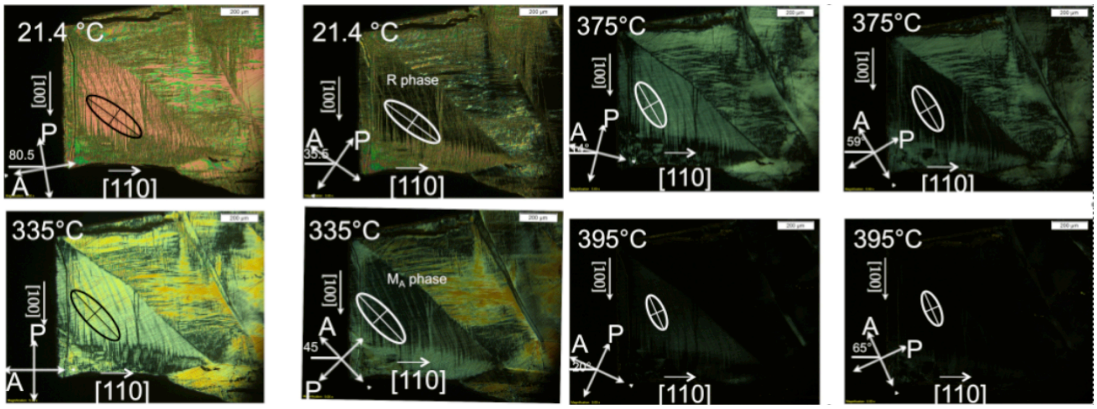

Fig. 2. PLM photos of (110) plate (0.023mm thick) of $Pb(Zr_{0.58}Ti_{0.42})O_3$ single crystal at different positions of crossed polarizers and temperatures

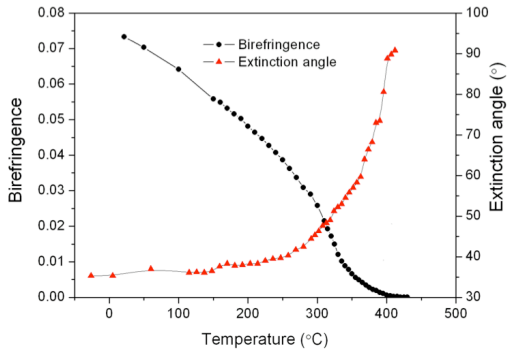

Fig. 3. The temperature dependence of birefringence and extinction angle of $Pb(Zr_{0.58}Ti_{0.42})O_3$ single crystal

Structural transition in $Pb(In_{1/2}Nb_{1/2})O_3$ under pressure

Muhtar Ahart[1](maihaiti@ciw.edu), Seiji Kojima[2], Z.-G. Ye[3], Russell J. Hemley[1]

[1]Geophysical Laboratory, Carnegie Institution of Washington,
5251 Broad Branch Rd., NW, Washington DC 2005

[2]Institute of Materials Science, University of Tsukuba,
Tsukuba, Ibaraki 305–8573, Japan

[3]Department of Chemistry and 4D LABS, Simon Fraser University,
Burnaby, BC, V5A 1S6, Canada

The Pb-based perovskite relaxor ferroelectrics and related materials are being used in a new generation of electromechanical devices. They have high piezoelectric coefficients with electromechanical deformations one order of magnitude larger than those of conventional high piezoelectric $PbZrO_3$-$PbTiO_3$ (PZT) ceramics [1,2]. The exceptional electromechanical properties of these Pb-based materials have generated intense interest in both scientific and industrial communities. While extensive theoretical and experimental studies have advanced our understanding of relaxors [3-8], their properties are still poorly understood. These difficulties stem from the complexity of these materials, which have a high degree of compositional, structural, and polar disorder.

Here we focus on the $Pb(B'_{1/2}B''_{1/2})O_3$-type relaxors, the degree of cation ordering at the B-site can depend on the heat treatment at high temperatures. A well-annealed sample of B-site ordered $Pb(Sc_{1/2}Nb_{1/2})O_3$ (PSN), $Pb(Sc_{1/2}Ta_{1/2})O_3$ (PST), and $Pb(In_{1/2}Nb_{1/2})O_3$ (PIN) undergoes a normal ferroelectric/antiferroelectric phase transition, while a quenched one with a B-site disorderd $Pb(B'_{1/2}B''_{1/2})O_3$ shows relaxor nature. Application of pressure can tune the physical properties of relaxors and introduce new phenomena [5,6].

We employed Raman scattering and x-ray diffraction to investigate the behavior of PIN under pressure up to 50 GPa at 300 K. Figure 1 shows a set of typical Raman spectra for PIN at selected pressures. The bands are broad in comparison to the first-order scattering of conventional ferroelectrics, such as $PbTiO_3$, which show sharp peaks in their polar phases. The sharp peak near the 370 cm^{-1} increases its intensity with pressure. The linewidth of the band at 550 cm^{-1} also increases with pressure, and two of the Raman peaks merge above 10 GPa. The structural phase transition is particularly associated with the splitting of the 50 cm^{-1} peak above 16 GPa. In most Pb-based relaxors, the Raman band at 50 cm^{-1} shows a slight hardening with pressure, but no splitting is observed at higher pressure. The pressure evolution of the diffraction patterns for PIN shows obvious splitting above 16 GPa, particularly for pseudo-cubic [110], [111] and [220] diffraction peaks; the results indicate a lowering symmetry transition in PIN.

In summary, we find that the Raman spectrum of PIN, contrary to most Pb-based relaxors, shows a splitting around 50 cm^{-1} peak above 16 GPa. The change is attributed to a structural phase transition from *R*3m to a non-cubic paraelectric phase above 16 GPa.

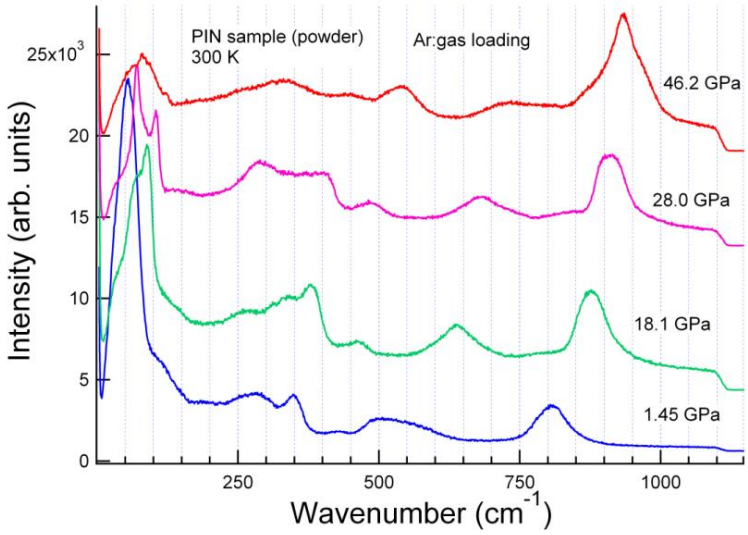

Figure 1. Representative Raman spectra of PIN at selected pressures.

This work was sponsored by the Carnegie/Department of Energy Alliance Center (CDAC, DE-FC03-03NA00144).

References:

1. S.-E. Park and T.R. Shrout, J. Appl. Phys. **82**, 1804 (1997).
2. D. Viehland, A. Amin, and J.F. Li, Appl. Phys. Lett. **79**, 1006 (2001).
3. H. Fu, R.E. Cohen, Nature **403**, 281 (2000).
4. D. Vanderbilt and M.H. Cohen, Phys. Rev. B **63**, 094108 (2001).
5. B. Noheda, D. E. Cox, and G. Shirane, J. Gao and Z.-G. Ye, Phys. Rev. B **66**, 054104 (2002).
6. B. Chaabane, et al., Phys. Rev. B **70**, 134114 (2004).
7. G. A. Samara, Phys. Rev. B **71**, 224108 (2005).
8. M. Ahart, M. Somayazulu, R. E. Cohen, P. Ganesh, P. Dera, H. K. Mao, R. J. Hemley, Y. Ren, P. Liermann, and Z. Wu, Nature **451**, 545 (2008).

The effects of Oxygen vacancies on properties of PMN-25%PT: a first-principles-based study

Abdullah Al-Barakaty[1] and L. Bellaiche[2],

[1]Physics Department, Teacher College-Makkah, Umm Al-Qura University, KSA
[2]Physics Department, University of Arkansas, Fayetteville, AR 727701, USA

Relaxor-based single crystals such as $(PbMg_{1/3}Nb_{2/3}O_3)_{1-x}$-$(PbTiO3)_x$ (denoted as PMN-PT) have been reported to exhibit excellent electromechanical properties. The high electromechanical performance characteristics of the relaxor-PT solid solutions is found for compositions at or near the morphotropic phase boundary (MPB) separating the rhombohedral and tetragonal phases. In addition to this MPB area, PMN-PT solid solutions are interesting and challenging to mimic because one of its end-member (PMN) is considered as the prototype of relaxors while its other end-member (PT) is a prototype of classical ferroelectrics. Our aim is to investigate the effects of oxygen vacancies on properties of the disordered PMN-25%PT system.

In this work, we first extend the effective Hamiltonian of pure PMN-PT to PMN-PT compounds possessing oxygen vacancies, by adding energetic terms that characterize the interactions of oxygen vacancies with local dipoles and strains. Then, we perform Monte-Carlo (MC) simulations on 20x20x20 disordered supercells to study the influence of homogenous and inhomogeneous distributions of oxygen vacancies into physical properties. The distribution is called homogenous if the concentration of the three possible kinds of oxygen vacancies (to be denoted by OVx, OVy and OVz, respectively) are approximately equal to each other: OVh=OVx=OVy=OVz. It is called inhomogeneous if one kind at least is different from the average OVinh=(OVx+OVy+OVz)/3. The outputs of MC simulations are the local mode u (proportional to electric polarization), homogenous strain, piezoelectric and dielectric responses. Some preliminary results are indicated in Figures 1 and 2.

While the phases of OVh=0% (with no oxygen vacancies) and OVh=2.5% at low temperature are both rhombohedral ($|ux| = |uy| = |uz| > 0$), the low temperature phases of OVinh=2.5% is not rhombohedral any more. These results, as well as others (about the switching of polarization), will be discussed in details. In particular, a connection with random fields will be drawn.

This work is supported by ONR grants N00014-11-1-0384, N00014-08-1-0915 and N00014-07-1-0825 (DURIP).

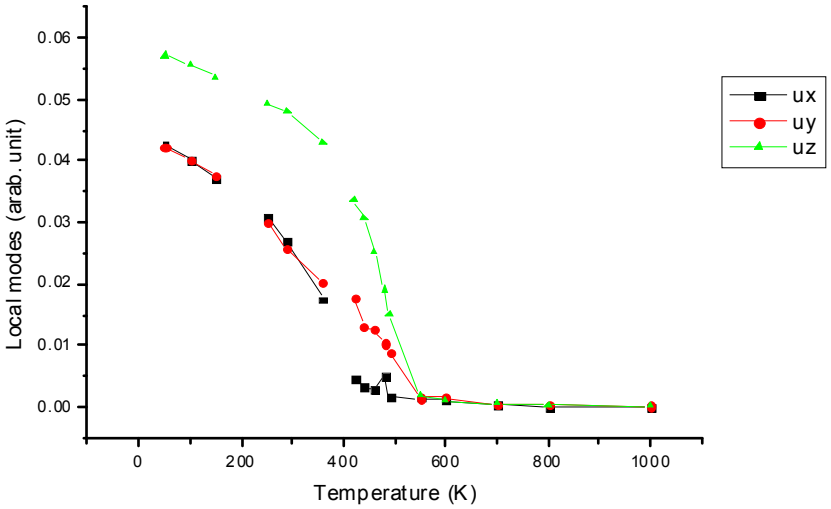

Figure 1: Local modes versus temperature for disordered PMN-25%PT with OVx=OVy=3% and OVz=1.5%. (OVinh=2.5%). The low temperature phase is monoclinic M_A (|ux|=|uy|<|uz|).

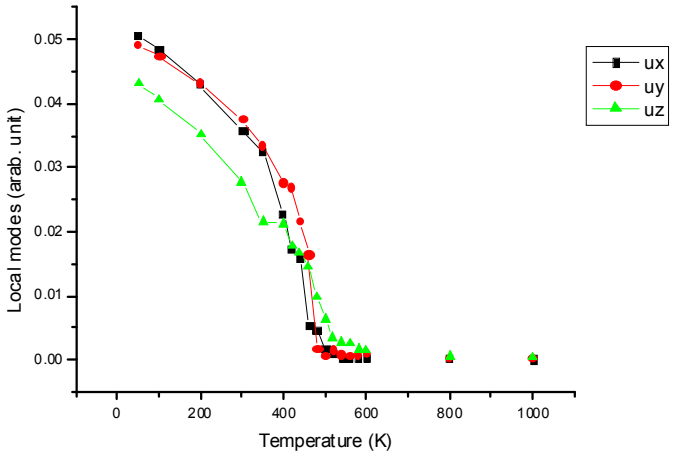

Figure 2: Local modes versus temperature for disordered PMN-25%PT with OVx=OVy=2% and OVz=3.5% (OVinh=2.5%). The low temperature phase is monoclinic M_B (|ux|=|uy|>|uz|).

Waterfall anomaly in $(Na_{0.5}Bi_{0.5})_{0.96}Ba_{0.04}TiO_3$ single crystal

P. Ondrejkovic[1], M. Kempa[1], J. Hlinka[1], J. Kulda[2], H. Luo[3], and Q. Zhang[3]

[1]*Institute of Physics, Academy of Sciences of the Czech Republic, Prague, Czech Republic*
[2]*Institut Laue-Langevin, Three-axis group, Grenoble, France*
[3]*Shanghai Institute of Ceramics, Chinese Academy of Sciences, Shanghai, China*

e-mail of the corresponding author: ondrejkovic@fzu.cz

Keywords: lead-free relaxor ferroelectric, morphotropic phase boundary, inelastic neutron scattering, phonon dispersions, waterfall anomaly, TO-TA coupling

Alkaline Bismuth titanate $(Na_{0.5}Bi_{0.5})_{1-x}Ba_xTiO_3$ (NBT-x%BT) solid solution is considered to rank among the most promising lead-free alternatives in actuator applications to the lead containing piezoelectric crystalline materials like $Pb(Mg_{1/3}Nb_{2/3})_{1-x}Ti_xO_3$ (PMN–PT), $Pb(Zn_{1/3}Nb_{2/3})_{1-x}Ti_xO_3$ (PZN-PT) or $Pb(Zr_xTi_{1-x})O_3$ (PZT). Why could the Bi containing material be a competitive alternative to the traditional lead containing materials? Both Bi^{3+} and Pb^{2+} cations share the identical electronic structure, high electric polarizability, and furthermore NBT-BT solid solution exhibits relaxor behavior and a smeared morphotropic phase boundary (MPB) between near-cubic rhombohedral and tetragonal phases like in PZT [1, 2]. The dielectric permittivity and piezoelectricity peak at MPB [3] where the coexistence of phases occurs. It means that the morphotropic NBT-BT is sensitive to electric field and consequently even relatively small electric field can irreversibly induce a ferroelectric phase in NBT-BT like in PMN relaxor [4,5].

Recently, NBT-BT single crystals with composition close to the MPB (x = 6 %) have been successfully grown by the top-seeded solution growth method [6]. Single crystal measurements show that [100], [110] and [111]-poled samples exhibit interesting piezoelectric and dielectric properties, which can be qualitatively explained by the effects of domain engineering [3]. The availability of single crystals made possible a more detailed investigation of lattice dynamics in this system, e.g. using Raman spectroscopy [7]. In this contribution, inelastic neutron scattering measurements on NBT-4%BT single crystal will be presented in a wide temperature range (80 – 900 K). The data have been partially published in Ref.8.

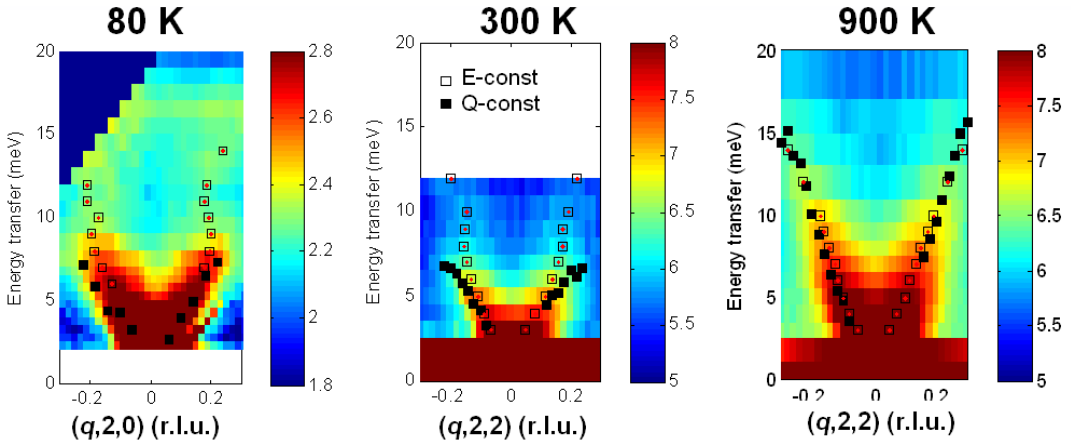

Fig. 1. Phonon dispersions of NBT-4%BT in the (220) and (020) Brillouin zones along the transverse direction at several temperatures. The collected data were independently analyzed as constant-energy scan sets (open squares: positions of Lorentzian bands) and constant-Q scan sets (full squares: frequencies of damped harmonic oscillators).

The aim of this presentation is to address the apparent vertical dispersion of soft branch (the so-called *waterfall anomaly*) in NBT-4%BT single crystal that is shown in Fig.1. The waterfall was first found in the PZN-PT relaxor crystals [9] and then observed in many other relaxor systems, e.g. PMN-PT [10]. Soon after its discovery, it was proposed that the phonon wave vector q_{wf}, at which the waterfall anomaly occurs, reflects the size of polar nanoregions in relaxors [9]. Nevertheless, the same phenomenon was also observed in simple non-relaxor ABO_3 perovskites (e.g. $BaTiO_3$ and $NaNbO_3$ single crystals [11,12]) in which the characteristic wave-vector value q_{wf} would indicate a domain size much smaller than the size of macroscopic ferroelectric domains. Therefore it is strongly suggested that the waterfall anomaly in relaxors is independent of the size of their polar nanoregions. The anomaly is also independent of chemical disorder, since although all these above mentioned compounds share the ABO_3 perovskite crystal structure, they differ significantly. The chemical disorder concerns the A-positions in NBT-BT, whereas rather B-positions in both PMN and PZN compounds. Moreover, the simple non-relaxor $BaTiO_3$ and $NaNbO_3$ perovskites are ideally free of disorder.

Our findings support a generic, anharmonic phonon-coupling nature of the waterfall anomaly [13] rather than a dependence on relaxor properties.

This work was partially supported by the Czech Ministry of Education (Project No. ME08109 and No. LG11024) and by the Grant Agency of the Czech Republic – the Czech Science Foundation (Project No. 202/09/H041), and by project No. SVV-2011-263307.

References:

[1] H. Simons, J. Daniels, W. Jo, R. Dittmer, A. Studer, M. Avdeev, J. Roedel, and M. Hoffman, *Appl. Phys. Lett.* **98**, 082901 (2011).

[2] S. Gorfman, D. S. Keeble, A.M. Glazer, X. Long, Y. Xie, Z.-G. Ye, S. Collins, and P.A. Thomas, *Phys. Rev. B* **84**, 020102(R) (2011).

[3] C. Chen, X. Jiang,Y. Li, F. Wang, Q. Zhang, and H. Luo, *J. of Appl. Phys.* **108**, 124106 (2010).

[4] J.E. Daniels, W. Jo, J. Roedel, and J.L. Jones, *Appl. Phys. Lett.* **95**, 032904 (2009).

[5] X. Zhao, W. Qu, X. Tan, A.A. Bokov, and Z.-G. Ye, *Phys. Rev. B* **75**, 104106 (2007).

[6] Q. Zhang, Y. Zhang, F. Wang, D. Lin, X. Li, X. Zhao, and H. Luo, *J. of Cryst. Growth* **312**, 457 (2010).

[7] I. Gregora, P. Ondrejkovic, E. Simon, M. Berta, M. Savinov, J. Hlinka, H. Luo and Q. Zhang , *Ferroelectrics* **404**, 220 (2010).

[8] P. Ondrejkovic, J. Hlinka, M. Kempa, J. Kulda, H. Luo, and Q. Zhang, *Phase Transitions* **84**, 829 (2011).

[9] P.M. Gehring, S.-E. Park, and G. Shirane, *Phys. Rev. Lett.* **84**, 5216 (2000).

[10] S. Wakimoto, C. Stock, Z.-G. Ye, W. Chen, P.M. Gehring, and G. Shirane, *Phys. Rev. B* **66**, 224102 (2002).

[11] G. Shirane, J.D. Axe, J. Harada, and A. Linz, *Phys. Rev. B* **2**, 3651 (1970).

[12] I. Tomeno, Y. Tsunoda, K. Oka, M. Matsuura, and M. Nishi, *Phys. Rev. B* **80**, 104101 (2009).

[13] J. Hlinka, S. Kamba, J. Petzelt, J. Kulda, C.A. Randall, and S.J. Zhang, *Phys. Rev. Lett.* **91**, 107602 (2003).

Molecular Dynamics Study of Local Structure and Dynamics in a Relaxor Ferroelectric

Hiroyuki Takenaka, Ilya Grinberg, and Andrew M. Rappe
[1] *The Makineni Theoretical Laboratories, Dept. of Chemistry, University of Pennsylvania, Philadelphia, PA 19104-6323,*
(Dated: December 2, 2011)

Recently, relaxor ferroelectrics have become important in technological applications resulting in a revival of interestn in this fundamental scientific problem. Compared with normal ferroelectrics, relaxor-based materials exhibit a stronger piezoelectric effect, a giant permittivity, and unique dielectric response which shows broadening peaks in temperature and frequency dispersion. Relaxors have been used in transducers for medical ultrasound equipment, actuators, electrical generators, infrared detectors and capacitors and are also expected to be useful for a variety of new applications. In terms of scientific interest, relaxors exhibit fascinating phase transitions on cooling. The inverse dielectric response starts deviating from the Curie-Weiss law at Burns temperature(T_d) significantly above the Curie temperature(T_c). These effects have been ascribed to the appearance of polar nanoregions (PNR) at T_b due to the random fields in the material, with the size and the interactions of the PNR increasing up to the freezing temperature (T_f). Despite many investigations of relaxors the detailed microscopic understanding of the connection between the structure and dynamics in relaxors is still lacking with no clear definition of the structural order parameter for the relaxor transitions.

In this work, we analyze the instantaneous $g(r,t)$, time-averaged $G(r,\omega=0)$ and dynamic $G(r,\omega)$ PDFs [1] obtained from molecular dynamics (MD) simulations of a 12×12×12 0.75$PbMg_{1/3}Nb_{2/3}O_3$-0.25$PbTiO_3$ (PMNT) supercell to examine the changes in local structure and dynamics through the relaxor phase transitions. Our previous atomistic simulations for this material has shown that even small 6×6 × 6 supercells exhibit all the dielectric signatures of relaxor behavior. [2] Comparison of our DPDF results with those of Dmowski et al shows good agreement between the experimental and computational DPDF intensity changes and suggests that our simulations are a good basis for investigating the structure and dynamics in relaxor ferroelectrics.

Analysis of cation-oxygen time-averaged and instantaneous PDFs clearly shows three phase transitions occurring at T_b=550 K, T^*=500 K and T_c=400 K. The values of all three transition temperatures are agreement with previous experimental work. We estimate the magnitude of Pb displacements by a difference in the Pb-O peak position from 2.8 Å peak position of the symmetric ($G(r,\omega=0)$ in the paraelectric (PE) phase and plot the $D_{\rm Pb}^{\rm Inst}$ obtained from $g(r,t=0)$ and $D_{\rm Pb}^{\rm avg}$ obtained from ($G(r,\omega=0)$ (Fig 1a). There are four distinct regions; at $T > Tb$, $D_{\rm Pb}^{\rm Inst}$ is small and $D_{\rm Pb}^{\rm avg}$ is zero. For 475 K< T <550 K, $D_{\rm Pb}^{\rm inst}$ increases rapidly, going from 0.15 Å to 0.35 Å while $D_{\rm Pb}^{\rm avg}$ is still zero corresponding to the dynamic relaxor phase. The increase in $D_{\rm Pb}^{\rm inst}$ is due to the greater local correlation between Pb displacements. Pb atoms displacements in the neighboring unit cells are coupled, so that a correlated displacement in the same direction (even if it is time-averaged to zero) allows a great magnitude of off-centering. The fact that a very local quantity such as Pb displacement magnitude shows order parameter behavior for a highly complex physical system such as relaxors is a signature of the local nature of the interactions underlying relaxor behavior.

To examine the correlations between Pb displacements, we investigate the temperature changes in peak heights of $g(r,t=0)$ for Pb-Pb partial PDFs (Figure 1b), plotting the heights of the Pb-Pb $g(r,t=0)$ along the (100), (110) and (111) directions. At $T > T_b$, we see that the data for (100), (110) and (111) all fall on the same curve, which can be fit to $g(r,t=0)=a+b/r^{1.5}$, indicating that the correlations and the potential energy surface is isotropic. Since the coupling constant is proportional to the square of the full width at half-maximum (FWHM), this means that the coupling between the displacements scales as r^3. This suggeststhat the interactions are purely or largely of the dipole-dipole kind. This is also the case for the Pb-Pb $g(r,t=0)$ of the PE phase of $PbTiO_3$ (Figure 1b). At 500 K, below T_b, the (110) and (111) data show only a slight difference from the (110) and (111) data at 600 K and both fall on the same curve. However, the (100) peak heights show two dramatic differences. First, they are larger and second, the dependence on r changes from $1/r^{1.5}$ to $1/r$. At 400 K the same behavior is observed, except that the data for the (100) direction are even higher, indicating stronger coupling between the nearest neighbor Pb atoms along the (100) direction.

Examination of the dynamic PDF data reveals the spatial extent of the correlation. Since DPDF intensity measures the in-phase oscillations of the atomic pairs, it is directly related to the in-phase oscillations of the individual dipole moments formed by the cation off-center displacement in its O cage. We find that all DPDFs exhibit peaks at 1-7 meV range, similar to the phonon energies at which the waterfall effect has been observed. The DPDF data along the (100) direction show a strong increase in the DPDF intensity at low ω starting at T_b. The intensity weakens as r increases from 4 Å to 20 Å, but the appearance of low-ω peaks at T_b and their shift to lower frequencies with lower T is present for all DPDF along the (100) direction as shown by the (400) peak DPDF data (Figure 2a). For the (110) and the

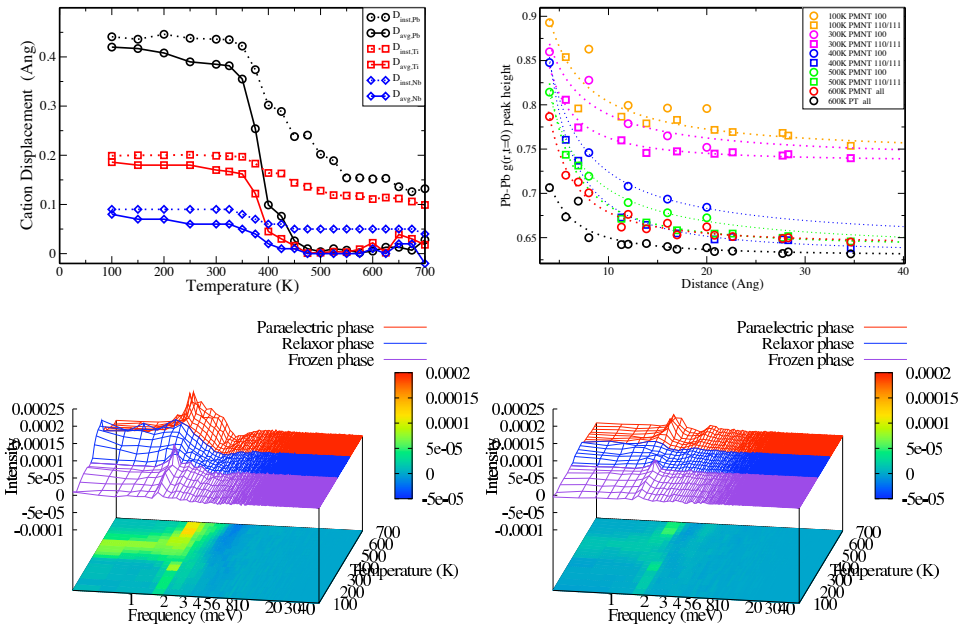

FIG. 1: a) The magnitude of the instantaneous and the time-averaged Pb, Nb and Ti off-center displacements as a function of temperature. (b) Pb-Pb $g(r, t = 0)$ peak heights versus distance for PMN-PT. Also shown are the rescaled peak height data for the Pb-Pb $g(r, t = 0)$ of the paraelectric phase of $PbTiO_3$. In the PE phase of PT and PMN-PT, the data for (100), (110) and (111) directions all fall on the same curve. For $T < T_b$, the data for (100) direction falls on a different curve from the data (110) and (111), indicating stronger coupling and higher correlation along the (100) direction. The lines through the data are given by the fit to $y{=}a{+}b/x$ for the (100) data, and to $y{=}a{+}b/x^{1.5}$ for all other data. (c) Dynamic Pb-Pb PDF for the (500) peak; strong intensity at low ω is present for $T < T_b$. (d) Dynamic Pb-Pb PDF for the (330) peak. Here, low intensity is observed for all T.

(111) directions, the increase in in-phase vibration intensity is observed for the short-range (110) and (111) peaks, but these effects decay dramatically with increasing distance, such that for the (330) and the (222) peaks, we find essentially zero DPDF intensity for all temperatures, indicating a complete lack of correlated in-phase oscillations. (Figure 2b). Thus, the region of correlation is strongly anisotropic, of cylinder-like shape, with a long axis along the (100) direction and with a radius of around 7.5 Å. This is slightly larger than the 5 Å estimated for the size of PNR by Gehring based on diffuse scattering data.

The current understanding of the relaxor transitions is that small and dynamic spherical PNR embedded into a paraelectric matrix form at T_b; the PNR then grow, show smaller polarization fluctuations and start to freeze in at T^*. At T_f a static inhomogeneous relaxor state is present consisting of static PNR in a statically non-polar matrix, with volume fraction of the PNR equal to 0.3. In contrast, we find strong anisotropy in the system for all temperatures, with the (100) direction showing strong correlation across several neighbor shells, however, for (110) and (111) only the nearest neighbor shells show correlations. Extending an analogy of Pirc and Blinc between the ferroelectric to paraelectric and the solid to liquid transition, we suggest that structure and dynamics of the relaxor phase are similar to those of water, where an overall dynamic nature is preserved while a random hydrogen bond network is formed, with preferential bonding directions and clusters of various sizes. In relaxors, at T_b a coupling network mediated by O atoms is formed on the Pb and the B-cation sublattices along the (100) directions. Similar to water, the directionality of the coupling gives rise to the complex dynamics.

[1] W. Dmowski, S. B. Vakhrushev, I.-K. Jeong, M. P. Hehlen, F. Trouw, and T. Egami, Phys. Rev. Lett. **100**, 137602 (2008).
[2] I. Grinberg, Y.-H. Shin, and A. M. Rappe, Phys. Rev. Lett. **103**, 197601 (2009).

Compositional inversion symmetry breaking in $PbTiO_3/SrRuO_3$ superlattices

S.J. Callori,[1] J. Gabel,[1] Dong Su,[2] J. Sinsheimer,[1] M.V. Fernandez-Serra,[1] and M. Dawber[1]

[1] *Department of Physics and Astronomy, Stony Brook University, Stony Brook, NY 11794-3800 USA*
[2] *Center for Functional Nanomaterials, Brookhaven National Laboratory, Upton, NY,USA*

Artificially layered oxide superlattices provide many opportunities to develop systems with novel and tunable properties. Perovskite oxides are particularly appealing to use as the parent materials for these artificial structures, as within relatively similar crystal structures a large number of distinct physical properties can be achieved by the placement of different cations on the A and B sites in the ABO_3 perovskite unit cell. As far as ferroelectric superlattices are concerned the insulating titanium perovskite oxides (e.g. $PbTiO_3$, $BaTiO_3$, $CaTiO_3$ and $SrTiO_3$) have to date been the most popular building blocks, but the need for new functionalities, particularly related to magnetism, demands that we expand this set.

The much-studied compound $SrRuO_3$ provides the proof of concept that metallic magnetic oxides can transform into thin-film dielectric components in certain heterostructures. In bulk, $SrRuO_3$ has the distorted perovskite orthorhombic Pnma structure, is metallic, and is ferromagnetic below Tc = 160 K ; it is a commonly used electrode material for oxides, and the interface with ferroelectric oxides has been much studied. However, $SrRuO_3$ becomes insulating in layers of thickness less than 4 unit cells; this behavior has been observed in thin films [1–3], and in $SrTiO_3/SrRuO_3$ superlattices[4, 5]. As we will show here, a similar effect also occurs in $PbTiO_3/SrRuO_3$ superlattices, with single unit cell thick $SrRuO_3$ layers in which display clear ferroelectric hysteresis.

A second motivation for creating $PbTiO_3/SrRuO_3$ superlattices is that, as they have both A and B site variation, inversion symmetry can be compositionally broken [6, 7]. A result of compositionally breaking inversion symmetry is that an asymmetry is introduced in the ferroelectric double well potential which can lead to "self-poling" materials. Compositional breaking of inversion symmetry has been demonstrated experimentally in tri-color superlattices containing $BaTiO_3$, $CaTiO_3$ and $SrTiO_3$ [8, 9], but little attention has been paid to the significance of these effects in bi-color superlattices.

High quality $PbTiO_3/SrRuO_3$ superlattices were made using rf-magnetron sputter deposition. X-ray diffraction, transmission electron microscopy (TEM), and atomic force microscopy (AFM) were used to ascertain film quality as well as determine layer thickness to ensure a single unit cell $SrRuO_3$ layer. The superlattices were grown to all have 1 u.c. thick layers of $SrRuO_3$, but $PbTiO_3$ layers of different thickness.

In $PbTiO_3/SrRuO_3$ superlattices where the $SrRuO_3$ is one unit cell thick, stoichiometric interfaces will compositionally break inversion symmetry. However, non-stoichiometry, which could occur on the local level, even in a sample which is globally stoichiometric overall, could lead to interfaces which maintain inversion symmetry (see Fig 1). Synchrotron x-ray

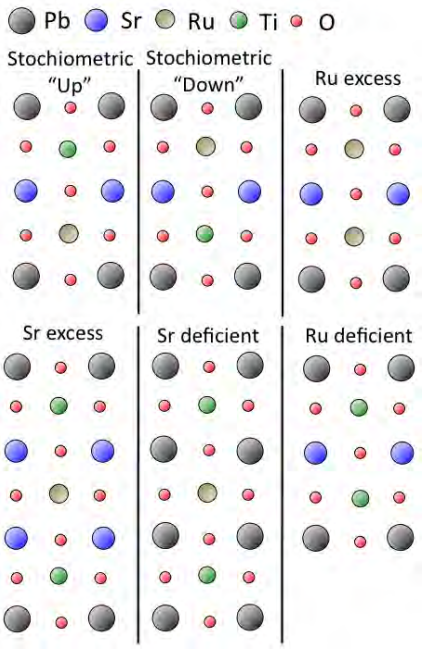

FIG. 1. *Six possible interfaces within a $PbTiO_3/SrRuO_3$ superlattice. The two marked "Stoichiometric" break inversion symmetry.*

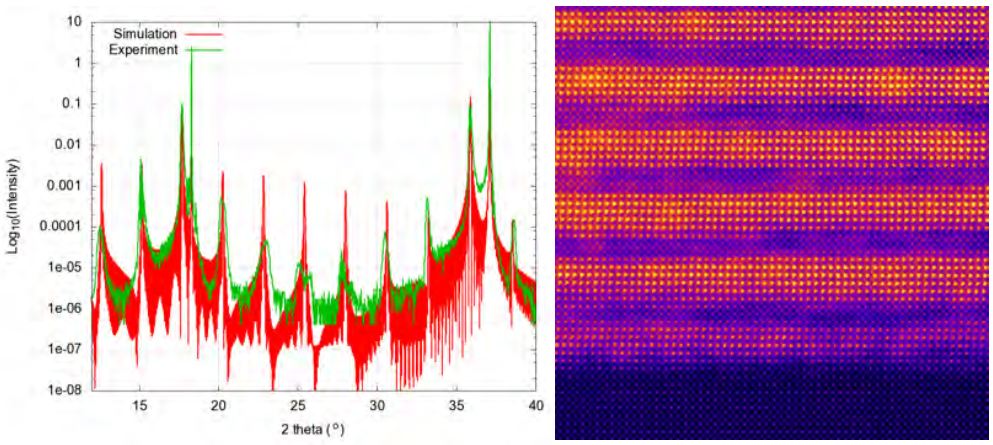

FIG. 2. *A 6/1 $PbTiO_3/SrRuO_3$ superlattice. Left: A $2\theta/\theta$ x-ray diffraction scan showing the 001 and 002 Bragg peaks, as well as superlattice satellite peaks. Right: A TEM image.*

diffraction at X22C at NSLS was performed and comparisons were made between simulated x-ray diffraction patterns for these interfaces and the experimentally measured patterns (Fig 2, left). These results tend to exclude the possibility of either the Sr or Ru excess interfaces. On the other hand as both Ru and Sr were found in the TEM image, (Fig 2, right) we can also exclude the Sr or Ru deficient interfaces, suggesting that we do indeed have the necessary interfaces to compositionally break inversion symmetry.

Our experimental evidence pointing towards stoichiometric, symmetry breaking interfaces is supported by the first principles calculations. Calculations were done to determine the formation energies of the possibly stoichiometric and non-stoichiometric. For most of the calculated superlattices, the stoichiometric interface was energetically preferred. Further evidence for the stoichiometric interface was obtained by measuring the average tetragonality (c/a) and polarization of the superlattices by x-ray diffraction and comparing to first principles results.

As the compositional breaking of inversion symmetry gives rise to novel dielectric properties, the samples dielectric constants were measured as a function of applied bias, and compared to the expected behavior predicted from an asymmetric double well potential. By combined analysis of ferroelectric hysteresis, dielectric response, leakage current and first principles calculations we have built a detailed picture of the role of the artificially layered structure and specifics of the interface in determining the properties of our artificial materials.

[1] D. Toyota, I. Ohkubo, H. Kumigashira, M. Oshima, T. Ohnishi, M. Lippmaa, M. Kawasaki, and H. Koinuma, *Appl. Phys. Lett.* **87**, 162508 (2005), *J. Appl. Phys* **99** 08N505 (2006).
[2] M. Schultz, S. Levy, J.W. Reiner and L. Klein, *Phys. Rev. B* **79** 123544 (2009).
[3] J. Xia, W. Siemons, G. Koster, M.R. Beasley and A. Kapitulnik, *Phys. Rev. B* **79**, 140407(R) (2009).
[4] M. Izumi, K. Nakazawa and Y. Bando, *J. Phys. Soc. Japan* **67** 651 (1998).
[5] H. Kumigashira, M. Minohara, M. Takizawa, A. Fujimori, D. Toyota, I. Ohkubo, M. Oshima, M. Lippmaa, and M. Kawasaki, *Appl. Phys. Lett.* **92** 122105 (2008).
[6] N. Sai, B. Meyer, and D. Vanderbilt, *Phys. Rev. Lett.*, **84**, 5636 (2000).
[7] N. Sai, B. Meyer, and D. Vanderbilt, *Fundamental Physics of Ferroelectrics*, , 218 (2001).
[8] M.P. Warusawithana, E.V. Colla, J.N. Eckstein, and M. B. Weissman *Phys. Rev. Lett.* **90** 036802 (2003).
[9] H.N. Lee, H.M. Christen, M.F. Chisholm, C.M. Rouleau and D.H. Lowndes, *Nature* **433**, 395 (2005).

Ferroelectric and Dielectric Properties of $BaTiO_3/Ba_{(1-x)}Sr_xTiO_3$ Superlattices

N. Ortega, Ashok Kumar, and R.S. Katiyar
Department of Physics and Institute of Functional Nanomaterials, University of Puerto Rico, San Juan, Puerto Rico 00931-3343

Artificially designed superlattices (SL) composed of alternate layers of $BaTiO_3$ (BT) and $SrTiO_3$ (ST) have attracted interests due to the possibility of producing superior and novel functional properties, which have potential for device applications. We have fabricated SL of $BT/Ba_{(1-x)}Sr_xTiO_3$ (BST) with x = 0, 0.3, 0.4, 0.5, 0.6, 0.7, 1, utilizing multi-targets and pulsed laser deposition technique. The modulation period (Λ) in all SL was Λ= 80 Å and the total thickness of each SL films was ~600 nm. The x-ray diffraction revealed well oriented (00l) perovskite structure and the so-called satellite peaks. The polarized Raman spectra showed a substantial transformation of the ferroelectric E(1TO) soft mode, depending on the ratio of Ba/Sr in the BST layer. The dielectric constant of SL showed linear frequency dispersion above 20 kHz, and their values are in the range of 400 to 900 at 1 kHz, while the tangent loss values were below 0.1 at 1 kHz. Well defined ferroelectric loops were observed in all of the superlattices at different frequencies (1 kHz-10 kHz), with remanent polarization ($2P_r$) ~10 $\mu C/cm^2$. An improvement in the saturation of the ferroelectric loop was observed with increase of Ba composition in BST layer. All of the fabricated superlattices show very low leakage current far above its coercive field.

Engineered polarization rotation in $PbTiO_3/CaTiO_3$ superlattices

J. Sinsheimer,[1] S.J. Callori,[1] Y. Benkara,[1] B. Bein,[1] J. Daley,[1] D. Su,[2] and M. Dawber[1]

[1] *Department of Physics and Astronomy, Stony Brook University, Stony Brook, NY 11794-3800 USA*
[2] *Center for Functional Nanomaterials, Brookhaven National Laboratory, Upton, NY,USA*

Large piezoelectric responses, such as those seen in $PbZr_xTi_{1-x}O_3$ in the vicinity of the compositional morphotropic phase boundary, can occur when the direction of the polarization in a ferroelectric material can rotate. Here we show experimentally that a similar enhancement of the piezoelectric response can be achieved in artificially layered epitaxial superlattices composed of alternating layers of $PbTiO_3$ and $CaTiO_3$ deposited on $SrTiO_3$ substrates by RF magnetron sputtering. The exceptional quality of our samples is demonstrated by x-ray diffraction and transmission electron microscopy.

The structural and functional properties of the materials have been measured as a function of relative layer thickness, and plotted in Fig 1 in terms of the $PbTiO_3$ volume fraction

$$X = \frac{N_{PTO}}{N_{PTO}+N_{CTO}}$$

where N refers to the number of unit cells of the material type (indicated by the subscript) in each bilayer. Electrically measured ferroelectric polarization and dielectric constants, corroborate the enhancement of d_{33} we have measured experimentally at volume fractions between 0.8 and 0.9 using piezoforce microscopy.

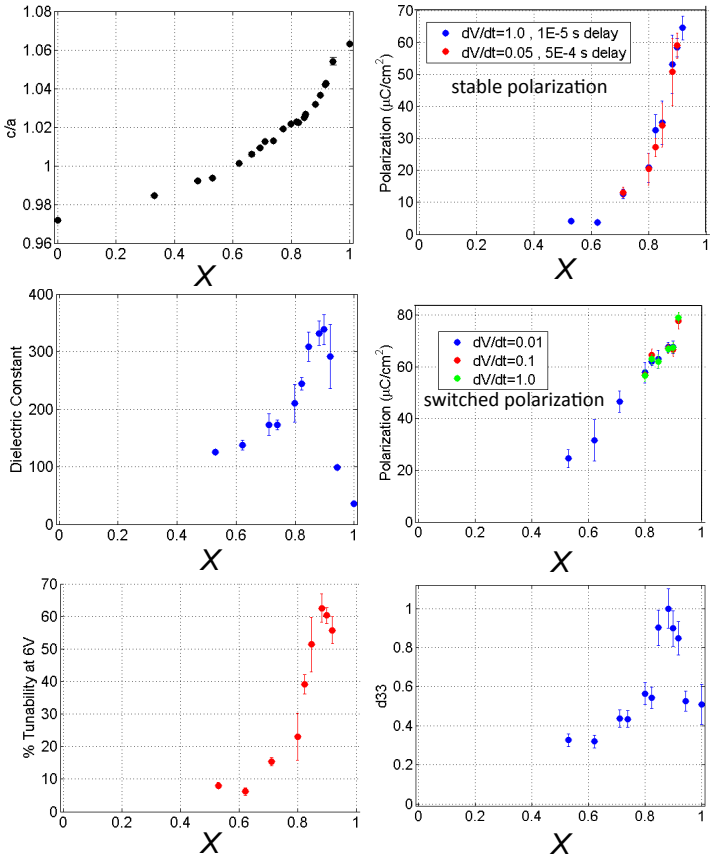

FIG. 1. *Experimentally measured properties of the superlattice as a function of the $PbTiO_3$ volume fractoin X. Left column, Top: Tetragonality.Left column, Middle: Dielectric constant at zero applied field. Left column, Bottom: Percent tunability of the dielectric constant for an applied voltage of 6V. Right column, Top: Stable ferroelectric polarization, Right Column, Middle: Total switched polarization (this is greater than the stable polarization as some of the polarization relaxes back to it's original configuration after switching). Right Column, Bottom: out of plane piezoresponse to an electric field applied out of plane, ie. d_{33}, units are arbitrary.*

The structural changes which allow polarization rotation have been directly measured using grazing incidence in-plane x-ray diffraction (at NSLS X21 and X22C) (Fig. 2) which show in-plane polarization components developing, initially along (100) transitioning to (110) as the thickness of $PbTiO_3$ layers in the superlattice is changed. Finally, the domain structure has been imaged with piezoforce microscopy, further confirming polarization rotation and explaining the unusual switching dynamics observed in our electrical characterization.

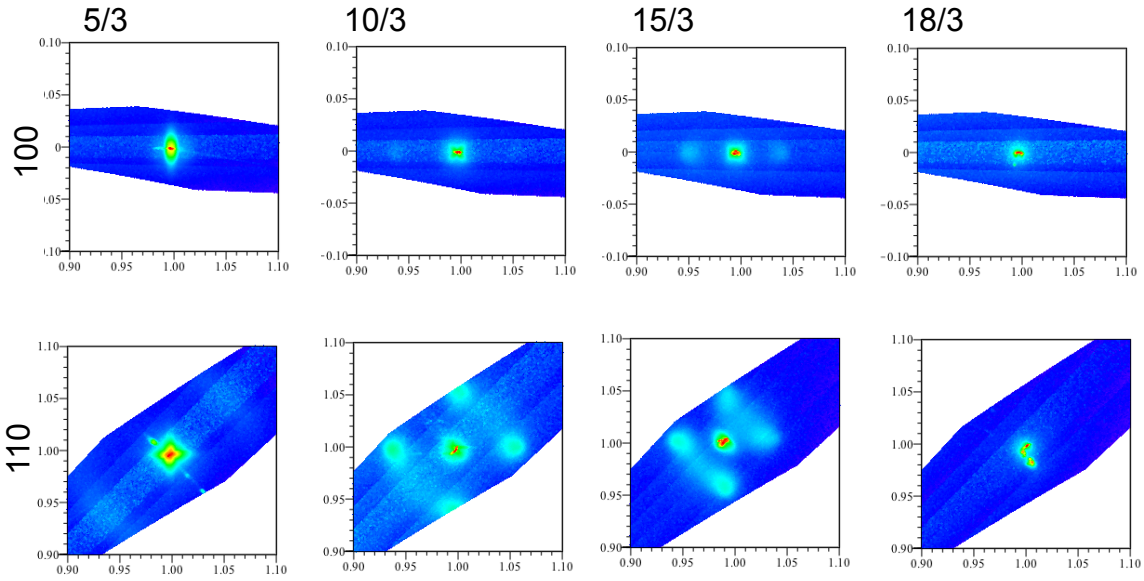

FIG. 2. *Grazing incidence surface x-ray diffraction was performed at the NSLS X21 and X22C beamlines allowing us to map in plane periodicities in reciprocal space in the vicinity of the substrate, which show how the polarization directions change as the thickness of the $PbTiO_3$ layer is changed. Shown are in-plane maps around the 100 and 110 $SrTiO_3$ substrate peaks for 4 samples going from 5/3 to 18/3, ie. the $PbTiO_3$ layer thicknesses within each bilayer is 5 units cells in the first map and 18 unit cells in the last. The $CaTiO_3$ layer within each bilayer is 3 unit cells thick.*

Our results are interesting as they highlight a route to engineering enhanced piezoresponse through the layering of material with competing desires regarding their polarization direction, even when the entire film is epitaxially constrained to a substrate.

Phase transitions in epitaxial $PbTiO_3/BiFeO_3$ superlattice from first principles

Yurong Yang[1,2], Wei Ren[1], Massimiliano Stengel[3] , X. H. Yan[2], and L. Bellaiche[1]

[1]*Physics Department & Institute for Nanoscience and Engineering, University of Arkansas, Fayetteville, Arkansas 72701, USA*

[2]*Physics Department, Nanjing University of Aeronautics and Astronautics, Nanjing 210016, China*

[2]*Institut de Ciència de Materials de Barcelona (ICMAB-CSIC), Campus UAB, 08193 Bellaterra, Spain*

Multiferroic $BiFeO_3$ (BFO) exhibits long-range-ordered and coupled electric and magnetic degrees of freedom in their bulk or low-dimensional forms [1,2], which partly explains why they are being so much studied. Heterostructures containing BFO have recently become an active research topic [3,4]. Here, we investigate the effect of epitaxial strain on properties of (001) $PbTiO_3/BiFeO_3$ (PTO/BFO) short-period superlattice (SL) films by performing first-principle calculations.

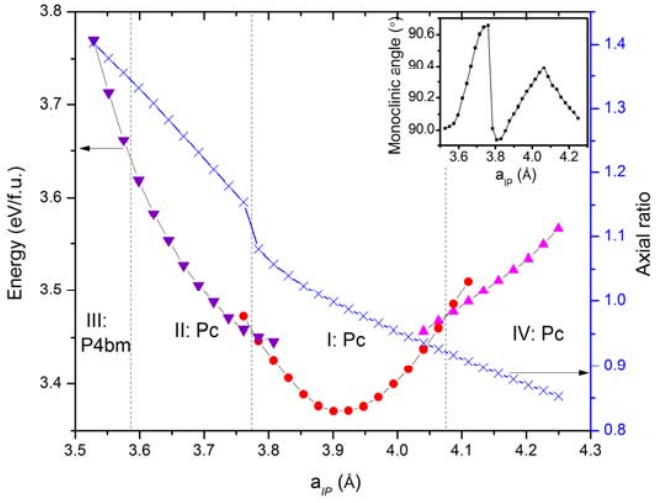

Figure 1. Predicted total energy (left vertical axis) and axial ratio (right vertical axis) versus the in-plane lattice parameter for the equilibrium phases in the $[PTO]_3/[BFO]_3$ superlattice. The inset displays the monoclinic angle.

Four phases and two resulting isosymmetric strain-induced phase transitions are discovered in the PTO/BFO SL. In the monoclinic *Pc* Phase-I and monoclinic *Pc*

Phase-II, which occur for in-plane lattice parameters ranging between 3.77 $<a_{IP}<$ 4.07 Å and 3.59 $<a_{IP}<$ 3.77 Å, respectively, the polarization and the axis about which the antiphase oxygen octahedra tilt rotate when varying the epitaxial strain. Giant out-of-plane polarization and large out-of-plane octahedra tilting are also found in the monoclinic *Pc* Phase-II. For the large compressively-strained PTO/BFO SL films (namely, for a_{IP} less than 3.59 Å), the equilibrium phase is now tetragonal *P4bm*. This phase is denoted as Phase-III, and is characterized by giant out-of-plane polarization and large out-of-plane octahedra tilting. Finally, for a_{IP} around 4.07 Å (which corresponds to tensile strains), the monoclinic *Pc* Phase-I transforms to a third monoclinic *Pc* state (Phase-IV). This latter state exhibits large in-plane polarization but also, surprisingly, a nonzero out-of-plane polarization. Unexpected in-phase out-of-plane octahedra tilting and inhomogenous cation motions are also found in this Phase-IV. Layer-by-layer decomposition of polarization and of oxygen octahedral tilting will also be presented, along with properties of pure (001) PTO and BFO films, in order to better understand the origins of the four aforementioned phases in the SL.

This work is supported by the Department of Energy, Office of Basic Energy Sciences, under contract ER-46612, ONR Grants N00014-11-1-0384 and N00014-08-1-0915, and NSF grants DMR-1066158 and DMR-0701558. Some computations were also made possible thanks to the ONR grant N00014-07-1-0825 (DURIP), a Challenge grant from the Department of Defense, and the MRI grant 0722625 from NSF.

References:

1.G. Catalan and J. F. Scott, Adv. Mater. **21**, 2463 (2009).

2. Wei Ren and L. Bellaiche, Phys. Rev.Lett. **107**, 127202 (2011).

3. Y. W. Li, Y. D. Shen, F. Y. Yue, Z. G. Hu, X. M. Ma, and J. H. Chu, J. Cryst. Growth **312**, 617 (2010).

4. L. Palova, P. Chandra, and K. M. Rabe, Phys. Rev. Lett. **104**, 037202 (2010).

Folded acoustic phonons in infrared spectroscopy of $BaTiO_3/SrTiO_3$ superlattices

V. Železný[1], C. Kadlec[1], A. Soukiassian[2], X.X. Xi[3], D.G. Schlom[2]

[1] Institute of Physics, ASCR, Na Slovance 2, 182 21 Praha 8, Czech Republic
[2] Department of Materials Science and Engineering, Cornell University, Ithaca, New York, 14853-1501, USA
[3] Department of Physics, Temple University, Philadelphia, Pennsylvania 19122, USA

In infinitive single crystalline samples acoustic phonons are infrared inactive because they have no electric dipole connected with their motion to couple to applied field and conservation laws for impulse and energy are not satisfied because of great difference between the velocities of light and sound. The situation is radically changed in a piezoelectric multilayer (superlattice) media. In a periodic superlattice, a new translational symmetry results in the folding of the Brillouin zone into a mini-Brillouin zone due to the artificial periodicity defined by the superlattice. This folding of the acoustic phonon branches gives rise to additional optic-phonon-like modes of the superlattice with non-zero frequencies at the center of the Brillouin zone. The folding of phonon dispersion causes an intersect of light-phonon dispersions and satisfies resonance condition. The mechanical deformation in piezoelectric materials produces electric polarization, which already can couple to external electric field. A quantitative explanation of the data can be improved in terms of a simple theory which involves the activation of the acoustic phonons due to their interaction with soft mode. Periodic superlattices of semiconductors and other materials have been extensively studied using spontaneous Raman scattering techniques since 1980s. Surprisingly little attention to our knowledge has been paid to the infrared studies of superlattices so far.
Here we report a experimental study of acoustic phonon modes in a $BaTiO_3/SrTiO_3$ ferroelectric perovskite superlattice. The reflectance measurements were performed on fully commensurate $[(BaTiO_3)_8/(SrTiO_3)_4]_{50}$ and $[(BaTiO_3)_8/(SrTiO_3)_4]_{40}$ superlattices fabricated from 8 and 4 unit cell thick $BaTiO_3$ and $SrTiO_3$ layers, respectively, repeated 40 or 50 times along the growth direction. They were grown by reactive molecular-beam epitaxy on (110) $DyScO_3$ and (110) $SmScO_3$ single crystal substrates. We demonstrate that the folded acoustic modes can be effectively observed by the far-infrared reflectivity (FIR) and terahertz reflectivity techniques. The both techniques give very similar results in the overlapping spectral range. Clear absorption features of first-order acoustic phonons in the spectra of perovskite $BaTiO_3/SrTiO_3$ superlattice are present. The observed frequencies match well with the calculated acoustic branches evaluated using their sound velocity. The high-order folded modes are very weak and therefore are not usually observed. This contrasts with semiconductor superlattices where up to 7 orders folded phonons have been observed but it is in agreement with Raman observation.
The experimental data provide a basis for creating a model, which explain the mechanism which makes the acoustic mode to be infrared active. Evidence exists of a strong coupling in these piezoelectric materials between acoustic vibrations and polarization. The presence of a permanent polarization below T_C leads to a strong electro-optic coupling which is proportional to the ferroelectric polarization. These two specific features, namely a strong coupling between acoustic vibrations and polarization, and between the latter and radiation, form a base for strong elasto-optic coupling operative in the ferroelectric phase.

This work was partially supported by the Grant Agency of the Czech Republic under Contract No. P204/11/1011 and by the Ministry of Education of the Czech Republic under Contract ME08109.

MEYER-NELDEL RULE FOR ELECTRICAL CONDUCTIVITY OBSERVATION IN xNBT–(1-x)LMT CERAMICS

Saulius Rudys[1], Maksim Ivanov[1], Juras Banys[1], Robertas Grigalaitis[1], Nikolai P. Vyshatko[2], Aleksandr D. Shilin[2], Andrei N. Salak[2]

[1]Faculty of Physic, Vilnius University, Sauletekio str. 9 III 817, LT-10222, Vilnius, Lithuania

[2]Institute of Solid State and Semiconductor Physics, P. Brovka str. 17, 220072 Minsk, Belarus

Lead-free ferroelectric ceramics with a perovskite structure based on $(Na_{0.5}Bi_{0.5})TiO_3$ (NBT) and $La(Mg_{0.5}Ti_{0.5})O_3$ (LMT) solid solutions were investigated using broadband dielectrics spectroscopy methods. Dielectric properties of the NBT–LMT ceramics in 100 Hz – 1 GHz frequency band were presented in [1].

In this work, the xNBT–(1-x)LMT ceramics with x equal to 0.80, 0.85, 0.90 and 0.95 were studied in 300 – 820 K temperature range and 1 MHz – 1 GHz frequency band. Dielectric measurements were carried out using Agilent 8714ET vector network analyzer with coaxial line setup. Since coaxial line is highly prone to oxidation, the measurements were done in argon atmosphere on cooling with a rate of 1 K/min. All samples were coated with Pt electrodes.

The impedance parameters were calculated using the dielectric data obtained from coaxial line measurements.

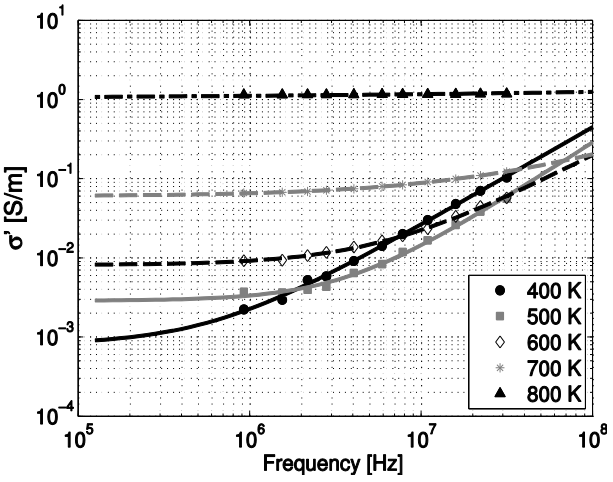

Figure 1. Frequency dependence of electric conductivity of xNBT–(1-x)LMT ceramics with x = 0.95.

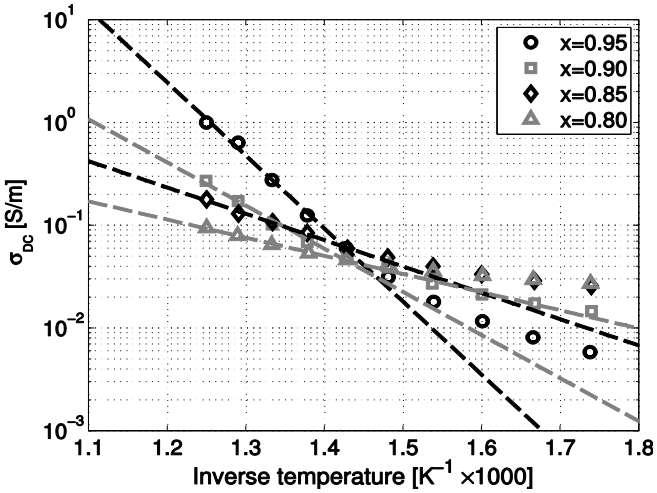

Figure 2. Static conductivity of xNBT–(1-x)LMT ceramics with different values of mole fraction of NBT as a function of inverse temperature.

Because of argon atmosphere, very high conductive losses were observed. These losses can be associated with loss of oxygen leaving ceramics at such conditions, thus forming mobile vacancies. This is why the conductivity-temperature dependencies were calculated from the dielectric data. It is possible to derive DC conductivity value having sufficient frequency data.

Solid lines in figure 1. represent the fit of the data with the following equation:

$$\sigma = A \cdot f^{n} + \sigma_{DC}.$$

Here, A and n are constants which describe frequency dependence of conductivity, and σ_{DC}

is DC conductivity. In all cases the frequency range of 1 MHz – 40 MHz was used to fit experimental data. Dependencies of static conductivity for all ceramics on inverse temperature are shown in figure 2. Solid lines represent the Arrhenius law fit:

$$\sigma_{DC} = \sigma_{DC0} \cdot e^{-\frac{E_A}{kT}}.$$

Here, σ_{DC0} represents infinite temperature static conductivity, E – activation energy, T – temperature and k – Boltzmann constant.

Step changing of activation energy was obtained on 690K, which is probably related to phase transition like in pure NBT from paralastic to ferroelastic phases [2]. The activation energy and σ_{DC0} dependence vs. NBT concentration is shown on figure 3.

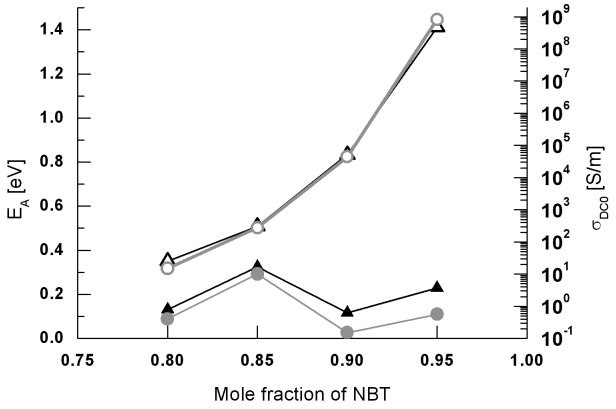

Figure 3. Activation energy (triangles) and conductivity prefactor (circles) of the static conductivity of xNBT–(1-x)LMT ceramics versus the NBT mole fraction at the temperatures lower 690K (filled dots) and higher 690K (empty dots).

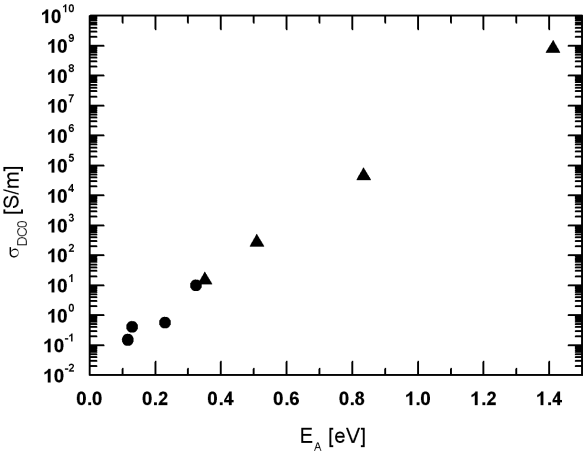

Figure 4. MN plot at the temperatures lower 690K (circles) and higher 690K (triangles).

It looks like E_A dependence on $\log(\sigma_{DC0})$ is linear:

$$\log(\sigma_{DC0}) = a + b \cdot E_A$$

Here a and b are constants. This relation is known as the Meyer-Neldel (MN) rule [3].

The performed measurements allow to conclude that increase of LMT content lowers the activation energy of static electric conductivity, which is related to oxygen vacancies. At high temperatures (above 700 K) conductivity is lower when LMT content is increased. At figure 4 we can see a straight line, which means that MN rule is valid at both phases. The origin of MN rule in NBT–LMT ceramics is not known yet.

References

[1] Saulius Rudys, Maksim Ivanov, Juras Banys, Nikolai P. Vyshatko, Aleksandr D. Shilin & Andrei N. Salak (2011): Dielectric and Impedance Spectroscopy of xNBT–(1-x)LMT Ceramics,Ferroelectrics, 417:1, 143-150.

[2] Dorcet, V; Trolliard, G.; Reinvestigation of Phase Transitions in Na0.5Bi0.5TiO3 by TEM. Part II: Second Order Orthorhombic to Tetragonal Phase Transition, Chemistry of materials 20(15) (2008)

[3] W. Meyr and H. Neldel, Z. Techn. Phys. (Leipzig) 12, 588 (1937).

Raman and IR phonons in $Sr_xBa_{1-x}Nb_2O_6$ single crystals

E. Buixaderas[1]*, I. Gregora[1], J. Hlinka[1], J. Dec[2]

[1]*Institute of Physics, ASCR, Na Slovance 2, 182 21 Prague 8, Czech Republic*
[2]*Institute of Materials Science, University of Silesia, Pl-40-007 Katowice, Poland*

The strontium barium niobate $Sr_xBa_{1-x}Nb_2O_6$ (SBN) is a ferroelectric family of solid solutions in which the content of Sr strongly influences the structure, the dielectric behavior and Curie temperature, among other properties. For Sr content $0.25 < x < 0.75$ the family crystallizes in an unfilled tetragonal tungsten-bronze structure, where a framework of oxygen octahedra, with Nb atoms at their centers, is linked forming three types of channels along the *c*-axis: square, pentagonal and triangular ones.[1] The general formula $(A)_2(B)_3(C)_1Nb_2O_6$ allows three metallic atoms to enter into the channels. The A site (inside the squared channels) is partially occupied by Sr, the B site (inside the pentagonal channels) by Sr and Ba, and the C site (inside the smallest triangular channels) is empty in SBN. The intrinsic disorder of the structure (due to partial occupancy of the channels) is the source of many unusual properties, as the strong dielectric anisotropy, and the change of dielectric character from ferroelectric to relaxor on increasing the Sr content ($x > 0.48$).[2,3] The Ba/Sr ratio affects the occupancy of the sites and, presumably, the dynamics of the phase transition.

The crystal structure of SBN in the paraelectric phase is tetragonal, probably with the centrosymmetric point group 4/*mmm*, like in other tungsten bronzes.[4,5] The ferroelectric phase is also tetragonal with the space group *P*4*bm*.[1,6] An incommensurate modulation related to the positions of oxygen atoms is present in the crystal with a two-dimensional modulation vector $\mathbf{q}=(¼+\delta)(\mathbf{a}^* \ \mathbf{b}^*)+½\mathbf{c}^*$. This modulation is enhanced by the Sr content.[7]

Dynamics of the phase transition was studied by Raman spectroscopy for several compositions.[8,9,10,11] New phonon modes were observed below the phase transition due to the symmetry change, but no clear soft mode was found. Phonon anomalies were seen, however, in some tungsten bronzes.[9,12]

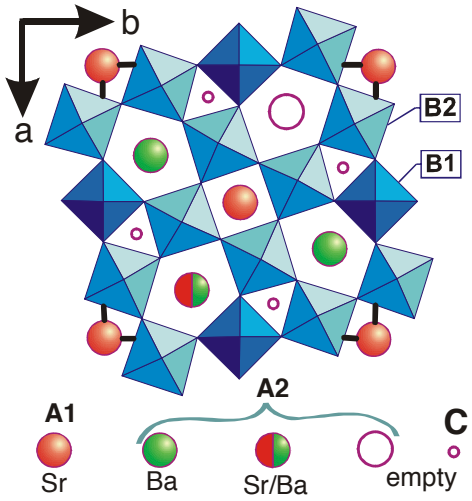

FIG. 1: Structure of the SBN crystals.

IR reflectivity spectrum of SBN-61 was studied by some of us, together with the broad dielectric spectra from THz down to MHz.[13] No soft mode was evidenced and a strong and broad relaxation appeared to be responsible for the transition. The relaxation obeys a classical slowing down from the GHz to MHz range, and it was assigned to dynamic disorder of Sr and Ba atoms at pentagonal sites. Supporting this picture, central peaks at very high temperatures were discovered by Brillouin scattering,[14] and neutron scattering[15] in SBN-70 and SBN-45 (halfwidth ~ 3meV) and assigned to the anharmonic hopping motion of Ba/Sr atoms in B sites.

Although the prevailing mechanism for the ferroelectricity in tungsten bronze samples seems to be of order-disorder type, some questions remain to be answered: what is the order parameter of the transition? Is the shift of

metallic cations relevant for the ferroelectricity? It is also not clear how the different occupancy of the sites in the channels affects the phonon parameters in the low frequency part of the spectra.

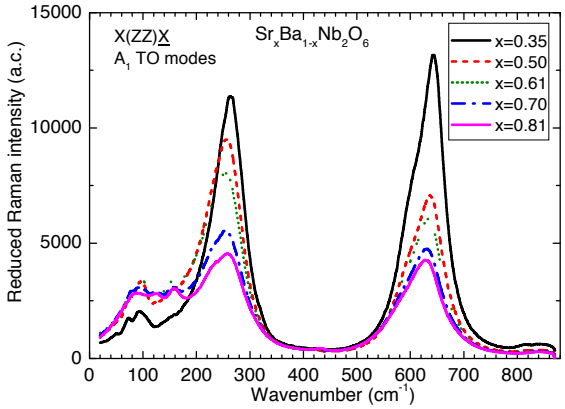

FIG. 2: Raman spectra of SBN crystals with different Sr content at room temperature in the X(ZZ)X configuration.

In these studies we measured different SBN crystals with concentrations ranging from $x = 0.35$ to 0.81 using IR reflectivity and Raman spectroscopy in the temperature interval 15-700 K. The aim of the studies is to compare past Raman data with new acquired data in more compositions and mainly with IR data, which are mostly absent in the literature.

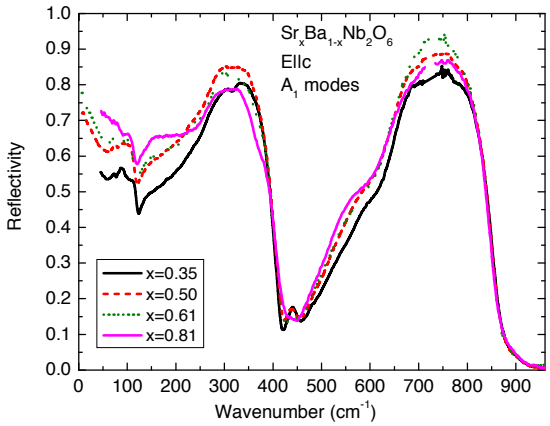

FIG. 3: IR reflectivity spectra of SBN crystals with different Sr content at room temperature for the **E||c** polarization.

We have studied the influence of the Sr/Ba distribution on the phonon parameters and we have focused on the ferroelectric member of the family ($x = 0.35$). This compound, with $T_C \sim 460$ K, is no relaxor and has no Sr/Ba disorder in the pentagonal channels. Therefore it can help to better understand the microscopic mechanism of the ferroelectricity in tungsten bronzes.

Financial support from the Czech Ministry of Education is acknowledged (Project MSMT ME08109).

* electronic address: buixader@fzu.cz

[1] P. B. Jamieson, S. C. Abrahams and J. L. Bernstein, *J. Chem. Phys.* **48**, 5048 (1968).
[2] A.M. Glass, *J. Appl. Phys.* **40**, 4699 (1969).
[3] T. Lukasiewicz, M. A. Swirkowicz, J. Dec, W. Hofman, W. Szyrski, *J. Crystal Growth* **310**, 1464 (2008).
[4] G. Burns, J.D. Axe and D.F. O'Kane, *Sol. State Comm.* **7**, 933 (1969).
[5] J. R. Oliver, R. R. Neurgaonkar and L. E. Cross, *J. Appl. Phys.* **64**, 37 (1988).
[6] T. Woike, V. Petříček, M. Dušek, N. K. Hansen, P. Fertey, C. Lecomte, A. Arakcheeva, G. Chapuis, M. Imlau and R. Pankrath,. *Acta Crystallogr B* **59**, 28 (2003).
[7] J. Schefer, D. Schaniel, V. Petříček,T. Woike, A. Cousson and M. Wohlecke, *Z. Kristallogr.* **223**, 399 (2008).
[8] K.S. Rustamov, V.S. Gorelik, Y.S. Kuzminov, C.V. Peregudov and M.M. Sushchinskyy, *Fizika Tverdogo Tela* **18**, 3416 (1976).
[9] G. Burns, F.H. Dacol, R.R. Neurgaonkar, A.S. Bhalla, and R. Guo, *Ferroelectrics* **108**, 189 (1990).
[10] R. E. Wilde, *J. Raman Spectrosc.* **22**, 321(1991).
[11] C. David, A. Tunyagi, K. Betzler, and M. Wöhlecke, Phys. stat. sol. (b) 244, 2127 (2007).
[12] L. C. Bobb, J. Dahl, I. Lefkowitz, and L. Muldawer, *Ferroelectrics* **1**, 247 (1970).
[13] E. Buixaderas, M. Savinov, M. Kempa, S. Veljko, S. Kamba, J. Petzelt, R. Pankrath and S. Kapphan, *J. Phys.: Condens. Matter* **17**, 653 (2005).
[14] F.M. Jiang, J.H. Ko, S. Kojima, *Phys. Rev. B* **66**, 184301 (2002).
[15] F. Prokert, *Phys. Status Solidi b* **113**, 239 (1982).

EPR study of $KTaO_3$:Mn nanopowder

I.S. Golovina[1], B.D. Shanina[1], I.N. Geifman[2]

[1]Institute of Semiconductor Physics of NASU, Pr. Nauki 41, 03028 Kiev, Ukraine

[2]Quality Engineering Education, Inc., Buffalo Grove, IL 60089, USA

Recently, Kleeman with co-workers studied $KTaO_3$ doped with Mn [1-3]. Average grain size of the ceramics was 1-5 μm. The appearance of ferroelectric and ferromagnetic orderings in microregions, namely the states of spin and orientation glasses, has been established. That allowed authors to attribute $K(Mn)TaO_3$ to the subclass of electro-magnetic materials, categorized as disordered multiferroics.

In the present work nanoscaled powders of $KTaO_3$ doped with different amount of manganese were synthesized for the first time. Ta powder, KNO_3, KOH and $Mn(NO_3)_2*6H_2O$ were used as the row materials for the synthesis. The concentrations of the $Mn(NO_3)_2*6H_2O$ varied from 0.1 to 20 mol.%. Morphology of the particles was studied by TEM. The location of Mn^{2+} ions in the host lattice and the type of interaction between Mn^{2+} ions were defined at every doping level by using an EPR method. X-band EPR spectra of $KTaO_3$:Mn nanopowders were obtained within the temperature interval of 77-620 K. The effect of the dopant concentration was investigated. Comparison analysis between spectroscopic parameters of single- and nanocrystals of $KTaO_3$:Mn was made.

As was shown by TEM, the particles are mostly of rectangular parallelepiped shaped with sizes of about 60 nm in side of square cross section and of 100-150 nm in length. The EPR spectra exhibit two types of signals. Signals of the first type (I, II and III in Fig.1) having the linewidth 400-1400 Oe are attributed to the FMR lines. Their intensities strongly correlate with the concentration of the $Mn(NO_3)_2*6H_2O$ and reasonably correspond to the nanoclusters formed of Mn^{2+} ions. Within the clusters an exchange coupling between Mn^{2+} ions is so strong that the long-range magnetic order appears. Signal of the second type (noticed as Mn^{2+} in Fig.1) is a conventional EPR line. It corresponds to the individual paramagnetic Mn^{2+} ions, which are non-interactive at concentrations <5 mol.% of $Mn(NO_3)_2*6H_2O$ (Fig.2). In the case the spectrum is described by the spin-Hamiltonian of axial symmetry with parameters: g=2.0022, D=0.0170 cm^{-1}, A=85*10^{-4} cm^{-1}. At concentrations from 5 to 15 mol.% the magnetic dipole interaction between individual Mn^{2+} ions appears which results in the broadening of the hyperfine resonance lines. At concentrations >15 mol.% additionally the exchange coupling begins and enhances untill at 20 mol.% the hyperfine structure of Mn^{2+} EPR spectrum disappears completely. Meanwhile, at 15-20 mol.% the intensity of the FMR signals

(especially, of signal I) increases sufficiently, reflecting the appearance of the long-range magnetic order in the nano(micro)regions. It should be noted that both individual Mn^{2+} ions and the clusters are located in the vicinity of the nanoparticle surface. In other words, they are randomly distributed surface impurity centers. As shown in Fig.2, the EPR spectrum of small ammount of individual Fe^{3+} ions was also registered. Fe^{3+} is an unavoidable impurity in the $KTaO_3$:Mn nanopowder.

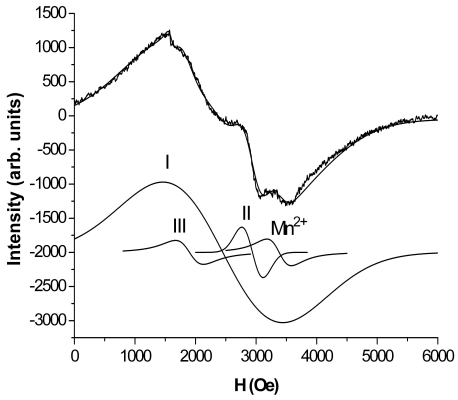

Fig.1. Experimental and theoretical EPR spectra of $KTaO_3$:Mn (15 mol.% of $Mn(NO_3)_2*6H_2O$).

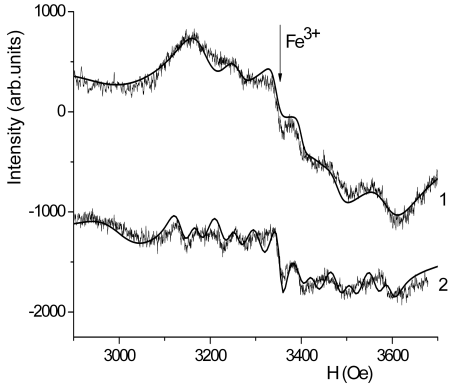

Fig.2. Experimental and theoretical EPR spectra of two samples with different amount of Mn^{2+}: 1 - 0.1 and 2 - 5 mol.% of $Mn(NO_3)_2*6H_2O$.

From the temperature dependences of the EPR spectra it was established that Mn^{2+} ions are situated in the static structural positions in $KTaO_3$:Mn nanopowder. Most likely, they replace Ta^{5+} ions and occupy the centrosymmetric places. In such a case an oxygen vacancy can be a charge compensator. If compare with a single-crystal $KTaO_3$:Mn, the charge compensator in the nanopowder is located at more distance from the Mn^{2+} ion leading to the subsequent lowering of the axial constant *D*.

References

1. V. Shvartsman, S. Bedanta, P. Borisov, W. Kleemann, A. Tkach, and P. M. Vilarinho, Phys. Rev. Lett. **101**, 165704 (2008).

2. W. Kleemann, S. Bedanta, P. Borisov, V.V. Shvartsman, S. Miga, J. Dec, A. Tkach, and P.M. Vilarinho, Eur. Phys. J. B **71**, 407 (2009).

3. V. Shvartsman, S. Bedanta, P. Borisov, W. Kleemann, A. Tkach, and P. M. Vilarinho, J. Appl. Phys. **107**, 103926 (2010).

Evaluation of defect dipole dissociation energy in rare earth and magnesium co-doped $BaTiO_3$ by TSDC (Thermally Stimulated Depolarization Current) measurement

Noriyuki Inoue[1, 2], Russell A. Maier[1], Atsushi Honda[2], Hiroshi Takagi[2] and Clive A. Randall[1]
[1]The Pennsylvania State University, [2]Murata Manufacturing Co., Ltd.

1. INTRODUCTION

There are many large application demands for the multilayer ceramic capacitors (MLCC) with longer lifetime in higher electric fields and temperatures. It is known that the degradation of MLCC under high temperature and high electric field is caused by the oxygen vacancy migration[1-4], and the degradation is suppressed by some dopants[3-8].

In this study, we focused on the oxygen vacancy in the rare earth-magnesium co-doped $BaTiO_3$, which exhibits high reliability in MLCC[8-9]. TSDC (thermally stimulated depolarization current) measurements were conducted and were sensitive to defect dipoles and ionic space charge contributions.

Earlier TSDC measurements have been shown to be a useful tool to analyze oxygen vacancies in simple dielectric materials, such as Fe-$SrTiO_3$, in terms of defect dipoles and ionic space charge distributions[10-19]. Oxygen vacancies in acceptor doped samples were trapped by the acceptor and make defect dipoles in the initial state. The oxygen vacancies dissociated from the dopants to free ionic space charges under the influence of the electric field at high temperatures[10-12]. We studied the behavior of oxygen vacancy under different temperatures and electric fields, and the kinetics of dissociation can be deduced from the change of defect dipole to ionic space charge.

2. EXPERIMENTAL PROCEDURE

$(Ba_{0.94}R_{E0.06})(Ti_{0.97}Mg_{0.03})O_3$ (R_E = Dy, Ho) samples were synthesized by conventional solid-state reactions. The starting materials were $BaCO_3$, TiO_2, $R_{E2}O_3$, and MgO, of which purities were higher than 99.9%. These materials were mixed in the desired stoichiometry for $(Ba_{0.94}R_{E0.06})(Ti_{0.97}Mg_{0.03})O_3$ and were ball-milled to achieve proper mixing. The milled fine powders were calcined in air at 1250°C. So-called ceramic green sheets were obtained by the doctor blade method, and then they were stacked and pressed. The monolithic samples were formed into 7 mm × 7 mm × 1.2 mm in size. These samples were sintered at 1500°C in air to obtain dense ceramics > 95% *T.D.*

TSDC measurements were performed using a pA meter (Hewlett Packard 4140B). In this study, the typical profile of TSDC measurement procedures are as follows: the specimen was heated to a polarization temperature T_P, T_P = 120° - 260°C, and polarized for different polarization time, t_P, t_P = 100 - 10800 sec. using a constant dc electric field, E_P, E_P = 100 V/mm. It was then cooled to a starting temperature T_0, T_0 = 100°C, while maintaining the electric field. The E_P was removed and electrodes were then short-circuited for 10 min to depolarize some polarization with short relaxation times and to stabilize the current values at T_0. Then TSDC was recorded as a function of temperature at a constant heating rate q, q = 4°C/min.

3. RESULTS AND DISCUSSION

Figure 1 shows typical results of TSDC measurements on $(Ba_{0.94}Ho_{0.06})(Ti_{0.97}Mg_{0.03})O_3$ with polarization field E_p = 100 V/mm and polarization temperature T_P = 140°C. The spectra indicate two peaks at temperatures around 150°C and 250°C, respectively. Using the theoretical origins of TSDC, we can deduce the fundamental origins of the depolarization currents associated with each peak.[9–18]

A low temperature peak around 150°C is identified to be of dipole origin and is assumed to be the associated defect dipole of oxygen vacancy and an acceptor ion occupying the Ti site in $BaTiO_3$. A high temperature peak around 250°C is identified to be of ionic space charge movements. The temperature, which shows maximum current density, T_m, of high temperature peak increased in a stronger polarization condition. This tendency is known to be caused by the charge pile up and the formation of ionic space charge regions.

These two kinds of peaks were observed in all samples and can be distinguished through experimental methods.

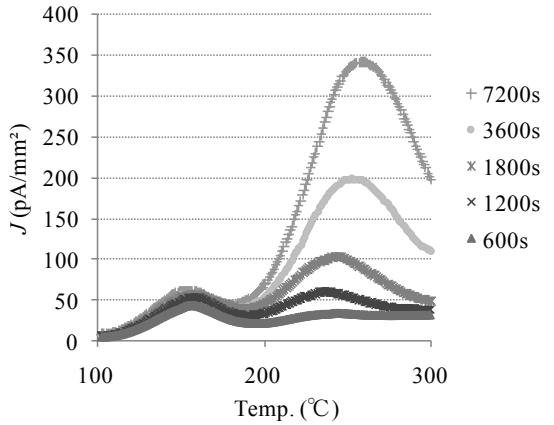

Fig. 1. TSDC spectra for $(Ba_{0.94}Ho_{0.06})(Ti_{0.97}Mg_{0.03})O_3$ with E_P = 100 V/mm, T_p = 140°C, and t_p = 600 – 7200 s.

Figure 2 show the polarization time dependence of defect dipole peak intensities for $(Ba_{0.94}Dy_{0.06})(Ti_{0.97}Mg_{0.03})O_3$ for the polarization conditions: E_P = 100 V/mm and T_p = 220°C. Defect dipole depolarization peaks showed a constant decrease with t_p. These peak intensity decreases were caused by the oxygen vacancy dissociation from defect dipoles to free ionic space charges.

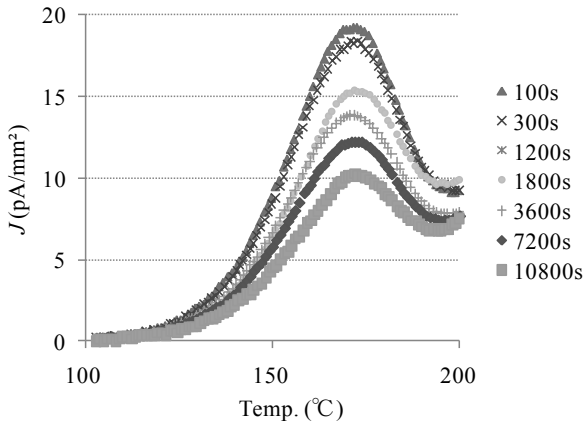

Fig. 2. TSDC spectra for $(Ba_{0.94}Dy_{0.06})(Ti_{0.97}Mg_{0.03})O_3$ with E_P = 100 V/mm, T_p = 220°C, and t_p = 100 – 10800 s.

Figure 3 shows the polarization time dependence of the current density maximum for defect dipole peaks, J_{max} for $(Ba_{0.94}Dy_{0.06})(Ti_{0.97}Mg_{0.03})O_3$. A significant decrease in J_{max} in this t_p range occurred for T_p > 200°C by the dissociation reaction of defect dipoles.

During TSDC measurements, three distinguishable states are considered: (A) initial state: associated random defect dipoles, (B) second state: oriented defect dipoles, and (C) final state: ionic space charges dissociate from the defect dipoles and move freely. Such a consecutive reaction model is one possible candidate to evaluate the kinetics of the dissociation reaction. However, the data of state (A) is the concentration of random defect dipoles and cannot be obtained by TSDC measurement.

In the case of the $(Ba_{0.94}Dy_{0.06})(Ti_{0.97}Mg_{0.03})O_3$ sample, the orientation of defect dipoles by electric field, reaction (A) to (B), is almost completed by 200°C, and oxygen vacancy dissociation reaction begins over 200°C, so the reaction rate constant of (A) to (B) is much larger than the one of (B) to (C). As a result, it is possible to assume the dissociation reaction (B) to (C) as a pseudo-1st order reaction. Fitting results by the 1st order reaction for defect dipole concentration decreases for T_p > 200°C in $(Ba_{0.94}Dy_{0.06})(Ti_{0.97}Mg_{0.03})O_3$ are shown in Fig. 3. A significant linear correlation was obtained from the fitting, and the reaction rate constants were evaluated by the 1st order rate reaction. Figure 4 shows the Arrhenius plot of the dissociation reaction for $(Ba_{0.94}Dy_{0.06})(Ti_{0.97}Mg_{0.03})O_3$. The evaluated activation energy of the dissociation reaction was 1.2 eV.

We also observed the change of dissociation energy by the resistivity degradation of the sample by applying electric field at high temperature. The change of the energy was comparable with the calculated oxygen vacancy stabilization energy by *ab-initio* calculation for rare earth and magnesium co-doped $BaTiO_3$ model[9].

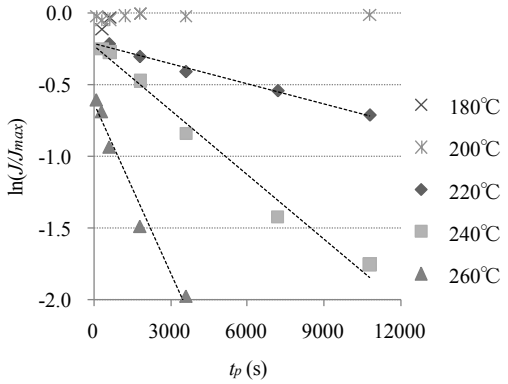

Fig. 3. Polarization time dependence of $\ln(J/J_{max})$ for $(Ba_{0.94}Dy_{0.06})(Ti_{0.97}Mg_{0.03})O_3$ with E_P = 100 V/mm, T_p = 220 - 260°C, and t_p = 100 - 10800s.

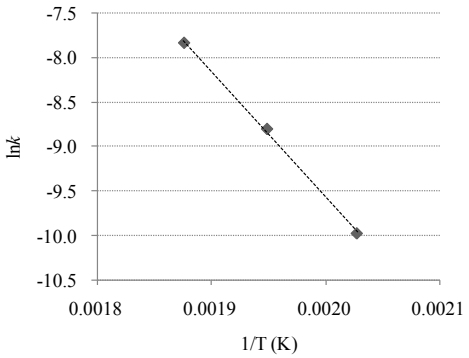

Fig. 4. Arrhenius plot for $(Ba_{0.94}Dy_{0.06})(Ti_{0.97}Mg_{0.03})O_3$, where k is dissociation reaction rate constant.

4. REFERENCES

[1] G. Yang, *et al*., *J. Appl. Phys.* **94**, 5990 (2003).
[2] R. Waser, *et al*., *Mater. Sci. Eng*., **A 109**, 171 (1989).
[3] Y. Nakano, *et al*., *Ceram. Trans.*, **32**, 119 (1993).
[4] H. Saito, *et al*., *Jpn. J. Appl. Phys. Part 1*, **30**, 2307 (1991).
[5] Y. Sakabe, *et al*., *Jpn. J. Appl. Phys.,* **41**, 5668 (2002).
[6] H. Kishi, *et al*., *Jpn. J. Appl. Phys*., **38**, 5452 (1999).
[7] Y. Tsur, *et al*., *J. Electroceram.,* **7**, 25 (2001).
[8] T. Okamatsu, *et al*., *Key Eng. Mater.,* **421-422**, 301 (2010).
[9] A. Honda, *et al*., *Key Eng. Mater.,* **485**, 23 (2011).
[10] W. Liu and C. A. Randall, *J. Am. Ceram. Soc.*, **91**, 3245 (2008).
[11] W. Liu and C. A. Randall, *J. Am. Ceram. Soc.*, **91**, 3251 (2008).
[12] S. Yoon, *et al*., *J. Am. Ceram. Soc*., **92**, 1766 (2009).
[13] P. Braunlich, Thermally Stimulated Relaxation in Solids. Springer, New York (1979).
[14] T. Fukami, *et al*., *Jpn. J. Appl. Phys.*, **26**, 46 (1987).
[15] S. Devautour, *et al*., *J. Appl. Phys.*, **82**, 5057 (1997).
[16] T. Hino, *IEEE Trans. Electr. Insul.*, **EI-15**, 301 (1980).
[17] I. Chen, *J. Appl. Phys*., **47**, 2988 (1976).
[18] H. Nicholas and J. Woods, *Br. J. Appl. Phys.*, **15**, 783 (1964).
[19] C. Bucci and R. Fieschi, *Phys. Rev. Lett.*, **12**, 16 (1964).
[20] R. D. Shannon and O. T. Prewitt, *Acta. Cryst.* **B-25** ,925 (1968).
[21] K. Takada, *et al*., *Adv. Ceram*., **19**, 147 (1987)
[22] C. Freeman, *et al*., *J. Mater. Chem.*, **21**, 4861 (2011).

Direct Atomic-Scale Measurement of Oxygen Stoichiometry in Cobaltite Thin Films

Young-Min Kim,[1]Michael D. Biegalski,[1]Jun He,[1,2] Hans M. Christen,[1] Sokrates T. Pantelides,[2.1] Stephen J. Pennycook,[1] Albina Y. Borisevich[1]

[1]Oak Ridge National Laboratory, Oak Ridge, TN
[2]Vanderbilt University, Nashville, TN

Functionality of ionic materials and devices exemplified by solid oxide fuel cells and memristors is underpinned by the dynamics of oxygen vacancies. Of interests for these applications is vacancy injection and annihilation at the gas-solid surfaces, vacancy transport in the bulk and across the internal interfaces, as well as vacancy ordering and associated changes in the connectivity of the host lattice. These processes are sensitively affected by the presence of structural defects, interfaces, and strain field that couple to the electrochemical potential of oxygen in the host lattice. Hence, to decipher the interplay between local ionic and physical phenomena and to elucidate contributions of defects and interfaces to the oxygen transport properties, local probing of oxygen distribution with atomic precision is required. Here, we explore a direct approach to mapping oxygen concentration in ionic oxides via unit-cell-by-unit-cell lattice parameter mapping by aberration-corrected scanning transmission electron microscopy (STEM) [1] and explore the coupling between the ionic behavior and collective tilts in the network of oxygen octahedra.

As a model system, we chose lanthanum/strontium cobaltite ($La_{0.5}Sr_{0.5}CoO_{3-x,}$ LSCO), a prototypical material for SOFC cathodes. In the pristine state, LSCO is characterized by the presence of the $a^-a^-a^-$ tilt system giving rise to the rhombohedral $R\bar{3}c$ state. At the same time, vacancy ordering occurs in the (001) pseudocubic direction, forcing tetragonal symmetry. This symmetry mismatch suggests that tilts can affect the vacancy ordering [2]. Here, LSCO films were grown by Pulsed Laser Deposition in identical conditions on two different substrates, $La_{0.3}Sr_{0.7}Al_{0.65}Ta_{0.35}O_3$ (LSAT, cubic) and $NdGaO_3$ (NGO, orthorhombic). These substrates have nearly identical lattice parameters, but different symmetry of the oxygen octahedral network. STEM imaging revealed oxygen vacancy ordering in both samples, as detected both by Electron Energy Loss Spectroscopy (EELS) and by lattice parameter mapping (Fig. 1). Surprisingly, the film on NGO appears to be a type of brownmillerite, $La_{0.5}Sr_{0.5}CoO_{2.5}$ [3], while the film on LSAT is less oxygen deficient. As oxygen-vacancy induced global expansivity have been demonstrated as a direct gauge to measure the overall oxygen content in bulk experiments [4], it is revealed that comparison of measured lattice parameters with the first-principles calculations on atomic scale allows us to reconstruct the local lattice spacing-oxygen concentrations trends. In $La_{0.5}Sr_{0.5}CoO_{2.5}$/NGO films, EELS reveals different valence states of Co at the interface for different interface terminations. These studies suggest that (1) changes in octahedral tilts can

induce changes in oxygen stoichiometry of the vacancy ordered structures and (2) local vacancy concentration can be quantitatively determined by STEM.

* This research is sponsored by the Materials Sciences and Engineering Division (YMK, JH, SJP, AYB) and Scientific User Facilities Division (MDB, HMC), Office of BES of the U.S. DOE, and by appointment (YMK) to the ORNL Postoctoral Research Program administered jointly by ORNL and ORISE.

References

[1] A. Borisevich et al., Phys. Rev. Lett. **105**, 087204 (2010).
[2] J. He et al., Phys. Rev. Lett. **105**, 227203 (2010).
[3] T. G. Parson et al., Chem Mater. **21**, 5527 (2009).
[4] X. Chen et al., Chem. Mater. **17**, 4537 (2005).

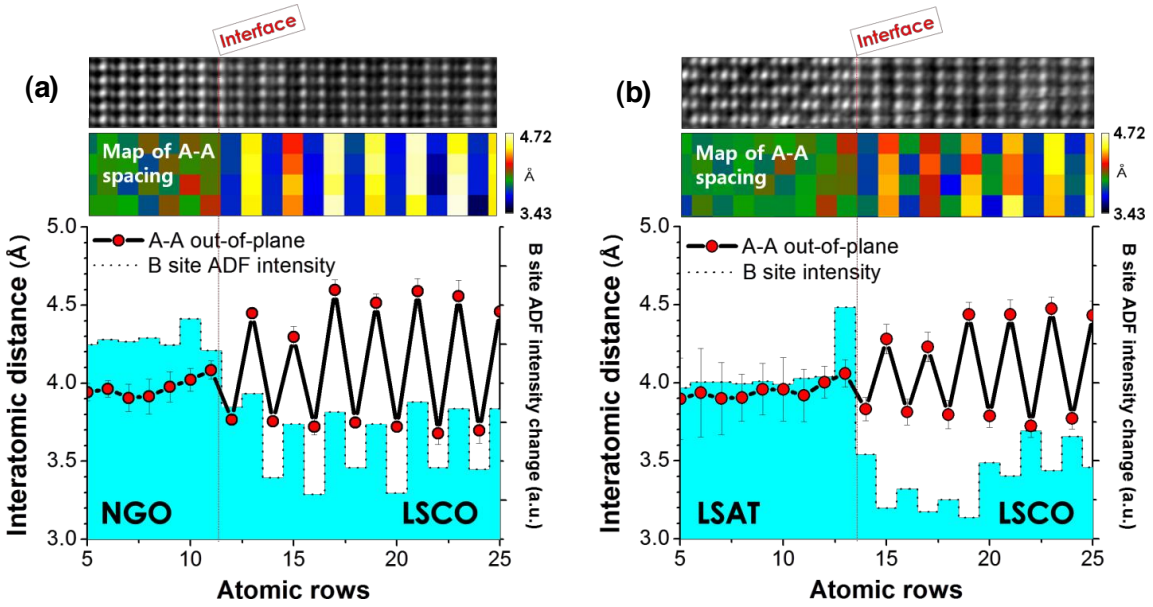

Figure 1. Unit-cell-by-unit-cell lattice parameter mappings from ADF STEM images: Top-most images on both sides represent ADF STEM images of (a) LSCO on NGO and (b) LSCO on LSAT, respectively, taken at the direction of pseudo-cubic [110]. The false color maps underneath the respective ADF images describe how much the interatomic distance of A-site cations in the ABO_3 structure vary two-dimensionally. Averaged change of the lattice parameter over all rows of the maps and the variation of B-site ADF intensities are plotted at the bottoms of each image. Note that the interfaces are clearly defined by tracking the B-site cation ADF intensities across the interface.

Development of molecular-beam epitaxy for in-situ synchrotron x-ray study of layered complex oxides

J. H. Lee,[1] S.-H. Chang,[2] I. C. Tung,[3] S. Nakhmanson, J. Eastman,[2] D. Fong,[2] H. Hong,[1] J. W. Freeland[1]

[1] Advanced Photon Source, Argonne National Laboratory, Argonne, Illinois 60439, USA

[2] Materials Science Division, Argonne National Laboratory, Argonne, Illinois 60439, USA

[3] Materials Science and Engineering, Northwestern, Evanston, Illinois 60208 USA

The layered complex oxide materials offer a broad range of functionalities including ferroelectric, magnetic, and catalytic properties. Unfortunately, the growth of such oxide materials remains a major challenge due to the lack of quantitative feedback during synthesis. For the systematic exploration of oxide synthesis, we have developed world's first reactive molecular-beam epitaxy system with in-situ synchrotron x-ray scattering capability. Our molecular-beam epitaxy is equipped with a x-ray diffractometer, a highly concentrated ozone supply, and differentially-pumped effusion cells. During synthesis, x-ray reflectivity, x-ray crystal truncation rod, and reflection high electron energy diffraction can provide real-time information on surface reconstructions, interdiffusion at the interface, film relaxation, and composition. Our initial x-ray studies have been focused on the growth of PbO, TiO2, and the layered oxide PbSr2Ti2O7 by using reactive molecular-beam epitaxy. Layered oxide PbSr2Ti2O7 is predicted to exhibit exceptional dielectric and piezoelectric behavior, but has never been synthesized before.[1] Layering of each oxide layer (PbO, SrO, and TiO2) at growth temperature has been investigated to improve film stoichiometry and structure. We anticipate that the

combination of reactive molecular-beam epitaxy and in situ x-rays will contribute substantially to the advancement of synthesis science for complex oxide heterostructures.

[1] S.M. Nakhmanson and I. Naumov, Phys. Rev. Lett. 104, 097601 (2010).

Ferroelectric PLZT Films Grown on Metal Foils by Chemical Solution Deposition

Beihai Ma, Manoj Narayanan, Shanshan Liu, Sheng Chao, Sheng Tong, and U. (Balu) Balachandran

Energy Systems Division, Argonne National Laboratory, Argonne, IL 60439, USA

Abstract – Ferroelectric $Pb_{0.92}La_{0.08}Zr_{0.52}Ti_{0.48}O_3$ films were formed on base metal foils by chemical solution deposition. Their dielectric properties were then characterized over a temperature range of -50 to 150ºC. The following results were obtained: a dielectric constant of ≈700 and dielectric loss of ≈0.07 at -50ºC, dielectric constant of ≈1300 and dielectric loss of ≈0.08 at 20ºC, and a dielectric constant of ≈2200 and dielectric loss of ≈0.06 at 150ºC. At room temperature, a leakage current density of ≈7 x 10^{-9} A/cm^2 and energy density of ≈85 J/cm^3 were measured.

INTRODUCTION

Embedding capacitors into printed wire boards (PWBs) is highly desirable to free up surface space, increase device reliability, minimize electromagnetic interference and inductance loss, and reduce manufacturing cost [1,2]. While this technology has primarily received attention for decoupling capacitors in microelectronic applications [3], it can also be extended to higher voltage applications. One area where it holds particular promise is applications that require high capacitance density and high volumetric efficiency, such as power electronics in plug-in hybrid electric vehicles. However, the integration of high-dielectric-constant (κ) ceramics into PWBs is challenging because of the incompatibility of the different processing conditions involved. Polymer layers in a PWB cannot withstand the high temperatures (600-800°C) required for processing the ceramic dielectric films to obtain the desired crystalline structures. Development of these crystalline structures becomes extremely difficult, if not impossible, at reduced processing temperatures [4]. Great success has been achieved by a film-on-foil approach where the ceramic films were first coated by chemical solution deposition on a thin base metal foil and crystallized at high temperatures [5-6]. These coated foils, film-on-foil capacitors, can then be embedded into PWBs. Here, we present our recent progress in the development of $Pb_{0.92}La_{0.08}Zr_{0.52}Ti_{0.48}O_3$ (PLZT 8/52/48) films on Ni foils.

EXPERIMENT

Nickel foils were mechanically polished and cleaned with acetone and then methanol prior to being coated. Precursor solutions of $LaNiO_3$ (LNO) and PLZT 8/52/48 were prepared by a modified 2-methoxyethanol synthesis route [7]. Detailed experimental conditions are reported elsewhere [8]. The LNO precursor solution (0.3 M) was first spin coated on Ni substrates, pyrolyzed at 450°C for 5 min, and annealed at 625°C for 2-5 min. This process was repeated three times to build the desired 0.4-μm buffer film. Subsequently, PLZT precursor solution (0.5 M) was spin coated on the LNO-buffered substrates, pyrolyzed at 450°C for 10 min, and annealed at 650°C for 2-5 min. This process was repeated to build the desired thickness. A final annealing at 650°C for 30 min was implemented to ensure complete transformation to the perovskite phase. All annealing and pyrolysis were done in air. Platinum (Pt) electrodes of ≈250-μm diameter and ≈100-nm thickness were deposited on the PLZT films by electron-beam evaporation. An Agilent E4980A precision LCR Meter was used to determine the capacitance and dissipation factor under an applied bias field. A Radiant Technologies Precision Premier II tester measured the hysteresis loops. A Keithley 237 high-voltage source meter measured the time-relaxation leakage current.

DISCUSSION

Figure 1 shows the dielectric constant and loss for PLZT/LNO/Ni capacitors as a function of applied field measured at -50, 20, and 150ºC. We obtained the following: at -50ºC and zero field, a dielectric constant of 700 and dielectric loss of ≈0.07; at room temperature and zero field, a dielectric constant of 1300 and dielectric loss of ≈0.08; and at 150ºC and zero field, dielectric constant of 2200 and dielectric loss of ≈0.06. The "dielectric tunability," defined as the dielectric constant at field E divided by the value at zero field, was determined to be ≈50% at room temperature and applied field E = 100 kV/cm. Beyond a field of 100 kV/cm, the dielectric constant changed more gradually.

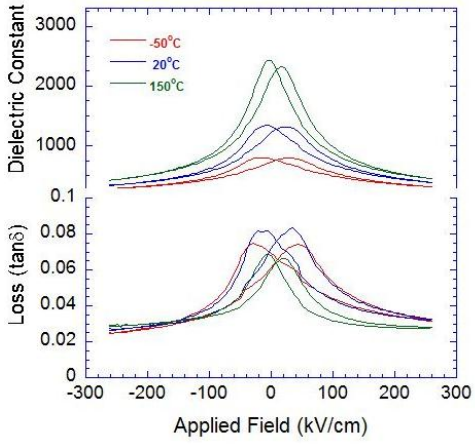

Figure 1. Field-dependent dielectric properties of PLZT/LNO/Ni capacitor at -50, 20, and 150ºC.

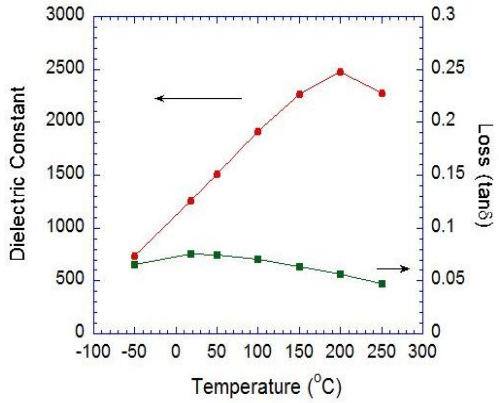

Figure 2. Temperature-dependent dielectric properties of PLZT/LNO/Ni capacitor.

The PLZT films deposited on LNO-buffered Ni foils were phase pure with no preferred crystallographic orientation. No crack or delamination occurred with PLZT films up to 5 µm. Figure 2 shows the temperature-dependent dielectric properties of a PLZT/LNO/Ni sample measured within the temperature range of -50 to 250°C. The dielectric constant increased while dissipation factor decreased with increasing temperature from room temperature to 200°C. Maxima of the dielectric constant and dissipation factor occurred at ≈200°C and room temperature, respectively.

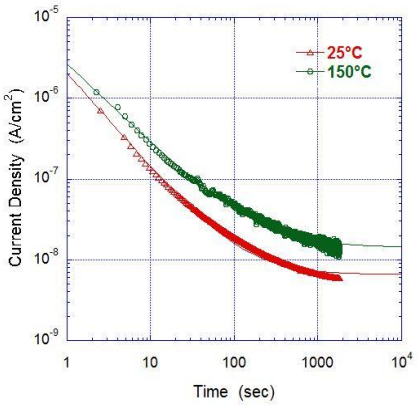

Figure 3. Time-relaxation current density of PLZT/LNO/Ni capacitor mearsured at room temperature and 150°C.

Figure 3 shows the time relaxation of the current density measured on a PLZT/LNO/Ni film-on-foil capacitor (1.15-µm thick PLZT) at 25°C and 150°C with a constant bias potential of 10 V (corresponding to an applied electrical field of ≈87 kV/cm) across the top and bottom electrodes. The measurements were conducted by keeping the top Pt electrode positive and the bottom Ni electrode grounded. Both curves showed strong initial time dependence, indicating depolarization effects. The current density measured at 150°C is roughly a factor of two higher than the value measured at 25°C. Fitting data to the Curie-von Schweidler equation [9], we obtained n = 0.99 and 0.97 and leakage current densities of 6.6 x 10^{-9} and 1.4 x 10^{-8} A/cm^2 at 25 and 150°C, respectively.

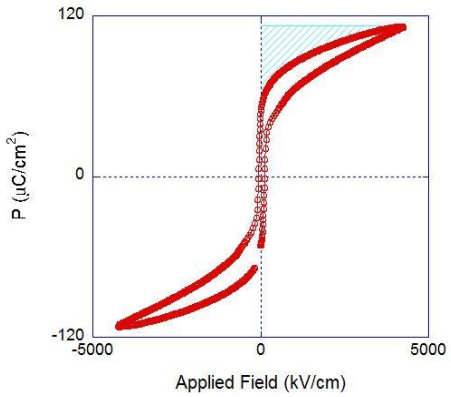

Figure 4. P-E loops of PLZT/LNO/Ni capacitor.

Figure 4 shows the high-field P-E loop with a maximum applied voltage of 500 V on a 1.15-µm-thick PLZT/LNO/Ni sample. By fitting and integration of the discharging portion of the P-E hysteresis loop curve, we measured an energy density of ≈85 J/cm^3.

CONCLUSIONS

We have grown high-quality PLZT on Ni foils to form film-on-foil capacitors that can be embedded into PWBs. Using an LNO buffer between PLZT and Ni foils not only obviates the parasitic low-permittivity interfacial NiO formation that would reduce the overall capacitance, but also allows the film-on-foil capacitors to be processed in air. With PLZT grown on LNO-buffered Ni, we measured a dielectric constant of ≈700 and dielectric loss of ≈0.07 at -50ºC, dielectric constant of ≈1300 and dielectric loss of ≈0.08 at 20ºC, and a dielectric constant of ≈2200 and dielectric loss of ≈0.06 at 150ºC. At room temperature, leakage current density of ≈7×10^{-9} A/cm^2 and energy density of ≈85 J/cm^3 were measured.

ACKNOWLEDGMENT

Work was supported by the U.S. Department of Energy, Vehicle Technologies Program, under Contract DE-AC02-06CH11357.

REFERENCES

[1] W. Borland, M. Doyle, L. Dellis, O. Renovales, and D. Majumdar, Mater. Res. Soc. Symp. Proc., 833, 143-151 (2005).
[2] D. Nelms, R. Ulrich, L. Schaper, and S. Reeder, Proceedings of the 48th IEEE Electronic Components and Technology Conference, pp. 247-251, Institute of Electrical and Electronic Engineers, Piscataway, NJ (1998).
[3] C. Chiang and D.B. Fraser, US Patent # 6949831B2, 2005.
[4] Y. Zhu, J. Zhu, Y.J. Song, and S.B. Desu, Appl. Phys. Lett., 73, 1958-1960 (1998).
[5] J. Ihlefeld, B. Laughlin, A. Hunt-Lowery, W. Borland, A. Kingon, and J.P. Maria, J. Electroceramics, 14 [2], 95-102 (2005).
[6] J.T. Dawley and P.G. Clem, Appl. Phys. Lett., 81, 3028 (2002).
[7] Q. Zou, H. E. Ruda, and B. G. Yacobi, Appl. Phys. Lett., 78, 1282-1284 (2001).
[8] B. Ma, D.K. Kwon, M. Narayanan, and U. Balachandran, Electroceramics 22, 383-389 (2007).
[9] K. Jonscher, *Dielectric Relaxation in Solids*, Chelsea Dielectrics Press, London (1983).

Influence of Symmetry on the Octahedral Rotations of Epitaxial $RNiO_3$ Thin Films

I. C. Tung,[1,2] Jian Liu,[3] B. Gray,[3] J. Chakhalian,[3] J. M. Rondinelli,[2] E. A. Karapetrova,[2] J. H. Lee,[2] M. J. Bedzyk,[1] and J. W. Freeland[2]

[1]*Department of Materials Science and Engineering, Northwestern University*
[2]*Advanced Photon Source, Argonne National Laboratory*
[3]*Department of Physics, University of Arkansas*

Understanding the structural and electronic behavior of ABO_3 thin films subjected to confinement, lattice misfit and broken symmetry at the interface in the ultra-thin limit is fundamentally important for the rational design of new materials [1]. However, the epitaxial strain will not only change the in-plane lattice constants but also the octahedral rotations connected to bond angles and crystallographic symmetry. Here we present a study of the effect of the bulk lattice symmetry on octahedral rotations under epitaxial strain in thin films of $RNiO_3$ (R=La, Pr, Nd) grown on various substrates by pulsed laser deposition. A combination of high-resolution x-ray diffraction, polarization-dependent soft x-ray absorption spectroscopy, and first-principles density functional calculations has been applied to elucidate structural and electronic properties of the samples.

Film structure was studied by X-ray scattering experiments in the X-ray Diffraction Facility at Northwestern University. Figure 1 shows the X-ray reflectivity along the 00L CTR of the 20 unit cell (u.c.) $LaNiO_3$ (LNO) and 15 u.c. $NdNiO_3$ (NNO) on $SrTiO_3$ (001) and the K = 0 reciprocal space maps around the off-specular (103) Bragg peaks are shown in the inset. Here we experimentally determine that out-of-plane lattice constants of the LNO film and NNO film are 3.83±1 Å and 3.75±1 Å, respectively. The results for NNO film are consistent with an out-of-plane contraction that is expected for a volume conservation scenario. Surprisingly, despite the LNO film was coherently strained by 1.8% tensile strain, it shows an out-of- plane lattice constant almost the same as the bulk value. The similarity in lattice mismatches and different in crystal structure between the films indicated that symmetry in addition to lattice matching is a critical factor in epitaxially strain thin film. This anomalous behavior indicates that there is probably a new strain-induced orbital configuration.

To explore possible modification of local Ni orbital configuration, XAS spectra of NNO and LNO films on STO substrates were measured where both films are in the metallic phase. To elucidate the origin of the unusual asymmetry in the strain-induced structural property and the coupling between epitaxial strain and oxygen octahedral rotations of strained $RNiO_3$ films, octahedral rotations in the strained perovskite oxide thin films grown by PLD were studied by measuring the oxygen positions via X-ray diffraction [2]. Using theory to gain insight into the strain response of the crystal structure, we are able to connect the octahedral rotation pattern to the magnitude of the Jahn-Teller distortion observed under strain.

This work made use of the J. B. Cohen X-Ray Diffraction Facility supported by the MRSEC program of the National Science Foundation (DMR-1121262) at the Materials Research Center of Northwestern University. Work at the Advanced Photon Source, Argonne is supported by the U.S. Department of Energy, Office of Science under Contract No. DE-AC02-06CH11357.

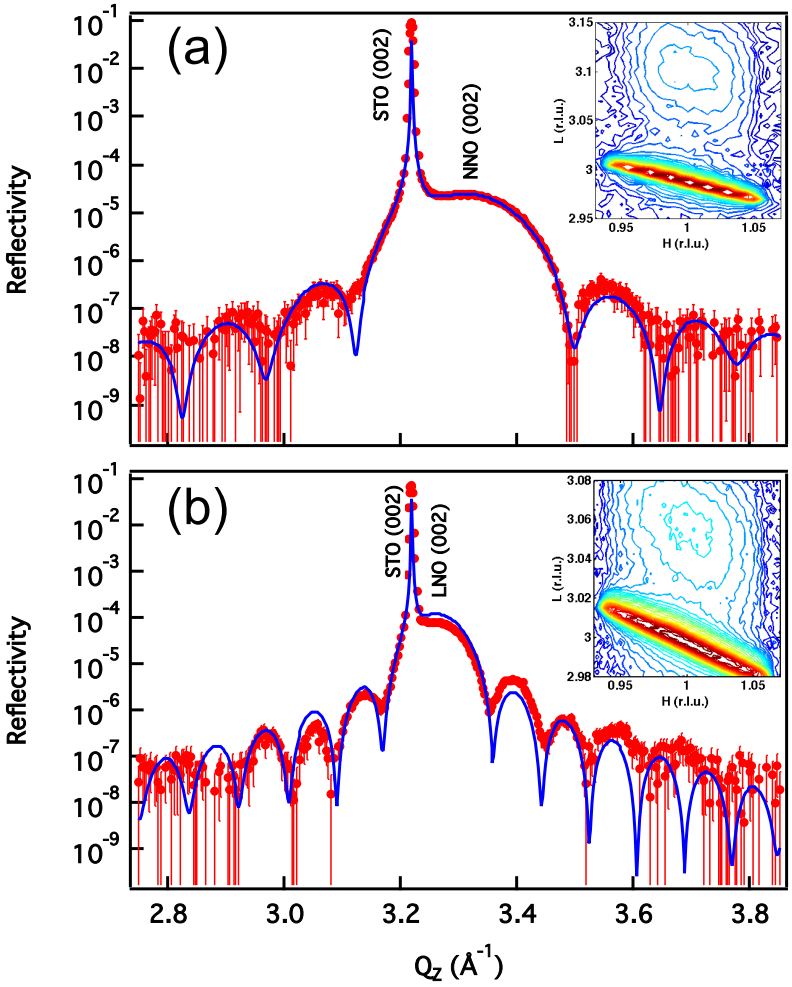

FIG. 1. X-ray diffraction data (dots) and fit (solid line) for scattering along the (00L) specular CTR through the (002) Bragg peaks of the $SrTiO_3$ substrate and (a) $LaNiO_3$ and (b) $NdNiO_3$ film. The inset shows the K=0 reciprocal space map around the (103) Bragg reflection for the (a) LNO and (b) NNO thin film and STO substrate.

[1] J. Chakhalian et al., *Phys. Rev. Lett.*, 107, 116805 (2011).
[2] S. J. May et al., *Phys. Rev. B,* 82, 014110 (2010).

Structural Investigation of Ultrathin $BiFeO_3$ Films on $SrTiO_3$ (001) Substrates

Yongsoo Yang[1], Christian M. Schlepütz[2], Carolina Adamo[3], Darrell G. Schlom[3] and Roy Clarke[1]
[1] *Department of Physics, University of Michigan, Ann Arbor, MI 48109, USA*
[2] *X-ray Science Division, Advanced Photon Source, Argonne National Laboratory, Argonne, IL 60439, USA*
[3] *Department of Materials Science and Engineering, Cornell University, Ithaca, NY 14853, USA*

Bismuth Ferrite ($BiFeO_3$: BFO) is one of very few materials exhibiting multiferroic properties at room temperature, being both ferroelectric ($T_C \sim 1103$ K) and G-type antiferromagnetic ($T_N \sim 643$K) [1]. In its bulk form, it possesses a rhombohedrally distorted quasi-cubic perovskite structure with ferrodistortive displacements along the (111) direction, giving rise to a spontaneous polarization in the same direction. The structure of epitaxial thin films, however, depends critically on the amount of substrate-induced strain. BFO thin films grown on $SrTiO_3$ (STO) substrates (-1.4% compressive strain) have been shown to exhibit an R-like monoclinic structure (M_A) for films thicker than 26 nm [2-3].

Although it is already reported that the BFO thin film structure depends strongly on thicknesses [4], few structural investigations on ultrathin films of less than 26 nm thickness were reported. We have studied five ultrathin BFO thin films (3, 4, 5, 6, and 10 unit cells thick) on STO substrates with surface x-ray diffraction (SXRD). Out-of-plane crystal truncation rods (CTRs) were measured for integer-order and half-integer-order peaks in terms of substrate (STO) reciprocal lattice units. Moreover, reciprocal space images during CTR scans, which are obtained from a PILATUS 100K area detector, allowed us to reconstruct 3-dimensional reciprocal space maps (RSMs).

Half-integer-order peak measurements showed that the half-order peaks exist only if h, k, and l are all half integer and $h \neq k$. (FIG. 1) This indicates that the films have an $a^0b^0c^-$ octahedra tilt pattern [4], which is incompatible with the theoretically estimated tilt pattern for R-like BFO films [2].

Furthermore, any monoclinic distortion results in a splitting pattern of the BFO film Bragg peaks in the 3D RSMs, which provides information about the film structure [2]. Although our experimental setup does not provide sufficient resolution to detect splittings in the in-plane direction, the expected out-of-plane splitting for the M_A phase should be observable. For the reported monoclinic shear angle of 0.65° [3], the out-of-plane splitting should be 0.068 in reciprocal lattice units of cubic STO, as experimentally observed for thicker films [2]. As can be seen in FIG. 2, we do not observe any such splitting in the RSMs of ultrathin film peaks.

Our results indicate that ultrathin BFO films have a structure which is different compared to the reported structures of thicker films. Further studies are ongoing to quantify the octahedra tilt angles from the measured half-order peaks, and to investigate the structural trend as a function of film thickness beyond 10 unit cells.

Acknowledgments: This work is supported in part by the U.S. Department of Energy (Contract No. DE-FG02-06ER46273). Measurements were performed at sector 13-BMC, 13-IDC, and 33-IDD, Advanced Photon Source, Argonne National Laboratory, USA (The APS is operated under DOE contract No. DE-AC02-06CH11357).

References:

[1] J. Wang et al., *Science* **299**, 1719 (2003).
[2] H. Christen et al., *Phys. Rev. B* **83**, 144107 (2011).
[3] M. Holcomb et al., *Phys. Rev. B* **81**, 134406 (2010) .
[4] M. Glazer, *Acta Cryst.* **A31**, 756 (1975) .
Corresponding author: Yongsoo Yang, e-mail: ysyang@umich.edu

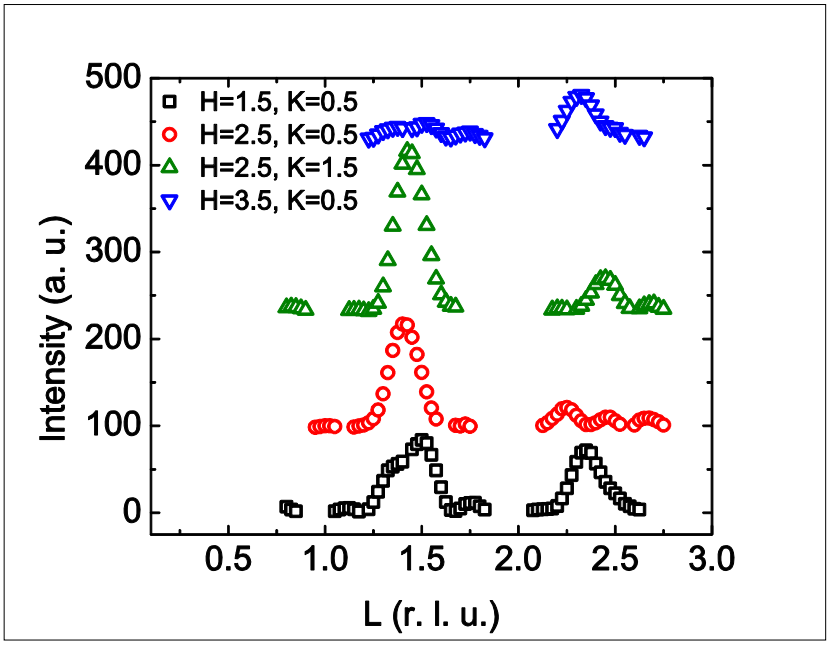

FIG. 1 Half-order peaks of 6ML film.

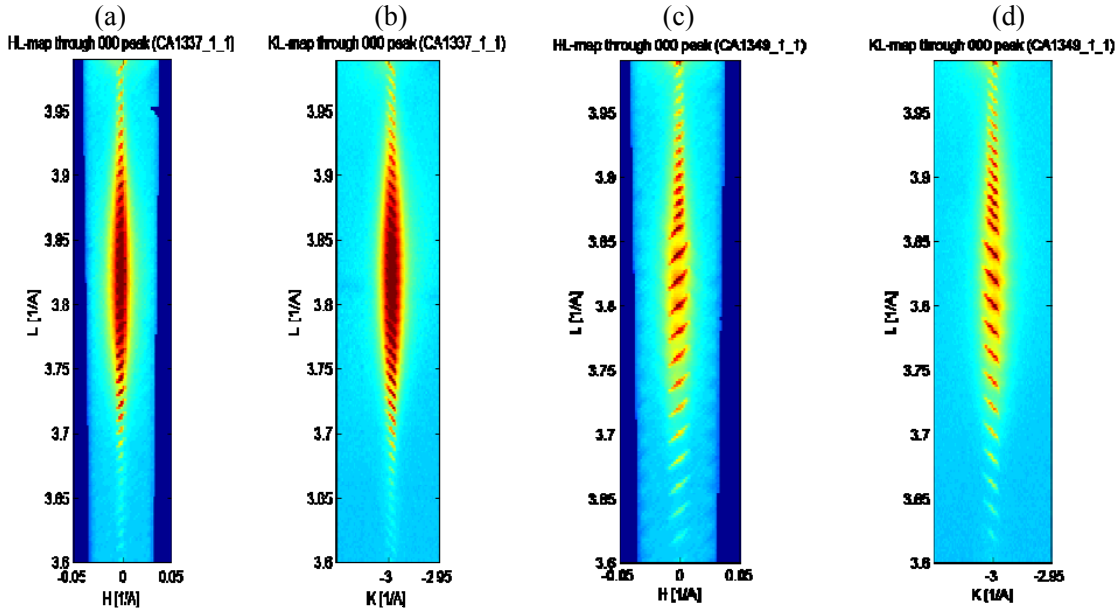

FIG. 2 Reciprocal space maps for BFO $(303)_{pc}$ peak. (a) HL-map of 10 monolayer (ML) film (b) KL-map of 10ML film (c) HL-map of 6ML film (d) KL-map of 6ML film

The fine structures of intense signals are CTRs of the STO substrate. They are actually continuous rods in reciprocal space, but we discretely sampled the reciprocal space during the scan, which resulted in those fine structures.